MAGNETOTUNNELLING IN SEMICONDUCTOR HETEROSTRUCTURES

by

TIMOTHY MARK FROMHOLD, B.Sc.

Thesis submitted to the University of Nottingham

for the degree of Doctor of Philosophy

May 1990

CONTENTS

CHAPTER FIVE: TRANSVERSE MAGNETOTUNNELLING IN ASYMMETRICALLY-DOPED (InGa)As/InP SINGLE-BARRIER HETEROSTRUCTURES

ABSTRACT

Experimental studies of magnetotunnelling in heterostructures have revealed series of resonances due to electrons tunnelling from a 2DEG in a lightly-doped emitter into magnetoquantised states in the collector contact of a single-barrier structure (Hickmott, 1987 and Snell et al. 1987) or in the quantum well of a double-barrier structure (Eaves et al., 1988 and Leadbeater et al., 1989). These experiments are very suitable for theoretical analysis since a transverse magnetic field (parallel to the barrier interfaces) has little effect on the electronic states of the 2DEG, provided the diamagnetic energy is much less than the binding energy of the bound state of the accumulation layer potential. The tunnelling electrons then have a small range of transverse momenta between $+p_F$ and $-p_F$, where $p_F = \hbar k_F$ is the Fermi momentum in the 2DEG. This range determines the positions of the orbit centres of the magnetoquantised states into which the electrons are injected after emergence from the tunnel barrier. For the single-barrier heterostructures described in this thesis, these are interfacial Landau states corresponding to classical orbits in which the electron skips along the barrier interface. For double-barrier structures there are interfacial states at high magnetic fields and traversing states at low magnetic fields. Owing to the high electric field in the quantum well, the corresponding classical orbits are cycloidal trajectories which intersect both barrier interfaces (traversing states) or just one barrier interface (skipping states).

The variation of the tunnel current I with magnetic field B and voltage V is calculated using the Bardeen transfer-Hamiltonian approach within a WKB approximation. The accumulation layer potential is modelled according to a simple variational solution. This enables a physical interpretation of the experimental results to be given in terms of the effect of the magnetic field on the effective barrier height and the amplitudes of the magnetoquantised wave functions at the barrier interfaces. Both of these effects are required to account for the observed dependence of current on magnetic field I(B) and the amplitudes of the oscillatory structure revealed in the derivative plots of dI/dB and d^2I/dB^2. The model accounts for:

(a) the observation of two series of resonances corresponding to $+p_F$ and $-p_F$ electrons in experiments on (InGa)As/InP single-barrier structures.

(b) the absence of the $+p_F$ series of resonances in GaAs/(AlGa)As single-barrier structures.

(c) the changeover from traversing to skipping states in GaAs/(AlGa)As double-barrier structures and the characteristic decrease in oscillatory amplitudes in the changeover region.

ACKNOWLEDGEMENTS

I would like to express my thanks to the following:

Drs F.W. Sheard and G.A. Toombs for excellent supervision, and in particular for their help and encouragement during the writing-up period.

Professor L. Eaves, Drs B.R. Snell and D.K. Maude, Mr E.S. Alves and Mr M.L. Leadbeater; without their ideas for the experiments and interpretative insight this thesis would not have been written.

Dr K.S. Chan who first developed the model of tunnelling into interfacial states.

All my friends and colleagues in Nottingham, in particular Tim Foster, Mark Leadbeater, Clare Foden, Richard Taylor, Geoffrey Whittington and David Hayes for their help, friendship and many invaluable discussions.

Professor C.A. Bates for allowing me to use the facilities of the Physics Department at Nottingham.

Mrs Margaret Carter for kindly word-processing labels for the diagrams.

Pamela Wise for her patience and skill in typing this script so excellently.

The SERC for the award of a grant and funds to attend conferences.

Finally, to my parents for their support and encouragement throughout my education.

CHAPTER ONE

A REVIEW OF THE BASIC PHYSICS AND PROPERTIES OF SEMICONDUCTORS

1.1 Introduction

For many years, the elemental semiconductors silicon and germanium have been widely used in the manufacture of transistors and integrated circuits. More recently, research interest has focussed on III-V semiconductor compounds, comprising elements from groups III and V of the periodic table. The properties of III-V compounds have been widely investigated since the low effective mass of conduction electrons in these materials suggests possible future applications in high speed devices. However, this advantage is partially offset by intrinsic alloy scattering processes which reduce the electron mobility (Bastard, 1983). The properties of bulk semiconductors have been reviewed by Smith (1978) and Seeger (1982).

The recent development of growth techniques such as molecular beam epitaxy (MBE), which allow crystals to be grown to monolayer precision, has led to a whole new class of semiconductor hetero-structures and superlattices (see, for example, Capasso, 1986). These structures, collectively referred to as low-dimensional structures (LDS), consist of layers of different compound semiconductor materials. Discontinuities in the band-edge energies of the

constituent bulk materials behave as potential steps to electron (or hole) motion normal to the interfaces. By varying the composition and dimensions of the layers, heterostructures containing effective potential energy wells or barriers can be grown which allow fundamental processes such as quantum confinement (Dingle et al., 1975) or quantum tunnelling (Esaki, 1986) to be studied. All the work presented in this thesis concerns electron tunnelling phenomena in single- and double-barrier III-V heterostructures.

This chapter begins with a discussion of the basic concepts of bulk semiconductor theory. The effective-mass equation describing the electronic eigenstates of a bulk crystal in the presence of perturbing electromagnetic fields is introduced, and solved for the case of crossed electric and magnetic fields. The effective-mass model is then extended to heterostructures in which the conduction band (CB) edge position appears as an effective potential energy term. Finally, the time-independent effective-mass formalism of electron tunnelling is outlined for the case of single- and double-barrier heterostructures.

1.2 Electrons in a Periodic Potential

The one-electron Schrödinger equation for electron motion in a perfectly periodic crystal lattice is

$$\left[\frac{-\hbar^2}{2m_0}\nabla^2 + V(\underline{r})\right]\Psi(\underline{r}) = E\,\Psi(\underline{r}) \quad , \tag{1.1}$$

where m_0 is the free electron mass. The potential energy $V(\underline{r})$ describes the electron-ion interaction and satisfies $V(\underline{r}) = V(\underline{r} + \underline{R})$ for all Bravais lattice vectors $\underline{R}$. The eigenfunctions of equation (1.1) are the Bloch functions

$$\Psi(\underline{r}) = N^{-\frac{1}{2}}\, u(\underline{r}) e^{i\underline{k}\cdot\underline{r}} \quad , \tag{1.2}$$

where N is the number of unit cells in the crystal and $\underline{k}$ is the electron wavevector, which is constrained to lie within the first Brillouin zone. The function $u(\underline{r})$ reflects the lattice periodicity, that is

$$u(\underline{r} + \underline{R}) = u(\underline{r}) \quad , \tag{1.3}$$

and is consequently referred to as the cell-periodic component of the Bloch function. Normalisation of the Bloch functions over the entire crystal volume requires that $u(\underline{r})$ is normalised over one unit cell.

To ensure that the properties of the Bloch functions $\Psi(\underline{r})$ are independent of the size of the crystal, the Born-von Karman periodic boundary condition

$$\Psi(\underline{r} + \underline{T}) = \Psi(\underline{r}) \tag{1.4}$$

is imposed,

where

$$\underline{T} = \sum_{i=1}^{3} \ell_i L_i \underline{a}_i \ ,$$

in which $\{\ell_i\}$ are integers, and $\{L_i\}$ are the crystal dimensions measured along the directions of the primitive lattice vectors $\{\underline{a}_i\}$. This condition requires that $e^{i\underline{k}.\underline{T}} = 1$ and is therefore only satisfied by a discrete set of electron wavevectors within the first Brillouin zone.

Substituting the Bloch wavefunction (1.2) into equation (1.1), $u(\underline{r})$ is found to satisfy

$$\left[\frac{(\underline{P} + \hbar\underline{k})^2}{2m_o} + V(\underline{r})\right] u(\underline{r}) = E\, u(\underline{r}) \ , \qquad (1.5)$$

where $\underline{P} = -i\hbar\underline{\nabla}$.

For given $\underline{k}$, this equation has an infinite number of solutions $u_{n\underline{k}}(\underline{r})$ which satisfy the periodic boundary condition (1.3). These solutions, and the associated set of discrete eigenvalues $E_n(\underline{k})$, are distinguished by the band index n. For given n, the energy levels $E_n(\underline{k})$ corresponding to the allowed values of $\underline{k}$ within the first Brillouin zone are collectively referred to as the nth energy band. Distinct energy bands are often separated by gaps in the energy spectrum which do not correspond to any allowed solutions of equation (1.1).

The core electrons of the constituent atoms are assumed to be localised at individual lattice sites forming, with the nucleus, a periodic array of positive ion cores. Only the valence electrons occupy extended Bloch eigenstates. At T = 0K, the highest occupied Bloch states are assumed to belong to the r^{th} band only. The position of these highest occupied energy levels relative to the top of the r^{th} band determines the intrinsic electrical properties of the crystal. It can be shown (see, for example Ashcroft and Mermin, 1976) that if the Bloch states within a particular band are either all occupied or all vacant, the electrons in that band carry no nett current when a voltage is applied to the crystal. Consequently, if the highest occupied levels at T = 0 K coincide with the top of the r^{th} band, referred to as the valence band, no bands are partially filled and the crystal is an insulator.

The temperature dependence of the electrical conductivity depends on the energy difference, or fundamental gap E_g, between the top of the valence band and the lowest unoccupied energy level at T = 0K, which defines the conduction band-edge energy. If, at temperature TK, the ratio kT/Eg is very small, few electrons are thermally excited into the conduction band and the material remains essentially insulating. For crystals with lower band gaps, kT/E_g may be sufficiently large that thermal excitation of electrons into the conduction band leads to a significant increase in conductivity. Such materials are referred to as intrinsic semiconductors.

The electrical properties of semiconductors depend on the conduction and valence band energy-wavevector relations $E_c(\underline{k})$ and $E_v(\underline{k})$ close to the band extrema. For all the semiconductor materials considered in this thesis, $E_c(\underline{k})$ has a minimum at $\underline{k} = 0$, referred to as the Γ-point of the Brillouin zone. Close to this point, $E_c(\underline{k})$ is given approximately by the Taylor expansion

$$E_c(\underline{k}) = E_c(0) + \frac{\hbar^2}{2} \sum_{i,j} \frac{k_i k_j}{m^*_{ij}} \tag{1.6}$$

where

$$m^*_{ij} = \hbar^2 \Big/ \left(\frac{\partial^2 E_c(\underline{k})}{\partial k_i \partial k_j}\right)_{\underline{k}=0}$$

is referred to as the effective-mass tensor by analogy with the kinetic energy of a free electron with momentum $\underline{p} = \hbar\underline{k}$.

Kane (1956, 1982) obtained a semi-empirical expression for m^*_{ij} using so-called $\underline{k}.\underline{p}$ perturbation theory. Equation (1.5) may be written in the form

$$(H_0 + H_1 + H_2)u_{n\underline{k}}(\underline{r}) = E_n(\underline{k})u_{n\underline{k}}(\underline{r}) \tag{1.7}$$

where $H_1 = \frac{\hbar}{m_0} \underline{k}.\underline{P}$

and $H_2 = \frac{\hbar^2 |\underline{k}|^2}{2m_0}$

For small $\underline{k}$, H_1 and H_2 act as perturbations to the Hamiltonian $H_o = \underline{P}^2/2m_o + V(\underline{r})$, for which the energy eigenvalues $E_n(0)$ and cell-periodic Bloch functions $u_{no}(\underline{r})$ are presumed known. The eigenfunctions $u_{n\underline{k}}(\underline{r})$ of equation (1.7) and the associated eigenvalues can be found using standard perturbation theory. Non-degenerate perturbation theory is applicable for energies close to the conduction band edge and gives, to first order

$$u_{c\underline{k}}(\underline{r}) = u_{co}(\underline{r}) + \frac{\hbar}{m_o} \sum_{n\neq c} \frac{\underline{k}.\langle no|\underline{P}|co\rangle \; u_{mo}(\underline{r})}{E_c(0) - E_n(0)} \tag{1.8}$$

and, to second order

$$E_c(\underline{k}) = E_c(0) + \frac{\hbar}{m_o} \underline{k}.\langle co|\underline{P}|co\rangle + \sum_{i,j} \frac{\hbar^2}{2m^*_{ij}} k_i k_j \tag{1.9}$$

where

$$\frac{m_o}{m^*_{ij}} = \delta_{ij} + \frac{2}{m_o} \sum_{n\neq c} \frac{\langle co|\underline{P}_i|no\rangle\langle no|\underline{P}_j|co\rangle}{E_c(0) - E_n(0)} \; . \tag{1.10}$$

For crystals with inversion symmetry, which includes III-V compounds, $\langle co|\underline{p}|co\rangle = 0$ and so equation (1.9) implies that the conduction band has a minimum at $\underline{k} = 0$.

The series expansion (1.10) for $m^*_{ij}{}^{-1}$ is dominated by the band for which $E_n(0)$ lies closest to $E_c(0)$, usually the valence band. Consequently, materials with small band gaps are expected to have light effective masses.

Equations (1.8), (1.9) and (1.10) describe parabolic bands and therefore only give an accurate quantitative description of the conduction bands of III-V semiconductor materials for energies within ~ 10 meV of the band edge (Blakemore, 1982). For higher energies, degenerate perturbation theory must be used to account for non-parabolicity. Nevertheless, these equations are useful in the development of effective-mass theory, which is used throughout this thesis to determine the electronic eigenstates of a crystal in the presence of perturbing electromagnetic fields.

1.3 General Properties of III-V Semiconductors

Every heterostructure described in this thesis is composed of III-V semiconductor materials which are binary or ternary compounds of elements from groups III and V of the periodic table. These elements crystallise in the zinc-blende structure, which consists of two interpenetrating face-centred cubic (fcc) sublattices. Each

sublattice contains either group III or group V atoms exclusively. Each atom is tetrahedrally bonded to four atoms of the opposite group. The bonding is partly covalent and partly ionic.

In the ternary III-V alloy $(In_xGa_{1-x})As$, gallium and indium atoms are assumed to be randomly distributed on the group III sublattice sites, with x giving the probability that any one site is occupied by an indium atom. For $x = 0.53$, this alloy has the same lattice constant as InP (5.8694 Å at 300 K) and can be grown on an InP substrate without lattice mismatch or strain at the interface. Similarly, $(Al_xGa_{1-x})As$ is lattice-matched to GaAs when $x \approx 0.3$. All following references to (AlGa)As and (InGa)As refer to these compositions.

The crystal lattice of III-V compounds is fcc and the basis contains one group III atom and one group V atom, which are displaced relative to each other by one quarter of the diagonal of the conventional fcc unit cell. The primitive lattice vectors of the fcc structure extend from an origin $\underline{0}$ at one corner of the conventional unit cell, to the mid-point of the three adjacent faces. The lattice vectors of the conventional unit cell are $a\underline{x}$, $a\underline{y}$ and $a\underline{z}$, where a is the lattice constant and the unit vectors $\underline{x}$, $\underline{y}$ and $\underline{z}$ extend along the three mutually perpendicular cell edges which meet at the origin $\underline{0}$. The Born-von Karman periodic boundary condition (1.4) is modified for III-V crystals so that $\{\underline{a}_i\}$ are the conventional lattice vectors rather than the primitive lattice vectors. Consequently, the components of the electron wavevector $\underline{k} = k_x\underline{x} + k_y\underline{y} + k_z\underline{z}$ must satisfy

$$k_x = \frac{2\pi\ell}{L_x}\ ,\ k_y = \frac{2\pi m}{L_y} \text{ and } k_z = \frac{2\pi n}{L_z} \tag{1.11}$$

where ℓ, m and n are integers and L_x, L_y, L_z are the crystal dimensions in the $\underline{x}$, $\underline{y}$ and $\underline{z}$ directions respectively.

Figure 1.1 shows the energy band structure of GaAs in the vicinity of the valence and conduction bands. GaAs is a direct-gap material, that is the lowest conduction band minimum and the highest valence band maximum are located at the same point in the Brillouin zone, in this case at $\underline{k} = 0$. The two highest valence bands are degenerate at $\underline{k} = 0$. Because these bands have different curvatures, corresponding to different effective masses, they are referred to as the light- and heavy-hole bands. The lower-lying valence band is called the split-off band in reference to spin-orbit splitting of the 4p orbitals which are occupied by the valence electrons of isolated group III and group V atoms.

In the vicinity of $\underline{k} = 0$, the conduction band of GaAs is practically isotropic and parabolic so that the effective mass m^* can be treated as a scalar quantity. For energies $\geq$ 10 meV, the band becomes increasingly nonparabolic and must be described by an energy-dependent effective mass. By solving equation (1.7) using degenerate perturbation theory, in which the unperturbed energy levels are the conduction band and uppermost valence band edges (2-level $\underline{k}.\underline{p}$ theory), $E_c(\underline{k})$ is found to be approximately (Kane, 1957)

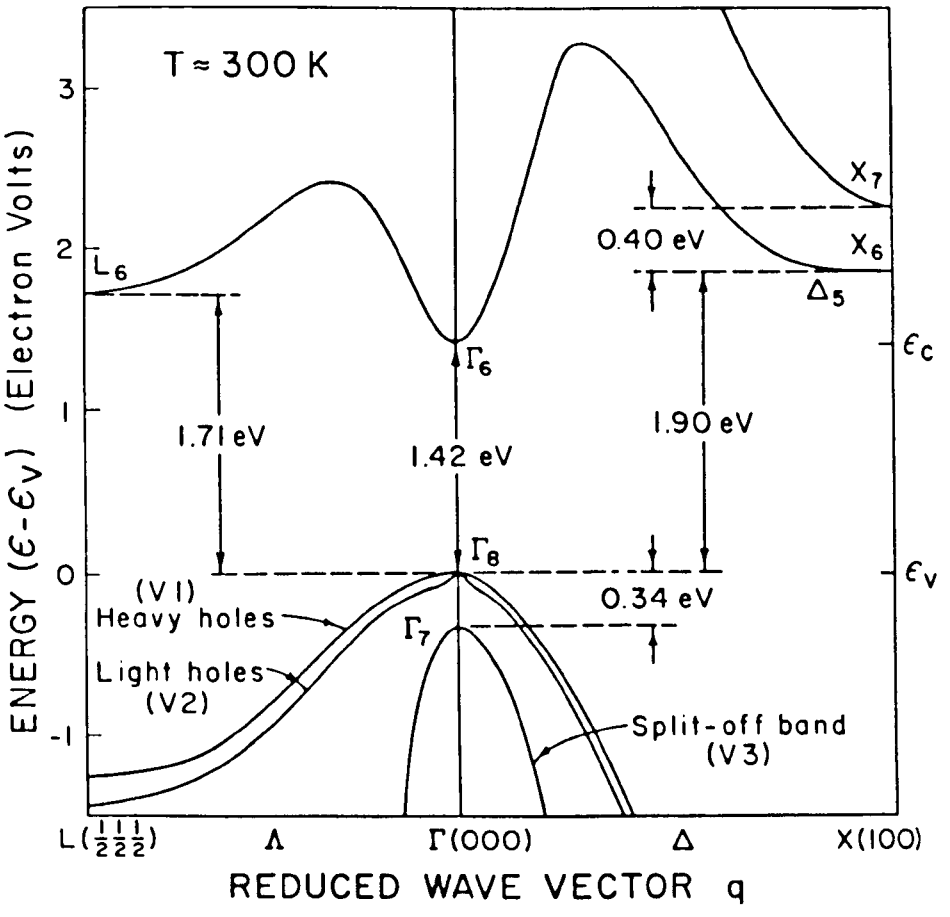

Figure 1.1 The band structure of GaAs in the vicinity of the energy gap between the valence and lowest conduction bands at T = 300 K. (After Blakemore, 1982).

$$E_c(\underline{k}) = \frac{\hbar^2 k^2}{2m^*(E_c)} , \qquad (1.12)$$

where $m^*(E_c) = m^*(1 + \alpha E_c)$ in which the nonparabolicity factor $\alpha \cong 1/E_g$. This expression is also applicable to (AlGa)As, (InGa)As and InP, which are all direct-gap semiconductors with similar band-structures to GaAs.

The presence of impurities in semiconductors can greatly affect the electrical characteristics. For example, silicon added to GaAs goes preferentially onto the Ga atom lattice and forms a shallow donor, with an energy level about 6 meV below the CB edge. The extra valence electron which Si (a group IV element) has, compared to Ga (a group III element) is not required for bonding and can be easily excited into the CB to form a free carrier. Low concentrations of donor impurities ($N_D \cong 10^{21}$ m^{-3}) give n^--type semiconductors. High concentrations ($N_D \cong 10^{23}$ m^{-3}) give n^+-type semiconductors. All the semiconductors studied in this thesis are n-type. Group II elements added to GaAs, preferentially occupy the group III atom sites, forming shallow acceptor levels close to the valence band. The addition of acceptor impurities forms p-type material in which the free carriers are positively-charged quasi-particles called holes.

1.4 The Effective-Mass Equation

In the presence of an external magnetic field $\underline{B} = \underline{\nabla} \times \underline{A}$, where $\underline{A}$ is the vector potential, and a perturbing electrostatic potential $\phi(\underline{r})$, which is either externally applied or associated with internal electric fields, the one-electron Schrödinger equation for conduction electrons in a semiconductor crystal is (neglecting spin interactions)

$$H\,\Psi(\underline{r}) = \left(\frac{(\underline{P} + e\underline{A})^2}{2m_0} + V(\underline{r}) - e\,\phi(\underline{r})\right)\Psi(\underline{r}) = E\Psi(\underline{r}), \qquad (1.13)$$

where -e is the electronic charge.

By analogy with the classical Hamiltonian of an electron in a magnetic field (see, for example, Dicke and Wittke, 1960), the operator $\underline{P} = -i\hbar\underline{\nabla}$, represents the classical canonical momentum $\partial L/\partial \dot{\underline{r}}$, where L is the Lagrangian.

The velocity operator $\underline{v}$ for an electron in a magnetic field is $\underline{v} = [\underline{r},H]/i\hbar = (\underline{P} + e\underline{A})/m_0$, so that the first term in equation (1.13) is simply the kinetic energy operator $m_0\underline{v}^2/2$.

If no perturbing electromagnetic fields are present, the eigenfunctions of equation (1.13) are bulk Bloch functions. Approximate solutions of equation (1.13) can therefore be expanded in terms of the complete set of Bloch functions, that is

$$\Psi(\underline{r}) = N^{-\frac{1}{2}} \sum_{n,\underline{k}} C_n(\underline{k})\, u_{n\underline{k}}(\underline{r})\, e^{i\underline{k}.\underline{r}} \qquad (1.14)$$

Using this wavefunction in equation (1.13) it can be shown (see for example Altarelli, 1988, or Ridley, 1988) that provided

(i) In the unperturbed system, the conduction electrons occupy energy levels $E_c(\underline{k}) = E_c(0) + \hbar^2 k^2/2m^*$ close to an isotropic conduction band minimum at $\underline{k} = 0$.

(ii) The Fourier components $\underline{A}_q$ and V_q of the perturbing magnetic and electrostatic potentials are only appreciable if $|\underline{q}| \ll 2\pi/a$, or equivalently the perturbing potentials vary slowly over a unit cell.

(iii) The matrix elements of $A(\underline{r})$ and $e\phi(\underline{r})$ are much smaller than the inter-band gaps $E_c(0) - E_n(0)$ $n \neq c$,

then the Fourier series $F(\underline{r}) = N^{-\frac{1}{2}} \sum_{\underline{k}} C_c(\underline{k})\, e^{i\underline{k}.\underline{r}}$,

satisfies

$$\left(\frac{(\underline{P} + e\underline{A})^2}{2m^*} - e\phi(\underline{r})\right) F(\underline{r}) = (E - E_c(0))\, F(\underline{r}) \,, \qquad (1.15)$$

in which the effects of the periodic crystal potential are incorporated into the effective mass. This equation is known as the isotropic, parabolic effective-mass equation.

The slowly-varying perturbing potentials only mix states within the same band so that for the conduction band, the perturbed wavefunction (1.14) becomes

$$\Psi(\underline{r}) = N^{-\frac{1}{2}} \sum_{\underline{k}} C_c(\underline{k})\, u_{c\underline{k}}(\underline{r})\, e^{i\underline{k}\cdot\underline{r}} \tag{1.16}$$

which, using the $\underline{k}.\underline{p}$ expression (1.8) for $u_{c\underline{k}}(\underline{r})$, may be written

$$\Psi(\underline{r}) = F(\underline{r})\, u_{co}(\underline{r}) + \sum_{\ell \neq c} \frac{-i\hbar\, (\underline{\nabla} F(\underline{r}).\underline{P}_{\ell c}) u_{\ell o}(\underline{r})}{m_o(E_c(0) - E_\ell(0))} \tag{1.17}$$

where $\underline{P}_{\ell c} = \langle \ell o | \underline{p} | co \rangle$.

To first order, $F(\underline{r})$ acts as a slow modulation to the rapidly-varying Bloch term $u_{co}(\underline{r})$ and is therefore referred to as an envelope or effective-mass wavefunction. The second-order term shows that the contribution made by the other $\underline{k} = \underline{0}$ Bloch functions is proportional to the gradient of the envelope function. This term must be included when deriving the boundary conditions which $F(\underline{r})$ must satisfy at the interface between two different semiconductor materials.

Provided that the perturbing electric field does not destroy the bandstructure, its main effect is to shift the band edge positions by an amount equal to the local electrostatic potential energy $-e\phi(\underline{r})$. This effect is referred to as band bending. If a nonparabolic band is described by an effective mass which depends on

the energy of the electron relative to the band edge, as in equation (1.12), then band bending causes the effective mass to vary with position. In this case, the effective-mass equation is usually written (Lassnig, 1985)

$$\left((\underline{P} + e\underline{A}).\left(\frac{1}{m^*(T(\underline{r}))}\right).(\underline{P} + e\underline{A}) - e\phi(\underline{r})\right) F(\underline{r}) = (E - E_c(0))F(\underline{r}) \tag{1.18}$$

where $T(\underline{r}) = E - E_c(0) + e\phi(\underline{r})$ is the semiclassical local kinetic energy. The kinetic energy operator is written in a way which retains the Hermitian character of the Hamiltonian following Ben-Daniel and Duke (1966).

The expectation values of operators involving the free electron mass (such as the velocity operator $\underline{v} = (-i\hbar\underline{\nabla} + e\underline{A})/m_0$), can be found using the approximate wavefunction (1.17).

However, for parabolic, isotropic conduction bands, the same result is obtained using the effective-mass wavefunction $F(\underline{r})$ to evaluate the expectation value of a modified operator, in which the effective mass m^* replaces the free electron mass. Consequently, an electron in a crystal responds to electromagnetic fields in the same way as a free electron of mass m^*.

1.5 The Effect of Crossed Electric and Magnetic Fields on the Conduction Band Eigenstates of a Bulk Semiconductor

The classical equation of motion of an electron of mass m^* in the presence of electric ($\underline{F}$) and magnetic ($\underline{B}$) fields is

$$m^* \frac{d\underline{v}}{dt} = -e(\underline{F} + \underline{v} \times \underline{B}) \tag{1.19}$$

where $\underline{v}$ is the velocity of the electron. In crossed electric ($\underline{E} = -F\underline{x}$) and magnetic ($\underline{B} = B\underline{z}$) fields, assuming $\underline{v}(t = 0) = 0$ and $\underline{r}(t = 0) = 0$ the solutions of equation (1.19) are

$$x = \frac{F}{\omega_c B}(1 - \cos\omega_c t) ,$$

$$y = \frac{F}{\omega_c B}(\omega_c t - \sin\omega_c t) ,$$

and $$z = 0 ,$$

where $\omega_c = Be/m^*$ is the cyclotron frequency. In the x-direction the electron executes simple harmonic motion. Electronic motion in the y-direction contains both simple harmonic and translational components, which result in an average drift velocity of $v_d = F/B$.

Consequently, the electron executes cycloidal motion along electrostatic equipotentials as shown in Figure 1.2. The drift velocity v_d in the direction perpendicular to both the electric and magnetic fields is responsible for the classical Hall effect.

For this crossed-field configuration, the parabolic, isotropic effective-mass equation (1.18) is, in the Landau gauge $\underline{A} = (0, Bx, 0)$

$$H\,\Psi(x,y,z) = \left(-\frac{\hbar^2}{2m^*}\frac{\partial^2}{\partial x^2} + \frac{(-i\hbar\frac{\partial}{\partial y} + eBx)^2}{2m^*} - \frac{\hbar^2}{2m^*}\frac{\partial^2}{\partial z^2} - eFx\right)\Psi(x,y,z)$$

$$= E\,\Psi(x,y,z) \quad . \tag{1.20}$$

The canonical momentum operators $-i\hbar\partial/\partial y$ and $-i\hbar\partial/\partial z$ commute with H so that the envelope functions $\Psi(x,y,z)$ are of the form

$$\Psi(x,y,z) = \psi(x)\, e^{ik_y y}\, e^{ik_z z} \tag{1.21}$$

in which the electron wavevector components are related to the canonical momentum eigenvalues $p_y = \hbar k_y$ and $p_z = \hbar k_z$. The x-dependent factor $\psi(x)$ satisfies the 1D Schrödinger equation

$$H\;\psi(x) = \left[-\frac{\hbar^2}{2m^*}\frac{\partial^2}{\partial x^2} + \frac{1}{2}m^*\omega_c{}^2\,(x + \frac{\hbar k_y}{Be})^2 - eFx\right]\psi(x) = E_{x,y}\psi(x)$$

(1.22)

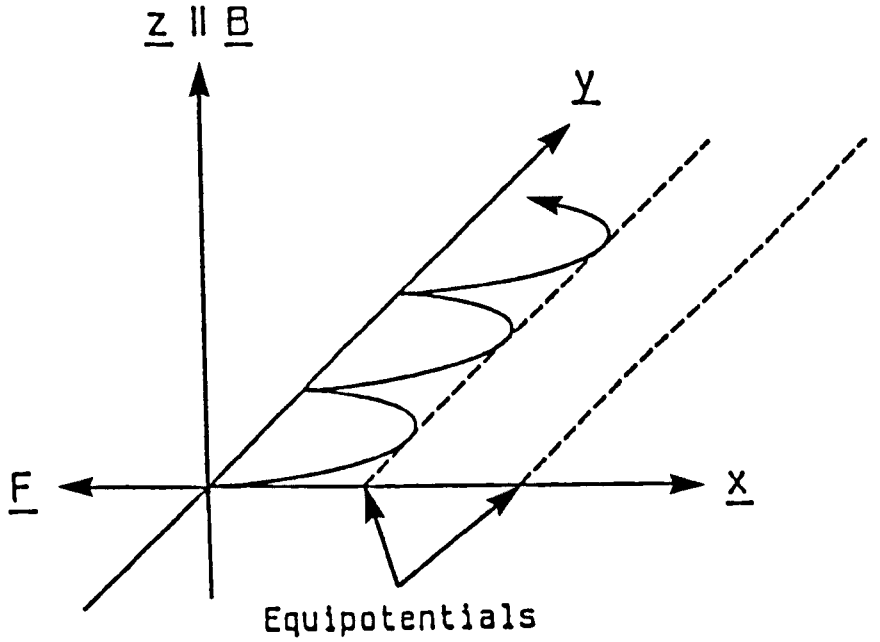

Figure 1.2 Projection in the x-y plane of the classical cycloidal orbit traversed by an electron in crossed electric ($-\underline{F} \parallel \underline{x}$) and magnetic ($\underline{B} \parallel \underline{z}$) fields. The electron is constrained to move within electrostatic equipotentials in the x-direction and has nett translational velocity $v_d = F/B$ in the y-direction.

where

$$E_{x,y} = E - \frac{\hbar^2 k_z^2}{2m^*}$$

gives the energy associated with motion perpendicular to the magnetic field.

The one-dimensional potential energy in equation (1.22) is the sum of the electrostatic potential energy -eFx, and the potential energy of a linear simple harmonic oscillator (SHO) centred at $X_0 = -\hbar k_y/Be$, and of angular frequency equal to the classical cyclotron frequency ω_c. Classically, this term is the kinetic energy $T_y(x)$, associated with motion in the y-direction, of an electron with canonical momentum $p_y = \hbar k_y$. This kinetic energy varies with position as momentum is transferred between the x-and y-components by the action of the Lorentz force. The classical kinetic energy associated with motion in the x-direction is $T_x(x) = E_x - T_y(y) + eFx$ so that the motion is effectively constrained by the potential energy well $V(x) = T_y(x) - eFx$ which appears in the Hamiltonian of equation (1.22). The electric field term shifts the oscillator origin from $X_0 = -\hbar k_y/eB$ to $X = -(\hbar k_y/Be) + m^* v_d/Be$, so that equation (1.22) may be written in the form

$$\left(-\frac{\hbar^2}{2m^*}\frac{\partial^2}{\partial x^2} + \frac{1}{2}m^*\omega_c^2(x - X)^2\right)\psi(x) = \left(E_{x,y} - \frac{m^* v_d^2}{2} + eFX\right)\psi(x) \quad . \qquad (1.23)$$

The eigenvalues of this equation are the SHO eigenvalues $(n + \frac{1}{2})\hbar\omega_c$ and the eigenfunctions are the SHO eigenfunctions $\phi_n(x - X)$ centred at X. Consequently, the eigenvalues of equation (1.20) are

$$E_n(k_y, k_z) = (n + \frac{1}{2})\hbar\omega_c - eFX + \frac{m^* v_d^2}{2} + \frac{\hbar^2 k_z^2}{2m^*} \qquad (1.24)$$

with corresponding eigenfunctions

$$\Psi_{n,k_y,k_z}(x,y,z) = A_n \phi_n(x - X) e^{ik_y y} e^{ik_z z} \qquad (1.25)$$

where $n = 0,1,2 \ldots$ and A_n are normalising constants.

It can be shown (see, for example, Cohen-Tannoudji et al., 1977) that the expectation value of the y-component of velocity of an electron in the eigenstate Ψ_{n,k_y,k_z} is

$$\langle v_y \rangle = \frac{1}{\hbar} \frac{\partial E_n(k_y,k_z)}{\partial k_y} = \frac{F}{B} = v_d \qquad (1.26)$$

which equals the classical drift velocity and is identical for every eigenstate of equation (1.20).

The first term on the RHS of equation (1.24) gives the quantised energy associated with orbital motion perpendicular to the magnetic field. The second term is the electrostatic potential energy

at the orbit centre. The third term gives the kinetic energy associated with the transverse drift of the orbit centre. The final term gives the kinetic energy associated with motion parallel to the magnetic field.

If no electric field is applied, these eigenvalues become

$$E_n(k_z) = (n + \tfrac{1}{2})\hbar\omega_c + \frac{\hbar^2 k_z^{\,2}}{2m^*} , \qquad (1.27)$$

where the quantised energy levels associated with motion perpendicular to the magnetic field are referred to as Landau levels. Classically, the electrons execute helical motion around the z-axis, which corresponds to circular cyclotron orbits of angular frequency ω_c when projected in the x-y plane.

By considering the boundary conditions (1.11) which k_y and k_z must satisfy, the energy density of states (DOS) per unit area perpendicular to the magnetic field is found to be (see, for example, Ridley 1988),

$$D(E) = 2(eB/h) \sum_n D(E_z^n)\ \theta(E_z^n) \qquad (1.28)$$

$$\text{where} \quad \theta(E_z^n) = \begin{cases} 0 \ ; \ E_z^n < 0 \\ 1 \ ; \ E_z^n \geq 0 \end{cases} ,$$

$D(E_z^n) = L_z(m^*/\pi\hbar)(2m^*E_z^n)^{-\frac{1}{2}}$ is the density of states for motion in the z-direction, and $E_z^n = E - (n + 1/2)\hbar\omega_c$ is the energy associated with motion in this direction, of an electron, with total energy E, which occupies the n^{th} Landau level. The factor of 2 arises from spin degeneracy. The total DOS D(E) is shown in Figure 1.3. In a real system, the singularities which occur when $E = (n + 1/2)\hbar\omega_c$ are smoothed by collision broadening, which is not included in the single-particle Hamiltonian. The lifetime of the eigenstates corresponding to each Landau level is approximately equal to the momentum relaxation time τ_m, so that the collision broadening ΔE_u satisfies

$$\Delta E_u \geq \hbar/\tau_m \tag{1.29}$$

In order to obtain well-defined Landau levels, this broadening must be much less than the level splitting, that is

$$\Delta E_u << \hbar\omega_c = \frac{2\pi\hbar}{T} \tag{1.30}$$

where T is the classical cyclotron period.
This inequality can only be satisfied provided

$$T << 2\pi\tau_m \quad , \tag{1.31}$$

so that the electron must be able to complete whole cyclotron orbits before scattering.

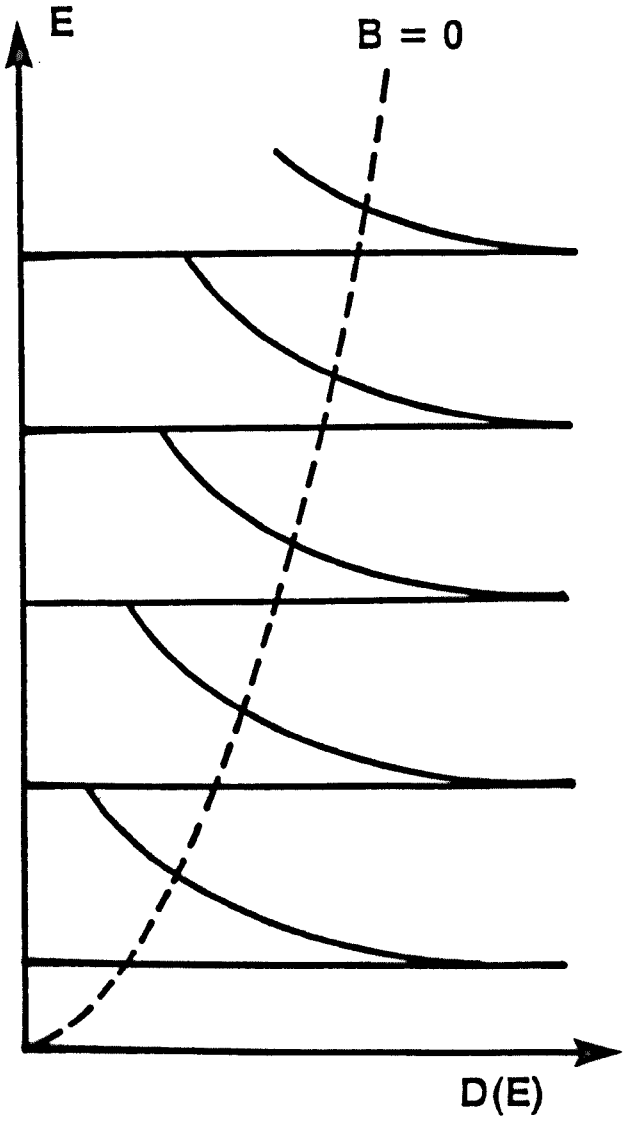

Figure 1.3 Energy density of states D(E) in the conduction band of a bulk semiconductor subject to a strong magnetic field (solid curves). The separation between adjacent maxima is $\hbar\omega_c$. The broken curve shows the conduction band density of states in zero magnetic field.

1.6 Heterojunctions

A heterojunction comprises two different semiconductor materials which meet at a common interface. The bulk band structure is assumed to be unaffected by the loss of translational symmetry right up to the interface. However, there is usually a discontinuity in the band edge positions due primarily to the different electron affinities of the two materials. In equilibrium, band bending occurs near the interface to maintain a uniform chemical potential, or Fermi level, throughout the structure. This is achieved by charge transfer, which forms regions in which there is nett charge, referred to as space-charge regions. These space-charge regions create an electric field normal to the interface. The potential variation associated with this field leads to band bending which shifts the occupied energy levels in each material until the chemical potential is uniform.

Figure 1.4 shows a heterostructure comprising two materials labelled L and R which occupy semi-infinite regions to the left and right of the y-z plane. The conduction band edge energies are $E_L(0)$ and $E_R(0)$ respectively where $E_L(0) < E_R(0)$.

The Schrödinger equation for conduction electrons in this system is

$$\left(\frac{-\hbar^2\nabla^2}{2m_o} + V(\underline{r}) - e\phi(x)\right)\Psi(\underline{r}) = E\,\Psi(\underline{r}) \qquad (1.32)$$

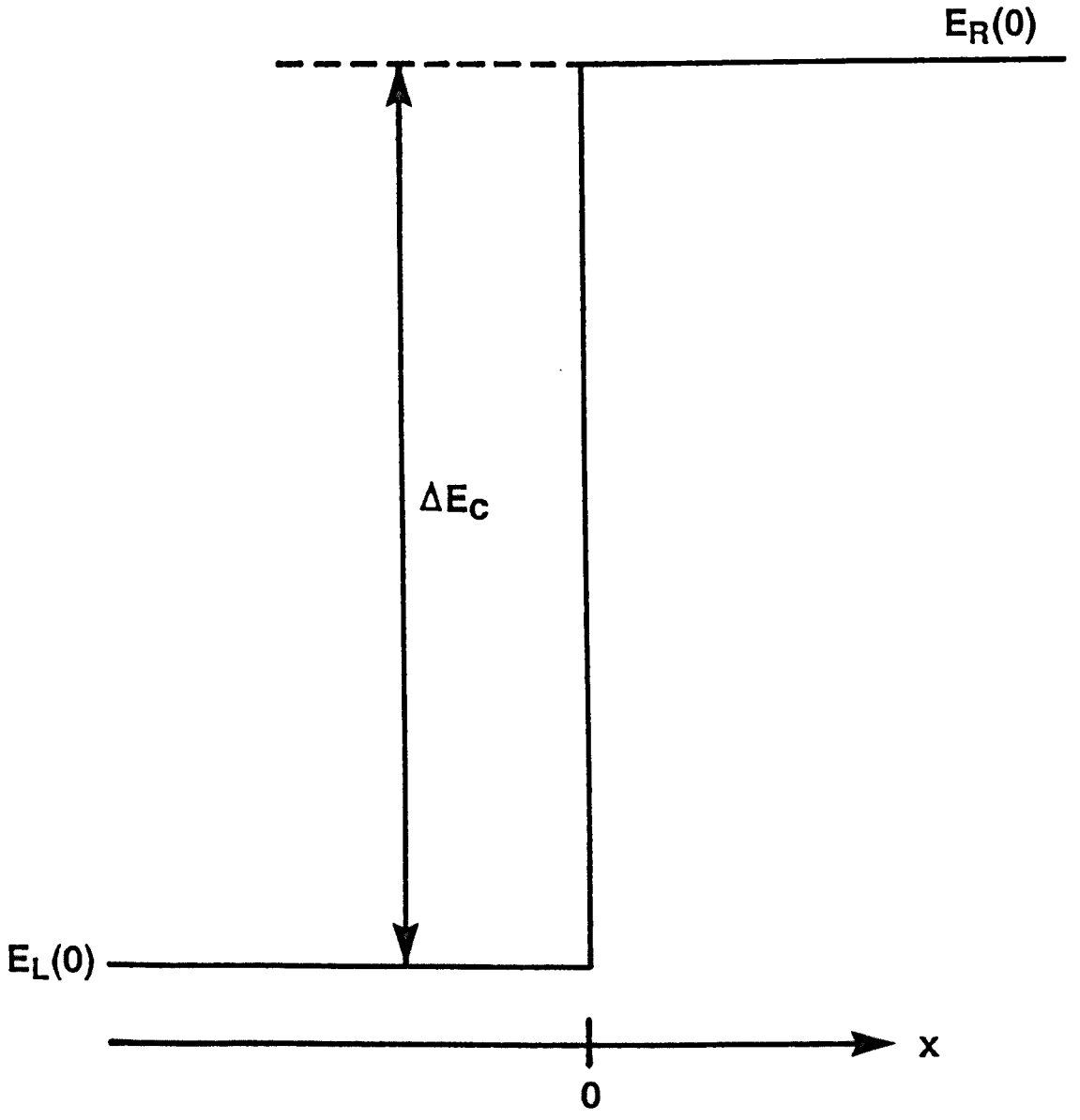

Figure 1.4 Conduction band profile of an idealised heterojunction comprising different semiconductor materials which meet at a common interface (x = 0). The conduction band offset $\Delta E_C = E_R(0) - E_L(0)$ is the difference between the band-edge energies of the high- and low-gap materials.

where the potential energy

$$V(\underline{r}) = \begin{cases} V_L(\underline{r}) \; ; \; x < 0 \\ V_R(\underline{r}) \; ; \; x \geq 0 \end{cases}$$

describes the interaction between the electrons and the lattice potential of each material.

The electrostatic potential $\phi(x)$, associated with the space-charge regions is a function of x- alone since the electrons are free to move parallel to the interface. The solutions of equation (1.32) can be expanded as a linear combination of the Bloch functions of the two materials (Lassnig, 1985) so that

$$\Psi(\underline{r}) = \sum_{n,\underline{k}} C_n^L(\underline{k}) \; \Psi_{n,\underline{k}}^L(\underline{r}) \; \theta(-x) + C_n^R(\underline{k}) \; \Psi_{n,\underline{k}}^R(\underline{r}) \; \theta(x) \qquad (1.33)$$

where $\theta(x)$ is the unit step function defined by

$$\theta(x) = \begin{cases} 0 \; ; \; x < 0 \\ 1 \; ; \; x \geq 0 \; . \end{cases}$$

Just as for bulk crystals, the envelope functions

$$F_L(\underline{r}) = \sum_{\underline{k}} C_n^L(\underline{k}) \; e^{i\underline{k}.\underline{r}} \text{ and } F_R(\underline{r}) = \sum_{\underline{k}} C_n^R(\underline{k}) \; e^{i\underline{k}.\underline{r}}$$

satisfy the effective-mass equations

$$\left(-\frac{\hbar^2}{2m_L^*}\nabla^2 - e\phi(x)\right) F_L(\underline{r}) = (E - E_L(0))\, F_L(\underline{r}) \; ; \; x < 0 \tag{1.34}$$

and

$$\left(-\frac{\hbar^2}{2m_R^*}\nabla^2 - e\phi(x)\right) F_R(\underline{r}) = (E - E_R(0))\, F_R(\underline{r}) \; ; \; x \geq 0 \; . \tag{1.35}$$

If the effective mass and conduction band edge are allowed to vary with x, these equations may be combined to give

$$\left(-\frac{\hbar^2}{2}\,\underline{\nabla}.\left(\frac{1}{m^*(x)}\,\underline{\nabla}\right) + E_c(x)\right) F(\underline{r}) = EF(\underline{r}) \tag{1.36}$$

where

$$m^*(x) = \begin{cases} m_L^* \; ; \; x < 0 \\ m_R^* \; ; \; x \geq 0 \end{cases}$$

and

$$E_c(x) = \begin{cases} -e\phi(x) + E_L(0) \; ; \; x < 0 \\ -e\phi(x) + E_R(0) \; ; \; x \geq 0 \end{cases} ,$$

describes the spatial variation of the conduction band edge. This so-called conduction band profile appears in equation (1.36) as an effective potential energy term. Consequently, the band-edge discontinuity has the same effect on electron motion normal to the interface as a potential energy step of height $\Delta E_c = E_R(0) - E_L(0)$. Since the effective potential energy in equation (1.36) is a function of x alone, $F(\underline{r})$ may be written in the form

$$F(\underline{r}) = F(x)\, e^{ik_y y}\, e^{ik_z z} \quad . \tag{1.37}$$

Even though k_y and k_z are conserved quantities, the transverse kinetic energy $E_{y,z}$ is not conserved because the effective mass varies with position. However, provided this mass variation is small, $E_{y,z} \cong \hbar^2(k_y^2 + k_z^2)/2m^*_L$.

Within this approximation, F(x) satisfies

$$\left(-\frac{\hbar^2}{2}\frac{d}{dx}\left(\frac{1}{m^*(x)}\right)\frac{d}{dx} + E_c(x)\right) F(x) = E_x\, F(x) \quad , \tag{1.38}$$

where $E_x = E - E_{y,z}$ is the energy associated with motion normal to the interface, which is only conserved when the effective mass is taken to be spatially invariant.

1.7 Interfacial Matching Conditions for the Effective-Mass Wavefunctions

Assuming that $F(x)$ is continuous at a heterojunction interface so that

$$F(0_-) = F(0_+) \tag{1.39}$$

Hermann and Weisbuch (1977) showed by integrating equation (1.38) between $-\delta$ and δ and letting $\delta \to 0$, that the first derivative must satisfy

$$\left(\frac{1}{m^*(x)} \frac{dF(x)}{dx}\right)_{0_-} = \left(\frac{1}{m^*(x)} \frac{dF(x)}{dx}\right)_{0_+} . \tag{1.40}$$

In order for these matching conditions to be physically meaningful, they must guarantee the conservation of probability flux at the interface. Provided that both constituent materials of the heterojunction have parabolic conduction bands, the solutions $\Psi(\underline{r})$ of equation (1.32) are given piecewise by equation (1.17), in which the cell-periodic Bloch functions and the band-edge energies are understood to be those of the low-gap material for $x < 0$, and of the high-gap material for $x \geq 0$.

At some point on the plane $x = x_0$, the probability flux carried in the x-direction by $\Psi(\underline{r})$ is

$$P(x_0) = \mathrm{Im}\,\frac{\hbar}{m_0}\,\Psi^*(\underline{r})\,\frac{\partial\Psi(\underline{r})}{\partial x} \tag{1.41}$$

which is related to the local current density $J(x_0) = eP(x_0)$. If $\Psi(\underline{r})$ is an eigenfunction of equation (1.32), $|\Psi(\underline{r})|^2$ is conserved so that $P(x_0)$ must be continuous everywhere and in particular at the interface. However, since the position of any real interface cannot be specified on an atomic scale, it is meaningless to think in terms of flux conservation at some arbitrary interface. Instead we require conservation of the average flux evaluated over one or more unit cells close to the interface.

Close to x_0, this average flux is

$$\bar{P}(x_0) = \frac{1}{\Omega}\int_{\Omega} P(x_0)\,d\Omega \tag{1.42}$$

where Ω is the volume of integration.

Combining equations (1.17), (1.41) and (1.42), it can be shown (see, for example, Altarelli, 1988) that provided $u_{n\underline{k}}(\underline{r})$ varies slowly with transverse wavevector,

$$\bar{P}(x_0) = \mathrm{Im}\left(\frac{\hbar}{m_i^*}\,F^*(x)\frac{dF(x)}{dx}\right)_{x=x_0} \tag{1.43}$$

where m_i^* is given by the scalar form of the effective-mass tensor (1.10) and equals m_L^* if $x < 0$ and m_R^* if $x \geq 0$.

Consequently, for parabolic bands, equations (1.39) and (1.40) do ensure that the average flux is conserved at an interface. In order that these matching conditions also guarantee average flux conservation for nonparabolic bands, this average flux must equal

$$\bar{P}(x_0) = \mathrm{Im}\left(\frac{\hbar}{m^*(x)}\, F^*(x)\, \frac{dF(x)}{dx}\right)_{x=x_0} \qquad (1.44)$$

For a Bloch electron with total energy $E(\underline{k}) = \hbar^2(k_x^2 + k_y^2 + k_z^2)/2m^*(1 + \alpha E)$, described by the envelope function $F(x) = e^{ik_x x}$, equation (1.44) predicts

$$\bar{P}(x_0) = \hbar k_x/m^*(1 + \alpha E)\ , \qquad (1.45)$$

whereas the exact expression equals the expectation value of the longitudinal velocity component

$$\frac{1}{\hbar}\frac{\partial E}{\partial k_x} = \hbar k_x/m^*(1 + 2\alpha E)\ . \qquad (1.46)$$

For Bloch electrons in a nonparabolic band, the average flux predicted by equation (1.44) is clearly inaccurate, so that equations (1.39) and (1.40) do not guarantee exact flux conservation. However, provided α is small, the difference between equations (1.45) and (1.46) is also small and the boundary condition (1.40) appropriate to the parabolic case may be used.

1.8 Quantum-Mechanical Tunnelling in Semiconductor Heterostructures

In classical mechanics, a particle which is incident on a potential energy barrier of height greater than the incident kinetic energy is reflected with 100% certainty. Similarly, if the incident kinetic energy exceeds the potential energy barrier height, the particle is certain to be transmitted.

In quantum mechanics, however, this is not the case. If an electron is incident with kinetic energy less than the potential energy barrier height, it can penetrate into the barrier, or classically forbidden region.

If the potential barrier is finite in length, the electron has a finite probability of being transmitted. This is the basis of quantum-mechanical tunnelling which is described in detail for electrons in free space in most quantum mechanics texts. With the advent of growth techniques such as molecular beam epitaxy, it is possible to grow heterostructures with sharp, strain-free interfaces. We have already seen that the conduction band discontinuity in a heterojunction acts as a potential energy step. Similarly, a layer of high band-gap material which separates two regions of lower-gap material acts as a rectangular potential energy barrier to electron motion normal to the interface. Such heterostructures are well suited to the experimental study of quantum tunnelling since by varying the composition and thickness of the layers, potential

barriers of different widths and heights can be obtained. The influence of these device parameters on the tunnelling process can be compared with theoretical models of tunnelling.

Here we discuss the coherent effective-mass model of tunnelling which is applicable to electrons occupying current-carrying eigenstates of the entire system. Tunnelling between localised quasi-bound states is discussed in Chapter 3 within the framework of the sequential transfer-Hamiltonian model.

Figure 1.5 shows the conduction band profile of a single-barrier heterostructure containing n^+ contacts in which the electrostatic potential energy variation is not sufficiently rapid to cause bound state formation.

The conduction band effective-mass equation for this system is

$$\left(-\frac{\hbar^2}{2}\,\underline{\nabla}\cdot\left(\frac{1}{m^*(x)}\right)\underline{\nabla} + E_c(x)\right) F(\underline{r}) = EF(\underline{r}) \qquad (1.47)$$

where

$$m^*(x) = \begin{cases} m_L^* & ; x < -b \\ m_B^* & ; -b \le x \le 0 \\ m_L^*(1 + \alpha(E - E_c(x))) & ; x > 0 \end{cases} .$$

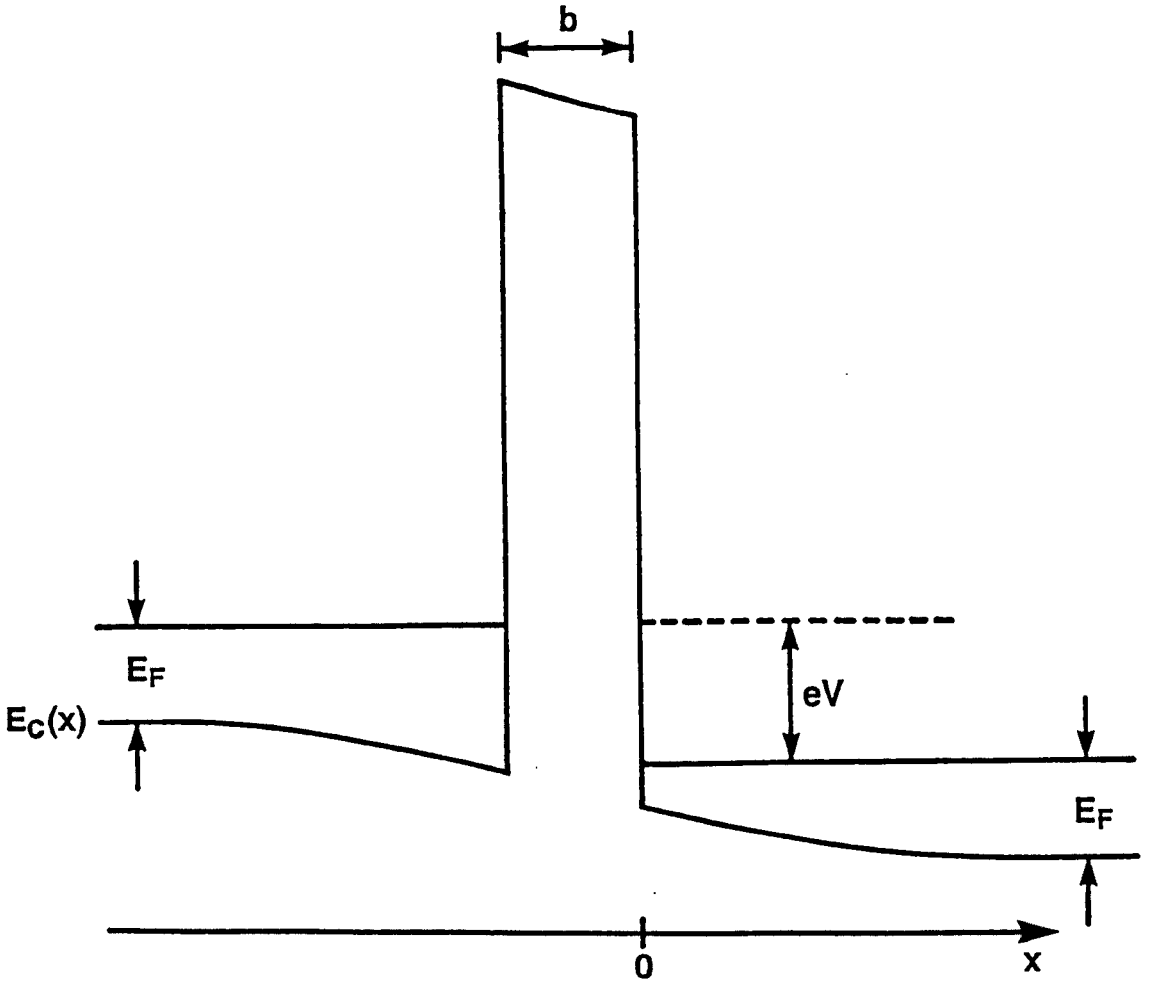

Figure 1.5 Schematic conduction band profile $E_C(x)$ of a single-barrier heterostructure containing heavily n-doped contacts, with the same bulk Fermi energy E_F. For the bias voltage shown, the electrostatic potential variation in the contact regions is insufficient to cause bound-state formation.

An energy-dependent mass is used for $x > 0$ because, due to the electrostatic potential dropped across the barrier, electrons may be injected far above the band edge of the right-hand collector contact.

Since electron motion is unconstrained parallel to the interfaces, the solutions of equation (1.47) are of the form (1.37) where $F(x)$ satisfies the approximate 1D equation

$$\left(-\frac{\hbar^2}{2}\frac{d}{dx}\left(\frac{1}{m^*(x)}\right)\frac{d}{dx} + E_c(x)\right) F(x) = E_x\, F(x) \qquad (1.48)$$

in which $E_x = E - \hbar^2(k_y^2 + k_z^2)/2m_L^*$.

Piecewise WKB solutions of this equation which represent an electron incident on the barrier from the left are

$$F(x) = \begin{cases} A\, k^{-\frac{1}{2}}(x)\, e^{i\int_x^{-b} k(x)dx} + Bk^{-\frac{1}{2}}(x)\, e^{-i\int_x^{-b} k(x)dx} & ; x \le -b \\ C\, \mu^{-\frac{1}{2}}(x)\, e^{-\int_{-b}^{x} \mu(x)dx} + G\mu^{-\frac{1}{2}}(x)\, e^{\int_{-b}^{x} \mu(x)dx} & ; -b \le x \le 0 \\ D\, \alpha^{-\frac{1}{2}}(x)\, e^{i\int_0^x \alpha(x)dx} & ; x \ge 0 \end{cases} \qquad (1.49)$$

where the functions

$$\alpha(x) = k(x) = (2m_L^*(E_X - E_C(x)))^{\frac{1}{2}}/\hbar \quad ,$$

and

$$\mu(x) = (2m_B^*(E_C(x) - E_X))^{\frac{1}{2}}/\hbar \quad ,$$

assume that $E_C(x)$ varies sufficiently slowly that terms involving $dm^*(x)/dx$ may be neglected. In the classically allowed regions, $F(x)$ is valid provided the change in potential energy which occurs over one local wavelength $\lambda(x) = 2\pi/k(x)$ or $2\pi/\alpha(x)$ is small compared with the kinetic energy $2\pi^2\hbar^2/m^*(x)\lambda^2(x)$. The same validity requirement applies in the barrier region where $\lambda(x) = 2\pi/\mu(x)$ is the distance over which $F(x)$ changes by a factor of approximately $e^{2\pi}$.

Neglecting terms involving $dk(x)/dx$ (valid provided the WKB validity requirements are satisfied), the average probability flux incident on the left-hand barrier interface is, combining equations (1.44) and (1.49),

$$\bar{P}(-b_-) = \frac{\hbar|A|^2}{m_L^*} \quad , \tag{1.50}$$

and the average transmitted flux is

$$\bar{P}(0_+) = \hbar|D|^2/m^*(0_+) \tag{1.51}$$

where $m^*(0_+) = m_L^*(1 + \alpha(E - E_c(0_+)))$.

The barrier transmission coefficient, defined to be the average transmitted flux divided by the average incident flux, is given by

$$T = \frac{\bar{P}(0_+)}{\bar{P}(-b_-)} = \frac{m_L^*}{m^*(0_+)} \left|\frac{D}{A}\right|^2 \tag{1.52}$$

The relation between A and D, found by imposing the matching conditions (1.39) and (1.40) on F(x) at each barrier interface (see, for example, Merzbacher, 1970), is such that

$$T = \frac{16\,(m_L^*/m^*(0_+))\mu(-b_+)\mu(0_-)k(-b_-)\alpha(0_+)e^{-2\int_{-b}^{0}\mu(x)dx}}{(\mu^2(0_-) + (m_B^*/m^*(0_+))^2\alpha^2(0_+))(k^2(-b_-) + (m_L^*/m_B^*)^2\mu^2(-b_+))} \tag{1.53}$$

If the effective mass and electrostatic potential do not vary with position so that $k(x) = \alpha(x) = k$ and $m^*(x) = m^*$ for all x, equation (1.53) becomes

$$T = \frac{16\mu^2k^2e^{-2\mu b}}{(\mu^2 + k^2)^2} \tag{1.54}$$

which is identical to the standard free electron result, except that μ and k depend on m^* rather than m_0. Equation (1.53) is used throughout this thesis in the interpretation of expressions for tunnelling transition rates, derived using the transfer-Hamiltonian tunnelling formalism, (see Chapter 3).

1.9 Resonant Tunnelling

Figure 1.6 shows the conduction band profile of a symmetric double-barrier resonant-tunnelling structure (DBRTS), containing two layers (2 and 4) of high-gap semiconductor material, each of which acts as a potential energy barrier to electron motion in the x-direction. For electrons incident from the left with longitudinal kinetic energy $E_x < \Delta E_c$, the global transmission coefficient of this system is found just as for the single-barrier structure, by matching the piecewise solutions of the effective-mass equation at each interface. This transmission coefficient is (Azbel, 1983, and Ricco and Azbel, 1984)

$$T_{2B} = \left[1 + \frac{4R_B}{T_B^2} \sin^2(kw - \theta)\right]^{-1} \qquad (1.55)$$

where θ is a measure of the degree of wavefunction penetration into the barrier region (Toombs and Sheard, 1989), T_B is the transmission coefficient of each barrier, considered in isolation and R_B is the reflection coefficient which equals the reflected flux divided by the

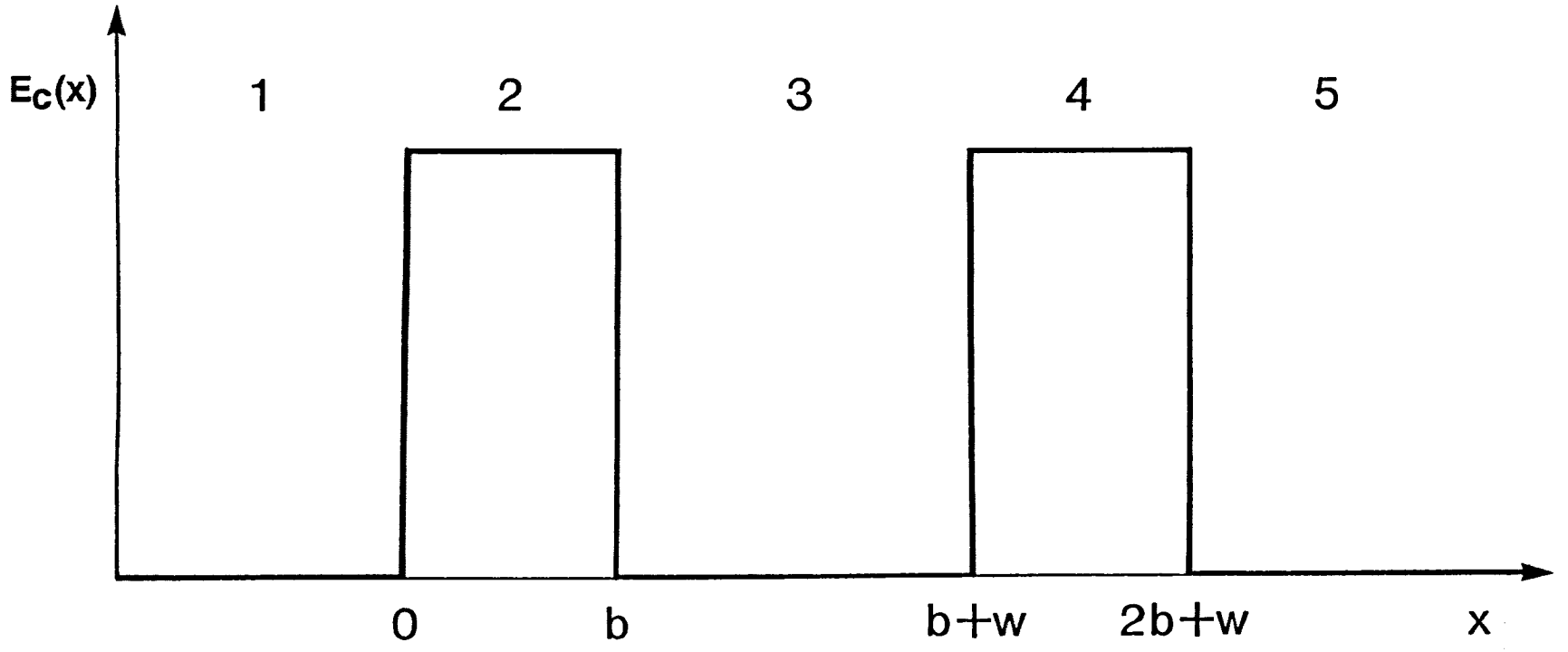

Figure 1.6 Schematic conduction band profile of a symmetric DBRTS in which the two layers (2 and 4) of high band-gap material act as potential barriers to electron motion normal to the interfaces.

incident flux. Figure 1.7 shows T_{2B} for barriers of height 300 meV and width 40 Å. The well width is 100 Å and the effective mass is taken to be $m^* = 0.07\ m_0$ throughout the device. The transmission coefficient shows a series of sharp maxima, at which the peak height equals unity. This phenomenon is known as resonant tunnelling. It can be seen from equation (1.55) that this occurs whenever $kw - \theta = n\pi$, where n is a non-negative integer. This is almost exactly the same as the quantisation condition for the energy levels E_n of the isolated quantum well formed by extending the two barrier layers to $\pm\infty$. Therefore, the transmission coefficient has a maximum whenever the incident energy E_x coincides with the quasi-bound states of the quantum well.

Weil and Vinter (1987) and Sheard and Toombs (1988) have calculated the voltage-dependence of the tunnel current which flows through a symmetric double-barrier structure in which, at low temperatures, the conduction electrons in the n^+ emitter and collector contacts form degenerate 3D Fermi gases of Fermi energy E_F.

Whenever the n^{th} bound state energy E_n, measured relative to the conduction band edge of the emitter contact, lies in the range $0 \leq E_n \leq E_F$, the transmission coefficient of electrons incident on the LH barrier with kinetic energy $E_x = E_n$, equals unity. With increasing voltage, the bound state energy E_n, and consequently the resonant kinetic energy E_x, both fall. The occupied electron states in the n^+ emitter lie within a Fermi sphere in $\underline{k}$-space, so that the

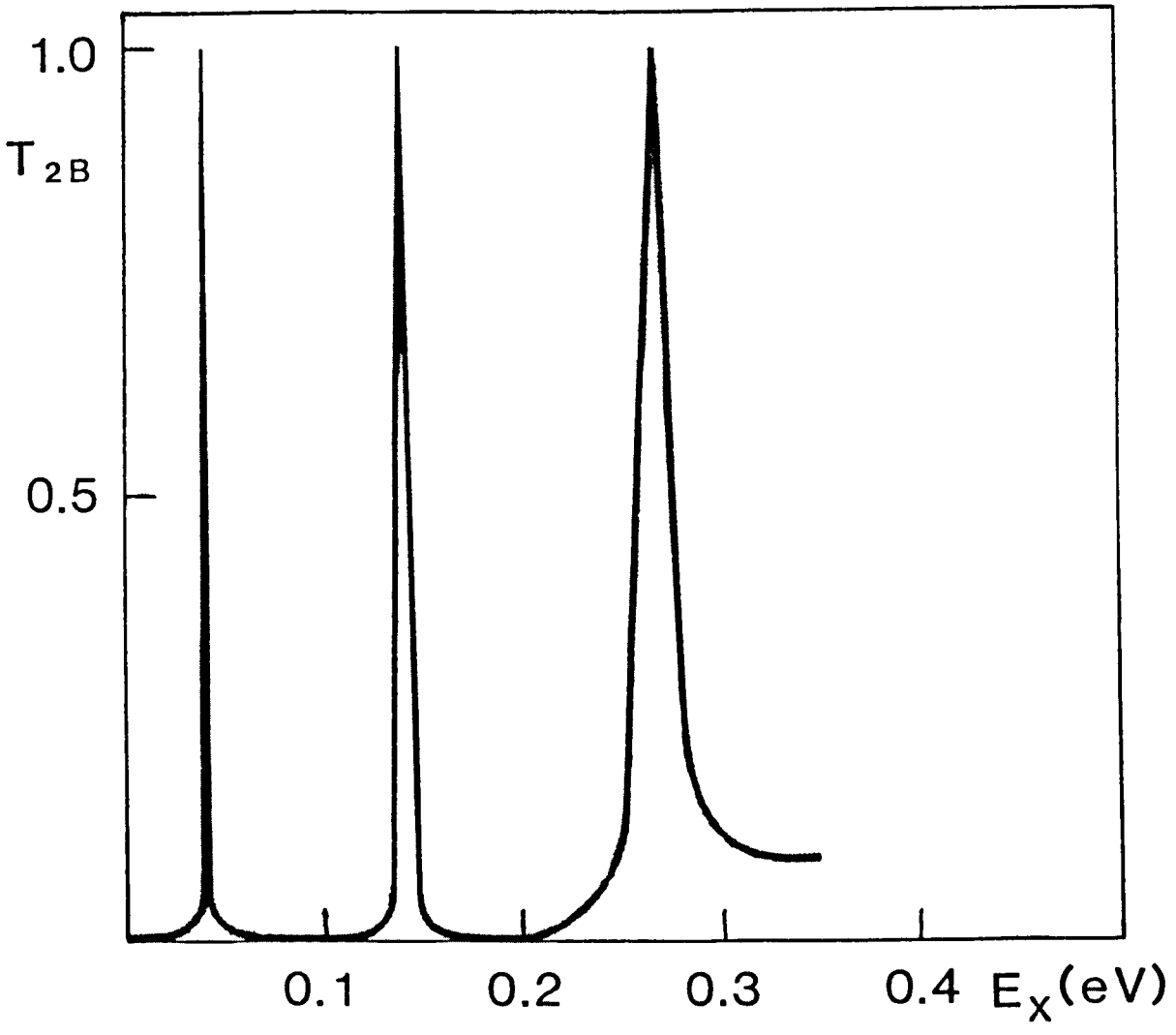

Figure 1.7 The transmission coefficient T_{2B} of a symmetric double-barrier structure as a function of longitudinal kinetic energy E_x. The potential barriers are of height 300 meV and width 40 Å. The well is of width 100 Å and the effective mass of the low band-gap material is taken to be $m^* = 0.07\ m_o$. (After Toombs and Sheard, 1989).

number of electrons per unit energy $N(E_x)$, which are resonant with the n^{th} bound state increases with decreasing E_x and increasing voltage. These electrons make the major contribution to the tunnel current, which consequently rises with voltage as shown in Figure 1.8, reaching a maximum when E_n coincides with the conduction band edge of the emitter contact. When the bound state energy falls below this conduction band edge, the tunnel current drops rapidly, giving rise to a region of negative differential resistance (NDR), which is characteristic of resonant tunnelling. Resonant tunnelling in heterostructures was first observed at liquid helium temperatures by Chang et al. (1974). Since then, improvements in sample quality have extended the temperature range for the observation of NDR up to room temperature (Morkoc, 1986, and Goodhue, 1986), and raised the measured peak-to-valley ratios in the current-voltage characteristics to 63:1 in an (InGa)As/AlAs/InAs DBRTS at a temperature of 77 K (Broeckaert, 1988).

Henini et al. (1989) and Leadbeater et al. (1989) have observed up to 70 regions of NDR in the current-voltage characteristics of GaAs/(AlGa)As based DBRTS containing wide-wells (600 Å - 1800 Å) which support many bound states. Electron tunnelling in such wide-well structures, in the presence of a transverse ($\underline{B} \perp \underline{I}$) magnetic field is considered in Chapter 7 of this thesis.

A time-dependent formalism of resonant tunnelling was first proposed by Luryi (1985), in which electron transmission is regarded

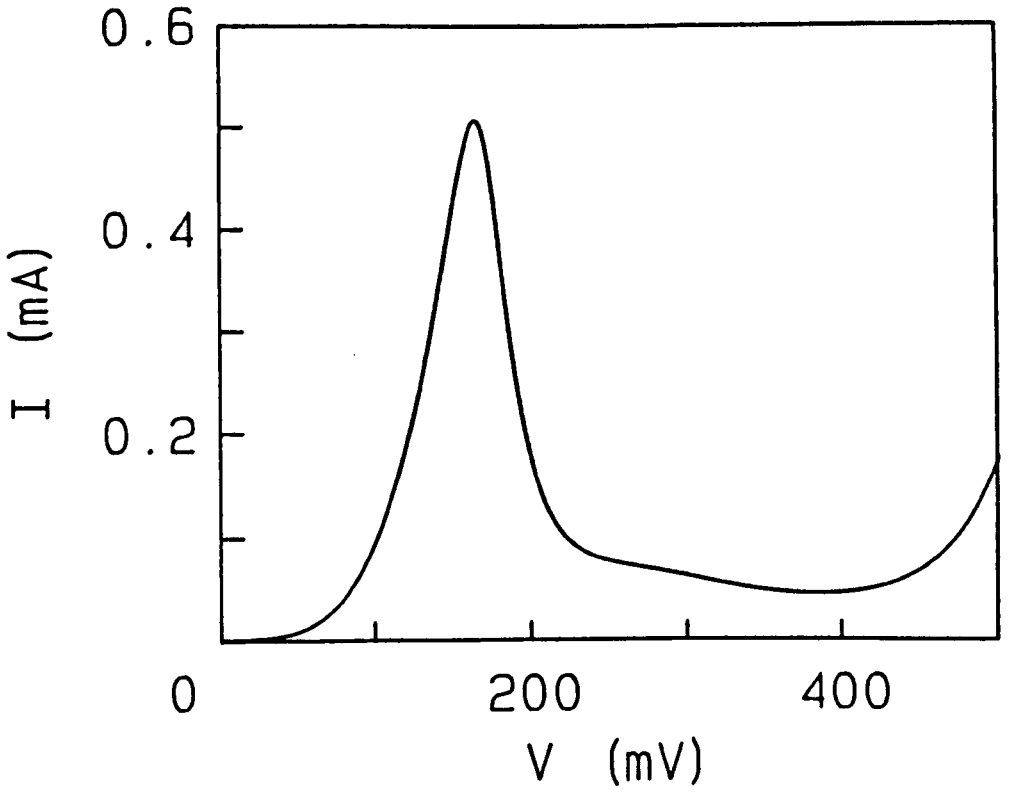

Figure 1.8 Current-voltage characteristic of a symmetric DBRTS with n^+ contacts, showing the region of negative differential resistance which occurs as the bound state energy in the well falls below the conduction band edge of the emitter contact.

as two successive transitions, first from the emitter into the well and then from the well into the collector. Payne (1986) and Weil and Vinter (1987) used the Bardeen transfer-Hamiltonian formalism, discussed in Chapter 3, to show that the sequential model of resonant tunnelling and the time-independent model, based on the global transmission coefficient of the system, both give identical expressions for the resonant current flowing through a symmetric DBRTS with heavily n-doped emitter and collector contacts. Sheard and Toombs (1988) have shown that the two approaches also give the same resonant current for an asymmetric DBRTS.

Detailed comparison of the coherent and sequential tunnelling models is given by Buttiker (1988) and in the review article by Mendez (1988).

CHAPTER TWO

THE ELECTROSTATICS AND ELECTRONIC ENERGY LEVELS OF ASYMMETRICALLY-DOPED SINGLE-BARRIER TUNNELLING STRUCTURES

2.1 Introduction

Hickmott (1987) and Snell et al. (1987) have investigated the effect of a quantising magnetic field $\underline{B}$ on the tunnel current $\underline{I}$ which flows through n-type single-barrier heterostructures when a lightly-doped emitter is biassed negatively relative to a heavily-doped collector contact (forward bias). When the magnetic field is applied in the plane of the barrier ($\underline{B} \perp \underline{I}$), oscillatory structure is observed in the voltage- and field-dependence of the tunnel current, and more clearly in the first and second derivatives.

This chapter aims to establish the general properties of the single-barrier structures under forward-bias conditions and in zero magnetic field. The nature of the occupied energy levels is of particular importance, since this must be taken into account in the development of an appropriate magnetotunnelling formalism.

2.2 Constructional Details of the Single-barrier Structures

The composition and schematic conduction band profile of the single-barrier structures is shown in Figure 2.1, together with the coordinate axes referred to throughout this thesis. Detailed specifications of each structure are given in Chapters 5 and 6.

The heavily-doped capping layer 1 acts as a reservoir which supplies electrons to the 'active' layers 2, 3 and 4 which determine the electrical properties of the device, and comprise a single layer of high band-gap barrier-acting material (InP or (AlGa)As) sandwiched between two lower band-gap contact layers ((InGa)As or GaAs). These contact layers are lightly n-doped ($N_D \cong 10^{21}$ m^{-3}) on the LHS of the barrier and heavily n-doped ($N_D \cong 10^{23}$ m^{-3}) on the RHS of the barrier. The n^+ buffer layer 5 is deposited on the substrate.

All reported measurements were performed at liquid helium temperatures (T = 4.2 K). At these low temperatures, the chemical potential, or Fermi level, in the n^- layer lies close to the donor binding energy.

The high concentration of donor impurities in the n^+ layer causes sufficient overlap between adjacent donor state wavefunctions that the impurity levels form an impurity band which merges with the conduction band. At liquid helium temperatures, electrons from ionised donors in the n^+ layer occupy conduction band states up to the Fermi energy E_{FR}, thus forming a degenerate three-dimensional electron gas (3DEG) in the right-hand contact.

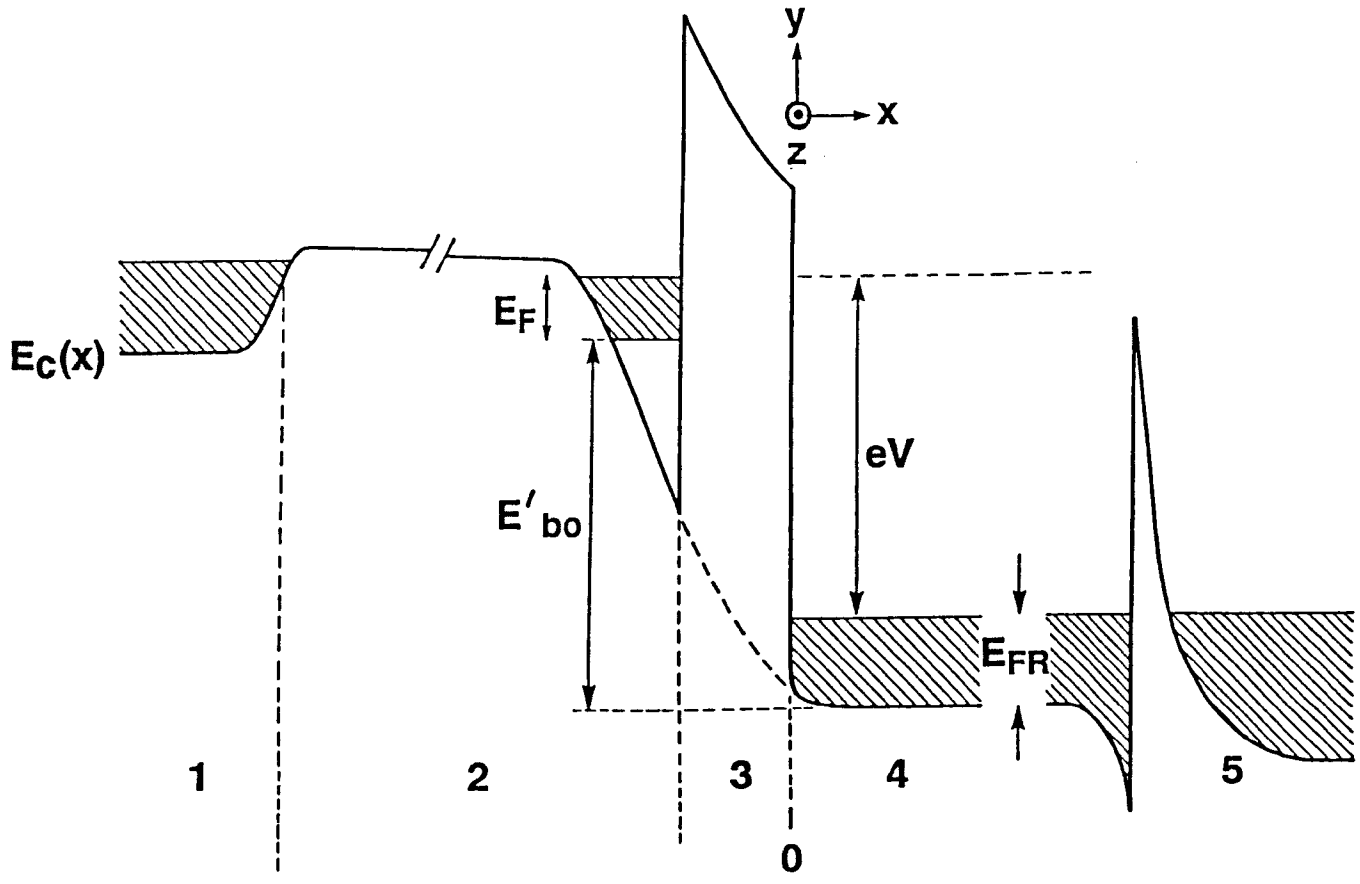

Figure 2.1 Conduction band profile $E_C(x)$ of the asymmetrically-doped single-barrier structures. Under forward-bias conditions, a 2DEG is formed in the n^- layer, adjacent to the barrier.

Assuming the conduction band of the n^+ material is isotropic, E_{FR} is related to the donor density N_D m^{-3} by

$$E_{FR}\,(1 + \alpha E_{FR}) = \frac{\hbar^2}{2m_L^*}\,(3\pi^2\,N_D)^{\frac{2}{3}} \qquad (2.1)$$

where m_L^* is the conduction band-edge effective mass and α is the nonparabolicity parameter defined in equation (1.12). When non-parabolicity is included, E_{FR} is lower than the parabolic-band value given by the RHS of equation (2.1).

2.3 Equilibrium Electrostatics

When no bias is applied, the heterostructure is in equilibrium and a constant Fermi level is maintained throughout the device. This is achieved by the transfer of electrons from the n^+ region into lower-lying conduction band states in the n^- layer. This transfer of electrons leaves behind fixed positive space charge in the n^+ contact which, in the absence of negative space charge in the barrier region, creates an electric field at the LHS of the barrier, directed towards the n^- layer, normal to the barrier interface. The electronic potential energy therefore increases in the n^- layer with distance from the barrier, so that the transferred electrons are attracted to the interface, forming an accumulation layer of negative charge. This accumulated charge screens the electric field which exists at the LH barrier interface so that a finite potential is

dropped across the n^- layer. Similarly, the electric field created at the RH barrier interface by electron depletion from the n^+ layer, is screened by the fixed positive space charge, resulting in a finite potential difference across this layer. Charge transfer occurs until the sum of the potentials dropped across the n^-, barrier, and n^+ regions equals $(E_{FR} + E_D)/e$ where E_D is the donor binding energy.

Measurements of the capacitance-voltage characteristics reveal the existence of positive space charge in the barrier region of the (InGa)As/InP samples (Snell, 1987a) and negative space charge in the GaAs/(AlGa)As devices (Hickmott, 1988). This negative space charge is sufficiently high that in equilibrium, the n^--layer of the GaAs/(AlGa)As structures is depleted close to the barrier interface (Hickmott,1985) and electron accumulation only occurs in response to an applied forward bias.

2.4 Non-equilibrium Electrostatics

If a forward bias V is applied which raises the electronic potential energy in the LH n^+ reservoir (layer 1 in Figure 2.1), relative to the RH n^+ reservoir (layer 4), the difference between the left- and right-hand Fermi levels equals eV, and the system is no longer in equilibrium. However, provided the rate of electron diffusion through the n^- layer is high compared with the tunnelling transition rate, the Fermi levels of the 2DEG and LH reservoir are approximately equal and lie close to the donor level in the bulk of

the n^- layer, away from the accumulation region. Consequently, the LH reservoir, the donors in the bulk of the n^- layer, and the 2DEG are all in approximate equilibrium. The electrostatic potential dropped across the neutral region of the n^- layer can be deduced by comparing the forward-bias current-voltage characteristic of the tunnelling structures with that of a bulk n^- control sample. For the (InGa)As samples, this potential difference is found to be small ($\leq$ 3 mV) compared with the applied voltage, over the entire range of bias used in the transverse magnetotunnelling experiments of Snell et al. (1987).

Provided that the tunnelling rate is also small compared with the LO phonon emission rate, which is the dominant energy relaxation mechanism of hot electrons in III-V materials at 4.2 K (see, for example, Ridley 1988), electrons injected into the n^+ contact cool rapidly to the bulk Fermi energy E_{FR}, leaving unoccupied states in the n^+ layer, below the Fermi level of the 2DEG. Consequently, although the n^- and n^+ layers are each in approximate local equilibrium, they are not in equilibrium with one another. Neglecting the small chemical potential difference between the LH reservoir and the 2DEG, the difference between the Fermi levels of the 2DEG and n^+ collector contact equals the work$^{in}_{\wedge}$eV done by an external voltage source in returning a thermalised electron to the n^-layer.

An applied forward bias enhances the electric field at the LH barrier interface. If sufficiently large electrostatic potential variations occur over short distances in the accumulation layer, the

energy associated with motion normal to the barrier interface may be quantised, leading to the formation of bound states as shown in Figure 2.1.

Strictly, these states are 'quasi-bound' since the accumulated electrons eventually undergo tunnelling transitions into the n^+ layer.

Assuming the validity of the isotropic effective-mass equation (1.36) for the rapidly-varying accumulation layer potential, the envelope wavefunctions of the i^{th} bound state may be written

$$\Psi_i(x, y, z) = \frac{\psi_i(x)}{(L_y L_z)^{\frac{1}{2}}} e^{ik_y y} e^{ik_z z} , \quad i = 0,1,2 \ldots \qquad (2.2)$$

where $L_y L_z$ is the cross-sectional area.
Neglecting conduction band nonparabolicity, the x-dependent factors $\psi_i(x)$ satisfy the 1-D Schrödinger equation.

$$\left(\frac{-\hbar^2}{2m_L^*} \frac{d^2}{dx^2} + E_c(x)\right) \psi_i(x) = E'_{bi} \psi_i(x) \quad i = 0,1 \ldots \qquad (2.3)$$

where

$$E_c(x) = \begin{cases} -e\phi(x) & ; \ x < -b \text{ or } x > 0 \\ \Delta E_c - e\phi(x) & ; \ -b \leq x \leq 0 \end{cases}$$

The origin of the energy scale is taken to be the conduction band edge in the n^+ layer, far away from the barrier interface.

The bound state energy, E'_{bi}, is related to the total energy, $E_i(k_y, k_z)$ by

$$E_i(k_y, k_z) = E'_{bi} + \frac{\hbar^2(k^2_y + k^2_z)}{2m_L^*} \tag{2.4}$$

The transverse plane wave states associated with each bound state are occupied up to the LH Fermi level. These occupied states are referred to as subbands. From the boundary conditions (1.11), the density of states (DOS), per spin, per unit cross-sectional area L_yL_z is, for the i^{th} subband

$$D_i(E) = \frac{m_L^*\theta(E - E'_{bi})}{2\pi\hbar^2} \tag{2.5}$$

where $\theta(E - E'_{bi})$ is the unit step function. When only the lowest subband is occupied, the accumulated electrons form a two-dimensional electron gas (2DEG). If more than one subband is occupied, the system is not strictly 2D since there is still a limited degree of freedom normal to the interface via inter-subband scattering. The formation of 2DEGs in the accumulation layers of all the tunnel structures described in this thesis has been confirmed experimentally (Eaves et al., 1987 and Hickmott, 1985a).

From equation (2.5), the Fermi energy E_F of the 2DEG, measured from the bound state energy E'_{bo} is related to the sheet electron concentration n_s by

$$E_F = \frac{\pi\hbar^2 n_s}{m_L^*} \quad . \tag{2.6}$$

In $\underline{k}$-space at T = 0 K, the occupied states lie within a Fermi circle in the k_y-k_z plane, centred at the origin and of radius equal to the magnitude of the Fermi wavevector $k_F = [2m_L^* E_F]^{\frac{1}{2}}/\hbar$.

The electrostatic potential $\phi(x)$ in equation (2.3) is related to the space-charge density $\rho(x)$ through Poisson's equation

$$\frac{d}{dx}\left[\epsilon_r(x)\,\frac{d\phi(x)}{dx}\right] = -\frac{\rho(x)}{\epsilon_o} \tag{2.7}$$

where $\epsilon_r(x)$ is the local dielectric constant given by

$$\epsilon_r(x) = \begin{cases} \epsilon_{rL} \; ; \; x < -b \text{ or } x > 0 \\ \epsilon_{rH} \; ; \; -b \leq x \leq 0 \end{cases} ,$$

in which the subscripts L and H refer to the low and high band-gap materials.

Assuming that the charge due to the accumulated electrons is much greater than that due to ionised donors in the n^- layer, $\rho(x)$ depends on the bound state wavefunctions $\psi_i(x)$ through

$$\rho(x) = - e\sum_i n_i \left|\psi_i (x)\right|^2 \qquad (2.8)$$

where n_i is the sheet electron concentration in the i^{th} subband. The set of equations (2.3) for each subband are coupled through the dependence of the electrostatic potential on the bound state wavefunctions and must therefore be solved self-consistently. Variational methods have been used to obtain approximate solutions of equation (2.3) for heterojunctions in which the accumulated electrons occupy truly bound eigenstates.

When only one subband is occupied, these solutions are usually based on the Fang-Howard trial wavefunction (Fang and Howard, 1966)

$$\psi_{FH}(x) = \begin{cases} - \dfrac{(b + x)}{(2a^3{}_0)^{\frac{1}{2}}} e^{\frac{b+x}{2a_0}} & ; x \leq -b \\ 0 & ; x > -b \end{cases} \qquad (2.9)$$

where a_0 is the variational parameter which minimises the bound state energy for given 2DEG sheet electron concentration n_s.

This wavefunction was first proposed to describe electrons in the inversion layer of silicon MOSFETS. Calculations reported by Stern (1972) and in the general review of the properties of 2D systems by Ando, Fowler and Stern (1982) also refer mainly to silicon MOSFETS.

By definition, the Fang-Howard wavefunction neglects penetration into the barrier region. This is a reasonable approximation for silicon/silicon dioxide interfaces but not necessarily for III-V heterostructures which generally have lower conduction band offsets.

Bastard (1983) used a modified Fang-Howard wavefunction,which includes barrier-penetration, specifically to calculate the lowest bound state energy for (InGa)As/InP heterojunctions. It was shown that for these structures less than 4% of the charge in the 2DEG is located within the barrier. For GaAs/(AlGa)As-based systems, both the conduction band offset and the effective mass of the barrier material are higher, so that the penetration of the wavefunction is even less important. Consequently, the Fang-Howard wavefunction gives a reasonably accurate description of the 2DEGs formed in the accumulation layers of III-V tunnel structures provided that the barrier is also sufficiently wide to prevent significant penetration of the electron wavefunction.

The simplicity of the Fang-Howard wavefunction facilitates the analytic treatment of the effect of a perturbing transverse

magnetic field on 2DEG states, given in Chapter 4.

The electrostatic potential energy $-e\phi(x)$, which determines the conduction band profile, is found by solving Poisson's equation throughout the device subject to the boundary conditions

$$-e\phi(x \to -\infty) = eV + E_{FR} \tag{2.10}$$

$$\left.\frac{d\phi(x)}{dx}\right|_{x \to -\infty} = 0 \tag{2.11}$$

$$-F_L = \left.\frac{d\phi(x)}{dx}\right|_{x \to -b_-} = n_s e/\varepsilon_0\varepsilon_{rL} \tag{2.12}$$

$$\left.\frac{d\phi(x)}{dx}\right|_{x \to -b_+} = \frac{\varepsilon_{rL}}{\varepsilon_{rH}} \left.\frac{d\phi(x)}{dx}\right|_{x \to -b_-} \tag{2.13}$$

$$\left.\frac{d\phi}{dx}\right|_{x \to 0_+} = \frac{\varepsilon_{rH}}{\varepsilon_{rL}} \left.\frac{d\phi(x)}{dx}\right|_{x \to 0_-} \tag{2.14}$$

Equation (2.11) states the requirement that the electric field vanishes in the n^- layer, far from the barrier interface. Equation (2.12) relates the electric field F_L at the LH barrier interface to the 2DEG sheet electron concentration and follows directly from Gauss' law. Equations (2.13) and (2.14) follow from continuity of the normal component of electric displacement.

Solving Poisson's equation for the accumulation layer charge distribution specified by the Fang-Howard wavefunction (2.9) and imposing the boundary conditions (2.10) and (2.12) gives

$$-e\phi(x) = \frac{n_s e^2}{2\varepsilon_0 \varepsilon_{rL}} \left(6a_0 - \left(6a_0 - 4(x+b) + \frac{(x+b)^2}{a_0}\right) e^{\frac{x+b}{a_0}}\right)$$

$$+ eV + E_{FR} - \frac{3a_0 n_s e^2}{\varepsilon_0 \varepsilon_{rL}} \quad ; x \leq -b \quad . \qquad (2.15)$$

The bound state energy is found by minimising the energy expectation value $\langle\psi_{FH}|H|\psi_{FH}\rangle$ where H is the effective-mass Hamiltonian (2.3) in which the potential energy is given by equation (2.15). For given n_s, the required variational parameter (Stern, 1972)

$$a_0 = \left(\frac{8\varepsilon_0 \varepsilon_{rL} \hbar^2}{33\, e^2 m_L^* n_s}\right)^{\frac{1}{3}} \quad , \qquad (2.16)$$

is related to the mean stand-off distance $-\langle x+b\rangle$, of the 2DEG from the LH barrier interface by

$$-\langle x+b\rangle = 3a_0 \quad . \qquad (2.17)$$

The bound state energy E_{bo}, measured relative to the electrostatic potential energy at $x = -b$, is (Stern, 1972)

$$E_{bo} = \frac{5\hbar^2}{2\, m_L^*\, (2a_o)^2} \quad . \tag{2.18}$$

Measured relative to the origin of the energy scale, $E_c(x \to \infty)$, this bound state energy is given by

$$E'_{bo} = E_{bo} - e\phi(-b) = \frac{5\hbar^2}{2m_L^*\,(2a_o)^2} + eV + E_{FR} - \frac{3a_o\, n_s e^2}{\varepsilon_o\, \varepsilon_{rL}} \tag{2.19}$$

From equation (2.15), the potential energy gained as an electron in the n^- layer moves away from the LH barrier interface is, in the limit $x \to -\infty$

$$eV_a = -e\phi(x \to -\infty) + e\phi(x = -b) = \frac{3n_s\, e^2\, a_o}{\varepsilon_o\, \varepsilon_{rL}} \quad . \tag{2.20}$$

Comparing this with the expressions for E_F and E_{bo} given in equations (2.6) and (2.18), it is clear that $eV_a \neq E_F + E_{bo}$. This lack of self-consistency is one of the shortcomings of the Fang-Howard wavefunction which is avoided by the use of two-parameter wavefunctions such as that of Bastard (1983).

Measurements of the capacitance-voltage characteristics have revealed the existence of positive space charge in the barrier region of the (InGa)As/InP structures (Snell, 1987a). Solving Poisson's equation assuming uniform positive space charge of density Ne m^{-3}, and imposing the boundary condition (2.13) gives

$$-e\phi(x) = \frac{e^2}{\varepsilon_0\,\varepsilon_{rH}}\left((Nb - n_s)x + \frac{Nx^2}{2}\right) + \frac{e^2}{\varepsilon_0}\left(\frac{Nb^2}{2\varepsilon_{rH}} - n_s\left(\frac{b}{\varepsilon_{rH}} + \frac{3a_0}{\varepsilon_{rL}}\right)\right)$$

$$+ eV + E_{FR} \qquad (2.21)$$

$$; -b \leq x \leq 0 \quad .$$

Consequently, the electronic potential energy at the LH barrier interface exceeds that at the RH barrier interface by

$$eV_b = -e\phi(-b) + e\phi(0) = \frac{e^2 b}{\varepsilon_0\,\varepsilon_{rH}}\left(n_s - \frac{Nb}{2}\right) \quad . \qquad (2.22)$$

The electrostatic potential variation in the n^+ layer is modelled using Thomas-Fermi screening theory (see, for example, Ashcroft and Mermin, 1976). This semiclassical theory is valid provided that the change in electronic potential energy which occurs over one Thomas-Fermi wavelength $\lambda_{FR} = 2\pi/k_{FR}$ is small compared with the local Fermi energy, and predicts

$$-e\phi(x) = -e\phi_s\, e^{\frac{-x}{\ell_s}} \quad ; x > 0 \qquad (2.23)$$

where the Thomas-Fermi screening length ℓ_s satisfies

$$\ell_s^{\,2} = 2E_{FR}\,\varepsilon_0\,\varepsilon_{rL}\,(3N_D\,e^2)^{-1} \quad . \qquad (2.24)$$

The potential ϕ_s at the RH barrier interface is obtained by matching the derivatives of equations (2.21) and (2.23) using the electric displacement continuity condition (2.14). The required value of ϕ_s is

$$\phi_s = e\ell_s(Nb - n_s)/\varepsilon_o\,\varepsilon_{rL} \quad . \tag{2.25}$$

Owing to the high donor density $N_D \cong 10^{23}\ m^{-3}$ in the n^+ contact, the screening length ℓ_s is small. Consequently, ϕ_s is also small and is neglected when calculating the eigenvalues of the n^+ layer in the presence of a transverse magnetic field (see Section 4.3). At fixed forward bias V, the 2DEG electron concentration $n_s(V)$ is found by solution of the energy conservation equation

$$eV_a + eV_b - e\phi_s = eV + E_{FR} \tag{2.26}$$

where eV_a, eV_b and ϕ_s are given as functions of n_s in equations (2.20), (2.22) and (2.25).

2.5 Calculation of the 2DEG Sheet Electron Density as a Function of Forward-bias Voltage

The data points in Figure 2.2 show the 2DEG sheet electron concentration in the (InGa)As/InP single-barrier structures measured for a variety of forward-bias voltages. These values of n_s were deduced from the periodicity of maxima observed in the first derivative of the magneto-current I(B), measured under forward-bias

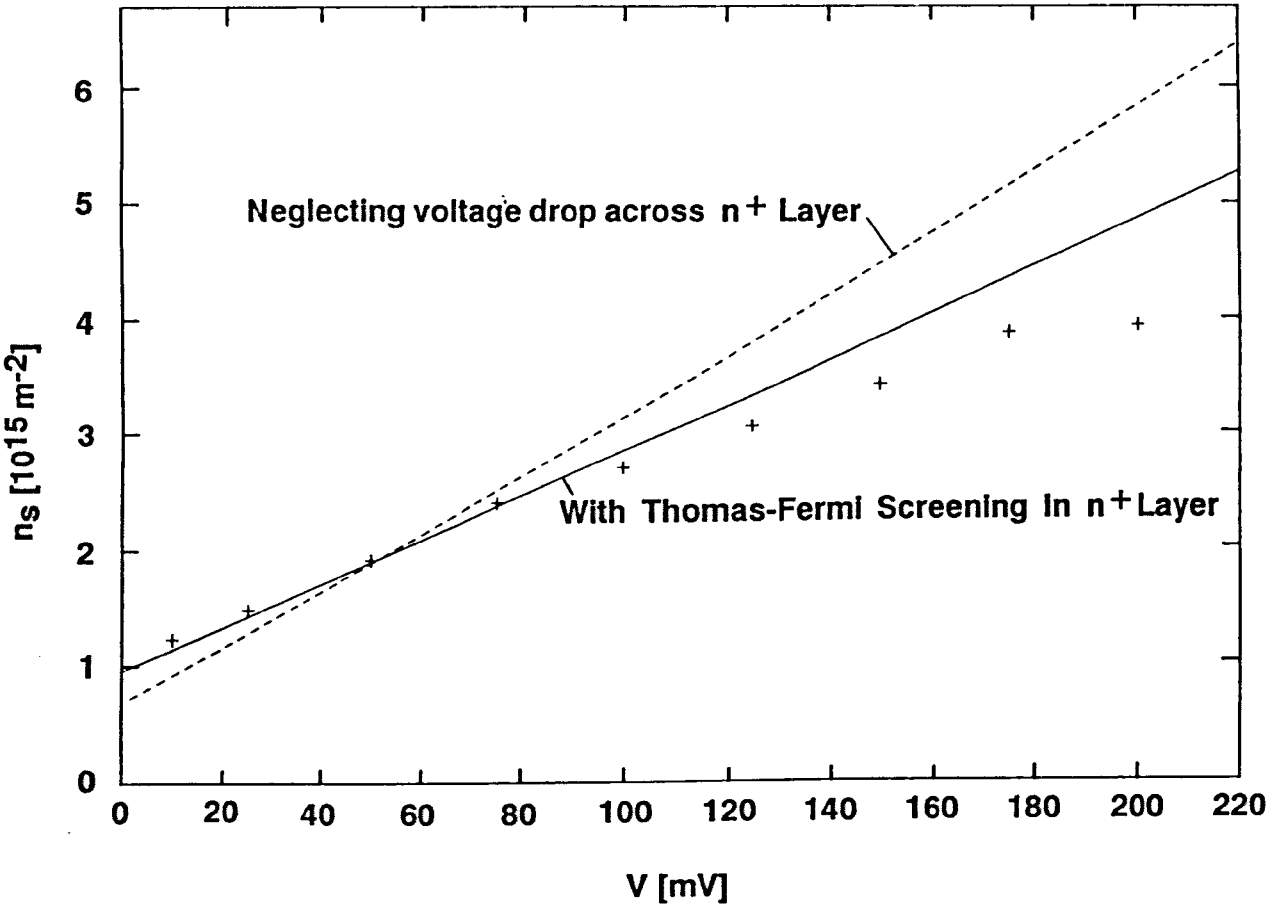

Figure 2.2 Comparison between the 2DEG sheet electron concentration in the (InGa)As/InP structures measured (+) as a function of applied bias, with theoretical values based on the Fang-Howard model of the bound state and solution of Poisson's equation throughout the structure (a) including Thomas-Fermi screening in the n^+ layer (solid curve) and (b) neglecting the voltage dropped across the n^+ layer (broken curve).

conditions, and in the presence of a longitudinal magnetic field ($\underline{B} \parallel \underline{I}$) (Snell, 1987a). In this geometry, the magnetic field quantises the transverse motion of the 2DEG electrons into discrete Landau levels. Chan et al. (1987) have modelled the I(B) characteristics using a self-consistent calculation of the 2DEG bound state energy and sheet electron concentration based on a two-parameter variational wave-function. This model predicts maxima in dI/dB whenever $E_F(B = 0) = \pi\hbar^2 n_S/m_L^* = (n + \phi)\hbar\omega_c$ where $E_F(B = 0)$ is the zero-field Fermi energy and ϕ is a field-independent phase factor.

Consequently, the zero-field sheet electron concentration can be determined from the periodicity of maxima in dI/dB, plotted as a function as 1/B.

The solid line in Figure 2.2 shows the voltage-dependence of n_S, calculated from equation (2.26). Reasonable agreement is obtained with the measured values if uniform positive space charge of density 10^{23} e m^{-3} is included in the barrier region.

This charge density equals the nominal doping concentration in the n^+ layer, which suggests that dopant atoms may have diffused into the barrier region. However, unintentional doping to this high level is unlikely, and the apparent barrier space charge is probably associated with surface states formed at the barrier interfaces (Snell, 1987a).

The discrepancy between the observed and calculated electron densities, at high bias voltages, is probably due to the breakdown of

Thomas-Fermi screening theory as the change in electronic potential energy occuring over one Fermi wavelength becomes comparable with the local Fermi energy. Although the validity of Thomas-Fermi theory is questionable at high forward bias, the broken curve in Figure 2.2 shows that the agreement with experiment is far worse if the voltage dropped across the n^+ layer is totally neglected.

The calculated $n_s(V)$ variation allows the 2DEG variational parameter a_o, Fermi energy E_F and bound state energy E_{bo}' to be determined for given forward bias. The electrostatic potential energy variation, and consequently the conduction band profile follow directly from equations (2.15), (2.21) and (2.23).

2.6 The Constant Capacitance Approximation

The calculated 2DEG sheet electron concentration varies almost linearly over the range of bias shown in Figure 2.2. Consequently, $n_s(V)$ may be written, to good approximation

$$n_s(V) = C(V + V_{FB})/e \qquad (2.27)$$

where C is the (constant) capacitance per unit area and V_{FB} is the reverse-bias voltage for which there is no accumulated charge in the n^- layer, and therefore no band bending. For this reason V_{FB} is referred to as the flat-band voltage. For the (InGa)As/InP structures, $C \cong 4.25 \times 10^{-3}$ F m^{-2} and $V_{FB} \cong 50$ mV (Snell, 1987a). In the absence of space charge in the barrier region, the predicted

flat-band voltage is $V_{FB} = E_{FR}/e \equiv 17$ mV. The higher measured value of V_{FB} indicates the existence of positive space charge in the barrier.

Within the constant capacitance approximation, the 2DEG Fermi energy (2.6) is a linear function of voltage given by

$$E_F = \frac{\pi \hbar^2 C(V + V_{FB})}{m_L^* e} = \frac{\hbar^2 k_F^2}{2m_L^*} \quad . \qquad (2.28)$$

2.7 Summary

The application of a forward-bias voltage to an asymmetrically n-doped single-barrier structure leads to the formation of a 2DEG in the n^- emitter contact, adjacent to the barrier. The bound state energy and mean stand-off distance of the 2DEG can be obtained as functions of the sheet electron concentration n_S from a variational calculation based on the Fang-Howard trial wavefunction.

The voltage-dependence of n_S calculated using the Fang-Howard model of the 2DEG is in reasonable agreement with that measured for the (InGa)As/InP samples, assuming the existence of positive space charge 10^{23} e m^{-3} in the barrier region. Once n_S is known, the conduction band profile can be calculated by solving Poisson's equation throughout the device.

CHAPTER THREE

THE BARDEEN TRANSFER-HAMILTONIAN FORMALISM OF ELECTRON TUNNELLING

3.1 Introduction

In Section 1.7 the average flux carried over one or more unit cells by the conduction band eigenstates of a perturbed crystal lattice, was shown to depend only on the associated envelope functions and on the effective mass of the conduction electrons. In Section 1.8, the transmission coefficient of a single-barrier heterostructure was calculated in the presence of slowly-varying electrostatic potentials by using WKB envelope functions to determine the mean incident and transmitted fluxes carried by extended conduction band eigenstates.

Such time-independent models of electron tunnelling are, however, inapplicable when electronic motion in the tunnelling direction is sufficiently constrained that bound or quasi-bound eigenstates are formed. This constraint may be due to rapid variation of the conduction band edge position, which is the case for the 2DEG states discussed in Chapter 2, or due to confinement by a transverse (in-plane) magnetic field, which leads to the formation of Landau and interfacial Landau states as described in Chapter 4.

These bound eigenstates carry no probability flux in the direction of confinement and therefore give no information about the tunnel current $\underline{I}$. Since all the tunnelling problems discussed in this thesis involve electron tunnelling from 2DEG states into magnetically-quantised interfacial states, an alternative time-dependent tunnelling formalism is required.

The transfer-Hamiltonian approach (Duke, 1969) is explicitly time-dependent since tunnelling is described as a sequential process in which electrons make transitions between eigenstates of left-hand (LH) and right-hand (RH) 'subsystems' comprising the barrier region and either the LH or the RH contact regions respectively.

The transfer-Hamiltonian method was first developed by Oppenheimer (1928) to calculate the ionisation rate of atomic hydrogen in a high electric field. Bardeen (1961) used a similar time-dependent approach to describe electron tunnelling in metal-insulator-metal systems when one, or both, of the metals are superconducting.

In this chapter, a generalised version of the Bardeen transfer-Hamiltonian formalism is described which allows for the presence of a transverse magnetic field ($\underline{B} \perp \underline{I}$). The effect of conduction band nonparabolicity in the RH collector contact is also included through an energy- and position-dependent effective mass.

Guided by the time-independent calculations of Section 1.8, this formalism involves only the envelope functions of the LH and RH eigenstates. Some justification for this assumption is given in Section 3.6 where the transmission coefficient of a single square barrier is calculated within the transfer-Hamiltonian approximation, and shown to be identical to the more usual time-independent expression (1.53).

In Section 3.7, an expression for the transition rate between bound eigenstates of two weakly-coupled square wells is derived and interpreted semiclassically.

3.2 The Conduction Band Effective-mass Equation for a Single-barrier Heterostructure in the Presence of a Transverse Magnetic Field ($\underline{B} \perp \underline{I}$)

The results derived in this chapter are applicable to direct-gap single-barrier heterostructures in which any electric or magnetic fields preserve the invariance of the effective-mass Hamiltonian under translations parallel to the barrier interfaces.

The most general system which satisfies these requirements includes an inhomogeneous electric field, $\underline{E}(x)$ normal to the barrier interfaces and a uniform transverse magnetic field ($\underline{B} \parallel 0\underline{z}$) represented by the vector potential in the Landau gauge $\underline{A} = (0, Bx, 0)$. Referred to the co-ordinate axes of Figure 2.1, the conduction band effective-mass equation for this system is

$$H_T \Psi_T^n (x,y,z) = E_T^n \Psi_T^n (x,y,z) \quad , \tag{3.1}$$

where the isotropic effective-mass Hamiltonian is, from equation (1.18)

$$H_T = -\frac{\hbar^2}{2} \frac{\partial}{\partial x} \left(\frac{1}{m^*(x)} \frac{\partial}{\partial x} \right) + \frac{(-i\hbar \frac{\partial}{\partial y} + eBx)^2}{2m^*(x)} - \frac{\hbar^2}{2m^*(x)} \frac{\partial^2}{\partial z^2} + E_c(x) \; . \tag{3.2}$$

For nonparabolic bands, the effective mass is an implicit function of the total energy E_T^n given by

$$m^*(x) = \begin{cases} m_L^* [1 + \alpha_L (E_T^n - E_c(x))] & ; \; x < -b \\ m_B^* & ; \; -b \leq x \leq 0 \\ m_R^* [1 + \alpha_R (E_T^n - E_c(x))] & ; \; x > 0 \end{cases} \quad ,$$

where m_B^* is the band-edge effective mass of the barrier material, m_L^* and m_R^* are the band-edge masses of the LH and RH contact materials, and α_L and α_R are the corresponding nonparabolicity factors.

Lassnig (1987) has shown, using 3-level $\underline{k}.\underline{p}$ theory that the effective mass falls linearly with energy below the conduction band edge. This reduction in mass increases the wavefunction amplitudes in the barrier, and consequently the tunnelling transition rates. However, for high and wide barriers, the electron wavefunctions decay rapidly in the barrier region so that the bound-state eigenvalues, which determine the allowed, energy-conserving transitions, are fairly insensitive to the parameters of the barrier material, and in particular the effective mass. Since the interpretation of magnetotunnelling data presented in Chapters 5 and 6 depends primarily on the conservation requirements which must be satisfied in tunnelling transitions, rather than on the absolute transition rates, the effective mass in the barrier material is taken to be the band-edge mass m_B^*.

From equation (3.2), H_T is invariant under translation parallel to the barrier interfaces, and therefore has eigenfunctions Ψ_T^n of the form

$$\Psi_T^n (x,y,z) = (L_y L_z)^{-\frac{1}{2}} \psi_T^n (x) \, e^{ik_y y} \, e^{ik_z z} \qquad (3.3)$$

where $L_y L_z$ is the cross-sectional area, and k_y, k_z are the transverse wavevector components. Substituting equation (3.3) into equation (3.1), $\psi_T^n(x)$ is found to be a normalised solution of the one-dimensional Schrödinger equation

$$\left(-\frac{\hbar^2}{2}\frac{d}{dx}\left(\frac{1}{m^*(x)}\frac{d}{dx}\right) + \frac{\hbar^2 k_z^{\,2}}{2m^*(x)} + E_{EFF}(x)\right)\psi_T^n(x) = E_T^n\,\psi_T^n(x) \qquad (3.4)$$

where the effective potential energy

$$E_{EFF}(x,\, k_y,\, E_T^n) = E_c(x) + E_{MAG}\,(x,\, k_y,\, E_T^n)$$

is the sum of the conduction band profile and the SHO magnetic potential energy (MPE)

$$E_{MAG}\,(x,\, k_y,\, E_T^n) = \frac{B^2e^2}{2m^*(x)}\left(x + \frac{\hbar k_y}{Be}\right)^2 \quad .$$

The MPE depends on the transverse wavevector component k_y, which determines the orbit centre, and also on the energy eigenvalues E_T^n through the effective mass. Since the eigenvalues of equation (3.4) influence the Hamiltonian in this way, they must be calculated self-consistently.

The kinetic energy $E_z = \hbar^2 k_z^{\,2}/2m^*(x)$, associated with motion parallel to the magnetic field varies with position normal to the barrier interface due to changes in the effective mass. This kinetic energy variation may be interpreted as an additional x-dependent potential, just as the semiclassical kinetic energy associated with motion along the y-axis is referred to as the magnetic potential energy.

However, since the effective mass variations are small for all the heterostructures discussed in this thesis, $m^*(x)$ can be taken to equal m_L^* throughout. Within this approximation,

$$[\frac{-\hbar^2}{2m^*(x)} \frac{\partial^2}{\partial z^2}, H] = 0$$

so that $E_z = \hbar^2 k_z^2 / 2m_L^*$ is conserved. This simplification is central to the model of magnetotunnelling in single-barrier structures presented in Chapters 5 and 6. Subtracting this constant kinetic energy E_z from both sides of equation (3.4) yields a new eigen-equation with eigenvalues equal to the electron energy associated with motion in the x-y plane, perpendicular to the magnetic field. The solutions of this equation are considered in detail in Chapter 4.

3.3 Definition of the Left- and Right-hand Sub-Hamiltonians of a Single-barrier Structure

In this section left- and right-hand sub-Hamiltonians H_L and H_R are defined in terms of the effective-mass Hamiltonian H_T of the entire system. The systems described by H_L and H_R are referred to as left- and right-hand subsystems of the single-barrier structure and contain the barrier region and either the LH or RH contact regions respectively.

The left-hand sub-Hamiltonian H_L is defined by

$$H_L(x,y,z,P_x,P_y,P_z) = \begin{cases} H_T(x,y,z,P_x,P_y,P_z) \; ; \; x \leq 0 \\ H_T(0,y,z,P_x,P_y,P_z) \; ; \; x > 0 \end{cases} \tag{3.5}$$

where $\underline{P} = -i\hbar\underline{\nabla}$.

For the purposes of this definition, the effective mass in equation (3.2) is understood to depend on the energy eigenvalues $\{E_L^{\ell}\}$ of H_L, rather than on $\{E_T^{n}\}$, and the conduction band-edge energy at x = 0 is taken to be $E_c(0) = E_c(x \to 0-)$, that is the band-edge position in the high-gap material close to the RH barrier interface. Since H_L retains the invariance of H_T under translation parallel to the barrier interfaces, its eigenfunctions are of the form

$$\Psi_L^{\ell}(x,y,z) = (L_y L_z)^{-\frac{1}{2}} \psi_L^{\ell}(x) \, e^{ik_y^L y} \, e^{ik_z^L z} \; , \tag{3.6}$$

where k_y^L and k_z^L are transverse wavevector components and $\psi_L^{\ell}(x)$ satisfies equation (3.4), in which the energies and wavevector components are understood to be those associated with Ψ_L^{ℓ}, and $E_{EFF}(x, k_y^L, E_L^{\ell}) = E_{EFF}(0-, k_y^L, E_L^{\ell})$; $x \geq 0$.

Similarly, the RH sub-Hamiltonian H_R is defined by

$$H_R(x,y,z,P_x,P_y,P_z) = \begin{cases} H_T(x,y,z,P_x,P_y,P_z) \; ; \; x \geq -b \\ H_T(-b,y,z,P_x,P_y,P_z) \; ; \; x < -b \end{cases} \tag{3.7}$$

where the effective mass in equation (3.2) is understood to depend on the energy eigenvalues $\{E_R^r\}$ of H_R, and the conduction band-edge energy at $x = -b$ takes the limiting value of $E_c(x)$ in the barrier region as $x \to -b_+$. In this definition, H_R is separable and thus has eigenfunctions of the form

$$\Psi_R^r(x,y,z) = (L_y L_z)^{-\frac{1}{2}} \psi_R^r(x) \, e^{ik_y^R y} \, e^{ik_z^R z} \tag{3.8}$$

where $\Psi_R^r(x)$ satisfies the one-dimensional Schrödinger equation (3.4) in which $E_{EFF}(x, k_y^R, E_R^r) = E_{EFF}(-b_+, k_y^R, E_R^r) \; ; \; x \leq -b$.

Following Bardeen (1961), the sub-Hamiltonians H_L and H_R are defined so that the effective 1-D potential energy $E_{EFF}(x, k_y, E)$ is constant in the RH and LH contact regions respectively. However, since the transfer-Hamiltonian formalism is only applicable to systems which contain a high and wide barrier (see Section 3.4), the x-components of the eigenfunctions Ψ_L^ℓ and Ψ_R^r decay rapidly in the barrier and are, therefore, quite insensitive to the precise definition of the sub-Hamiltonians in the regions of assumed constant potential.

It follows from the definition (3.5) of H_L that $\{\psi_L^\ell\}$ are exact eigenfunctions of H_T for $x \leq 0$ but not for $x > 0$, that is

$$H_T \psi_L^\ell \begin{cases} = E_L^\ell \psi_L^\ell \; ; \; x \leq 0 \\ \neq E_L^\ell \psi_L^\ell \; ; \; x > 0 \end{cases} \quad . \tag{3.9}$$

Similarly,

$$H_T \psi_R^r \begin{cases} = E_R^r \psi_R^r \; ; \; x \geq -b \\ \neq E_R^r \psi_R^r \; ; \; x < -b \end{cases} \quad . \tag{3.10}$$

These results are used in the next section which shows how electron tunnelling can be described in terms of transitions between eigenstates of the left- and right-hand subsystems.

3.4 Calculation of the Rate of 'Tunnelling' Transitions between Eigenstates of the Left- and Right-hand Sub-Hamiltonians

Provided that the potential energy barrier is high and wide, the x-components of the left- and right-hand eigenfunctions ψ_L^ℓ and ψ_R^r, decay rapidly in the barrier region so that

$$\int_V \Psi_L^{\ell *} \Psi_R^r \, dV \ll 1 \quad , \tag{3.11}$$

where the integral is evaluated over the entire heterostructure. Since the left- and right-hand eigenfunctions are approximately orthogonal, they may be used as a basis set from which time-dependent wavefunctions of the whole system may be constructed as follows:

$$\Psi_T(x,y,z,t) = \sum_n a_n(t) \, \Psi_L^n(x,y,z) \, e^{-iE_L^n t/\hbar}$$

$$+ \sum_j c_j(t) \, \Psi_R^j(x,y,z) \, e^{-iE_R^j t/\hbar} \quad , \tag{3.12}$$

where the summations are over all left- and right-hand eigenstates. Neglecting overlap integrals between left- and right-hand eigenfunctions, normalisation of Ψ_T requires

$$\sum_n |a_n(t)|^2 + \sum_j |c_j(t)|^2 = 1 \quad . \tag{3.13}$$

Suppose that at $t = 0$, $c_j(0) = 0$ for all j and $a_n(0) = \delta_{n\ell}$ where

$$\delta_{n\ell} = \begin{cases} 1 \; ; \; n = \ell \\ 0 \; ; \; n \neq \ell \end{cases} .$$

At $t = 0$, $\Psi_T(x,y,z,0) = \Psi_L^{\ell}(x,y,z)$ so that the electron initially appears to occupy the eigenstate Ψ_L^{ℓ} of the LH subsystem. Since Ψ_L^{ℓ} is not an eigenstate of the whole system, Ψ_T evolves with time according to the time-dependent Schrödinger equation

$$i\hbar \frac{\partial \Psi_T}{\partial t} = H_T \Psi_T \quad . \tag{3.14}$$

Substituting equation (3.12) into this equation gives

$$i\hbar \sum_n \dot{a}_n(t) \Psi_L^n e^{-iE_L^n t/\hbar} + \sum_n E_L^n a_n(t) \Psi_L^n e^{-iE_L^n t/\hbar}$$

$$+ i\hbar \sum_j \dot{c}_j(t) \Psi_R^j e^{-iE_R^j t/\hbar} + \sum_j E_R^j c_j(t) \Psi_R^j e^{-iE_R^j t/\hbar}$$

$$= \sum_n a_n(t) H_T \Psi_L^n e^{-iE_L^n t/\hbar} + \sum_j c_j(t) H_T \Psi_R^j e^{-iE_R^j t/\hbar} \quad . \tag{3.15}$$

The expansion coefficients change with time thereby mixing additional LH and RH eigenstates into the wavefunction $\Psi_T(x,y,z,t)$, and inducing transitions from the initial state Ψ_L^{ℓ}. If the subsystem eigenfunctions Ψ_L^n and Ψ_R^j were exact eigenfunctions of H_T, the expansion coefficients would remain constant in time, for any choice

of initial state and no transitions would occur. Similar time-dependent coefficients are found in conventional time-dependent perturbation theory where, in contrast to the tunnelling problem, transitions occur between exact, orthogonal eigenfunctions of an approximate (unperturbed) Hamiltonian.

In the limit of an infinite potential energy barrier, exact eigenfunctions of the whole system can be constructed from the left- and right-hand eigenfunctions. The transfer-Hamiltonian tunnelling formalism is therefore perturbative in the sense that when the barrier is relaxed to a physically realistic height, the change in the LH and RH eigenfunctions must be small, so that the approximate orthogonality requirement (3.11) is satisfied.

Transitions from the initial state Ψ_L^ℓ into eigenstates of the RH subsystem describe electron tunnelling since the mean x-coordinate of the electron moves from an initial value to the left of the barrier to a new position on the RHS of the barrier, characteristic of the RH eigenstate Ψ_R^r.

The probability $P_{\ell r}(t)$ that at time t the electron has made a transition from Ψ_L^ℓ into the r^{th} RH eigenstate Ψ_R^r is

$$P_{\ell r}(t) = \int_V \Psi_R^{r*}(x,y,z)\ \Psi_T(x,y,z,t)\ dV \qquad (3.16)$$

which, neglecting overlap integrals between the LH and RH eigenstates becomes

$$P_{\ell r}(t) = |c_r(t)|^2 \tag{3.17}$$

To calculate $c_r(t)$, the inner product of Ψ_R^r and equation (3.15) is taken. Since the eigenstates of each subsystem are orthogonal, this gives

$$i\hbar \sum_n \dot{a}_n(t) \left(\int_V \Psi_R^{r*} \Psi_L^n \, dV\right) e^{-iE_L^n t/\hbar} + \sum_n E_L^n a_n(t) \left(\int_V \Psi_R^{r*} \Psi_L^n \, dV\right) e^{-iE_L^n t/\hbar}$$

$$+ i\hbar \dot{c}_r(t) e^{-iE_R^r t/\hbar} + E_R^r c_r(t) e^{-iE_R^r t/\hbar}$$

$$= \sum_n a_n(t) \left(\int_V \Psi_R^{r*} H_T \Psi_L^n \, dV\right) e^{-iE_L^n t/\hbar} + \sum_j c_j(t) \left(\int_V \Psi_R^{r*} H_T \Psi_R^j \, dV\right) e^{-iE_R^j t/\hbar} .$$

(3.18)

This expression can be simplified by estimating the magnitudes of the expansion coefficients and their derivatives. Differentiating equation (3.13) with respect to t gives

$$\sum_n a_n(t) \dot{a}_n^*(t) + a_n^*(t) \dot{a}_n(t) + \sum_j c_j(t) \dot{c}_j^*(t) + c_j^*(t) \dot{c}_j(t) = 0$$

(3.19)

whence, from the initial conditions

$$a_n(0) = \delta_{n\ell}$$

and

$$c_j(0) = 0 \ ,$$

$\dot{a}_\ell(0) = 0$. The evolution of Ψ_T is therefore slow so that at time t the expansion coefficients may be approximated by

$$\left.\begin{aligned} a_n(t) &= \delta_{n\ell} \\ \dot{a}_n(t) &= 0 \end{aligned}\right\} \text{ for all } n \qquad (3.20)$$

Equation (3.18) can be further simplified by writing

$$\int_V \Psi_R^{r*} H_T \Psi_R^j \, dV = \int_{V_L} \Psi_R^{r*} H_T \Psi_R^j \, dV + \int_{V_R} \Psi_R^{r*} H_T \Psi_R^j \, dV, \quad (3.21)$$

where the regions V_L and V_R include all space to the LHS and RHS respectively of the plane $x = s$ where $-b \leq s \leq 0$. From equation (3.7), $H_T = H_R$ for all $x \geq -b$ so that $H_T = H_R$ everywhere in V_R. Similarly from equation (3.5), $H_T = H_L$ everywhere in V_L.

The integral over V_L in equation (3.21) is negligible since the x-component of each eigenfunction ψ_R^r decays rapidly in the barrier region. Equation (3.21) may therefore be written to good approximation

$$\int_V \psi_R^{r*} H_T \psi_R^j \, dV \cong \int_{V_R} \psi_R^{r*} H_R \psi_R^j \, dV = E_R^j \delta_{rj} \tag{3.22}$$

Substituting equations (3.20) and (3.22) into equation (3.18) gives

$$\begin{aligned} i\hbar \dot{c}_r(t) e^{-iE_R^r t/\hbar} + E_L^\ell \left(\int_V \psi_R^{r*} \psi_L^\ell \, dV\right) e^{-iE_L^\ell t/\hbar} + E_R^r c_r(t) e^{-iE_R^r t/\hbar} \\ = \left(\int_V \psi_R^{r*} H_T \psi_L^\ell \, dV\right) e^{-iE_L^\ell t/\hbar} + E_R^r c_r(t) e^{-iE_R^r t/\hbar} \end{aligned} \tag{3.23}$$

whence

$$i\hbar \dot{c}_r(t) = \left(\int_V \psi_R^{r*} (H_T - E_L^\ell) \psi_L^\ell \, dV\right) e^{-i(E_L^\ell - E_R^r)t/\hbar} . \tag{3.24}$$

In time-dependent perturbation theory, a formally identical equation leads to the Fermi golden rule for the transition rate between two orthogonal eigenstates ψ_L^ℓ and ψ_R^r of an unperturbed system when the perturbed Hamiltonian is H_T (see, for example, Merzbacher, 1970).

Integration of equation (3.24) gives a similar golden rule for the electronic transition rate $W_{\ell r}$ from the eigenstate Ψ_L^{ℓ} of the LH subsystem into the eigenstate Ψ_R^{r} of the RH subsystem.

This transition rate is

$$W_{\ell r} = \frac{2\pi}{\hbar} \left(\left| M_{\ell r} \right| \right)^2 \delta(E_L^{\ell} - E_R^{r}) \tag{3.25}$$

where

$$M_{\ell r} = \int_V \Psi_R^{r*} \, (H_T - E_L^{\ell}) \, \Psi_L^{\ell} \, dV \quad . \tag{3.26}$$

The delta function in equation (3.25) ensures that transitions only occur between states of the same energy.

3.5 An Expression for the Transition Matrix Element $M_{\ell r}$

In this section the matrix element $M_{\ell r}$ is expressed in the form of a one-dimensional probability flux which depends only on the x-dependent factors $\psi_L^{\ell}(x)$ and $\psi_R^{r}(x)$ of the LH and RH eigenfunctions, and their derivatives.

The integral in equation (3.26) can be evaluated over the regions V_L and V_R defined in the previous section, giving

$$M_{\ell r} = \int_{V_L} \Psi_R^{r*} \, (H_T - E_L^{\ell}) \, \Psi_L^{\ell} \, dV + \int_{V_R} \Psi_R^{r*} \, (H_T - E_L^{\ell}) \, \Psi_L^{\ell} \, dV \quad . \tag{3.27}$$

The integral over V_L vanishes since $H_T = H_L$ everywhere in this region and $H_L\Psi_L^{\ell} = E_L\Psi_L^{\ell}$.

Since in addition, $H_T = H_R$ everywhere in V_R, equation (3.27) becomes

$$M_{\ell r} = \int_{V_R} \Psi_R^{r*} \, (H_R - E_L^{\ell}) \, \Psi_L^{\ell} \, dV \quad , \tag{3.28}$$

which may be expressed in the more symmetrical form

$$M_{\ell r} = \int_{V_R} \left[\Psi_R^{r*} \, (H_R - E_L^{\ell}) \, \Psi_L^{\ell} - \Psi_L^{\ell} \, (H_R^{*} - E_R^{r}) \, \Psi_R^{r*}\right] dV \quad , \tag{3.29}$$

where the extra term in the integrand vanishes because $H_R^{*}\Psi_R^{r*} = (H_R\Psi_R^{r})^{*}$ $= (E_R\Psi_R^{r})^{*} = E_R\Psi_R^{r*}$.

In the original Bardeen formalism, which includes no magnetic fields, this additional term contains the sub-Hamiltonian H_R rather than its complex conjugate H_R^{*}. This is because when $\underline{B} = 0$, the effective-mass Hamiltonian is real, so $H_R^{*} = H_R$.

Using equations (3.6) and (3.8) for $\Psi_L^{\ell}(x,y,z)$ and $\Psi_R^{r}(x,y,z)$ in equation (3.29) and setting $E_L^{\ell} = E_R^{r}$ for energy conserving transitions gives

$$M_{\ell r} = \frac{1}{L_y L_z} \int_{z=0}^{L_z} \int_{y=0}^{L_y} \int_{x=s}^{\infty} \left[e^{-ik_y^R y} e^{-ik_z^R z} \psi_R^{r*}(x) (H_R - E_R^r) e^{ik_y^L y} e^{ik_z^L z} \psi_L^{\ell}(x) \right.$$

$$\left. - e^{ik_y^L y} e^{ik_z^L z} \psi_L^{\ell}(x) (H_R^* - E_R^r) e^{-ik_y^R y} e^{-ik_z^R z} \psi_R^{r*}(x) \right] dx\, dy\, dz$$

(3.30)

where the integral over V_R has been expressed as a triple integral over the x, y and z co-ordinates of this region. It follows from the definition (3.7) of H_R that for $x \geq -b$,

$$(H_R - E_R^r) e^{ik_y^L y} e^{ik_z^L z} \psi_L^{\ell}(x) =$$

$$e^{ik_y^L y} e^{ik_z^L z} \left(-\frac{\hbar^2}{2} \frac{d}{dx} \left(\frac{1}{m^*(x)} \frac{d}{dx} \right) + \frac{\hbar^2 k_z^{L2}}{2m^*(x)} + E_{EFF}(x, k_y^L, E_R^r) - E_R^r \right) \psi_L^{\ell}(x)$$

(3.31)

where $E_{EFF}(x, k_y^L, E_R^r)$ is the effective potential energy of the RH subsystem, given for $x \geq -b$ in equation (3.4).

Similarly,

$$(H_R^* - E_R^r)\, e^{-ik_y^R y}\, e^{-ik_z^R z}\, \psi_R^{r*}(x) =$$

$$e^{-ik_y^R y}\, e^{-ik_z^R z} \left(-\frac{\hbar^2}{2}\frac{d}{dx}\left(\frac{1}{m^*(x)}\frac{d}{dx}\right) + \frac{\hbar^2 k_z^{R2}}{2m^*(x)} + E_{EFF}\,(x, k_y^R, E_R^r) - E_R^r\right) \psi_R^{r*}(x)$$

(3.32)

Substituting equations (3.31) and (3.32) into equation (3.30) gives

$$M_{\ell r} = \int_{z=0}^{L_z} \frac{e^{i(k_z^L - k_z^R)z}}{L_z}\, dz \int_{y=0}^{L_y} \frac{e^{i(k_y^L - k_y^R)y}}{L_y}\, dy$$

$$\times \int_{x=s}^{\infty} \Big\{ -\frac{\hbar^2}{2}\left[\psi_R^{r*}(x)\frac{d}{dx}\left(\frac{1}{m^*(x)}\frac{d\psi_L^{\ell}(x)}{dx}\right) - \psi_L^{\ell}(x)\frac{d}{dx}\left(\frac{1}{m^*(x)}\frac{d\psi_R^{r*}(x)}{dx}\right)\right]$$

$$+ \psi_R^{r*}(x)\,\psi_L^{\ell}(x)\left[\frac{\hbar^2\,(k_z^{L2} - k_z^{R2})}{2m^*(x)} + E_{EFF}\,(x, k_y^L, E_R^r) - E_{EFF}(x, k_y^R, E_R^r)\right]\Big\}\, dx$$

(3.33)

Since all allowed wavevector components satisfy the periodic boundary conditions (1.11), the integrals over y and z vanish unless $k_y^L = k_y^R$

and $k_z^L = k_z^R$, in which case they equal unity. Transitions therefore only occur between states with identical transverse wavevector components so that the matrix element (3.33) becomes

$$M_{\ell r} = -\frac{\hbar^2}{2} I_{\ell r} \, \delta_{k_y^L, k_y^R} \, \delta_{k_z^L, k_z^R} \tag{3.34a}$$

where

$$I_{\ell r} = \int_{x=-\infty}^{\infty} \theta(x-s) \left[\psi_R^{r*}(x) \frac{d}{dx}\left(\frac{1}{m^*(x)} \frac{d\psi_L^{\ell}(x)}{dx}\right)\right.$$

$$\left. - \psi_L^{\ell}(x) \frac{d}{dx}\left(\frac{1}{m^*(x)} \frac{d\psi_R^{r*}(x)}{dx}\right)\right] dx \tag{3.34b}$$

in which $\theta(x - s)$ is the unit step function defined in equation (1.33).

Evaluating the integral in equation (3.34b) by parts and imposing the boundary conditions

$$\psi_L^{\ell}(x) \text{ and } \frac{d\psi_L^{\ell}(x)}{dx} \to 0 \text{ as } x \to +\infty \quad \text{and}$$

$$\psi_R^{r*}(x) \text{ and } \frac{d\psi_R^{r*}(x)}{dx} \to 0 \text{ as } x \to -\infty$$

gives

$$I_{\ell r} = - \int_{-\infty}^{\infty} \frac{1}{m^*(x)} \left(\psi_R^{r*}(x) \frac{d\psi_L^{\ell}(x)}{dx} - \psi_L^{\ell}(x) \frac{d\psi_R^{r*}(x)}{dx} \right) \delta(x-s)\, dx \qquad (3.35)$$

from which it follows that

$$I_{\ell r} = - \frac{1}{m^*(s)} \left(\psi_R^{r*}(x) \frac{d\psi_L^{\ell}(x)}{dx} - \psi_L^{\ell}(x) \frac{d\psi_R^{r*}(x)}{dx} \right)_{x=s} \qquad (3.36)$$

The plane separating the regions V_L and V_R was chosen to lie within the barrier, rather than at an interface, to avoid the problem of which effective mass should be chosen at the interface. From equation (3.2), $m^*(s) = m_B^*$ for all s within the barrier region. Throughout this thesis equation (3.36) is evaluated in the limit $x \to 0_-$, that is close to the RH barrier interface.

Combining equations (3.34) and (3.36) gives, finally

$$M_{\ell r} = i\hbar\, J_{\ell r}\, \delta\, k_y^L, k_y^R\, \delta\, k_z^L, k_z^R \qquad (3.37)$$

where

$$J_{\ell r} = \frac{-i\hbar}{2m_B^*} \left[\frac{d\psi_L^{\ell}(x)}{dx} \psi_R^{r*}(x) - \psi_L^{\ell}(x) \frac{d\psi_R^{r*}(x)}{dx} \right]_{x=0_-}$$

has the same form as the probability flux carried by a single wavefunction (see, for example, Merzbacher, 1970).

For any single-barrier tunnelling problem, once the LH and RH eigenvalues, and the x-dependent factors of the associated eigenfunctions are known, allowed tunnelling transitions can be identified, and the transition rates calculated using equations (3.25) and (3.37).

3.6 Calculation of the Transmission Coefficient of a Rectangular Potential Energy Barrier

In this section, the transmission coefficient of a rectangular potential energy barrier is calculated using the transfer-Hamiltonian formalism, and shown to be identical to the more usual time-independent expression (1.53).

In the absence of magnetic fields, the effective potential energy variation in a single-barrier heterostructure, is described by the spatial dependence of the conduction band edge, $E_c(x)$. If no space-charge regions are present, the high band-gap material forms a rectangular potential energy barrier as shown in Figure 3.1.

The envelope eigenfunctions of the LH and RH subsystems are of the form given in equations (3.6) and (3.8) where $\psi^{\ell}_{L}(x)$ satisfies

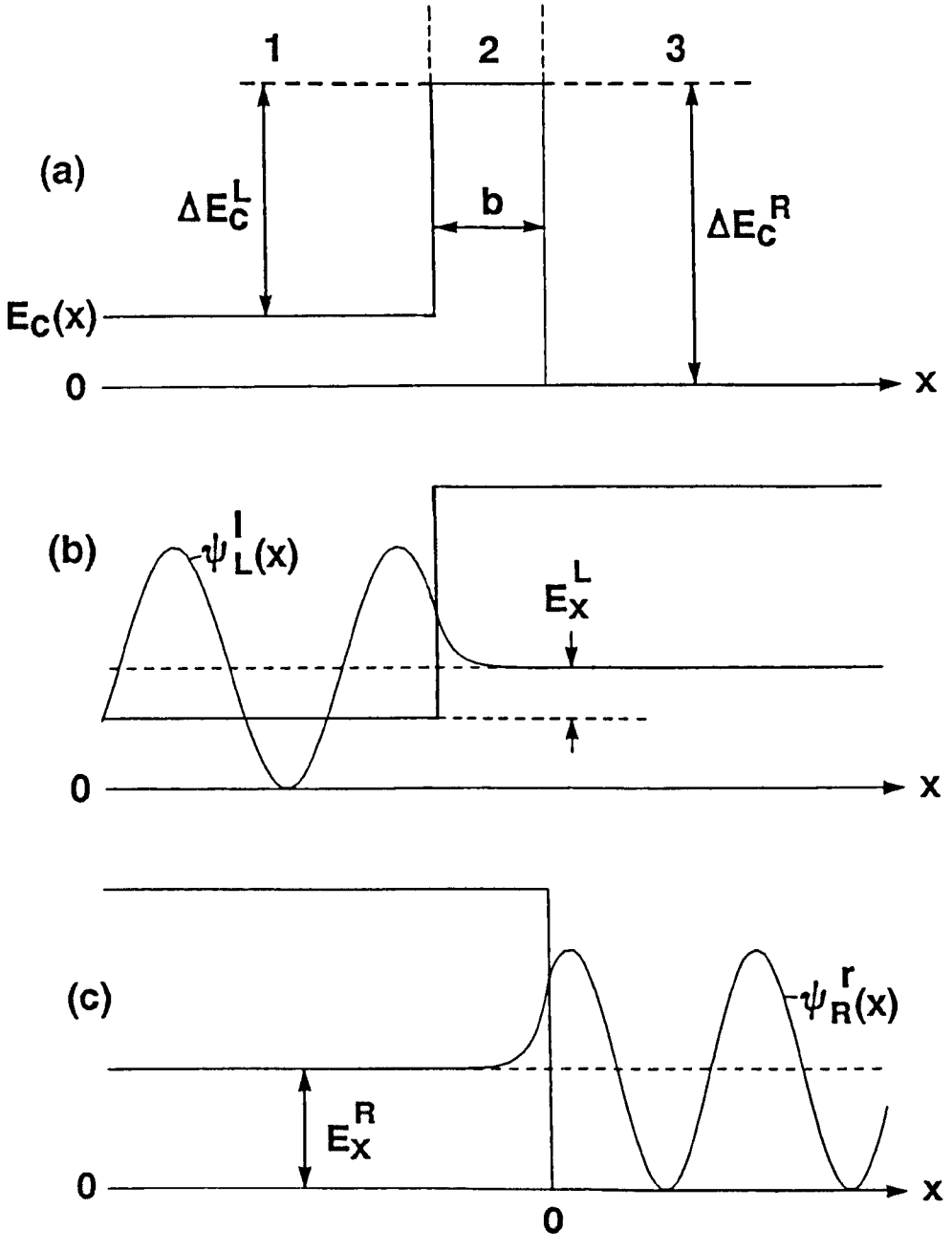

Figure 3.1 (a) The conduction band profile $E_c(x)$ of an idealised single-barrier heterostructure, together with the effective potential energy variation of (b) the left-hand subsystem and (c) the right-hand subsystem. Schematic left- and right- hand eigenfunctions $\psi_L^{\ell}(x)$ and $\psi_R^{r}(x)$ are also shown.

$$\left[-\frac{\hbar^2}{2}\frac{d}{dx}\left(\frac{1}{m^*(x)}\right)\frac{d}{dx}+E_c^L(x)\right]\psi_L^{\ell}(x)=\left[E_L^{\ell}-\frac{\hbar^2k_y^{L2}}{2m^*(x)}-\frac{\hbar^2k_z^{L2}}{2m^*(x)}\right]\psi_L^{\ell}(x) \tag{3.38}$$

where $E_c^L(x)=\begin{cases}\Delta E_c^R-\Delta E_c^L & ;\ x<-b\\ \Delta E_c^R & ;\ x\geq -b\end{cases}$,

and $m^*(x)=\begin{cases}m_L^* & ;\ x<-b\\ m_B^* & ;\ x\geq -b\end{cases}$.

Similarly, $\psi_R^r(x)$ satisfies

$$\left[-\frac{\hbar^2}{2}\frac{d}{dx}\left(\frac{1}{m^*(x)}\right)\frac{d}{dx}+E_c^R(x)\right]\psi_R^r(x)=\left[E_R^r-\frac{\hbar^2k_y^{R2}}{2m^*(x)}-\frac{\hbar^2k_z^{R2}}{2m^*(x)}\right]\psi_R^r(x) \tag{3.39}$$

$$\Delta E_c^R \quad ; \; x \leq 0$$

where $E_c^R(x) = \{$

$$0 \quad ; \; x > 0 \quad ,$$

and,

$$m_B^* \quad ; \; x \leq 0$$

$$m^*(x) = \{$$

$$m_R^* \quad ; \; x > 0 \quad .$$

The step-like potential energy profiles of the LH and RH subsystems are shown in Figure 3.1.

Solving equations (3.38) and (3.39) piecewise in each region and imposing the matching conditions (1.39) and (1.40) gives

$$\psi_L^{\ell}(x) = \begin{cases} A\, e^{ik_x^L(x+b)} + A\, \dfrac{[ik_x^L + \mu^L(m_L^*/m_B^*)]}{[ik_x^L - \mu^L(m_L^*/m_B^*)]}\, e^{-ik_x^L(x+b)} & ; \; x < -b \\ \dfrac{A\, 2ik_x^L}{[ik_x^L - \mu^L(m_L^*/m_B^*)]}\, e^{-\mu^L(x+b)} & ; \; x \geq -b \end{cases} \tag{3.40}$$

and,

$$\frac{B[ik_x^R + \mu^R(m_R^*/m_B^*)]}{[ik_x^R - \mu^R(m^*{}_R/m_B^*)]} e^{+ik_x^R x} + B\, e^{-ik_x^R x} \qquad ; x > 0$$

$$\psi_R^r(x) = \{ \tag{3.41}$$

$$\frac{B\ 2ik_x^R\ e^{\mu^R x}}{[ik_x^R - \mu^R(m_R^*/m_B^*)]}, \qquad ; x \leq 0$$

where the longitudinal wavevector components are related to the total energies E_L^ℓ and E_R^r by

$$k_x^L = [2m_L^* (E_L^\ell - \Delta E_c^R + \Delta E_c^L - \hbar^2(k_y^{L2} + k_z^{L2})/2m_L^*)]^{\frac{1}{2}}/\hbar$$

$$k_x^R = [2m_R^* (E_R^r - \hbar^2(k_y^{R2} + k_z^{R2})/2m_R^*)]^{\frac{1}{2}}/\hbar ,$$

the decay constants of the LH and RH eigenfunctions are

$$\mu^L = [2m_B^* (\Delta E_c^R - E_L^\ell + \hbar^2(k_y^{L2} + k_z^{L2})/2m_B^*]^{\frac{1}{2}}/\hbar$$

$$\mu^R = [2m_B^* (\Delta E_c^R - E_R^r + \hbar^2(k_y^{R2} + k_z^{R2})/2m_B^*]^{\frac{1}{2}}/\hbar ,$$

and A and B are normalisation constants.

The quantum numbers ℓ and r refer to the wavevector components (k_x^L, k_y^L, k_z^L) and (k_x^R, k_y^R, k_z^R) which specify individual LH and RH eigenstates.

Evaluating the wavefunctions (3.40) and (3.41) and their derivatives in the limit $x \to 0_-$, and using these results in equations (3.25) and (3.37), the transition rate $W_{\ell r}$ from the initial state Ψ_L^ℓ to the final state Ψ_R^r, is found to be

$$W_{\ell r} = \frac{8\pi \hbar^3 |A|^2 |B|^2 k_x^{L2} k_x^{R2} (\mu^L + \mu^R)^2 e^{-2\mu b} \delta k_y^L, k_y^R \delta k_z^L, k_z^R \delta(E_L^\ell - E_R^r)}{m_R^{*2} [k_x^{L2} + \mu^{L2}(m_L^*/m_B^*)^2][\mu^{R2} + (m_B^*/m_R^*)^2 k_x^{R2}]} \quad . \tag{3.42}$$

The total transition rate W_ℓ into all RH eigenstates which satisfy the transverse wavevector conservation requirement is found by integrating equation (3.42) over k_x^R, using the periodic boundary conditions (1.11) to determine the density of states. This transition rate is

$$W = \frac{4L_x |A|^2 |B|^2 \hbar^3}{m_R^{*2}} \int_{k_x^R=0}^{\infty} \frac{k_x^{L2} k_x^{R2} (\mu^L + \mu^R)^2 e^{-2\mu^L b} \delta(\Delta E) dk_x^R}{[k_x^{L2} + \mu^{L2} (m_L^*/m_B^*)^2][\mu^{R2} + (m_B^*/m_R^*)^2 k_x^{R2}]} \tag{3.43}$$

where L_x is the length of the RH (collector) contact and

$$\Delta E = E_R^r - E_L^\ell = \frac{\hbar^2}{2}\left(\frac{k_x^{R2}}{m_R^*} - \frac{k_x^{L2}}{m_L^*}\right) + \frac{\hbar^2}{2}\left(\frac{1}{m_R^*} - \frac{1}{m_L^*}\right)(k_y^{L2} + k_z^{L2}) + \Delta E_c^L - \Delta E_c^R \tag{3.44}$$

Using this relation to change the variable of integration in equation (3.43) from k_x^R to ΔE gives

$$W_\ell = \frac{4L_x|A|^2|B|^2\hbar}{m_R^*}\int_{\Delta E}\frac{k_x^{L2}\,k_x^R\,(\mu^L + \mu^R)^2\,e^{-2\mu^L b}\,\delta(\Delta E)\,d(\Delta E)}{\left[k_x^{L2} + \mu^{L2}(m_L^*/m_B^*)^2\right]\left[\mu^{R2} + (m_B^*/m_R^*)^2\,k_x^{R2}\right]} \tag{3.45}$$

whence

$$W_\ell = \frac{16\,L_x|A|^2|B|^2\hbar\,k_x^{L2}\,k_x^R\,\mu^{L2}\,e^{-2\mu^L b}}{m_R^*\left[k_x^{L2} + \mu^{L2}\,(m_L^*/m_B^*)^2\right]\left[\mu^{R2} + (m_B^*/m_R^*)^2\,k_x^{R2}\right]}\,, \tag{3.46}$$

where k_x^R satisfies $\Delta E(k_x^R) = 0$, to ensure energy conservation.

The position-dependent effective mass $m^*(x)$ couples the longitudinal and transverse components of motion so that the allowed value of k_x^R is a function of k_y^L and k_z^L and the transition rate W_ℓ depends on the kinetic energy associated with transverse motion. If

the effective mass is taken to be constant throughout the device, the longitudinal and transverse components of motion are decoupled, and the transition rate (3.46)then depends only on the incident kinetic energy of the electrons.

The transition rate W_ℓ gives the probability per unit time that an electron which initially occupies the state Ψ_L^ℓ is transmitted through the barrier. This transition rate may be expressed as the product of the barrier transmission coefficient, and the probability flux carried by the travelling wave component of Ψ_L^ℓ which propagates along the x-axis.

Using equations (1.41) and (3.40) to calculate the incident probability flux gives

$$W_\ell = \frac{|A|^2 \hbar k_x^L \, T_{TH}}{m_L^*} \quad , \tag{3.47}$$

where T_{TH} is the transfer-Hamiltonian expression for the barrier transmission coefficient.

Comparing equations (3.46) and (3.47) and setting the RH normalisation constant $B \cong L_x^{-\frac{1}{2}}$ for a high and wide barrier gives

$$T_{TH} = \frac{16(m_L^*/m_R^*)\, k_x^L\, k_x^R\, \mu^{L2}\, e^{-2\mu^L b}}{[k_x^{L2} + \mu^{L2}(m_L^*/m_B^*)^2][\mu^{R2} + (m_B^*/m_R^*)^2 k_x^{R2}]} \quad , \tag{3.48}$$

which is identical to the time-independent transmission coefficient (1.53) when band bending and nonparabolicity are neglected so that $m^*(0_+) = m_R^*$, $\mu(x) = \mu(-b_+) = \mu(0_-) = \mu^L$, $k(-b_-) = k_x^L$ and $\alpha(0_+) = k_x^R$. Duke (1969) demonstrated the equivalence of the time-independent and transfer-Hamiltonian transmission coefficients when $m_L^* = m_B^* = m_R^*$, but the more general case of unequal masses was not considered.

In any real system, space-charge regions give rise to electrostatic potential variations so that the effective potential energy barrier is not rectangular. However, provided these potentials are slowly varying, the transfer-Hamiltonian transmission coefficient T_{TH} can still be calculated from the WKB eigenfunctions of the LH and RH subsystems. Within the WKB approximation, T_{TH} is again found to be identical to the time-independent expression (1.53).

3.7 Application of the Transfer-Hamiltonian Formalism to Tunnelling Between Bound Eigenstates

In the previous section, the transfer-Hamiltonian transmission coefficient of a rectangular potential barrier was shown to be identical to the more familiar time-independent expression, derived from the current-carrying eigenstates of the system.

Time-dependent models of tunnelling were, however, primarily developed to calculate the transition rates between quasi-bound left- and right-hand eigenstates, such as the 2DEG states discussed in Chapter 2. Such states carry no current in the direction of confinement and cannot therefore be treated using a time-independent formalism. In this section, the transfer-Hamiltonian formalism is used to calculate the tunnelling transition rate between bound states of two weakly-coupled rectangular potential energy wells.

Figure 3.2 shows the conduction band profile of a heterostructure in which two different low band-gap materials act as potential energy wells to motion perpendicular to the interfaces. The potential energy profiles $E_c^L(x)$ and $E_c^R(x)$ of the LH and RH subsystems each contain one potential well as shown in Figures 3.2b and 3.2c. Both wells are assumed to be sufficiently deep and wide to support at least one bound eigenstate, for which the energy associated with motion normal to the interfaces is quantised. Solving equation (3.4) for $E_{EFF}(x) = E_c^L(x)$ or $E_c^R(x)$, the x-components $\psi_L^\ell(x)$ and $\psi_R^r(x)$ of the ℓ^{th} LH and r^{th} RH bound eigenstates with transverse wavevectors $\underline{k}_\parallel^L = (k_y^L, k_z^L)$ and $\underline{k}_\parallel^R = k(k_y^R, k_z^R)$ are of the

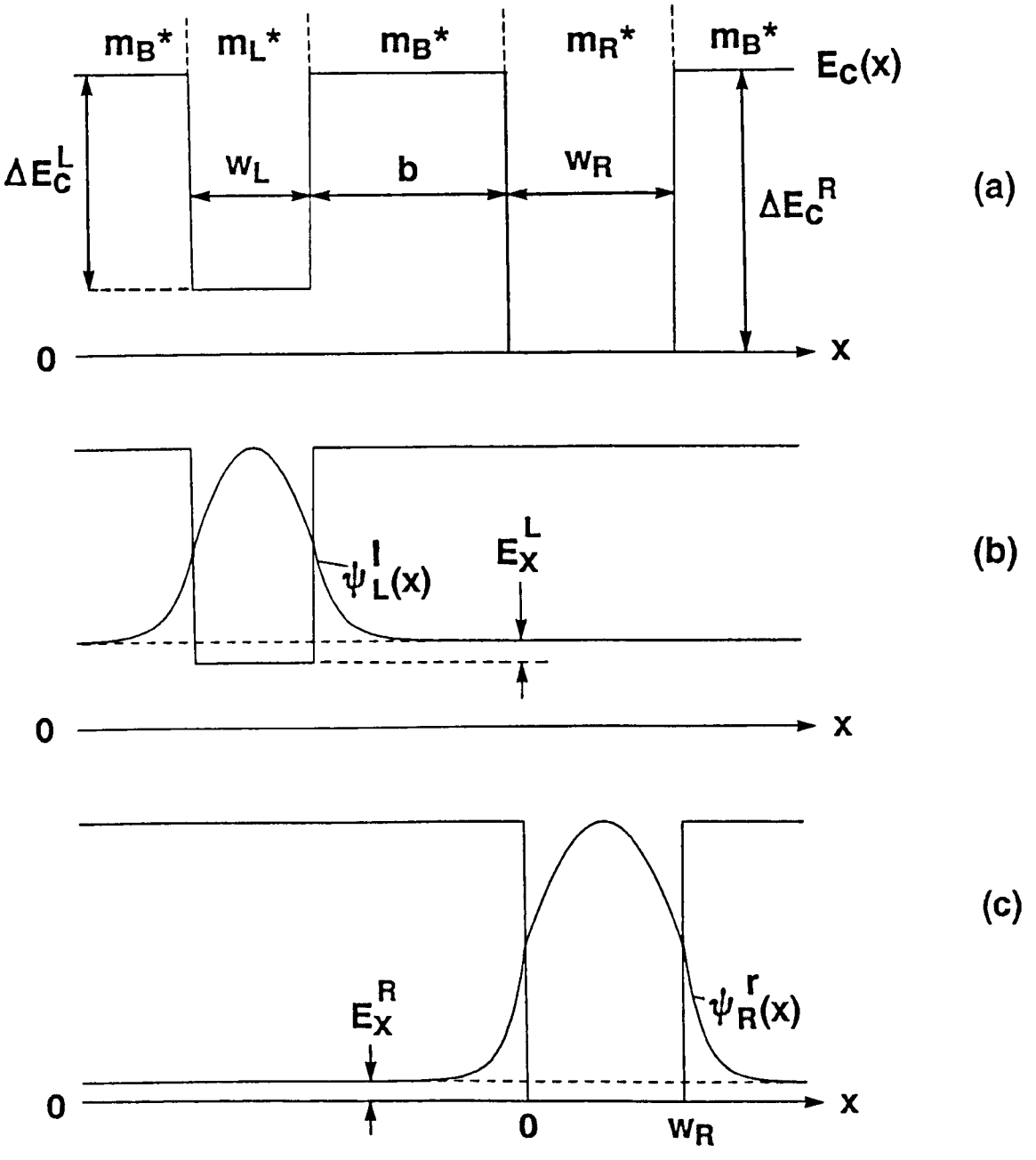

Figure 3.2 (a) The conduction band profile of a double-well heterostructure containing two different low band-gap materials. The effective potential energy variation of (b) the left-hand subsystem and (c) the right-hand subsystem are also shown, together with schematic left- and right-hand ground-state wavefunctions.

form

$$\psi(x) = \begin{cases} \dfrac{A\,k\,e^{\gamma(x - a_1)}}{\left[(m^*\gamma/m_B^*)^2 + k^2\right]^{\frac{1}{2}}} & ; x \leq a_1 \\ A \sin\left[k(x - a_1) + \delta\right] & ; a_1 < x < a_2 \\ \dfrac{A\,k\,(-1)^{\ell+1}\,e^{-\gamma(x - a_2)}}{\left[(m^*\gamma/m_B^*)^2 + k^2\right]^{\frac{1}{2}}} & ; x \geq a_2 \end{cases} , \qquad (3.49)$$

where for the LH subsystem,

$$m^* = m_L^*, \; a_1 = -(b + w_L), \; a_2 = -b \quad ,$$

$$\gamma = \gamma_L^{\ell} = \left[2m_B^* \left(\Delta E_c^R + \frac{\hbar^2 (k_y^{L2} + k_z^{L2})}{2m_B^*} - E_L^{\ell}\right)\right]^{\frac{1}{2}}/\hbar \quad ,$$

$$A = A_L^{\ell} = \left[\frac{k_{xL}^{\ell 2} + \gamma_L^{\ell 2}\,(m_L^*/m_B^*)}{\gamma_L^{\ell}\left[(m_L^*\gamma_L^{\ell}/m_B^*)^2 + k_{xL}^{\ell 2}\right]} + \frac{w_L}{2}\right]^{-\frac{1}{2}} \quad ,$$

$$\delta = \delta_L^{\ell} = \arctan\left(\frac{m_B^*\,k_{xL}^{\ell}}{m_L^*\,\gamma_L^{\ell}}\right) \qquad ; 0 \leq \delta_L^{\ell} \leq \pi/2 \quad ,$$

$k = k_{xL}^{\ell}$ is related to the total energy by

$$E_L^{\ell} = \Delta E_c^R - \Delta E_c^L + \frac{\hbar^2}{2m_L^*}\left(k_{xL}^{\ell 2} + k_y^{L2} + k_z^{L2}\right) ,$$

and satisfies the energy quantisation condition

$$k_{xL}^{\ell}\, w_L = \ell\pi - 2\delta_L^{\ell} \quad .$$

These expressions are easily adapted to the RH subsystem by substituting $\ell \to r$, $\underline{k}_{\|}^L \to \underline{k}_{\|}^R$ and making appropriate changes to the material parameters and interface positions.

Evaluating $\psi_L^{\ell}(x)$ and $\psi_R^r(x)$ and their derivatives in the limit $x \to 0_-$, and using these expressions in equations (3.25) and (3.37), the transition rate $W_{\ell r}$ from the ℓ^{th} bound state of the LH subsystem to the r^{th} bound state of the RH subsystem is found to be

$$W_{\ell r} = \frac{\pi\hbar^3\, k_{xL}^{\ell}\, k_{xR}^{r}}{8\, m_L^*\, m_R^* \left[\dfrac{k_{xL}^{\ell 2} + \gamma_L^{\ell 2}\,(m_L^*/m_B^*)}{\gamma_L^{\ell}\left[(m_L^*\gamma_L^{\ell}/m_B^*)^2 + k_{xL}^{\ell 2}\right]} + \dfrac{w_L}{2}\right]\left[\dfrac{k_{xR}^{r2} + \gamma_R^{r2}\,(m_R^*/m_B^*)}{\left[(m_R^*\gamma_R^{r}/m_B^*)^2 + k_{xR}^{r2}\right]} + \dfrac{w_R}{2}\right]}$$

$$\times \frac{4(\gamma_L^{\ell} + \gamma_R^{r})^2\, k_{xL}^{\ell}\, k_{xR}^{r}\,(m_L^*/m_R^*)\, e^{-2\gamma_L^{\ell} b}\, \delta(E_R^r - E_L^{\ell})\, \delta k_y^L,\, k_y^R\, \delta k_z^L,\, k_z^R}{\left[k_{xL}^{\ell 2} + (m_L^*/m_B^*)^2\, \gamma_L^{\ell 2}\right]\left[\gamma_R^{r2} + (m_B^*/m_R^*)^2\, k_{xR}^{r2}\right]}$$

(3.50)

where the delta function ensures that transitions only occur between eigenstates with the same total energy.

The transverse wavevector components must also be conserved so that $\gamma_L^{\ell} = \gamma_R^{r}$ and equation (3.50) becomes

$$W_{\ell r} = 2\pi\hbar \left[\frac{\hbar k_{xL}^{\ell}}{2m_L^* (w_L + 2L_{EFF}^{\ell})}\right]\left[\frac{\hbar k_{xR}^{r}}{2m_R^* (w_R + 2L_{EFF}^{r})}\right]$$

$$\times \frac{16\, \gamma_L^{\ell 2}\, k_{xL}^{\ell}\, k_{xR}^{r}\, (m_L^*/m_R^*)\, e^{-2\gamma_L^{\ell} b}\, \delta(E_R^r - E_L^{\ell})}{\left[k_{xL}^{\ell 2} + (m_L^* \gamma_L^{\ell}/m_B^*)^2\right]\left[\gamma_L^{\ell 2} + (m_B^* k_{xR}^{r}/m_R^*)^2\right]} \quad , \qquad (3.51)$$

where

$$L_{EFF}^{\ell} = \frac{k_{xL}^{\ell 2} + \gamma_L^{\ell 2}\, (m_L^*/m_B^*)}{\gamma_L^{\ell}\left[(m_L^* \gamma_L^{\ell}/m_B^*)^2 + k_{xL}^{\ell 2}\right]} \quad ,$$

and $$L_{EFF}^{r} = \frac{k_{xR}^{r2} + \gamma_L^{\ell 2}\, (m_R^*/m_B^*)}{\gamma_L^{\ell}\left[(m_R^* \gamma_L^{\ell}/m_B^*)^2 + k_{xR}^{r2}\right]} \quad .$$

The first bracketed term in equation (3.51) is the frequency of collisions which an electron, with longitudinal kinetic energy $\hbar^2 k_{xL}^{\ell 2}/2m_L^*$ makes classically with each wall of a confining potential

well of width $w_L + 2L^{\ell}_{EFF}$. The end correction $2L^{\ell}_{EFF}$ to the LH well width originates from quantum-mechanical penetration of the electron wavefunction into the classically forbidden regions at each side of the well.

If $m_B^* = m_L^*$, $L^{\ell}_{EFF} = 1/\gamma$, simply gives the penetration length over which the amplitude of the wavefunction falls to 1/e of its value at the barrier interface. In the limit of impenetrable barriers, $\gamma^{\ell}_L \to \infty$ and the end correction vanishes.

The second bracketed term in equation (3.51) is the frequency of the collisions which an electron moving with constant longitudinal speed $\hbar k^r_{xR}/m_R^*$ makes classically with each wall of a potential well of width $w_R + 2L^r_{EFF}$.

The final term in equation (3.51) is the transmission coefficient (1.53) of the central potential barrier if, in the absence of capping layers, free electrons incident from the left with kinetic energy equal to the mean longitudinal kinetic energy

$$\frac{\hbar^2 k^{\ell 2}_{xL}}{2m_L^*}$$

of the ℓ^{th} LH bound state, are partially transmitted into travelling wave states on the RHS of the barrier with longitudinal kinetic energy

$$\frac{\hbar^2 k_{xR}^{r2}}{2m_R^*}$$

equal to that of the r^{th} RH bound state.

3.8 Summary

The time-dependent tunnelling formalism developed in this chapter is applicable to tunnelling problems in single-barrier heterostructures provided that the effective-mass Hamiltonian is invariant under translation parallel to the barrier interfaces. In particular, the formalism may be used to describe electron tunnelling when a magnetic field is applied in the plane of the barrier, perpendicular to the tunnel current. In this geometry, the requirement that both the total energy and the transverse wavevector components be conserved in tunnelling transitions is of central importance to understanding the magnetotunnelling data presented in Chapters 5 and 6. The semiclassical analysis of the transition rate between bound eigenstates of two square wells provides guidance in the interpretation of more complicated expressions encountered in these magnetotunnelling problems.

CHAPTER FOUR

CALCULATION OF THE LEFT- AND RIGHT-HAND EIGENSTATES OF AN ASYMMETRICALLY-DOPED SINGLE-BARRIER HETEROSTRUCTURE UNDER FORWARD-BIAS CONDITIONS AND IN THE PRESENCE OF A TRANSVERSE MAGNETIC FIELD

4.1 Introduction

This thesis aims to study the effect of a transverse magnetic field on tunnelling transitions from the 2DEG states formed under forward bias in the accumulation layers of single- and double-barrier heterostructures. In order to describe these tunnelling processes within the transfer-Hamiltonian formalism, the energy eigenvalues and associated envelope eigenfunctions of the LH and RH subsystems must be found as functions of the transverse wavevector components k_y and k_z. Using these eigenvalues, the allowed energy- and transverse wavevector-conserving transitions can be identified.

The transitions rates, which determine the tunnel current, can then be calculated using the x-dependent factors of the associated effective-mass eigenfunctions.

In this chapter, the left- and right-hand eigenstates of the single-barrier structures described in Chapter 2 are determined, and interpreted in terms of the corresponding classical trajectories.

4.2 The Effect of a Transverse Magnetic Field on the 2DEG States of the Left-hand Subsystem

4.2.1 Introduction

In zero magnetic field, the LH sub-Hamiltonian H_L^o is given by the bracketed term on LHS of equation (1.36), where the effective potential energy is the conduction band profile $E_c(x)$ of the accumulation layer and barrier region for $x < 0$ and, by definition, equals $E_c(0-)$ for $x \geq 0$.

For given forward bias V, $E_c(x)$ is calculated as described in Chapter 2 by assuming that the potential energy well in the accumulation layer supports only one bound state, described by the Fang-Howard wavefunction.

Consequently, the bound state eigenfunctions of H_L^o are of the form

$$\Psi_L^o(x,y,z) = \frac{\psi_{FH}(x)}{(L_y L_z)^{\frac{1}{2}}} \, e^{ik_y y} \, e^{ik_z z} \quad , \tag{4.1}$$

and the associated eigenvalues are

$$E_L^o(k_y,k_z) = E'_{bo} + \frac{\hbar^2}{2m^*_L}(k_y^2 + k_z^2) \quad , \tag{4.2}$$

where E'_{bo} is the bound state energy (2.19), measured from the conduction band edge of the n^+ contact.

In addition, H_L^o has extended state eigenfunctions of the form

$$\psi_e^o(x,y,z) = \frac{\psi_e^o(x)}{(L_y L_z)^{\frac{1}{2}}} \, e^{ik_y y} \, e^{ik_z z} \quad , \tag{4.3}$$

corresponding to the eigenvalues

$$E_e^o(k_y, k_z) = E_{ex}^o + \frac{\hbar^2(k_y^2 + k_z^2)}{2m^*_L} \quad , \tag{4.4}$$

where, for extended states,

$$E_{ex}^o > E_c(-\infty) = E'_{bo} + E_F + E_D \quad . \tag{4.5}$$

In the presence of a transverse magnetic field $\underline{B} \parallel \underline{z}$, the LH sub-Hamiltonian H_L is, from equations (3.2) and (3.5)

$$H_L = H_L^o + H' \tag{4.6}$$

where

$$H' = \begin{cases} \dfrac{-i\hbar Bex}{m^*_L} \dfrac{\partial}{\partial y} + \dfrac{B^2e^2x^2}{2m^*_L} & ; \; x < 0 \\ 0 & ; \; x \geq 0 \; . \end{cases} \tag{4.7}$$

Equation (4.7) assumes that the magnetic field does not raise the 2DEG energy levels sufficiently for nonparabolicity effects in the n^- contact to become important.

4.2.2 Perturbation calculation of the 2DEG energy levels

In the 2DEG, electronic motion is constrained in the x-direction by the high electric field at the LH barrier interface. Consequently, for small magnetic fields, H' acts in equation (4.6) as a perturbation to the zero-field Hamiltonian H_L^o. When using perturbation theory, care must be taken however, because some eigenstates of H_L^o are degenerate due to the transverse kinetic energy.

Nondegenerate perturbation theory is only applicable if the matrix elements of H' vanish between the 2DEG states and all other degenerate eigenfunctions of H_L^o. This ensures that the first-order correction to the wavefunctions and the second-order contribution to the perturbed energy levels remain finite.

From equations (4.1) and (4.7), the matrix element of H' between the unperturbed 2DEG states with transverse wavevectors $\underline{k}'_{\|} = (k_y', k_z')$ and $\underline{k}_{\|} = (k_y, k_z)$ is

$$M_{bb}\,(\underline{k}'_{\|}, \underline{k}_{\|}) = \frac{J}{L_y L_z} \int_{y=0}^{L_y} e^{i(k_y-k_y')y}\,dy \int_{z=0}^{L_z} e^{i(k_z-k_z')z}\,dz \qquad (4.8)$$

where $J = \int_{x=-\infty}^{\infty} \psi^*_{FH}(x) \left(\frac{\hbar B e x k_y}{m^*_L} + \frac{B^2 e^2 x^2}{2m^*_L}\right) \psi_{FH}(x)\, dx$ (4.9)

Since k_y and k_z satisfy the periodic boundary conditions (1.11), the integrals over y and z are only non-zero when $\underline{k}_{\|} = \underline{k}'_{\|}$. Consequently, the matrix elements of H' vanish between all distinct bound eigenstates, including those which are degenerate.

Degenerate 2DEG and extended eigenstates have different transverse energies and therefore also have distinct transverse wavevector components. The matrix elements of H' therefore always vanish between such degenerate states.

Since the matrix elements of H' do vanish between the unperturbed 2DEG eigenfunctions and all other degenerate eigenfunctions of H^o_L, nondegenerate perturbation theory may be used to calculate the shift in the 2DEG energy levels caused by the magnetic field.

To first order, this energy shift is

$$\Delta E_L\,(k_y,k_z) = \int_V \Psi^{o*}_L\, H'\, \Psi^o_L\, dV \quad , \tag{4.10}$$

where the explicit position-dependence of the wavefunctions is omitted for clarity.

Substituting equations (4.1) and (4.7) into equation (4.10) gives

$$\Delta E_L(k_y,k_z) = \frac{\hbar k_y eB}{m^*_L}\langle x\rangle + \frac{e^2B^2}{2m^*_L}\langle x^2\rangle \quad , \tag{4.11}$$

where $\langle x\rangle = \int_{-\infty}^{-b} x|\psi_{FH}|^2\,dx$

$$= \int_{-\infty}^{-b} \frac{x(b+x)^2}{2a_0^3}\, e^{\frac{(b+x)}{a_0}}\, dx = -(b+3a_0) \quad ,$$

and $\langle x^2\rangle = \int_{-\infty}^{-b} x^2|\psi_{FH}|^2\,dx$

$$= \int_{-\infty}^{-b} \frac{x^2(b+x)^2}{2a_0^3}\, e^{\frac{(b+x)}{a_0}}\, dx$$

$$= b^2 + 6a_0b + 12a_0^2 \quad .$$

Hence ΔE_L may be written

$$\Delta E_L(k_y, k_z) = \frac{3B^2e^2a_0^2}{2m^*_L} - \frac{\hbar^2k_yk_0}{m^*_L} + \frac{\hbar^2k_0^2}{2m^*_L} \quad , \tag{4.12}$$

where

$$\hbar k_0 = Be(b+3a_0) \quad . \tag{4.13}$$

is simply the change in the y-component of momentum of an electron which moves classically from $x = -(b + 3a_0)$ (the mean stand-off position of the 2DEG) to $x = 0$ under the action of the Lorentz force.

Combining equations (4.2) and (4.12), the perturbed energy of a 2DEG electron, with wavevector components k_y and k_z, in a transverse magnetic field is

$$E_L(k_y, k_z) = E'_{bo} + \frac{3B^2e^2a_0^2}{2m^*_L} + \frac{\hbar^2(k_y - k_o)^2}{2m^*_L} + \frac{\hbar^2k_z^2}{2m^*_L} \quad . \quad (4.14)$$

From equation (1.26), the expectation value of the y-component of velocity of an electron in the 2DEG is related to its total energy by

$$\langle v_y(k_y) \rangle = \frac{1}{\hbar} \frac{\partial E_L(k_y, k_z)}{\partial k_y} = \frac{\hbar(k_y - k_o)}{m^*_L} \quad , \quad (4.15)$$

and vanishes for $k_y = k_o$.

Consequently, electrons which occupy perturbed 2DEG states with wavevector components $k_y = k_o$ and $k_z = 0$ have no transverse kinetic energy so that the bound state energy E'^{p}_{bo} of the perturbed system is

$$E'^{p}_{bo} = E_L(k_o, 0) = E'_{bo} + \Delta E'_{bo} \quad (4.16)$$

where $\Delta E'_{bo} = 3B^2e^2a^2_o/2m^*_L$ is the diamagnetic shift of the bound state energy. At T = 0K, all energy levels are occupied from the bound state energy to the left-hand Fermi level so that the Fermi energy of the perturbed 2DEG system is $E_F - \Delta E'_{bo}$, where E_F is the zero-field Fermi energy (2.6).

The 2DEG energy density of states depends only on the periodic boundary conditions satisfied by k_y and k_z, and is therefore unchanged by the magnetic field, which thus only affects the 2DEG sheet electron concentration through the small diamagnetic shift of the bound state energy. Since in general $\Delta E'_{bo} << E_F$ (see Section 4.2.3), the magnetic field has little effect on either the amount or distribution of accumulated charge. Changes in the 2DEG sheet electron concentration and in the zero-field conduction band profile can therefore both be neglected.

In $\underline{k}$-space, the occupied 2DEG states lie within a shifted Fermi circle of radius $k_F = (2m^*_L E_F)^{\frac{1}{2}}/\hbar$ and centred at $(k_o, 0)$ as shown in Figure 4.1.

The expectation value of the y-component of momentum of a 2DEG electron with transverse wavevector component k_y is, using equation (4.15)

$$p_{y'} = m^*_L\langle v_y(k_y)\rangle = \hbar k_{y'} \qquad (4.17)$$

where $k_{y'} = k_y - k_o$

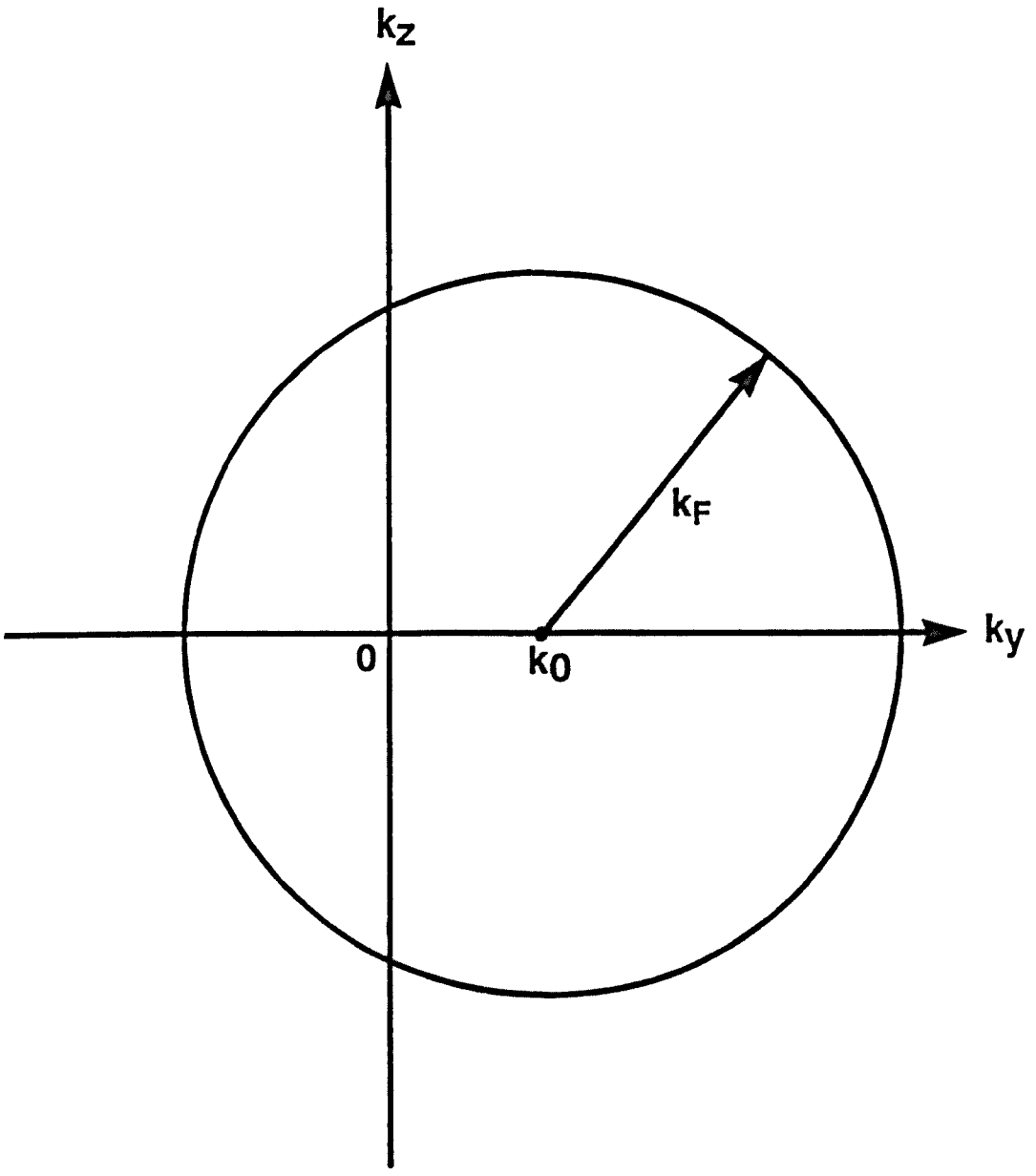

Figure 4.1 In the presence of a transverse magnetic field at T = 0K, the occupied 2DEG states lie within a Fermi circle in $\underline{k}$-space centred at $(k_y, k_z) = (k_0, 0)$, where $k_0 = Be(b + 3a_0)/\hbar$. Although the magnetic field shifts the distribution of occupied $\underline{k}$-states, it has no effect on the magnitude of the Fermi wavevector k_F, to first approximation.

It follows that the range of transverse momentum components corresponding to the occupied states in $\underline{k}$-space is

$$-p_F \leq p_{y'} \leq p_F \tag{4.18}$$

where $p_F = \hbar k_F$ is the Fermi momentum.

Thus, although the magnetic field shifts the $\underline{k}$-space distribution of occupied 2DEG states, it has no effect on the transverse velocity or momentum distributions.

4.2.3 Validity of the nondegenerate perturbation calculation

The first-order energy shift (4.11) can be written in the form

$$\Delta E_L(k_y, k_z) = \langle \frac{B^2e^2}{2m^*_L} (\bar{x}^2 + \frac{2\hbar k_y \bar{x}}{Be}) \rangle + \frac{B^2e^2}{2m^*_L} \langle (x - \bar{x})^2 \rangle \tag{4.19}$$

where $\bar{x} = \langle x \rangle = -(b + 3a_0)$.

The first term on the RHS of equation (4.19) is the expectation value of a constant perturbation which produces a bodily shift in the 2DEG energy levels, but has no effect on the unperturbed Fang-Howard wavefunction.

The spatially-varying perturbation contained in the second term on the RHS of equation (4.19) does influence the Fang-Howard wavefunction but its effect is small provided

$$\frac{B^2e^2}{2m^*_L} \langle (x - \bar{x})^2 \rangle = \Delta E'_{bo} = \frac{3}{2} m^*_L \omega_c^2 a_o^2 \ll E_F \ , \qquad (4.20)$$

that is , the diamagnetic shift of the bound state energy must be small compared with the minimum energy separation E_F between unperturbed bound and extended states which give non-vanishing matrix elements of H'.

For the (InGa)As/InP samples described in Chapter 5, $\Delta E'_{bo} \cong 4$ meV and $E_F \cong 17$ meV when V = 100 mV and B = 5T, so that nondegenerate perturbation theory is expected to be reasonably accurate.

By contrast, measurements on the GaAs/(AlGa)As samples described in Chapter 6 were performed up to higher fields of $\cong$ 18 T, for which $\Delta E'_{bo} \cong 14$ meV and $E_F \cong 18$ meV when V = 240 mV. The perturbation calculation is therefore of questionable validity at such high fields which may be sufficient to destroy the bound state (Helm et al., 1989).

4.3 Eigenstates of the Right-hand Subsystem in a Transverse Magnetic Field

4.3.1 Introduction

In the presence of a magnetic field $\underline{B} \parallel \underline{z}$, described by the vector potential $\underline{A}$ in the Landau gauge $\underline{A} = (0, Bx, 0)$, the RH eigenfunctions are of the form (3.8). It follows from equations (3.4) and (3.7) that the x-dependent factors satisfy

$$\left(-\frac{\hbar^2}{2}\frac{d}{dx}\left(\frac{1}{m^*(x)}\right)\frac{d}{dx} + \frac{\hbar^2 k_z^2}{2m^*(x)} + E_{EFF}(x)\right)\psi(x) = E_R(k_y,k_z)\,\psi(x) \tag{4.21}$$

where

$$E_{EFF}(x) = \begin{cases} E_c(x) + \dfrac{B^2e^2}{2m^*(x)}\left(x + \dfrac{\hbar k_y}{Be}\right)^2 & ; x > -b \\ E_{EFF}(-b_+) & ; x \le -b \end{cases},$$

and, neglecting the small potential dropped across the n^+ contact (see Section 2.4) so that $E_c(x) = 0$ for $x > 0$,

$$m^*(x) = \begin{cases} m_B^* & ; x \le 0 \\ m_L^*(1 + \alpha E_R) = \overline{m_L^*} & ; x > 0 \end{cases}.$$

The approximation $E_c(x) = 0;\ x > 0$ is used in all subsequent calculations of the RH eigenstates. Because the effective mass changes discontinuously at each barrier interface, the kinetic energy $E_z = \hbar^2 k_z^2/2m^*(x)$ associated with motion along the magnetic field direction is not conserved. However, generally $E_F << E'_{bo}$ so that this transverse kinetic energy is a small fraction of the total energy of each occupied 2DEG state. Neglecting conduction band nonparabolicity in the n^+ contact, E_z is conserved in tunnelling transitions and therefore makes the same small contribution to the total energy of accessible RH eigenstates. Consequently, E_z may be approximated by $\hbar^2 k_z^2/2m^*_L$ in equation (4.21) without significantly changing the solutions of interest. Within this approximation, the energy $E_n(k_y)$ associated with motion perpendicular to the magnetic field is conserved and equation (4.21) may be written

$$\left(-\frac{\hbar^2}{2}\frac{d}{dx}\left(\frac{1}{m^*(x)}\right)\frac{d}{dx} + E_{EFF}(x)\right)\psi(x) = E_n(k_y)\,\psi(x)\ , \qquad (4.22)$$

where $E_n(k_y) = E_R(k_y, k_z) - \hbar^2 k_z^2/2m^*_L$.

Since $\hbar^2 k_z^2/2m^*_L << E_R(k_y, k_z)$ for all accessible RH eigenstates, $E_R(k_y, k_z) \cong E_n(k_y)$ so that the effective mass defined in equation (4.21) can be approximated by $m^*(x) = \overline{m_L^*} \cong m^*_L\,(1 + \alpha E_n)$ for $x > 0$. This approximation totally decouples electron motion parallel and perpendicular to the magnetic field direction.

For all bias voltages, $E_F + E'_{bo} < E_c(-b_+)$,so that tunnelling only occurs into bound eigenstates of the RH subsystem with discrete energy levels $E_n(k_y)$ distinguished by the quantum number n. This set of eigenvalues depends on k_y through the orbit centre position X_{k_y} which determines the degree of electron confinement.

4.3.2 Qualitative discussion of the RH eigenvalues

Before calculating detailed solutions of equation (4.22), it is worthwhile considering the qualitative k_y-dependence of the eigenvalues $E_n(k_y)$. The effective potential energy $E_{EFF}(x)$ of the RH subsystem is shown schematically in Figure 4.2 for $k_y < 0$. If the orbit centre of the magnetic potential energy $X_{k_y} > 0$ ($k_y < 0$), two types of bound state may exist, classified according to the position of the energy level $E_n(k_y)$ relative to the MPE $E_{MAG}(0_+) = \hbar^2 k_y^2/2m^*(0_+)$ at the RH barrier interface. Each type of bound state corresponds to a distinct classical trajectory. The eigenvalues of the so-called bulk Landau states, such as the m^{th} level shown in Figure 4.2 satisfy

$$E_n(k_y) < E_{MAG}(0_+) \quad , \tag{4.23}$$

and correspond to classical orbits which are bounded by two soft turning points, B_1 and B_2. These orbits do not intersect with the potential barrier ($B_1 > 0$) and describe bulk cyclotron motion.

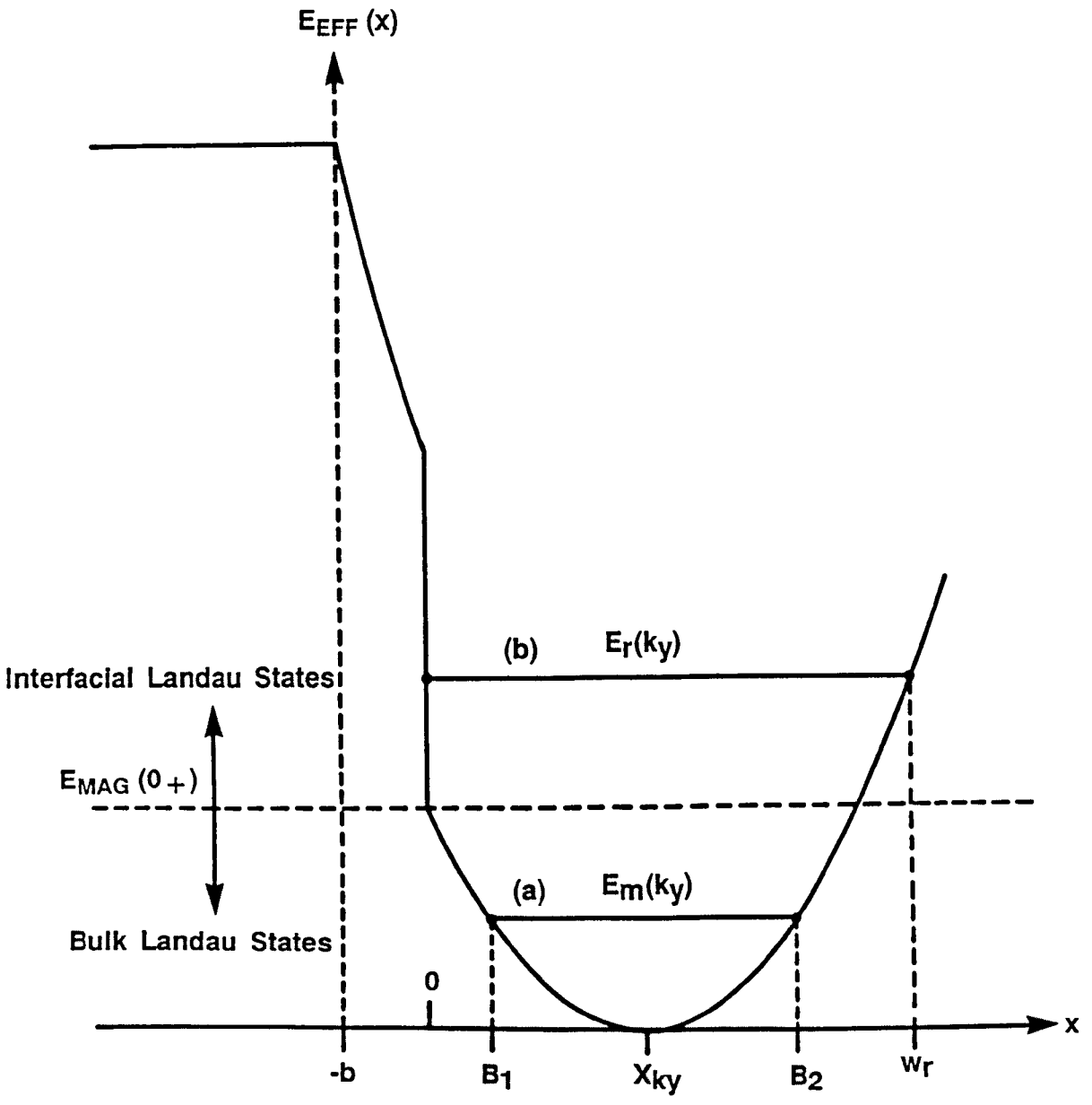

Figure 4.2 The effective potential energy of the RH subsystem shown schematically for $k_y < 0$ ($X_{k_y} > 0$). Bulk and interfacial Landau levels are classified, as shown, according to their positions relative to the magnetic potential energy E_{MAG} (0+) at the RH barrier interface.

The classical trajectory corresponding to the m^{th} bulk Landau level shown, is bounded by soft turning points B_1 and B_2, does not intersect with the barrier interface and describes bulk circular cyclotron orbits. By contrast, the classical trajectory corresponding to the r^{th} interfacial Landau state has a hard LH turning point at $x = 0$ from which the electron is specularly reflected and undergoes 'skipping' motion along the barrier interface.

Interfacial Landau levels such as the r^{th} level in Figure 4.2 satisfy

$$E_n(k_y) > E_{MAG}(0_+) \quad . \tag{4.24}$$

The associated classical orbit extends between the hard turning point at $x = 0$ and the soft RH turning point at $x = w_n$. Classically, the electron is specularly reflected at $x = 0$ and therefore describes skipping motion along the RH barrier interface. If the orbit centre $X_{k_y} < 0$ ($k_y > 0$), interfacial Landau states only are formed. The classical motion corresponding to interfacial and bulk Landau states is discussed more fully in Section 4.4.

Suppose that, for given $k_y < 0$, the n^{th} eigenvalue of equation (4.22) corresponds to a bulk Landau state. Within the WKB approximation, the value of $E_n(k_y)$ depends only on the MPE between the classical turning points and equals the n^{th} bulk Landau level,

$$E_n(k_y) = (n + \tfrac{1}{2})\hbar Be/\overline{m^*_L} \quad . \tag{4.25}$$

For given magnetic field, the orbit centre $X_{k_y} = -\hbar k_y/Be$ moves towards the RH barrier interface with increasing k_y (< 0) so that $E_{MAG}(0_+)$ falls. However, provided $(n + \tfrac{1}{2})\hbar Be/\overline{m^*_L}$ remains lower than $E_{MAG}(0_+)$, the WKB approximation (4.25) for $E_n(k_y)$ is unchanged.

A more complete calculation would reveal a slight increase in $E_n(k_y)$, because the shift in orbit centre increases the overlap between the bulk Landau state wavefunction and the perturbing potential energy barrier.

The transition from bulk to interfacial Landau levels occurs, for the n^{th} level, when $k_y = -(2(n+\frac{1}{2})Be/\hbar)^{\frac{1}{2}}$. For this value of k_y, $E_{MAG}(0_+)$ equals the n^{th} bulk Landau level so that the LH turning point changes from soft to hard. Further increasing k_y moves the orbit centre still closer to the RH barrier interface. This increases the confinement of the n^{th} bound state wavefunction, thereby raising the interfacial Landau level $E_n(k_y)$.

4.3.3 Calculation of the Interfacial Landau Levels

Vigneron and Ausloos (1978) considered the effect of a transverse magnetic field on the eigenstates of a heterojunction. The x-dependent eigenfunctions of this system satisfy a 1D Schrödinger equation in which the MPE and the stepped conduction band edge form a so-called bound oscillator potential. Piecewise solutions of this equation, on each side of the potential energy step, are the parabolic cylinder functions (Miller, 1965). In principle, exact eigenvalues of the system can be calculated from the requirement that the parabolic cylinder functions vanish as $x \to \pm\infty$, and by imposing the matching conditions (1.39) and (1.40) at the interface. However, analytical expressions for these eigenvalues can only be obtained for

certain conduction band offsets and SHO orbit centre positions. Johnson et al. (1987) calculated the energy levels of this bound oscillator system, as a function of orbit centre position, by solving the matching equations numerically.

From equations (2.21) and (4.21), the effective 1D potential energy of the RH subsystem of the single-barrier structures only contains terms linear or quadratic in x. Consequently, the parabolic cylinder functions are also piecewise solutions of equation (4.22). By numerically solving the matching equations for these solutions at each barrier interface, exact RH eigenvalues can, in principle, be obtained as a function of X_{k_y}. However, approximate analytical solutions of equation (4.22), calculated within the WKB approximation, lead to a more physical interpretation of the oscillatory structure observed in the forward-bias I(B) characteristics (see Chapter 5). Vawter (1968) found that WKB eigenvalues of the bound oscillator system never differ from the exact values by more than 10% and are generally accurate to within 1%. When uncertainties in the device parameters are considered, nominally exact numerical solutions of equation (4.22) are therefore likely to be no more physically realistic than the WKB solutions.

The turning points of the n^{th} interfacial Landau states occur at $x = 0$ and $x = w_n$. Consequently, piecewise solutions of equation (4.22) corresponding to these states are, to first order of the WKB approximation

$$\psi_n(x) = \begin{cases} C_n \mu_{n1}^{-\frac{1}{2}}(x)\, e^{-Q(x)} & ; x \leq 0 \quad \text{(a)} \\ D_n\, \alpha_n^{-\frac{1}{2}}(x)\, e^{iT(x)} + F_n\, \alpha_n^{-\frac{1}{2}}(x)\, e^{-iT(x)} & ; 0 < x \leq w_n \quad \text{(b)} \\ G_n\, \mu_{n3}^{-\frac{1}{2}}(x)\, e^{-Z(x)} & ; x \geq w_n \quad \text{(c)} \end{cases} \quad , \quad (4.26)$$

where $\mu_{n1}(x) = \begin{cases} [2m_B^*(E_{EFF}(x) - E_n)]^{\frac{1}{2}} / \hbar & ; -b < x \leq 0 \\ \mu_{n1}(-b_+) & ; x \leq -b \end{cases}$,

$$\alpha_n(x) = [2\overline{m^*_L}\,(E_n - E_{EFF}(x))]^{\frac{1}{2}} / \hbar \ ,$$

$$\mu_{n3}(x) = [2\overline{m^*_L}\,(E_{EFF}(x) - E_n)]^{\frac{1}{2}} / \hbar \ ,$$

and the integral functions

$$Q(x) = \int_x^0 \mu_{n1}(\bar{x})\, d\bar{x} \quad ,$$

$$T(x) = \int_x^{w_n} \alpha_n(\bar{x})\, d\bar{x} \quad ,$$

and $$Z(x) = \int_{w_n}^{x} \mu_{n3}(\bar{x})\, d\bar{x} \quad ,$$

all increase with distance from the turning points. These first-order solutions are locally valid provided either

$$\left| \frac{d\mu_{ni}(x)}{dx} \right| << |\mu_{ni}(x)|^2 \ , \ i = 1,3 \qquad (4.27)$$

or $$\left| \frac{d\alpha_n(x)}{dx} \right| << |\alpha_n(x)|^2 \qquad (4.28)$$

depending on the x-coordinate.

These requirements are satisfied if only a small fractional change in $\mu_{ni}(x)$ or $\alpha_n(x)$ occurs over a distance $2\pi/\mu_{ni}(x)$ or $2\pi/\alpha_n(x)$. Both inequalities are clearly violated at the RH turning point where $\alpha_n(w_n) = \mu_{n3}(w_n) = 0$, and the WKB wavefunction diverges. In order to calculate the interfacial Landau levels, more accurate solutions of equation (4.22) are required which can be matched at $x = w_n$.

If the potential energy varies almost linearly close to w_n, approximate solutions of equation (4.22) in this region are (see, for example, Capri, 1985)

$$\psi_n(x) = \begin{cases} A_n^+ \alpha_n^{\frac{1}{2}}(x)\, J_{\frac{1}{3}}(T(x)) + A_n^- \alpha_n^{\frac{1}{2}}(x)\, J_{-\frac{1}{3}}(T(x)) \; ; \; x \leq w_n \end{cases}$$

(4.29a)

$$\begin{cases} G_n^+ \mu_{n3}^{\frac{1}{2}}(x)\, I_{\frac{1}{3}}(T(x)) + G_n^- \mu_{n3}^{\frac{1}{2}}(x)\, I_{-\frac{1}{3}}(T(x)) \; ; \; x \geq w_n \end{cases}$$

(4.29b)

where $J_{\pm\frac{1}{3}}(x)$ are Bessel functions of the first kind and $I_{\pm\frac{1}{3}}(z)$ are the modified Bessel functions (Olver, 1965). Provided that the region of linear potential energy variation extends sufficiently far to the right of the turning point for the asymptotic forms of $I_{\pm\frac{1}{3}}(z)$ to be valid, then, for large x,

$$\psi_n(x) \cong (2\pi\, \mu_{n3}(x))^{-\frac{1}{2}} \left[(G_n^+ + G_n^-)\, e^{Z(x)} \right.$$

$$\left. + \left(G_n^+ e^{-\frac{i5\pi}{6}} - G_n^- e^{-\frac{i\pi}{6}}\right) e^{-Z(x)} \right]$$

(4.30)

which for $x \geq w_n$ has the same form as the WKB solution (4.26c). Since Z(x) increases with x, G_n^+ must equal $-G_n^-$ in order that $\psi_n(x)$ vanishes as $x \to \infty$. The Bessel function coefficients A_n^+ and A_n^- can then be related to G_n^- by imposing the matching conditions (1.39) and (1.40) on the small argument forms of equation (4.29) at $x = w_n$.

The required coefficients are

$$A_n^+ = A_n^- = G_n^- \quad . \tag{4.31}$$

Provided the region of linear potential energy variation extends sufficiently far left of the turning point that the asymptotic forms of $J_{\pm\frac{1}{3}}(T(x))$ may be used in equation (4.29a), $\psi_n(x)$ becomes

$$\psi_n(x) \equiv G_n^- \left(\frac{6}{\pi}\right)^{\frac{1}{2}} \alpha_n^{-\frac{1}{2}}(x) \cos\left[T(x) - \frac{\pi}{4}\right] \quad ; \; x << w_n \tag{4.32}$$

This expression takes the same form as the WKB solution (4.26b) and relates the expansion coefficients D_n and F_n. Provided the validity requirement (4.28) is satisfied, equation (4.32) is accurate throughout the classically allowed region.

Using Bessel functions to match WKB solutions across a soft turning point leads to the so-called connection formulae (see, for example, Merzbacher, 1970), of which the relation between equation (4.26c) and equation (4.32) is one example.

The quantisation condition for the interfacial Landau levels is obtained by imposing the matching conditions (1.39) and (1.40) on equations (4.26a) and (4.32) at $x = 0$. These conditions give

$$C_n \mu_{n1}^{-\frac{1}{2}}(0_-) = G_n^- \left(\frac{6}{\pi}\right)^{\frac{1}{2}} \alpha_n^{-\frac{1}{2}}(0_+) \cos\left[T(0_+) - \frac{\pi}{4}\right] \tag{4.33}$$

and

$$\frac{C_n}{m_B^*}\,\mu_{n1}^{\frac{1}{2}}(0_-)\left[1-\frac{1}{(2\mu_{n1}^2(0_-))}\frac{d\mu_{n1}(0_-)}{dx}\right]$$

$$=\frac{G_n^-}{m_L^*}\left(\frac{6\alpha_n(0_+)}{\pi}\right)^{\frac{1}{2}}\left[\sin\left[T(0_+)-\frac{\pi}{4}\right]-\left(\frac{\cos[T(0_+)-\pi/4]}{(2\alpha_n^2(0_+))}\right)\left(\frac{d\alpha_n(0_+)}{dx}\right)\right] \tag{4.34}$$

Eliminating G_n^- from equations (4.33) and (4.34) gives, after some algebra

$$\tan\left[T(0_+)-\frac{\pi}{4}\right]=\left(\frac{\overline{m_L^*}\,\mu_{n1}(0_-)}{m_B^*\,\alpha_n(0_+)}\right)\left(1-\frac{1}{(2\mu_{n1}^2(0_-))}\frac{d\mu_{n1}(0_-)}{dx}\right.$$

$$\left.+\frac{1}{(2\alpha_n^2(0_+))}\frac{d\alpha_n(0_+)}{dx}\right)\,. \tag{4.35}$$

The derivation of this equation assumes that the WKB validity requirements (4.27) and (4.28) are both satisfied at $x = 0$. Using these conditions to simplify equation (4.35) gives, to good approximation

$$\tan\left[\int_0^{W_n}\alpha_n(x)\,dx-\frac{\pi}{4}\right]=\frac{\overline{m_L^*}\,\mu_{n1}(0_-)}{m_B^*\,\alpha_n(0_+)} \tag{4.36}$$

It is easily verified by direct substitution that the n^{th} solution of this equation is

$$\int_o^{W_n} \alpha_n(x)\, dx = (n + \tfrac{1}{4})\pi + \tan^{-1}\left(\frac{\overline{m_L^*}\ \mu_{n1}(0_-)}{m_B^*\ \alpha_n(0_+)}\right) \qquad (4.37)$$

where $n = 0, 1, 2 \ldots$

and the inverse tangent lies in the range 0 to $\pi/2$ inclusive.

The integral on the LHS of equation (4.37) gives the phase change of the WKB wavefunction over the classically allowed region. In the limit of an impenetrable barrier at $x = 0$, $\mu_{n1}(0_-) \to \infty$ so that the energy quantisation condition (4.37) becomes

$$\int_o^{W_n} \alpha_n(x)\, dx = (n + \tfrac{3}{4})\, \pi \qquad (4.38)$$

Substituting the local semiclassical x-component of momentum $p_n(x) = \hbar\alpha_n(x)$ into this equation gives

$$2 \int_o^{W_n} p_n(x)\, dx = \int p_n(x)\, dx = (n + \tfrac{3}{4})\, h \qquad (4.39)$$

which, apart from the phase factor, is simply the Bohr-Sommerfeld canonical momentum quantisation condition (see, for example, Merzbacher, 1970).

If the impenetrable barrier is relaxed, the inverse tangent term in equation (4.37) decreases, thereby reducing the phase shift across the classically allowed region. Physically this arises from the penetration of the electron wavefunction into the barrier region.

To obtain an implicit expression for the energy levels $E_n(k_y)$ from equation (4.37), it is necessary to evaluate the phase change integral which, using the expression for $\alpha_n(x)$ given in equation (4.26), may be written

$$\int_o^{W_n} \alpha_n(x)\, dx = \frac{2\overline{m_L^*}\, E_n}{Be\hbar} \int_{u_o}^{1} (1 - u^2)^{\frac{1}{2}}\, du \qquad (4.40a)$$

where $$u(x) = Be\left(x + \frac{\hbar k_y}{Be}\right) / (2\overline{m_L^*}\, E_n)^{\frac{1}{2}} \qquad (4.40b)$$

and $$u_o = u(0) = \hbar k_y / (2\overline{m_L^*}\, E_n)^{\frac{1}{2}} \qquad (4.40c)$$

For interfacial Landau states, $E_n(k_y) \geq E_{MAG}(0_+) = \hbar^2 k_y^2 / 2\overline{m^*_L}$ so that u_o lies in the range $-1 \leq u_o \leq 1$. When $u_o = -1$, $k_y = -(2\overline{m^*_L} E_n)^{\frac{1}{2}}/\hbar$, which corresponds to the transition from interfacial to bulk Landau states.

The integral in equation (4.40) is easily evaluated giving,

$$\int_o^{W_n} \alpha_n(x)\, dx = \frac{\overline{m_L^*}\, E_n}{Be\hbar} \left(\frac{\pi}{2} - f(u_o)\right) \qquad (4.41)$$

where

$$f(u_0) = \sin^{-1} u_0 + u_0(1 - u_0^2)^{\frac{1}{2}} \qquad (4.42)$$

Combining equations (4.37) and (4.41), the interfacial Landau level quantisation condition becomes

$$\frac{\overline{m_L^*}\, E_n}{Be\hbar}\left(\frac{\pi}{2} - f(u_0)\right) = \left(n + \frac{1}{4}\right)\pi + \tan^{-1}\left(\frac{\overline{m_L^*}\, \mu_{n1}(0_-)}{m_B^*\, \alpha_n(0_+)}\right) . \qquad (4.43)$$

$$; \; n = 0, 1, \ldots$$

This implicit equation for $E_n(k_y)$ must in general be solved numerically. However, it is worthwhile considering the case of an infinite potential barrier, and $k_y = 0$ so that the orbit centre $X_{k_y} = -\hbar k_y/Be$ lies at the RH barrier interface. For this value of k_y, $u_0 = 0$ and equation (4.43) becomes

$$E_n(0) = 2\left(n + \frac{3}{4}\right)\hbar Be/\overline{m_L^*} \quad , \; n = 0, 1, 2 \ldots \qquad (4.44)$$

These are the odd-integer Landau levels corresponding to odd-parity SHO eigenfunctions which vanish at the RH barrier interface ($x = 0$).

Figure 4.3 shows interfacial and bulk Landau state dispersion curves $E_n(k_y)$ calculated numerically from equation (4.43), for the (InGa)As/InP structures described in Chapter 5. The dashed curve shows the MPE $E_{MAG}(0_+) = \hbar^2 k_y^2/2\overline{m_L}^*$, as a function of $k_y < 0$, and marks the transition between bulk and interfacial Landau states.

For given $k_y < 0$, any energy level lying below this curve corresponds to a bulk Landau state. Similarly, eigenvalues which exceed the MPE at $x = 0$ correspond to interfacial Landau states. The corresponding classical skipping trajectories are shown inset in Figure 4.3. The transition from interfacial to bulk Landau levels is discontinuous because the WKB phase change given by the RHS of equation (4.43) changes abruptly to $(n + \frac{1}{2})\pi$ as the LH turning point 'softens'. Interfacial Landau levels near this transition region are likely to be inaccurate since the WKB validity requirement (4.28) is violated close to $x = 0$.

From equation (1.26), the gradient $dE_n(k_y)/dk_y$ of the dispersion curves is proportional to the expectation value of the y-component of velocity. As expected, this mean velocity vanishes for the bulk Landau states, which correspond to closed circular cyclotron orbits, and is positive for interfacial Landau states, which correspond to skipping trajectories in which there is nett translational motion along the barrier interface.

Conduction band nonparabolicity in the n^+ collector leads to reduced separation of the higher-lying energy levels. This effect is

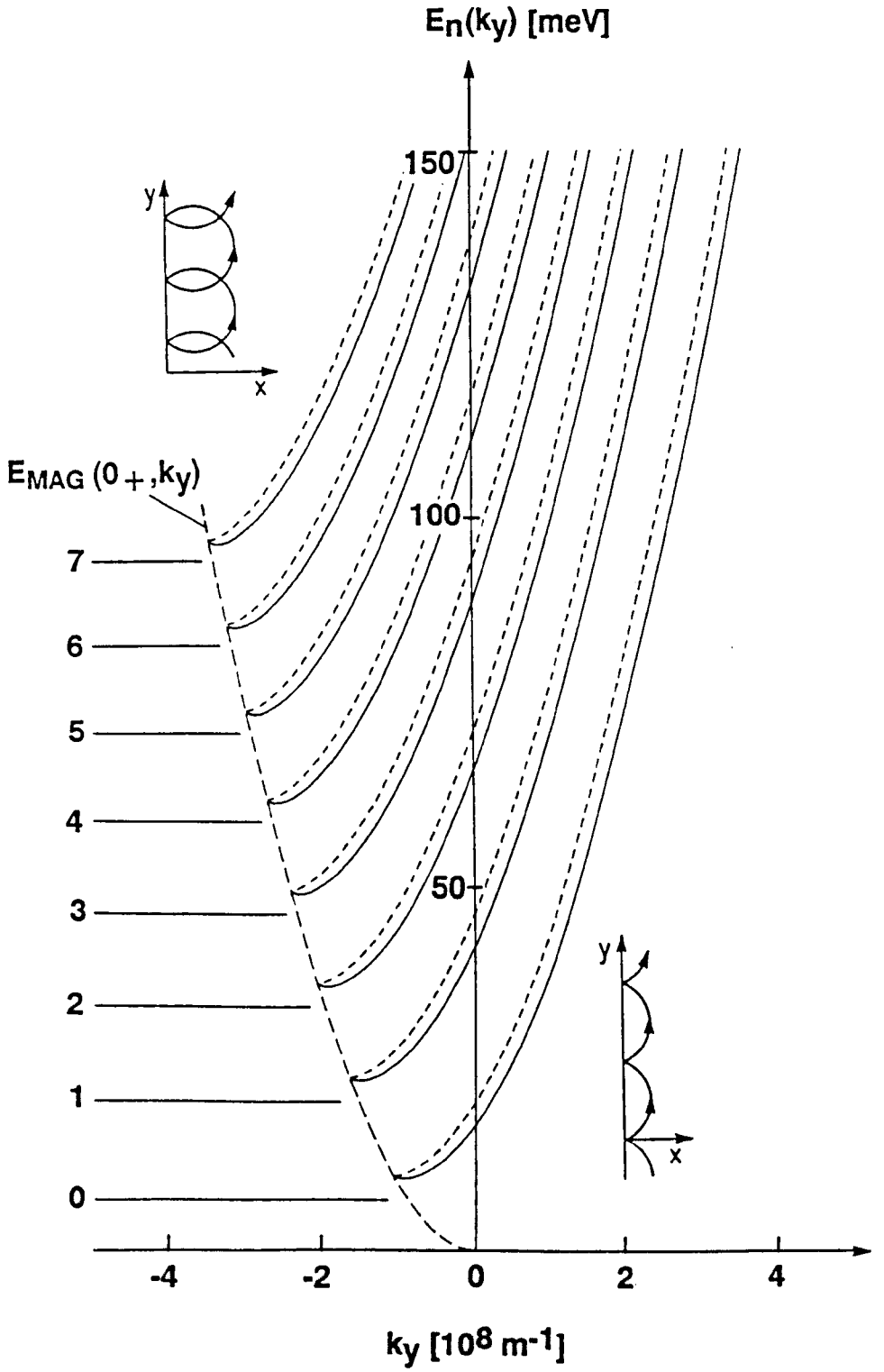

Figure 4.3 Bulk and interfacial Landau level dispersion curves $E_n(k_y)$, n = 0, 1, ... 7, calculated for the (InGa)As/InP single-barrier structures when B = 5 T and V = 100 mV. The nonparabolicity factor of the n^+ contact is taken to be $\alpha = 1.3$ eV^{-1}, and the conduction band offset either 230 meV (solid curves) or infinite (broken curves). The magnetic potential energy E_{MAG} (0_+, k_y) at the RH barrier interface is shown for $k_y < 0$ and marks the transition from bulk to interfacial Landau states. Inset are the classical skipping trajectories corresponding to interfacial states with $k_y < 0$ and $k_y > 0$.

most easily seen in the bulk Landau levels and also in the odd-integer Landau levels, which are the eigenvalues of the RH subsystem when $k_y = 0$.

The series of dotted curves show the interfacial Landau levels in the limit of an impenetrable potential barrier. The energy levels are raised owing to increased confinement of the electron wavefunctions. The percentage difference between interfacial levels calculated for finite and infinite potential energy barriers is smaller for higher-lying levels. This is because for high quantum numbers, the phase change in the energy quantisation condition (4.43) is dominated by the $(n + 1/4)\pi$ term. The inverse tangent term, which contains information about the barrier height, makes a comparatively small contribution ($\leq \pi/2$).

As shown in Figure 4.4, the function $f(u_0)$ defined in equation (4.42) is almost linear for $-1 \leq u_0 \leq 1$ and may be approximated by

$$f(u_0) \cong \frac{\pi}{2} u_0 \qquad (4.45)$$

Combined with the infinite-barrier approximation, this simplification of $f(u_0)$ enables approximate analytical expressions for the energy levels $E_n(k_y)$ to be found, which are within 10% of the exact numerical values. This approximation is widely used in the

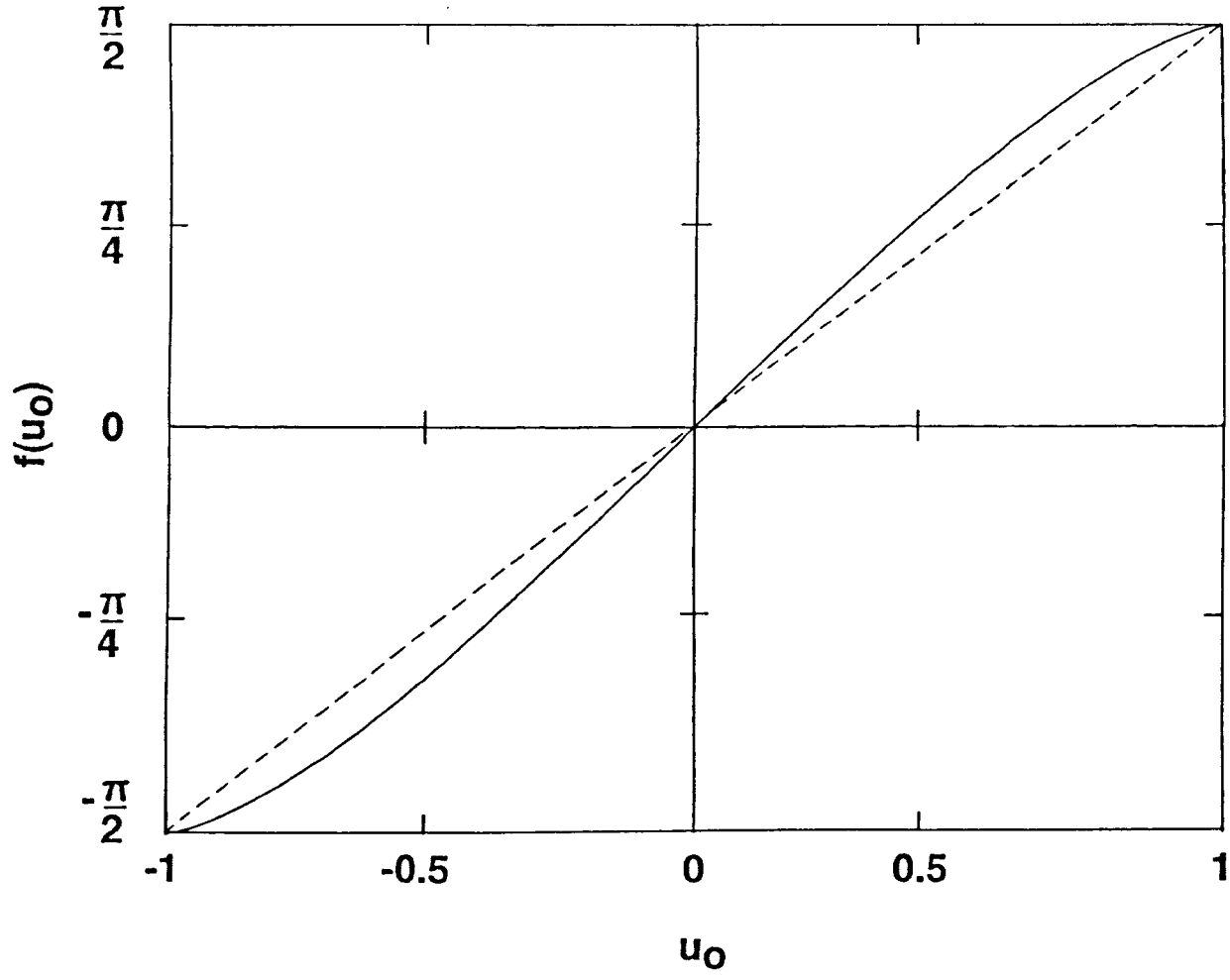

Figure 4.4 The solid curve shows the function $f(u_o)$ defined in equation (4.42), plotted over the range $-1 \leq u_o \leq 1$. Comparison with the broken line shows that $f(u_o) \cong \pi u_o/2$ over this range.

analytical treatment of magnetotunnelling given in Chapters 5 and 6 of this thesis.

4.4 Classical Trajectories of the Bulk and Interfacial Landau States

By analogy with equation (3.2), the classical Hamiltonian describing motion in the x-y plane corresponding to the Landau state Ψ_{n,k_y} is

$$H = \frac{p_x^2}{2m_L^*} + \frac{(p_y + eBx)^2}{2m_L^*} + E_c(x) \quad , \tag{4.46}$$

where p_x and $p_y = \hbar k_y$ are the canonical momentum components.

The classical trajectory is obtained from solution of Hamiltons equations

$$\dot{x} = \frac{\partial H}{\partial p_x} \quad (a) \quad , \quad \dot{y} = \frac{\partial H}{\partial p_y} \quad (b) \quad ,$$

(4.47)

$$\dot{p}_x = -\frac{\partial H}{\partial x} \quad (c) \quad , \quad \dot{p}_y = -\frac{\partial H}{\partial y} \quad (d) \quad .$$

For $x > 0$, $E_c(x) = 0$ and the electron moves under the influence of the Lorentz force alone. The solutions of equation (4.47) are well known for this case. When looking anti-parallel to the magnetic field, the electron moves anti-clockwise around a circle of radius $R_n = (2\overline{m_L^*}E_n)^{\frac{1}{2}}/Be$ with constant orbital speed $v_n = (2E_n/\overline{m_L^*})^{\frac{1}{2}}$ as shown in Figure 4.5. The x-coordinate of the centre of this circle is $X_{k_y} = -\hbar k_y/Be$. By definition, the energies and transverse wavevector components of bulk Landau states satisfy $k_y \leq -(2\overline{m_L^*}E_n)^{\frac{1}{2}}/\hbar$ so that

$$X_{k_y} = -\hbar k_y/Be \geq \frac{(2\overline{m_L^*}\,E_n)^{\frac{1}{2}}}{Be} = R_n \qquad (4.48)$$

and the electron completes closed, circular cyclotron orbits.

For interfacial Landau states $k_y > -(2\overline{m_L^*}E_n)^{\frac{1}{2}}/\hbar$ so that

$$X_{k_y} = -\hbar k_y/Be < \frac{(2\overline{m_L^*}\,E_n)^{\frac{1}{2}}}{Be} = R_n \quad . \qquad (4.49)$$

and the classical trajectory intersects with the RH barrier interface. Since the barrier is a classically forbidden region, which exerts no in-plane component of force, the electron is specularly reflected from the interface. As shown in Figure 4.5, the electron 'skips' along the barrier in a series of arcs of radius R_n. With each successive skip, the orbit centre moves discretely along the line $x = X_{k_y}$, so that the electron has a nett drift velocity in

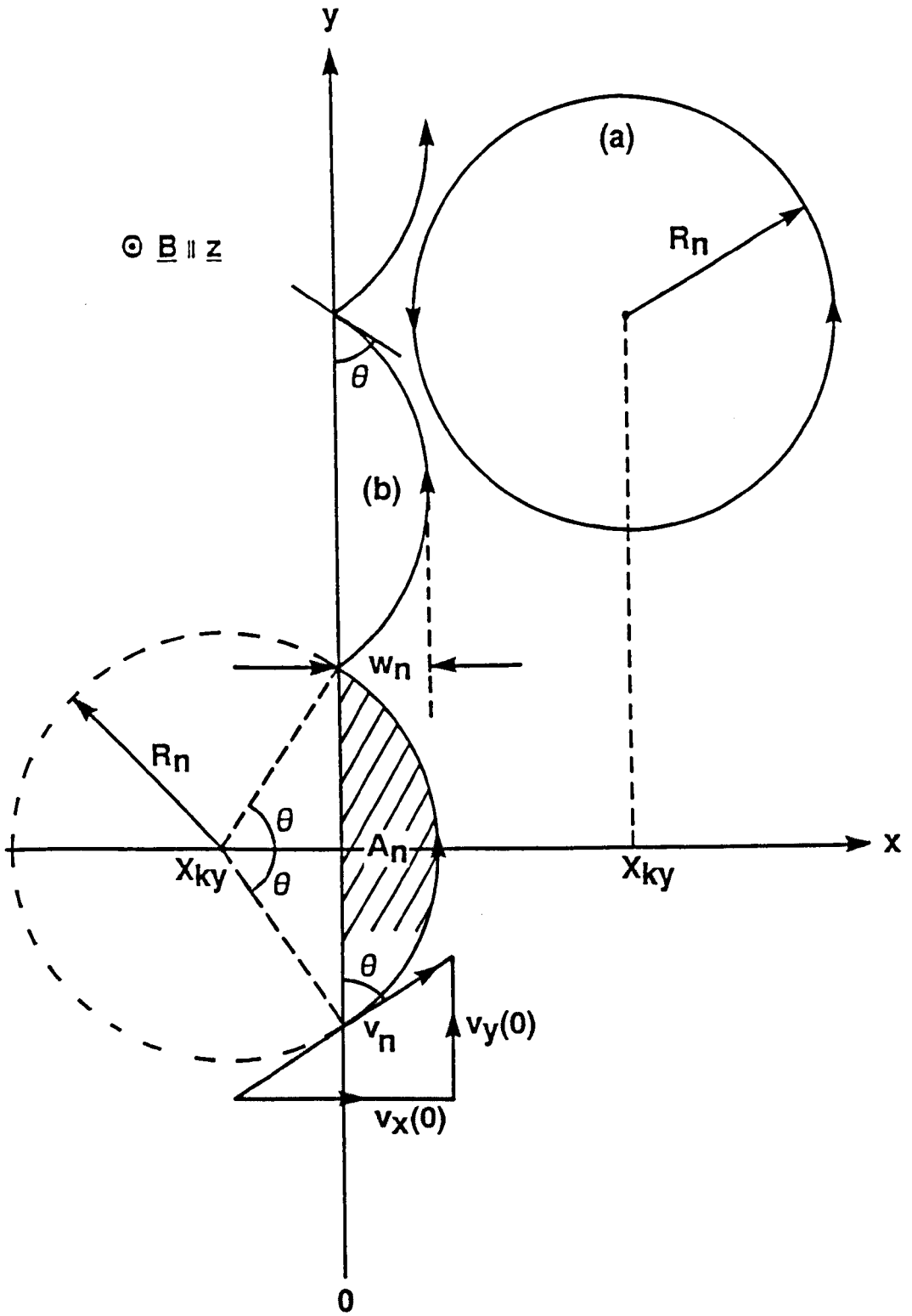

Figure 4.5 Projection in the x-y plane of (a) the classical cyclotron orbits corresponding to bulk Landau states and (b) the classical skipping orbits corresponding to interfacial Landau states. The WKB interfacial Landau level quantisation condition (4.43) leads to quantisation of the shaded area A_n, bounded by the electron path and the RH barrier interface.

the y-direction. This agrees with the quantum mechanical expectation value (1.26) which is proportional to the positive gradient of the interfacial Landau state dispersion curve. From equation (4.47b), the local y-component of velocity is

$$v_y(x) = \frac{(p_y + eBx)}{\overline{m_L^*}} = \frac{\hbar k_y + eBx}{\overline{m_L^*}} \qquad (4.50)$$

so that at the RH barrier interface,

$$v_y(0_+) = \hbar k_y / \overline{m_L^*}. \qquad (4.51)$$

The skipping electron moves with constant orbital speed $v_n = (2E_n/\overline{m_L^*})^{\frac{1}{2}}$ and is therefore incident on the barrier at an angle θ, given by

$$\theta = \cos^{-1}\left(\frac{v_y(0_+)}{v_n}\right) = \cos^{-1}\left(\frac{\hbar k_y}{(2\overline{m_L^*}\, E_n)^{\frac{1}{2}}}\right) = \cos^{-1} u_o$$

$$; \; 0 \leq \theta \leq \pi \;, \qquad (4.52)$$

which gives a physical interpretation of the variable u_o defined in equation (4.40).

The arclength S_n of the skipping orbit shown in Figure 4.5 is

$$S_n = 2R_n\theta = \frac{2(2\overline{m_L^*}\,E_n)^{\frac{1}{2}}\cos^{-1}u_o}{Be} \quad , \qquad (4.53)$$

so that the time-of-flight between successive skips is

$$T_n = \frac{S_n}{v_n} = \frac{2\overline{m_L^*}}{Be}\cos^{-1}u_o \quad . \qquad (4.54)$$

The frequency of classical collisions between the skipping electron and the RH barrier interface is therefore

$$F_n = \frac{1}{T_n} = \frac{Be}{2\overline{m_L^*}\cos^{-1}u_o} \quad . \qquad (4.55)$$

From equation (4.40c), $\cos^{-1}u_o = \pi$ for bulk orbits so that F_n simply equals the bulk cyclotron frequency $\omega_c/2\pi$.

When $k_y = 0$, the magnetic potential energy is centred at the RH barrier interface ($X_{k_y} = 0$), and the electron trajectory consists of a series of semicircles. From equation (4.40c), $\cos^{-1}u_o = \pi/2$ when $k_y = 0$ so that $F_n = \omega_c/\pi$. As expected this is twice the bulk cyclotron frequency.

As k_y is increased from zero, the orbit centre $X_{ky} = -\hbar k_y/Be$ moves further left of the RH barrier interface. In addition, equation (4.52) predicts that for given E_n, u_o increases towards unity so that the angle of incidence $\theta = \cos^{-1} u_o$ falls and the skipping frequency (4.55) rises.

This increased skipping frequency is central to the physical interpretation of the amplitudes of oscillatory structure observed under forward bias in the magneto-current and derivatives of the single-barrier structures (see Chapters 5 and 6).

It is clear from Figure 4.5 that the area A_n, enclosed by the RH barrier interface and the projection of the skipping orbit on the x-y plane is

$$A_n = R_n^2\,\theta - R_n^2 \cos\theta \sin\theta$$

$$= R_n^2 \left(\cos^{-1} u_o - u_o(1 - u_o^2)^{\frac{1}{2}}\right) \qquad (4.56)$$

$$= \frac{2\overline{m_L^*}\, E_n}{B^2 e^2} \left(\frac{\pi}{2} - f(u_o)\right)$$

where $f(u_o)$ is defined in equation (4.42).

Comparing equation (4.56) with the quantisation condition (4.43) gives, in the limit of an impenetrable barrier

$$A_n = \left(n + \frac{3}{4}\right) h/Be \quad , \qquad (4.57)$$

so that the area of the skipping orbit is quantised in units of h/Be, which is twice the area of n = 0 bulk cyclotron orbits. It follows that the magnetic flux $\phi_n = BA_n$ passing through this orbit is quantised in units of h/e.

4.5 Summary

In this chapter, the effect of a transverse magnetic field on occupied 2DEG states has been described using nondegenerate perturbation theory. The field causes a diamagnetic shift $\Delta E'_{bo}$ of the bound state energy and, in $\underline{k}$-space, the centre of the Fermi circle undergoes translation from $(k_y, k_z) = (0, 0)$ to $(Be(b + 3a_o)/\hbar, 0)$. However, provided $\Delta E'_{bo} << E_{FL}$ so that the use of non-degenerate perturbation theory is valid, the change in magnitude of the Fermi wavevector is negligible.

Electronic motion in the n^+ layer is constrained in the x-direction by the magnetic field and the potential energy barrier. This confinement quantises the energy associated with motion perpendicular to the magnetic field into bulk or interfacial Landau levels. Interfacial Landau states correspond to classical skipping trajectories which intersect with the barrier interface. The associated energy levels can be calculated within the WKB approximation and depend on the transverse wavevector component k_y, which determines the orbit centre position and consequent degree of magnetic confinement. The WKB energy quantisation condition leads to areal quantisation of the skipping orbit projection on the x-y plane.

CHAPTER FIVE

TRANSVERSE MAGNETOTUNNELLING IN ASYMMETRICALLY-DOPED (InGa)As/InP SINGLE-BARRIER HETEROSTRUCTURES

5.1 Introduction

In the previous chapter, the LH and RH eigenstates of an asymmetrically-doped single-barrier structure were calculated under forward-bias conditions, and in the presence of a transverse magnetic field $\underline{B} \parallel \underline{z}$. In this chapter, these results are used within a transfer-Hamiltonian formalism, to calculate the tunnel current due to electronic transitions from the 2DEG into interfacial Landau states in the n^+ collector contact. The predicted field-dependences of the tunnel current and derivatives are compared with measurements reported by Snell (1987a) and Snell et al. (1987).

5.2 Device Specifications

The heterostructures used in the experiments of Snell et al. were grown by metalorganic chemical-vapour deposition and consisted of the following layers, illustrated in Figure 2.1: (1) 8000 Å of (InGa)As, doped at $N_D = 10^{23}$ m^{-3}; (2) 8000 Å of (InGa)As, $N_D = 5 \times 10^{21}$ m^{-3}; (3) 168 Å of InP, $N_D = 6 \times 10^{21}$ m^{-3}; (4) 3600 Å of (InGa)As, $N_D = 10^{23}$ m^{-3}; (5) 2000 Å of InP, $N_D = 5 \times 10^{23}$ m^{-3}.

Using a nonparabolicity factor $\alpha = 5\ eV^{-1}$ (Sarkar et al., 1985) and taking the conduction band-edge mass of (InGa)As to be $0.041\ m_o$, the Fermi energy (2.1) in the n^+ contact is $E_{FR} \cong 16$ meV.

A conduction band offset $\Delta E_c = 230$ meV is assumed and the conduction band-edge mass of InP is taken to be $m_B^* \cong 0.077\ m_o$.

5.3 Experimental Magnetotunnelling Data

Figures 5.1 and 5.2 show the field-dependence of the tunnel current I(B) measured for a range of forward-bias voltages. The experimental techniques used to obtain these curves have been described in detail by Snell (1987a).

For all voltages, the tunnel current falls rapidly with increasing field, and for V = 100 mV, is almost quenched for $B \geq 15$ T. Weak oscillatory structure superimposed on this fall off is clearly revealed in the second derivative curves d^2I/dB^2, shown in Figures 5.1 and 5.3. For each bias voltage, two distinct series of oscillations are observed over clearly separated ranges of magnetic field. Those oscillations visible at low fields are collectively referred to as the $+p_F$ series, and those at higher fields the $-p_F$ series. With the exception of the last (highest-field) $-p_F$ oscillation observed for V = 100 mV, the oscillatory amplitudes of both series increase with field. In addition, with increasing voltage, the $+p_F$ oscillatory amplitudes weaken relative to those of the $-p_F$ series.

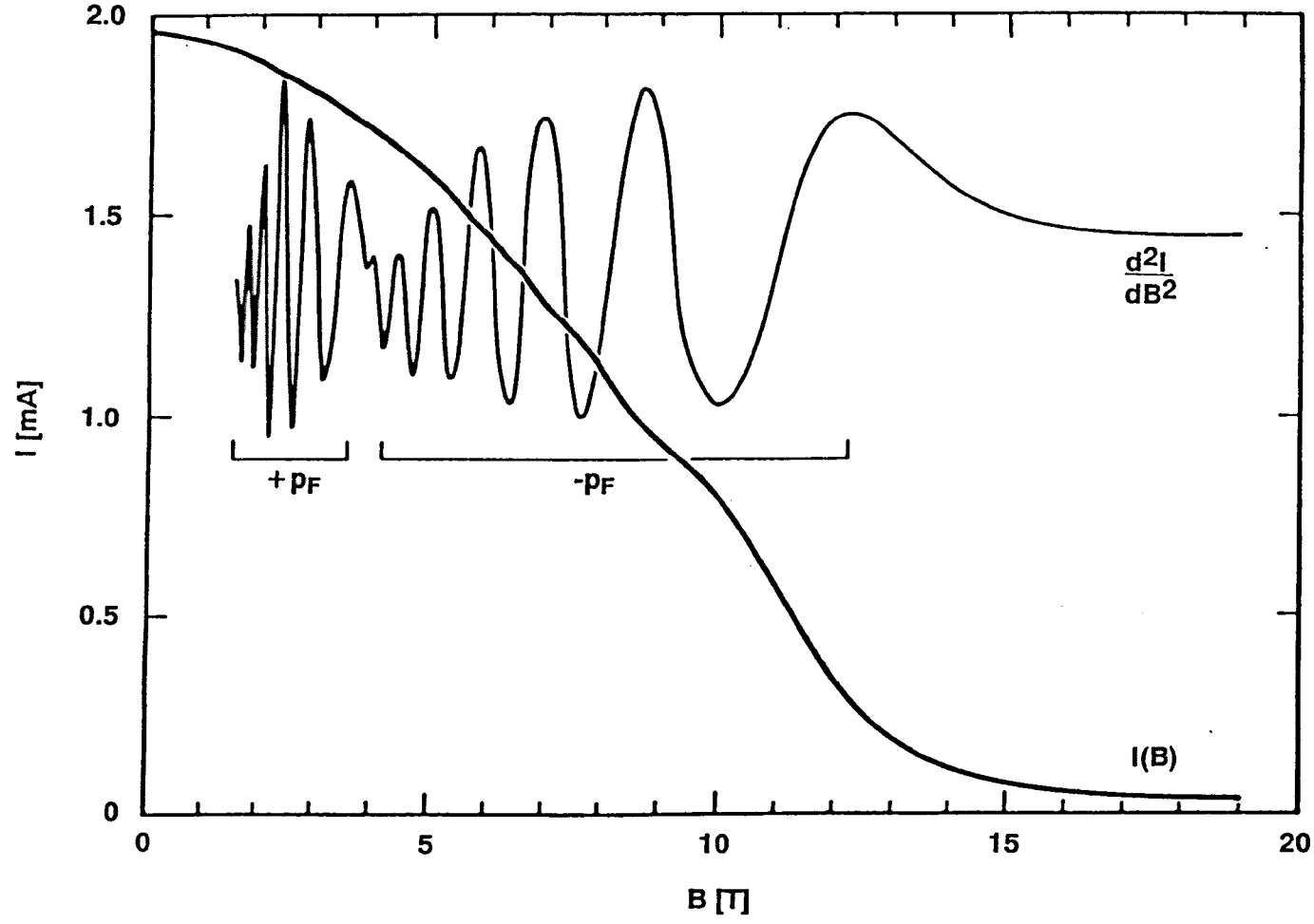

Figure 5.1 I(B) and d^2I/dB^2 characteristics of the (InGa)As/InP single-barrier structures measured for V = 100 mV at T = 4.2 K. The two distinct series of oscillations revealed in d^2I/dB^2 are distinguished by horizontal brackets. (After Snell et al., 1987).

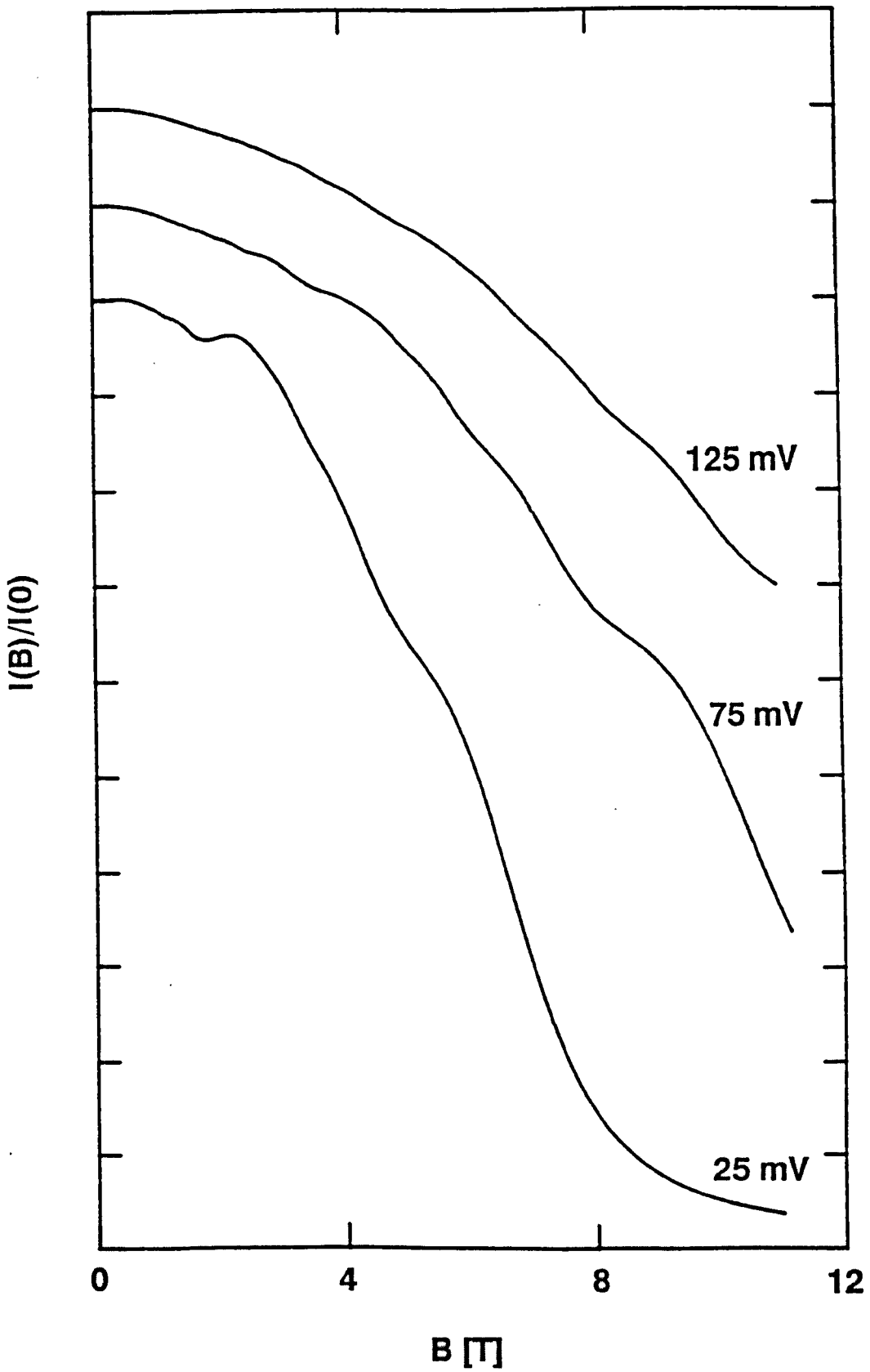

Figure 5.2 Normalised I(B) characteristics of the (InGa)As/InP samples measured at T = 4.2 K for a variety of forward-bias voltages. The y-axis intervals correspond to a change of 10% in I(B)/I(0). (After Snell, 1987a).

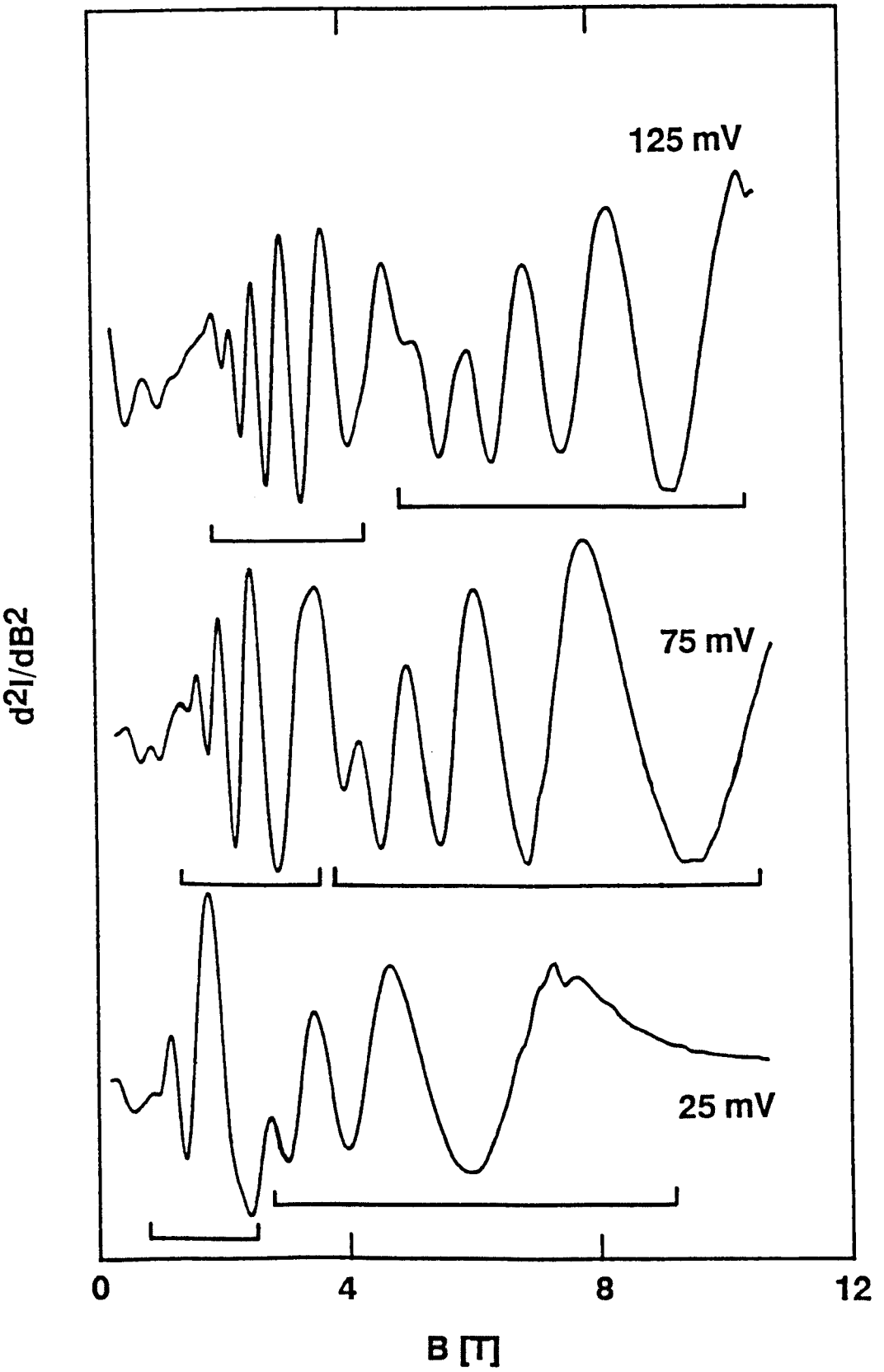

Figure 5.3 d^2I/dB^2 characteristics of the (InGa)As/InP samples measured at T = 4.2 K for a variety of forward-bias voltages. The $+p_F$ ($-p_F$) series of oscillations revealed at low (high) fields are distinguished by horizontal brackets. (After Snell, 1987a).

Both series of oscillations are periodic in 1/B (Snell, 1987a) with maxima occurring at the resonant field values $B_n^{\pm}$ given by

$$\left(\frac{1}{B_n^{\pm}}\right) = \frac{(n + \phi)}{B_{F\pm}(V)} \qquad ; n = 0, 1, .. \tag{5.1}$$

where ϕ is a field-independent phase factor and $B_{F\pm}(V)$ are voltage-dependent 'fundamental' fields which equal the reciprocal of the periodicities in 1/B of the $\pm p_F$ series. Figure 5.4 shows that both fundamental fields increase almost linearly with voltage. Since the oscillatory structure is evidently voltage-dependent, it cannot originate from the standard Shubnikov-de Haas effect in the n^+ layer (see, for example, Ridley, 1988), and is more likely to be associated with the strongly voltage-dependent tunnelling process.

A successful theory of magnetotunnelling in these single-barrier structures should explain the physical origin of the two series of oscillatory structure, give reasonable quantitative predictions for the voltage-dependence of the fundamental fields and, in addition, account for qualitative features such as the clear separation of the $\pm p_F$ series and the increase in oscillatory amplitudes generally observed with increasing magnetic field.

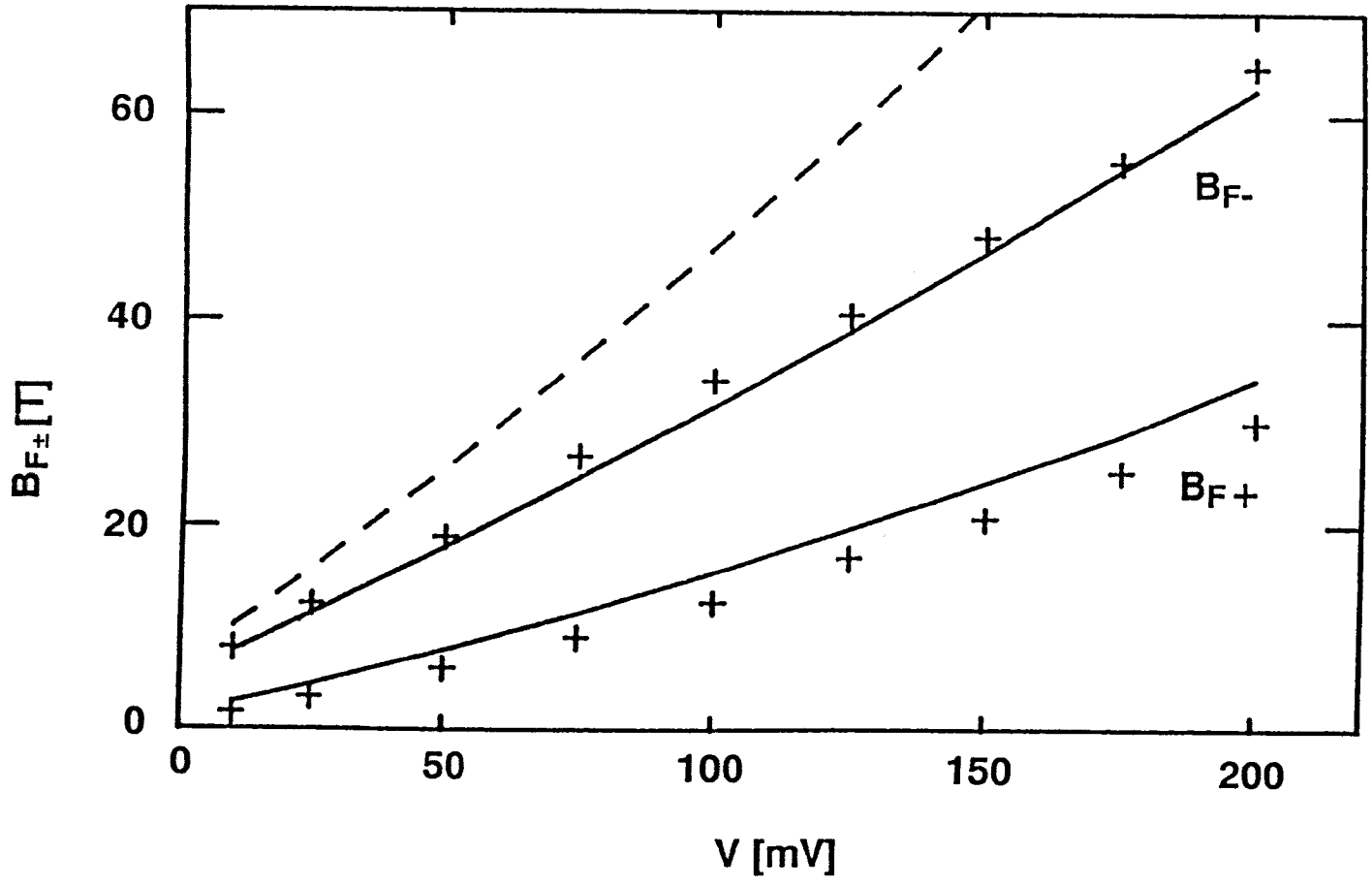

Figure 5.4 Plots of the fundamental magnetic fields $B_F^{\pm}$ as a function of applied forward-bias voltage, for the (InGa)As/InP single-barrier structures. The observed values are indicated by crosses. The solid lines show the theoretical values for tunnelling into interfacial Landau states, and the broken line shows the prediction for tunnelling into bulk Landau states.

5.4 A Transfer-Hamiltonian Model for the Tunnel Current

Under foward-bias conditions and in a transverse magnetic field, current flow through the device can be described within the transfer-Hamiltonian formalism in terms of transitions from the perturbed 2DEG states in the n^- emitter, into bulk or interfacial Landau states in the n^+ collector (see Chapter 4). These Landau states are magnetically confined perpendicular to the barrier interface and therefore carry no nett current in this direction. Current continuity is maintained in the n^+ contact by scattering processes which enable electrons to diffuse between localised Landau states with different orbit centre positions. At liquid helium temperatures, the dominant scattering mechanism of hot electrons in bulk n^+ (InGa)As is LO polar phonon emission(see, for example, Ridley 1988) which occurs at a rate of approximately 10^{13} s^{-1} (Lobentanzer et al., 1987). This scattering rate is much faster than the tunnelling transition rate-10^7 s^{-1} over the entire range of voltages studied (25 - 125 mV). Consequently, electrons injected into the n^+ collector cool rapidly to the bulk Fermi level E_{FR}, which is only weakly field-dependent (Brey et al., 1988).

For bias voltages V > 10 mV, $E'_{bo} > E_{FR}$ so that, as can be seen from Figure 2.1, the occupancies of states in the 2DEG and n^+ contact in the energy range $E'_{bo} \leq E \leq E'_{bo} + E_F$ can be taken as 1 and 0 respectively at $T \cong 4$ K.

The current is limited primarily by the tunnelling transition

rate and is therefore insensitive to changes in the LO phonon emission rate caused by the magnetic field. Consequently, transverse Shubnikov-de Haas oscillations (see, for example, Ridley, 1988) are unlikely to be seen, and the oscillatory structure observed in d^2I/dB^2 almost certainly originates from the effect of the magnetic field on the tunnelling process itself.

It was shown in Section 3.5 that tunnelling transitions in the presence of a transverse magnetic field, must conserve both the total energy and the transverse wavevector $\underline{k}_{\|}$. The current ΔI_n (k_y, k_z) due to wavevector-conserving transitions from the perturbed 2DEG state with $\underline{k}_{\|}$ = (k_y, k_z) into the n^{th} interfacial or bulk Landau state is

$$\Delta I_n (k_y, k_z) = e\, W_n (k_y, k_z) \tag{5.2}$$

where W_n (k_y, k_z) is the transition rate (3.25) which depends only on the x-dependent factors of the initial and final state wavefunctions.

Since these wavefunctions satisfy 1D Schrödinger equations of the form (4.22) which are independent of k_z, the transition matrix element (3.37) is also independent of k_z and is written $M_n(k_y)$. Combining equations (3.25) and (5.2) gives

$$\Delta I_n(k_y, k_z) = \frac{2\pi e}{\hbar} |M_n(k_y)|^2\, \delta(\Delta E_n(k_y)) \tag{5.3}$$

where

$$\Delta E_n(k_y) = E_L(k_y, k_z) - E_R(k_y, k_z)$$

$$= E'_{bo} + \frac{3}{2} m^*_L \omega_c^2 a_o^2 + \frac{\hbar^2(k_y - k_o)^2}{2m^*_L} - E_n(k_y) \quad ,$$

is the difference between the LH (2DEG) and RH (interfacial Landau) energy levels given by equations (4.14) and (4.22).

At fixed voltage and field, the current $I_n(V, B)$ resulting from all transitions into the n^{th} Landau state is obtained by integrating $\Delta I_n(k_y, k_z)$ over the range of occupied 2DEG states shown in Figure 4.1, using the periodic boundary conditions (1.11) to determine the density of states in $\underline{k}$-space. Provided the bias voltage is sufficiently large that the electrons tunnel into empty states in the n^+ layer ($V \geq 10$ mV), this current is

$$I_n(V, B) = \frac{L_y L_z e}{\pi\hbar} \int_{k_y'=-k_F}^{k_F} \int_{k_z=-k_z^R}^{k_z^R} |M_n(k_y)|^2 \, \delta(\Delta E_n) dk_z \, dk_y' \qquad (5.4)$$

where $k_y' = k_y - k_o$,

$$k_z^R = (k_F^2 - k_y'^2)^{\frac{1}{2}} \quad ,$$

and $L_y L_z$ is the cross-sectional area of the sample.

The expression for ΔE_n given in equation (5.3) is independent of k_z, so that the integral over k_z in equation (5.4) is easily evaluated giving

$$I_n(V, B) = \frac{2eL_yL_z}{\pi\hbar} \int_{k_y'=-k_F}^{+k_F} (k_F^2 - k_y'^2)^{\frac{1}{2}} |M_n(k_y)|^2 \delta(\Delta E_n)\, dk_y' \tag{5.5}$$

which, changing the variable of integration from k_y' to ΔE_n becomes

$$I_n(V, B) = \frac{2eL_yL_z}{\pi\hbar} \int \frac{(k_F^2 - k_y'^2)^{\frac{1}{2}} |M_n(k_y)|^2 \delta(\Delta E_n)\, d\Delta E_n}{\left(\frac{\hbar^2 k_y'}{m^*_L} - \frac{dE_n(k_y)}{dk_y}\right)} \tag{5.6}$$

The integral in equation (5.6) is evaluated over the range of ΔE_n corresponding to $|k_y'| \leq k_F$ and gives

$$I_n(V,B) = \frac{2eL_yL_z}{\pi\hbar} \sum_i \left\{ \frac{(k_F^2 - k_y'^2)^{\frac{1}{2}} |M_n(k_y)|^2}{\left| \frac{\hbar^2 k_y'}{m^*_L} - \frac{dE_n(k_y)}{dk_y} \right|} \right\}_{k_y' = k_{yi}'(n)} \tag{5.7}$$

where $\{k_{yi}'(n) = k_{yi}(n) - k_o;\ i = 1, 2, \ldots\}$ are the solutions of the energy conservation condition

$$\Delta E_n(k_y') = 0 \quad , \tag{5.8}$$

within the range $-k_F \leq k_{yi}'(n) \leq +k_F$.

This condition can be interpreted graphically by looking for intersections in the E - k_y plane between the n^{th} Landau state dispersion curve and the parabola

$$E(k_y) = \hbar^2(k_y - k_o)^2/2m^*_L + E'_{bo} \quad ; \; |k_y - k_o| \leq k_F \quad , \qquad (5.9)$$

which gives the energy, associated with motion perpendicular to the magnetic field, of the occupied 2DEG states.

As shown in Figure 5.5, each Landau state dispersion curve makes at most one intersection with the 2DEG parabola, so that the energy conservation equation (5.8) has a unique solution, $k_y'(n)$, in the specified range.

Thus, the series expansion (5.7) contains only one term and may be written

$$I_n(V,B) = \frac{eL_yL_z}{\pi^2} \left\{ \frac{(k_F^2 - k_y'^2)^{\frac{1}{2}}(2\pi|M_n(k_y)|^2/\hbar}{\left|\frac{\hbar^2 k_y'}{m^*_L} - \frac{dE_n}{dk_y}\right|} \right\}_{k_y'=k_y'(n)} \qquad (5.10)$$

Each intercept in Figure 5.5 corresponds to a conduction channel, comprising a set of 2DEG electrons with $|k_z| \leq (k_F^2 - k_y'^2(n))^{\frac{1}{2}}$, which contributes to the tunnel current. The total current flowing into all RH Landau states is

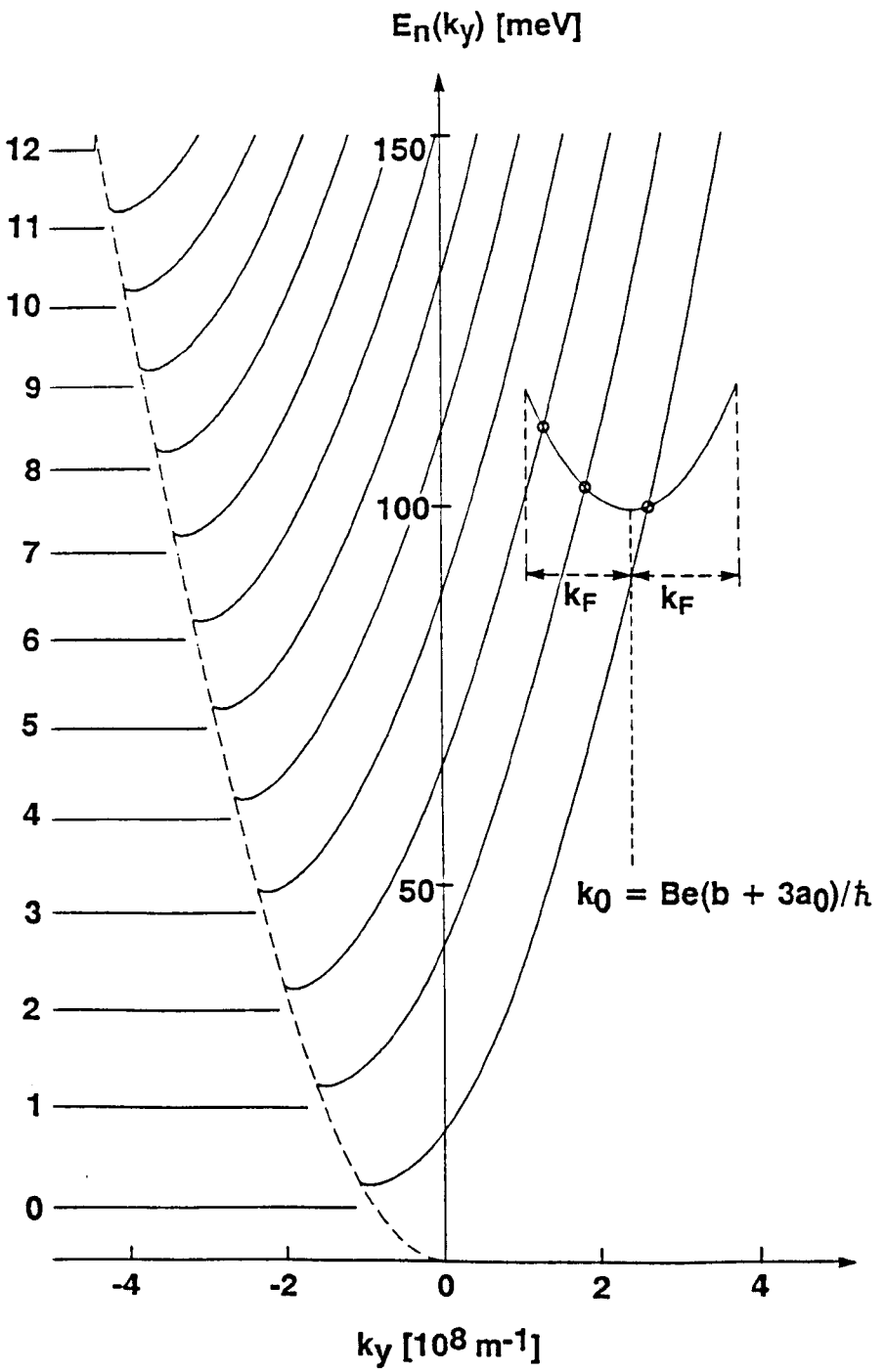

Figure 5.5 Bulk and interfacial Landau state dispersion curves $E_n(k_y)$ n = 0, 1, ... 12 of the (InGa)As/InP single-barrier structures calculated for V = 100 mV and B = 5 T, taking the nonparabolicity factor of (InGa)As to be $\alpha = 1.3\ eV^{-1}$, and assuming a finite conduction band offset $\Delta E_c = 230$ meV. The broken curve shows the magnetic potential energy at the RH barrier interface as a function of k_y and marks the transition from bulk to interfacial Landau states. The parabola centred at k_o shows the range of occupied 2DEG states calculated for the same voltage and field. Intercepts between the 2DEG and interfacial Landau state dispersion curves are marked by open circles and correspond to groups of 2DEG electrons which contribute to the tunnel current.

$$I(V,B) = \sum_{n:|k_y'(n) \leq k_F|} I_n(V,B) \qquad (5.11)$$

where the summation is over all open conduction channels. D'yakonov and Raikh (1985) derived a similar expression for the transverse magneto-current flowing through a single-barrier structure with heavily n-doped emitter and collector contacts.

It should be noted that all intersection points shown in Figure 5.5 correspond to interfacial Landau states. In fact, tunnelling into bulk Landau levels cannot occur in the (InGa)As/InP structures, owing to the low Fermi momentum $p_F = \hbar k_F$ of the 2DEG (see Section 5.7).

5.5 The Origin of the $\pm p_F$ Series of Oscillatory Structure Observed in d^2I/dB^2

Figure 5.5 shows the intersection points $\{k_y(n)\}$ for V = 100 mV and B = 5 T. Changing the magnetic field at constant bias alters both the 2DEG and Landau state dispersion curves, thereby shifting the intersection points. In this section, the $\pm p_F$ series of oscillatory structure observed in d^2I/dB^2 are shown to originate from the gain or loss of intercepts from the extremities of the 2DEG parabola.

The origin $k_o = Be(b + 3a_o)/\hbar$ of the parabolic 2DEG dispersion relation (5.9) increases with field so that, as can be seen from Figure 5.5, the range of occupied $\underline{k}$-states shifts to higher k_y values. Neglecting the small diamagnetic shift (4.20) in the bound state energy E'_{bo}, the range of occupied 2DEG energy levels $E'_{bo} \leq E \leq E'_{bo} + E_F$ shown in Figure 2.1 is, however, unchanged by the magnetic field.

Increasing the magnetic field also reduces the distance between the classical turning points of each interfacial Landau state. This increases the confinement of the associated wavefunctions, thereby raising the energy levels $E_n(k_y)$. It can be seen from Figure 5.5 that the combined effect of changing the 2DEG and Landau state dispersion curves causes the $+k_F$ extremity of the 2DEG parabola to make successive intersections with lower-index dispersion curves, as the magnetic field increases, so that new conduction channels are opened whenever $k_y'(n) = +k_F$. When this resonance condition is satisfied, 2DEG electrons with transverse momentum $p_y' = m_L^*\langle v_y \rangle = +p_F = +\hbar k_F$ tunnel into the n^{th} interfacial Landau state. As the field is further increased, the intercept moves away from the $+k_F$ extremity of the 2DEG parabola ($k_y'(n)$ decreases) and is eventually lost from the $-k_F$ extremity, resulting in the closure of the n^{th} conduction channel when $k_y'(n) = -k_F$. Thus, tunnelling into each interfacial Landau state only occurs over the field range $B_n^+ \leq B \leq B_n^-$, where $B_n^{\pm}$ are the resonant fields for which $k_y'(n) = \pm k_F$. For field values outside this range, the requirements of energy and transverse wavevector conservation cannot be satisfied for any transitions from the 2DEG into the n^{th} interfacial Landau state.

This successive opening and closure of tunnelling channels is intuitively expected to give rise to oscillatory structure in the magneto-current and derivatives, whenever intercepts are gained or lost from the extremities of the 2DEG parabola. The expression (A.2) for dI/dB given in Appendix 1, actually predicts over-dramatic oscillations since $dI/dB \rightarrow \pm\infty$ as $k_y'(n) \rightarrow \pm k_F$. Such divergent oscillations are not, of course, observed and arise from the neglect of energy level broadening in the transfer-Hamiltonian formalism. Nevertheless, the model clearly predicts two distinct series of oscillations in dI/dB; maxima associated with 2DEG electrons with transverse momentum $p_y' = +p_F$ tunnelling into interfacial Landau states; and minima associated with transitions made by 2DEG electrons with equal and opposite momentum $p_y' = -p_F$.

5.6 Calculation of the Periodicities of the $\pm p_F$ Series

Equation (A.2) of Appendix 1 predicts that extrema in dI/dB will be observed at the resonant field values $B_n^{\pm}$ for which the n^{th} interfacial Landau state dispersion curve passes through either extremity of the 2DEG parabola, that is

$$k_y(n) = k_o \pm k_F \quad , \tag{5.12}$$

and

$$E_n(k_o \pm k_F) = eV + E_{FR} \quad . \tag{5.13}$$

Snell et al. (1987) and Chan et al. (1988) derived approximate analytical expressions for $B_n^{\pm}$ by substituting equations (5.12) and (5.13) together with the linear approximation (4.42) for $f(u_o)$, in equation (4.43). In the limit of an infinite potential barrier at x = 0, this gives,

$$\frac{1}{B_n^{\pm}} = \frac{e\hbar}{\overline{m^*_L}\,(eV + E_{FR})(1 \mp u_F)}\left(2(n + \tfrac{3}{4}) + \frac{(b + 3a_o)(\tfrac{1}{2}\overline{m^*_L}(eV + E_{FR}))^{\frac{1}{2}}}{\hbar}\right), \tag{5.14}$$

where $$u_F = \frac{\hbar k_F}{[2\overline{m^*_L}(eV + E_{FR})]^{\frac{1}{2}}},$$

and $$\overline{m^*_L} = m^*_L(1 + \alpha(eV + E_{FR}))$$

is the electronic effective mass in the n^+ collector appropriate to the injection energy $eV + E_{FR}$.

Using the constant capacitance approximation (2.28), u_F may be written

$$u_F = \frac{\hbar}{e}\left[\frac{\pi C}{\overline{m^*_L}}\right]^{\frac{1}{2}} \tag{5.15}$$

and, apart from the weak voltage-dependence of the effective mass, depends only on the sample geometry and material parameters. Consequently, the RHS of equation (5.14) is independent of magnetic field so that the extrema in dI/dB are predicted to occur periodically in 1/B with the distinct periodicities

$$\Delta\left(\frac{1}{B_n}\right)_{\pm} = \frac{2e\hbar}{\overline{m^*_L}(eV + E_{FR})(1 \mp u_F)} = \frac{1}{B_{F\pm}(V)} \quad . \qquad (5.16)$$

Since u_F and $\overline{m^*_L}$ are only weakly voltage-dependent, the corresponding fundamental fields

$$B_{F\pm}(V) = \frac{\overline{m^*_L}(1 \mp u_F)(eV + E_{FR})}{2e\hbar} \qquad (5.17)$$

defined in equation (5.1) are expected to increase almost linearly with voltage, at distinct rates which depend only on fundamental constants and on the device geometry and material parameters.

Theoretical values of $B_{F\pm}(V)$ calculated from equation (5.17) are shown in Figure 5.4. The best fit to the data is obtained using $\alpha \simeq 1.3\ eV^{-1}$, which is lower than the value 5 eV^{-1} measured optically by Sarkar et al. (1985), but is reasonable considering the large range of injection energies (40 - 220 meV) investigated (Heiblum et al., 1987).

The theoretical fit to the data is remarkably good considering some of the approximations made in the model. The linearisation (4.45) of $f(u_0)$ made by Chan et al. (1988) is probably one of the most important approximations.

5.7 Tunnelling into Bulk Landau Levels Does Not Occur

The resonance conditions (5.12) and (5.13) can, in principle, also be satisfied whenever 2DEG electrons with transverse momentum $p_y' = \pm p_F$ tunnel into bulk Landau states, thereby giving rise to a third series of oscillations in dI/dB at the resonant field values B_n given by

$$\frac{1}{B_n} = \frac{(n + \frac{1}{2})\hbar e}{\overline{m^*_L}(eV + E_{FR})} \qquad n = 0,1,2 \ldots \tag{5.18}$$

The voltage-dependence of the associated fundamental field

$$B_F(V) = \frac{\overline{m^*_L}(eV + E_{FR})}{\hbar e} \tag{5.19}$$

is shown by the broken curve in Figure 5.4 for $\alpha = 1.3\ eV^{-1}$. The theoretical values of $B_F(V)$ cannot be reconciled with the data for any reasonable choice of α (Snell et al., 1987).

To further support the model of tunnelling into interfacial Landau levels, Sheard et al. (1988) used the following argument to prove that 2DEG electrons with $p_y' = \pm p_F$ ($k_y' = \pm k_F$) cannot make transitions into bulk Landau levels, and therefore do not give rise to oscillatory structure.

From Figure 4.5, 2DEG electrons with the transverse wave-vector component k_y only tunnel into bulk Landau states in the n^+ collector, if the classical orbit centre position exceeds the orbital radius, that is

$$X_{k_y} = -\frac{\hbar k_y}{Be} > R_n(k_y) = (2\overline{m^*_L}\, E_n(k_y))^{\frac{1}{2}}/Be \qquad (5.20)$$

For electrons with $k_y = (k_o + k_F)$ inequality (5.20) is never satisfied, since the corresponding orbit centre $X_{k_y} < 0$.

For electrons at the Fermi energy of the 2DEG with $k_y = (k_o - k_F)$ and $E_n(k_y) = eV + E_{FR}$, inequality (5.20) becomes

$$X_{-k_F} = \frac{\hbar}{B_n e}\left(\frac{B_n e}{\hbar}(b + 3a_o) - k_F\right) \geq \frac{(2\overline{m^*_L}\,(eV + E_{FR}))^{\frac{1}{2}}}{B_n e} \qquad (5.21)$$

which may be written

$$u_F \geq u_1 + 1 \quad , \qquad (5.22)$$

where

$$u_1 = B_n e(b + 3a_0)/(2\overline{m^*_L}(eV + E_{FR}))^{\frac{1}{2}} \quad ,$$

and u_F is given within the constant capacitance approximation by equation (5.15). For the (InGa)As samples, $C \simeq 4250\ \mu F\ m^{-2}$ (Snell et al., 1987), so that the highest possible value of u_F, corresponding to $\overline{m^*_L} = m^*_L$, is approximately 0.37. Since u_1 is always positive, inequality (5.22) cannot be satisfied and tunnelling into bulk Landau states does not occur. By contrast, in a metal-oxide semiconductor structure, the large and voltage-independent Fermi momentum in the metal allows the observation of tunnelling into bulk Landau levels in the semiconductor (Tsui, 1975).

5.8 Calculation and Interpretation of the 2DEG to Interfacial Landau State Transition Matrix Element

In order to evaluate the tunnel current (5.11) and, in particular, to give a physical explanation for the field-dependence of the oscillatory amplitudes observed in d^2I/dB^2, the squared transition matrix elements $|M_n(k_y)|^2$ must first be determined. In this section, an expression for $|M_n(k_y)|^2$ is derived from equation (3.37) using the x-dependent factors of the 2DEG and interfacial Landau state wavefunctions.

To obtain non-vanishing matrix elements, the 2DEG states are represented by a modified Fang-Howard wavefunction

$$\psi'_{FH}(x) \begin{cases} -(2a_0^3)^{-\frac{1}{2}} (x + b - \delta)\, e^{\frac{(x+b-\delta)}{2a_0}} & ; x \leq -b \\ \left(\frac{\mu_{n1}(-b_+)}{2a_0^3 \mu_{n1}(x)}\right)^{\frac{1}{2}} \delta\, e^{-\frac{\delta}{2a_0}}\, e^{-\int_{-b}^{x} \mu_{n1}(\bar{x})\, d\bar{x}} & ; x \geq -b \end{cases} \quad (5.23)$$

where the penetration parameter

$$\delta = \left(\frac{1}{2a_0} + \frac{m^*_L\, \mu_{n1}(-b_+)}{m^*_B}\right)^{-1} ,$$

and $\mu_{n1}(x)$ is the barrier decay function defined in equation (4.26).

This wavefunction has a finite amplitude throughout the barrier region and is similar to that of Bastard (1983), except that for $x \geq -b$, the uniformly decaying exponential function is replaced by a WKB solution which takes into account the electrostatic potential variations in the barrier region. The modified wavefunction (5.23) is normalised by neglecting the small fraction which penetrates into the barrier region. Over the ranges of bias and field studied, the penetration length $\mu_{n1}^{-1}(-b_+)$ over which the

amplitude of $\psi'_{FH}(x)$ in the barrier falls by a factor of approximately e^{-1} is much less than $2a_o$. Consequently, the decay parameter $\delta \equiv m_B^*/(m_L^* \mu_{n1}(-b_+))$. Within this approximation, and using the WKB validity condition (4.27) to justify the neglect of terms involving $d\mu_{n1}(x)/dx$, the derivative of $\psi'_{FH}(x)$ is

$$\frac{d\psi'_{FH}(x)}{dx} = \begin{cases} -(2a_o^3)^{-\frac{1}{2}} \left(1 + \frac{(x+b-\delta)}{2a_o}\right) e^{\frac{(x+b-\delta)}{2a_o}} & ; x \leq -b \\ -\frac{m^*_B}{m^*_L} \left(\frac{\mu_{n1}(x)}{2a_o^3 \mu_{n1}(-b_+)}\right)^{\frac{1}{2}} e^{-\int_{-b}^{x} \mu_{n1}(\bar{x})\, d\bar{x}} = -\mu_{n1}(x)\, \psi'_{FH}(x) & ; x \geq -b \end{cases} \tag{5.24}$$

where terms of order δ^2 and above are omitted.

To determine the transition matrix element (3.37), equations (5.23) and (5.24) are evaluated at the RH barrier interface giving

$$\psi'_{FH}(0_-) = \frac{m^*_B}{m^*_L} \left(2a_o^3\, \mu_{n1}(-b_+)\, \mu_{n1}(0_-)\right)^{-\frac{1}{2}} e^{-\int_{-b}^{0} \mu_{n1}(x)\, dx} \tag{5.25}$$

and,

$$\frac{d\psi'_{FH}(0_-)}{dx} = -\mu_{n1}(0_-)\,\psi'_{FH}(0_-) \quad . \tag{5.26}$$

To obtain similar limiting expressions for the interfacial state wavefunctions $\psi_n(x)$ and derivatives, these wavefunctions must be normalised. Neglecting penetration into the classically forbidden regions, normalisation of the WKB interfacial state wavefunctions (4.32) requires

$$\int_0^{w_n} |\psi_n(x)|^2\,dx = \frac{6|G_n^-|^2}{\pi}\int_0^{w_n} \alpha_n^{-1}(x)\cos^2\left(T(x) - \frac{\pi}{4}\right)dx = 1 \tag{5.27}$$

where $T(x) = \int_x^{w_n} \alpha_n(x)\,dx$.

Provided that the WKB validity condition (4.28) is satisfied, $\alpha_n(x)$ varies slowly over the distance $\simeq \pi/\alpha_n(x)$ required for the phase of the squared cosine term in equation (5.27) to change by π. Over this distance, the average value of the squared cosine term is approximately 1/2 so that equation (5.27) becomes

$$\left(\frac{3}{\pi}\right)\frac{\hbar|G_n^-|^2}{\overline{m^*_L}}\int_0^{w_n}\frac{dx}{v_n(x)} = 1 \tag{5.28}$$

where $v_n(x) = \hbar\alpha_n(x)/\overline{m^*_L}$ is the semiclassical local x-component of velocity.

The integral in equation (5.28) gives the time taken for the electron to move between the turning points of its classical skipping trajectory, that is

$$\int_0^{w_n} \frac{dx}{v_n(x)} = \frac{1}{2F_n} \tag{5.29}$$

where F_n is the classical skipping frequency (4.55) of electrons along the RH barrier interface. Combining equations (5.28) and (5.29), the required normalisation coefficient is

$$G_n^- = \left(\frac{2\pi \overline{m^*_L} F_n}{3\hbar}\right)^{\frac{1}{2}} \quad . \tag{5.30}$$

For low-index interfacial Landau states, the assumption that $\alpha_n(x)$ varies slowly over distances $\simeq \pi/\alpha_n(x)$ is invalid so that both the form (4.32) and the normalisation coefficient (5.30) of the associated WKB wavefunctions are of limited accuracy. The WKB approximation is thus not expected to give precise quantitative information about these low-index states.

Neglecting terms involving $d\alpha_n(x)/dx$, the derivative of $\psi_n(x)$ in the classically allowed region is

$$\frac{d\psi_n(x)}{dx} = 2\left(\frac{\overline{m^*_L} F_n}{\hbar}\right)^{\frac{1}{2}} \alpha_n^{\frac{1}{2}}(x) \sin\left(T(x) - \frac{\pi}{4}\right) \tag{5.31}$$

In the limit $x \to 0_+$, equations (4.32) and (5.31) become

$$\psi_n(0_+) = 2 \left(\frac{\overline{m^*_L}\, F_n}{\hbar}\right)^{\frac{1}{2}} \alpha_n^{-\frac{1}{2}}(0_+) \cos\left(\int_0^{w_n} \alpha_n(x)\, dx - \frac{\pi}{4}\right) \qquad (5.32)$$

and

$$\frac{d\psi_n}{dx}(0_+) = 2 \left(\frac{\overline{m^*_L}\, F_n}{\hbar}\right)^{\frac{1}{2}} \alpha_n^{\frac{1}{2}}(0_+) \sin\left(\int_0^{w_n} \alpha_n(x)\, dx - \frac{\pi}{4}\right) \qquad (5.33)$$

If follows from the energy quantisation condition (4.36) that

$$\cos\left(\int_0^{w_n} \alpha_n(x)\, dx - \frac{\pi}{4}\right) = \frac{(-1)^n\, \alpha_n(0_+)\, m^*_B}{\left(\alpha_n^2(0_+)\, m^{*2}_B + \mu_{n1}^2(0_-)\, \overline{m^*_L}^2\right)^{\frac{1}{2}}} \,, \qquad (5.34)$$

and

$$\sin\left(\int_0^{w_n} \alpha_n(x)\, dx - \frac{\pi}{4}\right) = \frac{(-1)^n\, \mu_{n1}(0_-)\, \overline{m^*_L}}{\left(\alpha_n^2(0_+)\, m^{*2}_B + \mu_{n1}^2(0_-)\, \overline{m^*_L}^2\right)^{\frac{1}{2}}} \,. \qquad (5.35)$$

Using these expressions in equations (5.32) and (5.33), and imposing the matching conditions (1.39) and (1.40) at the RH barrier interface, gives

$$\psi_n(0_-) = \psi_n(0_+) = 2 \left(\frac{\overline{m^*_L}\, F_n}{\hbar}\right)^{\frac{1}{2}} \frac{(-1)^n\, \alpha_n^{\frac{1}{2}}(0_+)\, m^*_B}{\left(\alpha_n^2(0_+)\, m^{*2}_B + \mu_{n1}^2(0_-)\, \overline{m^*_L}^2\right)^{\frac{1}{2}}} \,, \qquad (5.36)$$

and

$$\frac{d\psi_n(0_-)}{dx} = \frac{m^*_B}{m^*_L}\frac{d\psi_n(0_+)}{dx} = 2\left(\frac{m^*_L F_n}{\hbar}\right)^{\frac{1}{2}} \frac{(-1)^n \alpha_n^{\frac{1}{2}}(0_+)\,\mu_{n1}(0_-)\,m^*_B}{\left(\alpha_n^2(0_+)\,m^{*2}_B + \mu_{n1}^2(0_-)\,m^{*2}_L\right)^{\frac{1}{2}}}$$

$$= \mu_{n1}(0_-)\,\psi_n(0_-) \quad . \tag{5.37}$$

Substituting equations (5.25), (5.26), (5.36) and (5.37) into equation (3.37) it follows that

$$|M_n(k_y)|^2 = \frac{\hbar^4}{m^{*2}_B}\,\mu_{n1}^2(0_-)\,|\psi'_{FH}(0_-)|^2\,|\psi_n(0_-)|^2$$

$$= \hbar^2\left(\frac{\hbar\,k(-b_-)}{2(5a_0)m^*_L}\right)(F_n)\left(\frac{16m^{*2}_B\,\alpha_n(0_+)\,\mu_{n1}(0_-)\,k(-b_-)\,e^{-2\int_{-b}^{0}\mu_{n1}(x)dx}}{m^*_L\,m^*_L\,\mu_{n1}(-b_+)\left[(\alpha_n(0_+)m^*_B/m^*_L)^2 + \mu_{n1}^2(0_-)\right]}\right) ,$$

(5.38)

where, from equation (2.18),

$$\frac{\hbar\,k(-b_-)}{m^*_L} = \frac{\sqrt{5}\,\hbar}{2m^*_L\,a_0} = (2E_{bo}/m^*_L)^{\frac{1}{2}}$$

is the semiclassical longitudinal ($\parallel \underline{x}$) velocity component of the 2DEG electrons at the LH barrier interface, in zero magnetic field.

Since the motion of 2DEG electrons normal to the barrier interface is only slightly perturbed by the transverse magnetic field (see Section 4.2.2), this incident velocity is approximately equal to $\hbar k(-b_-)/m^*_L$ for all fields.

Each term in equation (5.38) can be interpreted semi-classically. The first bracketed term on the RHS is the frequency of the collisions which an electron moving with constant longitudinal kinetic energy E_{bo}, makes classically with each wall of a rectangular confining potential well of width $5a_o$, which is almost twice the mean 2DEG stand-off distance $3a_o$. Consequently, this term is approximately equal to the classical collision frequency between a 2DEG electron and the LH barrier interface.

Similarly, the second bracketed term in equation (5.38) is the classical skipping frequency (4.55) of an electron with transverse wavevector component k_y, which occupies the n^{th} interfacial Landau state.

Suppose that the effective potential energy barrier (including the magnetic term) is part of a system containing an n^+ emitter contact in which electrons with incident kinetic energy $E_{bo} = \hbar^2k^2(-b_-)/2m^*_L$ occupy travelling wave states. Then, the third term on the RHS of equation (5.38) is the WKB barrier transmission coefficient (1.53) when free electrons incident from the left with kinetic energy $\hbar^2k^2(-b_-)/2m^*_L \ll \hbar^2\mu^2_{n1}(-b_+)/2m^*_B$, are partially transmitted into travelling wave states in the n^+ collector with emergent longitudinal kinetic energy $\hbar^2\alpha_n^2(0+)/2\overline{m^*_L}$.

The squared matrix element $|M_n(k_y)|^2$ is thus formally identical to that derived in Section 3.7 for transitions between two weakly-coupled rectangular potential wells. In contrast to this earlier example however, the collision frequency terms in equation (5.38) contain no end corrections because the 2DEG and interfacial Landau state wavefunctions (5.23) and (4.32) are normalised by neglecting penetration into the classically forbidden regions.

In Section 5.12, this semiclassical interpretation of $|M_n(k_y)|^2$ is used to explain the field-dependence of the oscillatory amplitudes observed in d^2I/dB^2, by considering the effect of the field on both the barrier transmission coefficient and on the classical skipping frequencies of the interfacial electrons. The first (bracketed) term on the RHS of equation (5.38), identified as the classical collision frequency of the 2DEG electrons, is field-independent and thus has no effect on the envelope of the oscillatory amplitudes.

5.9 Simulation of the Tunnel Current I(B)

The first step in evaluating the tunnel current (5.11) for given voltage and field is to calculate the set of wavevector components $\{k_y'(n): |k_y'(n)| \leq k_F\}$ (see Figure 5.5) which satisfy the energy conservation requirement (5.8).

These wavevector components are obtained by numerical solution of equation (4.43) in which $E_n(k_y) = \hbar^2(k_y - k_o)^2/2m^*_L + E'_{bo}$, using the full expression (4.42) for $f(u_o)$. The effects of the finite barrier height and of nonparabolicity ($\alpha = 1.3\ eV^{-1}$) in the n^+ contact are also taken into account.

Once the allowed transverse wavevector components are known, the corresponding squared matrix elements (5.38) are calculated. The gradients dE_n/dk_y of the interfacial Landau state dispersion curves, are evaluated at each intersection point by numerical solution of the implicit equation for dE_n/dk_y obtained by differentiating equation (4.43) with respect to k_y. The current contribution $I_n(V, B)$ arising from tunnelling transitions into the n^{th} interfacial Landau state is then calculated by using these values in equation (5.10). The total tunnel current is the sum of these contributions.

Normalised current curves I(B)/I(0) calculated for a range of forward-bias voltages are shown in Figures 5.6, 5.7 and 5.8, together with the current contributions $I_n(B)$ n = 0,1, ... 9. Higher-index contributions are omitted for clarity.

The shapes of the calculated I(B) characteristics are in reasonable agreement with the corresponding experimental curves shown in Figures 5.1 and 5.2.

In particular, for V = 25 mV, the closure of the n = 4, 3, 2, 1 and 0 tunnelling channels imposes weak oscillatory 'shoulders' on

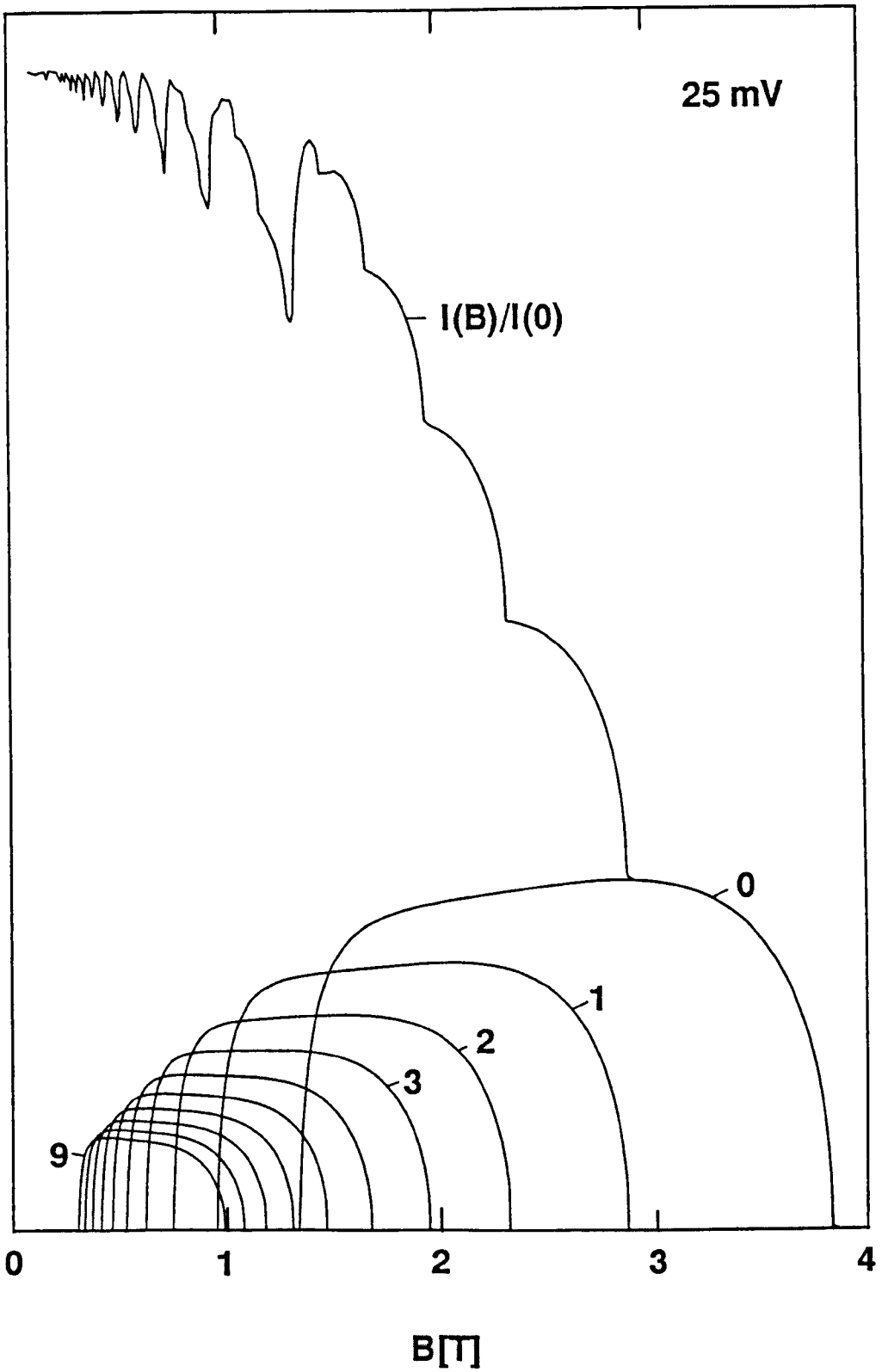

Figure 5.6 Normalised I(B) characteristics of the (InGa)As/InP single-barrier structures calculated for V = 25 mV, taking the nonparabolicity factor of (InGa)As to be $\alpha = 1.3\ eV^{-1}$, and assuming a conduction band offset $\Delta E_c = 230$ meV. The individual current contributions $I_n(B)$ n = 0, 1, ... 9 are also shown.

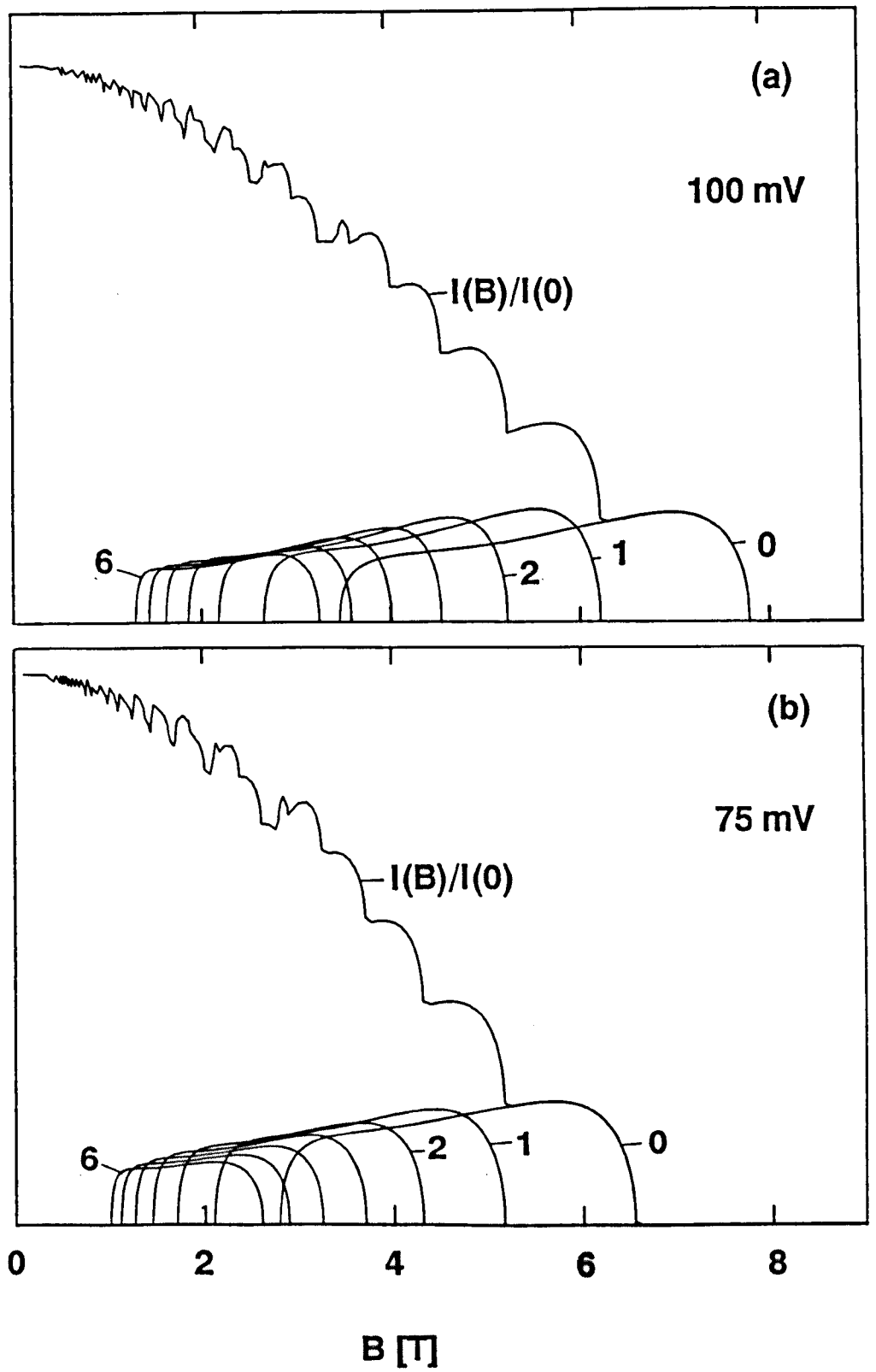

Figure 5.7 Normalised I(B) characteristics of the (InGa)As/InP single-barrier structures calculated for (a) 100 mV and (b) 75 mV, taking $\alpha = 1.3\ eV^{-1}$ and $\Delta E_c = 230$ meV. The individual current contribution $I_n(B)$ n = 0, 1, ... 6 are also shown.

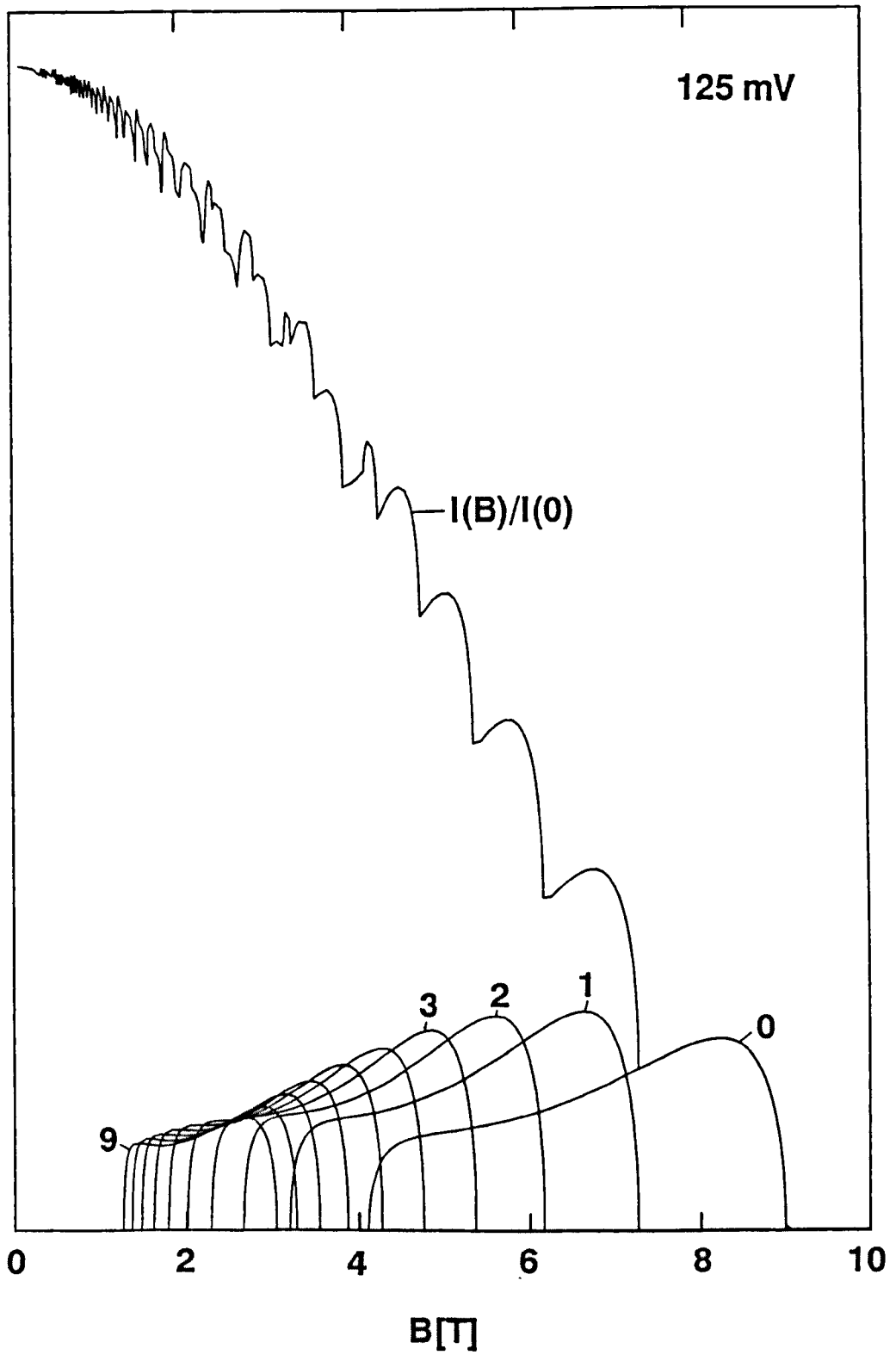

Figure 5.8 Normalised I(B) characteristics of the (InGa)As/InP structures calculated for V = 125 mV, taking α = 1.3 eV^{-1} and ΔE_c = 230 meV. The individual current contributions $I_n(B)$ n = 0, 1, ... 9 are also shown.

the decreasing part ($B \geq 1.5$ T) of both the measured and simulated curves.

In general however, the structure in the simulated curves is unrealistically sharp and pronounced. This is to be expected since the transfer-Hamiltonian formalism neglects energy level broadening and only encompasses elastic tunnelling transitions which also conserve the transverse wavevector. The measured current probably contains additional contributions from inelastic phonon-assisted and elastic impurity-assisted transitions (see, for example, Duke 1969), which change the electron wavevector. It follows that the opening and closure of elastic, wavevector-conserving conduction channels produces greater fractional changes in the calculated current, which contains no additional contributions.

For $V = 25$ mV and $V = 100$ mV, the calculated I(B) curves shown in Figures 5.6 and 5.7 fall to zero at field values $B_0^-(V)$ which are much lower than observed (Figures 5.1 and 5.2).

This discrepancy is due to inaccuracy of the WKB interfacial Landau levels in the quantum limit $n = 0$, and also of the perturbation calculation of the 2DEG energy levels at higher fields. Uncertainties in the conduction band offset, the effective mass in the barrier region and the nonparabolicity factor of (InGa)As also affect the values of $B_0^-(V)$ through their influence on the $n = 0$ dispersion curve.

For all voltages, the measured zero-field current density $I^m(0)$ is several orders of magnitude higher than the calculated value $I^c(0)$. For example, when V = 100 mV, $I^m(0) \cong 6.4 \times 10^4$ A m^{-2} whereas $I^c(0) \cong 72$ A m^{-2}. The magnitude of the tunnel current depends primarily on the decay function $\mu_{n1}(x)$ which appears exponentially in the transition rate (5.38). This decay function is calculated assuming that the effective mass in the barrier region equals the conduction band-edge mass of InP. However, Lassnig (1987) has shown using k.p theory that the effective tunnelling mass in III-V heterostructures falls almost linearly with energy $T(x) = E_c(x) - E_n(k_y)$ below the conduction band edge, that is

$$m^*(T(x)) = m^*_B(1 - \alpha T(x)) \quad , \tag{5.39}$$

where $\alpha \cong 1/E_g = 0.73$ eV^{-1} for InP at 4.2 K.

When V = 100 mV, the 2DEG electrons tunnel approximately 160 meV below the top of the InP barrier, for which the effective tunnelling mass (5.39) is approximately 0.88 m^*_B. This small reduction in mass increases the predicted zero-field tunnel current by approximately 4 times to $I^c(0) \cong 290$ A m^{-2}, in slightly better agreement with the measured value. Because the transition rate (5.38) depends exponentially on the tunnelling mass, the calculated current is extremely sensitive to the value of α. However, for V = 100 mV, comparable values of $I^c(0)$ and $I^m(0)$ are only obtained taking $\alpha \cong 3.5$ eV^{-1}, which is almost five times the k.p prediction. Nevertheless, such uncertainties in the tunnelling mass partially explain the discrepancies between $I^c(0)$ and $I^m(0)$.

Generalisation of Lassnig's k.p calculation to include the effect of a transverse magnetic field is not trivial and, since the main aim of this chapter is to explain the shapes, rather than the absolute values of the tunnel current and derivatives, the energy-dependence of the tunnelling mass is neglected.

5.10 Physical Explanation for the Field-Dependence and Relative Magnitudes of the Current Contributions $I_n(B)$

5.10.1 Introduction

Figures 5.6, 5.7 and 5.8 show the current contributions $I_n(B)$ calculated from equation (5.10) for a range of forward-bias voltages. For V = 25 mV each current contribution is almost symmetrical under reflection in the line $B = (B_n^+ + B_n^-)/2$ and attains a maximum value $I_n^{MAX} = I_n(B_n^{MAX})$, which increases with decreasing n. For higher biasses, I_n^{MAX} increases less rapidly with decreasing n and, for V = 100 mV and V = 125 mV, $I_0^{MAX} < I_1^{MAX}$. In addition, B_n^{MAX} approaches B_n^- so that the current contributions become increasingly asymmetric.

These trends are most easily understood in physical terms by considering the factors

$$N_n(B) = (k_F^2 - k_y'^2(n))^{\frac{1}{2}} \quad , \qquad (5.40)$$

$$W_n(B) = 2\pi |M_n(k_y(n))|^2/\hbar \quad , \tag{5.41}$$

and $$D_n(B) = |\hbar^2 k_y'(n)/m^*_L - dE_n/dk_y|^{-1} \tag{5.42}$$

of $I_n(B)$ given in equation (5.10). Each factor depends parametrically on magnetic field through the allowed transverse wavevector components $\{k_y(n)\}$. $W_n(B)$ is the 'normalised' transition rate obtained by integrating equation (3.25) over the energy range of all final states, in order to eliminate the delta function.

The field-dependence of each factor is shown in Figures 5.9 and 5.10 for V = 25 mV. The normalised transition rate $W_n(B)$ is, from equation (5.38), proportional to the product of the barrier transmission coefficient $T_n(B)$ and the classical interfacial skipping frequency $F_n(B)$, which are both shown in Figure 5.11. The physical reasons for the field-dependence of each factor are now considered in some detail, since this is also central to the interpretation of the oscillatory amplitudes of dI/dB and d^2I/dB^2 given in Sections 5.12 and 5.13.

5.10.2 Field-dependence of the factors $N_n(B)$, calculated for V = 25 mV

It follows from equation (5.40) and the $\underline{k}$-space distribution of occupied 2DEG states shown in Figure 4.1, that 2DEG electrons with the transverse wavevector component $k_y(n)$ have values of k_z in

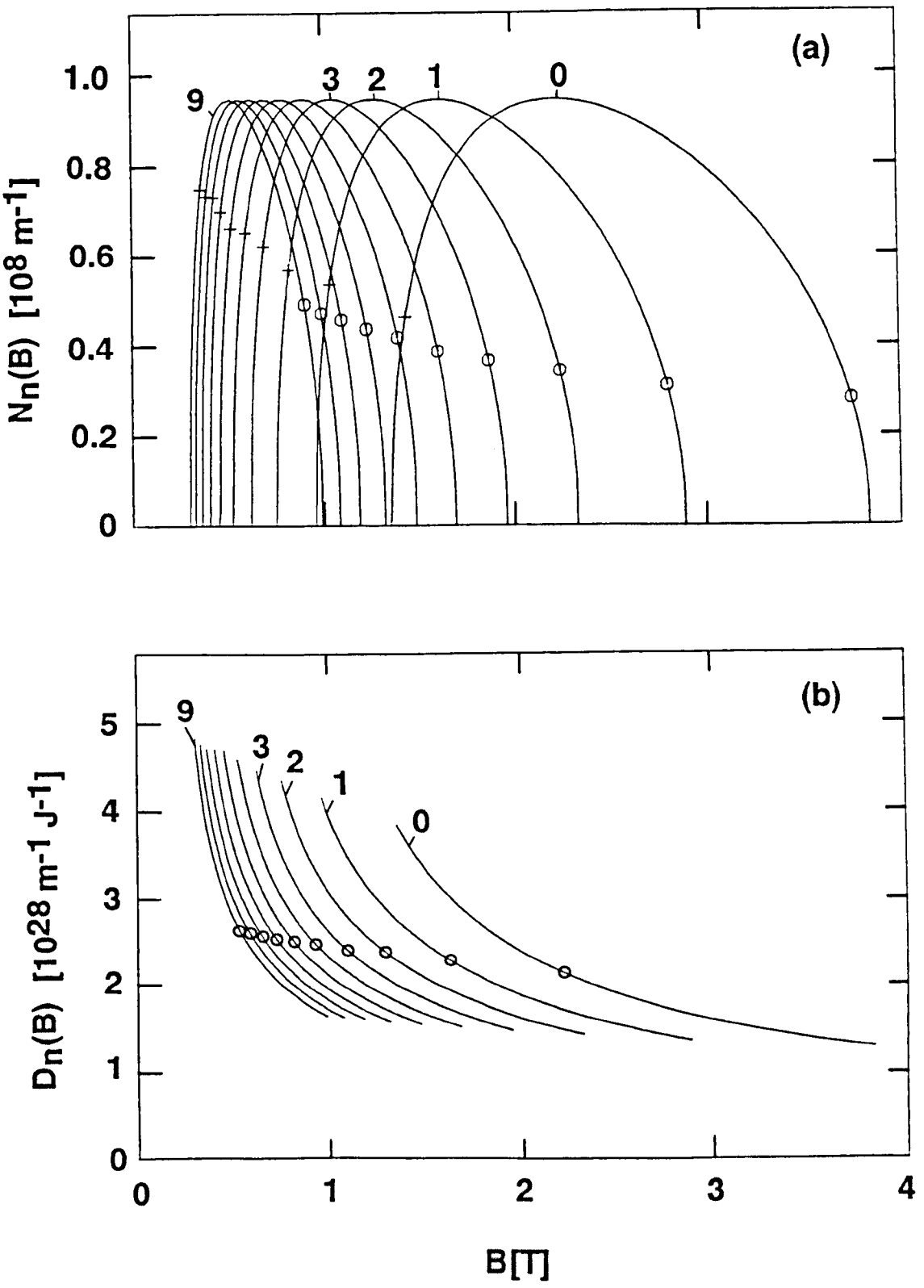

Figure 5.9 The factors (a) $N_n(B)$ and (b) $D_n(B)$, n = 0, 1, ... 9, calculated for V = 25 mV over the field ranges $B_n^+ \leq B \leq B_n^-$. The crosses (open circles) in (a) show the mean values $\bar{N}_n^+$ ($\bar{N}_n^-$). Each factor $N_n(B)$ attains a maximum $+k_F$ at the field value B_n°. The values of $D_n(B_n^\circ)$ are shown by open circles in (b).

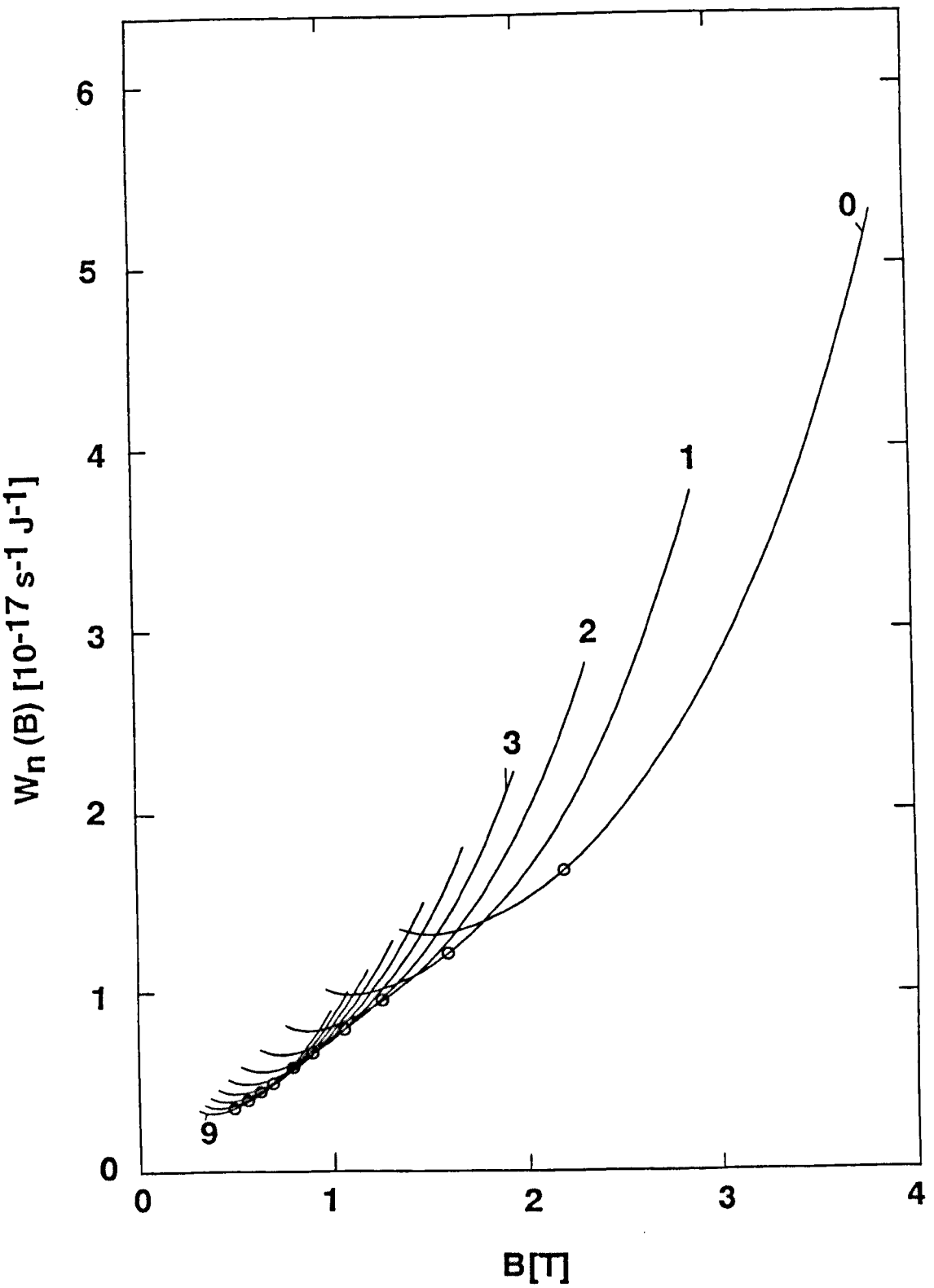

Figure 5.10 Normalised transition rates $W_n(B)$, n = 0, 1, ... 9, calculated for V = 25 mV over the field ranges $B_n^+ \leq B \leq B_n^-$. The open circles show the transition rates at the field values B_n° for which $N_n(B_n^\circ)$ attains a maximum value $+k_F$.

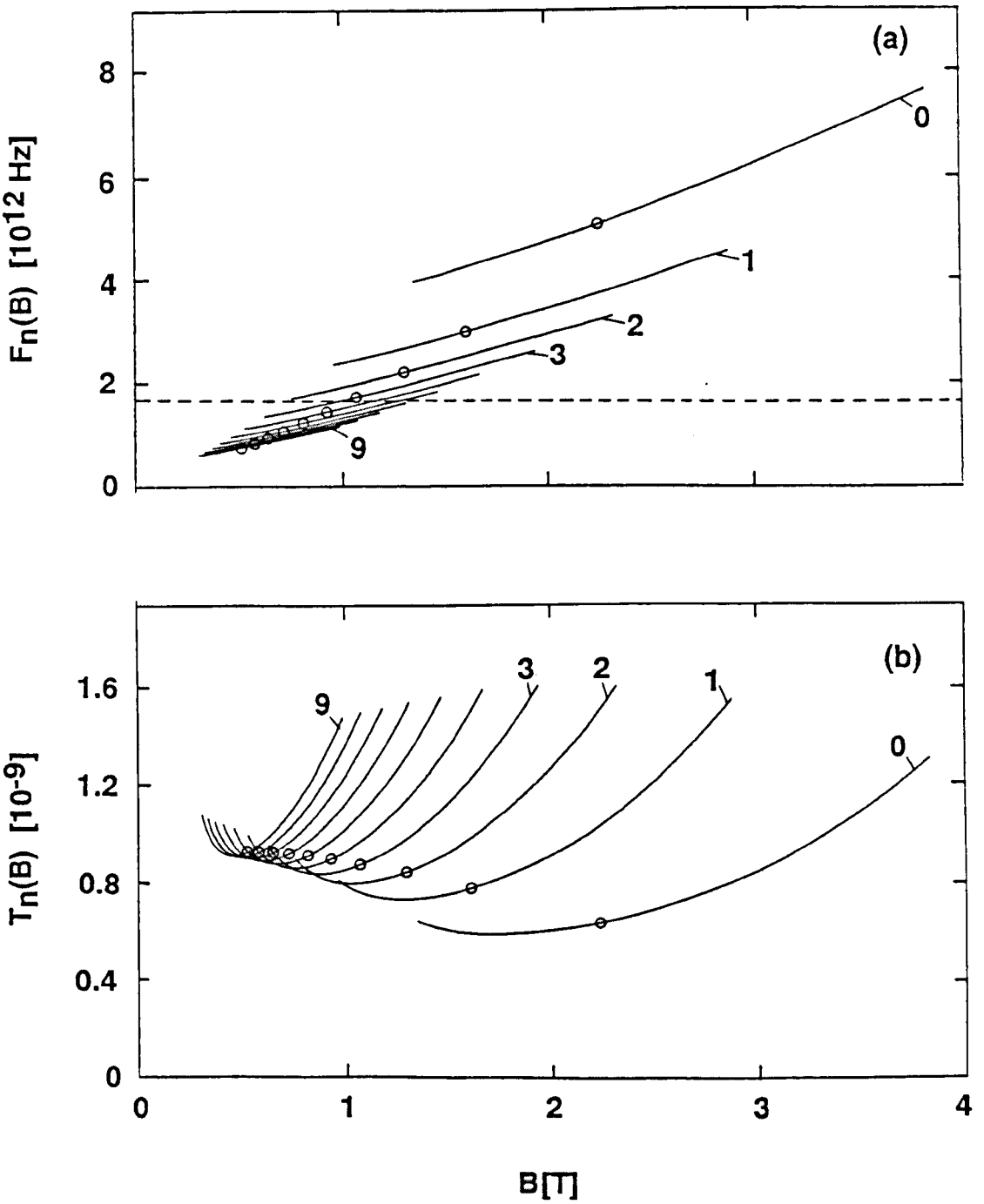

Figure 5.11 (a) Semiclassical interfacial state skipping frequencies $F_n(B)$ and, (b) barrier transmission coefficients $T_n(B)$, $n = 0, 1, \ldots 9$, calculated for $V = 25$ mV over the field ranges $B_n^+ \leq B \leq B_n^-$. The open circles show $F_n(B_n^\circ)$ and $T_n(B_n^\circ)$ where B_n° is the field value for which $N_n(B_n^\circ)$ attains a maximum value $+k_F$. The broken line in (a) shows the approximate LO phonon emission rate W_{LO} in bulk (InGa)As, divided by 2π.

the range $-N_n(B) \leq k_z \leq N_n(B)$. Thus, $N_n(B)$ is proportional to the number of electrons tunnelling into the n^{th} interfacial Landau state for given magnetic field. Figure 5.9a shows that $N_n(B) = 0$ when $B = B_n^{\pm}$ ($k_y'(n) = \pm k_F$) and attains a maximum value of $+ k_F$ at the field value B_n° for which the n^{th} interfacial state dispersion curve passes through the centre of the 2DEG parabola ($k_y'(n) = 0$).

5.10.3 Field-dependence of the factors $D_n(B)$ calculated for $V = 25$ mV

The factors $D_n(B)$ shown for $V = 25$ mV in Figure 5.9b are, from equation (5.42), related to the number of 2DEG and interfacial Landau states per unit energy, close to the intersection point $k_y(n)$. The reciprocal of $D_n(B)$ is proportional to the absolute change in the expectation value of the y-component of velocity of 2DEG electrons with transverse wavevector component $k_y(n)$ tunnelling into the n^{th} interfacial Landau state. This velocity change is greater for $-k_F$ electrons tunnelling when $B = B_m^-$ than for $+k_F$ electrons tunnelling at an adjacent resonant field $B_n^+ \simeq B_m^-$. Consequently, $D_n(B_n^+ \simeq B_m^-) > D_m(B_m^-)$.

Figure 5.9b also shows that for given n, $D_n(B_n^+) > D_n(B_n^-)$, the difference being primarily due to the opposite slopes at either extremity of the 2DEG parabola. The values of $D_n(B_n^{\pm})$ both decrease slowly with increasing $B_n^{\pm}$, as the gradients $dE_n(k_o \pm k_F)/dk_y$ increase.

5.10.4 Field-dependence of the barrier transmission coefficients $T_n(B)$ calculated for V = 25 mV

From equation (1.53), the barrier transmission coefficients $T_n(B)$ shown in Figure 5.11b depend exponentially on the decay functions $\mu_{n1}(x)$. From equations (4.21) and (4.26), $\mu_{n1}(x)$ depends on the sum of the conduction band profile $E_c(x)$ and the magnetic potential energy $E_{MAG}(x)$ in the barrier region, which determine the effective barrier height, and also on the tunnelling energy $E_n(k_y)$.

When $B = B_n^+$, 2DEG electrons with $k_y'(n) = +k_F$ tunnel into the n^{th} interfacial Landau state with orbit centre position

$$X_+ = -(b + 3a_o) - \frac{\hbar k_F}{B_n^+ e}, \qquad (5.43)$$

which, as shown in Figure 5.12 for the case n = 0, lies to the left of the mean 2DEG stand-off position <x>. As the intercept $k_y'(n)$ moves away from the $+k_F$ extremity of the 2DEG parabola with increasing field (see Figure 5.5), the orbit centre $X_{k_y(n)} = -(b + 3a_o) - \hbar k_y'(n)/Be$ moves along the x-axis towards the LH barrier interface, so that the mean magnetic potential in the barrier region decreases. It can be seen from Figure 5.5, that the tunnelling energy $E_n(k_y)$ also decreases as $k_y'(n)$ moves away from the $+k_F$ extremity of the 2DEG parabola. For fields just above B_n^+, $E_n(k_y)$ falls more rapidly than the mean magnetic potential energy in the barrier region. The effective barrier height therefore increases relative to

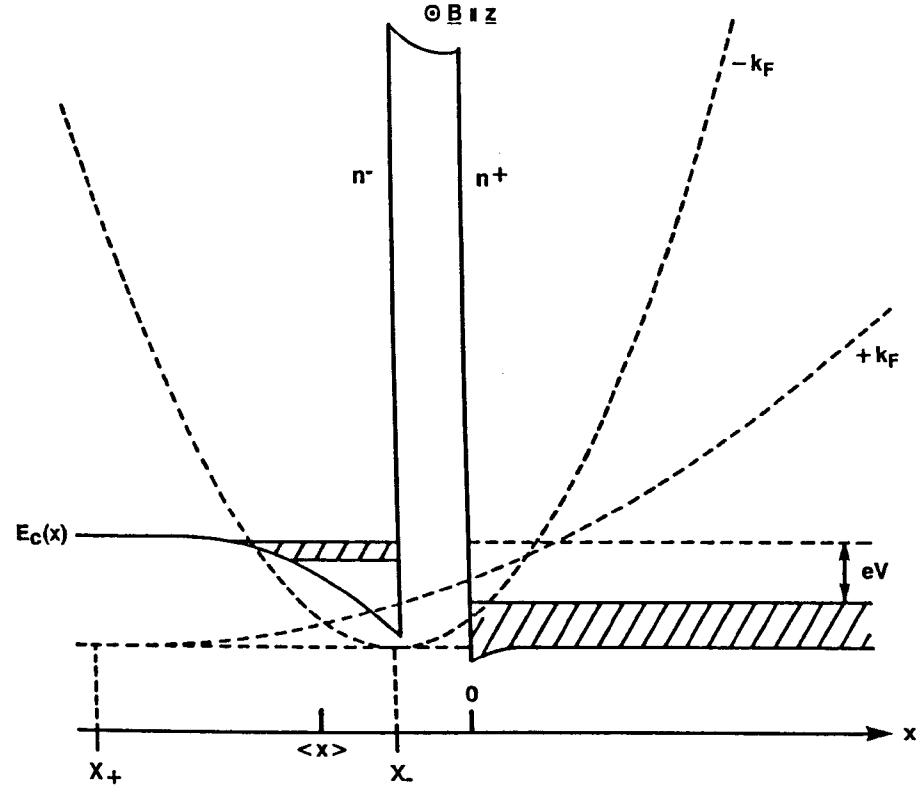

Figure 5.12 Conduction band profile $E_c(x)$ and magnetic potential energy (broken curves) experienced by 2DEG electrons with $k_y' = +k_F$ ($-k_F$) tunnelling into the n = 0 interfacial Landau state at the resonant fields $B_o^+ \cong 1.3$ T ($B_o^- \cong 3.8$ T) when V = 25 mV. The $\pm k_F$ orbit centre positions $X_\pm$ are indicated, together with the mean 2DEG stand-off position <x>. For illustration, the effective mass is taken to be m_L^* throughout the device. However, the position-dependent effective mass $m^*(x)$ used for all calculations in this chapter, gives similar magnetic potential energy variations.

$E_n(k_y)$ resulting in the reduced transmission clearly seen in Figure 5.11b. As $k_y'(n) \rightarrow 0$, $E_n(k_y)$ falls less rapidly than the magnetic potential energy in the barrier region, so that the total effective barrier height falls relative to $E_n(k_y)$, and the transmission coefficient rises. Maximum transmission is attained when $B = B_n^-$, and the orbit centre

$$X_- = -(b + 3a_o) + \frac{\hbar k_F}{B_n^- e} \qquad (5.44)$$

lies to the right of the mean 2DEG stand-off position, so that the mean magnetic potential in the barrier reaches a minimum as shown in Figure 5.12 for the case $n = 0$.

The tunnelling energy of 2DEG electrons with $k_y'(n) = \pm k_F$ equals $eV + E_{FR}$ so that the corresponding transmission coefficients $T_n(B_n^{\pm})$ depend only on the magnetic potential energy $E_{MAG}(x)$ in the barrier region, which raises the effective barrier height. Using $E_{MAG}(-b/2)$ to estimate the average increase in barrier height $\Delta E_n^{\pm}$ experienced by $\pm k_F$ electrons tunnelling into the n^{th} interfacial Landau state gives, from equation (4.21),

$$\Delta E_n^{\pm} \simeq \frac{1}{2m^*_B} \left(e(\frac{b}{2} + 3a_o)\, B_n^{\pm} \pm \hbar k_F\right)^2 \quad . \qquad (5.45)$$

Equation (5.45) predicts reduced transmission of $+k_F$ electrons as the effective barrier height increases with B_n^+, in agreement with the calculated variation of $T_n(B_n^+)$ shown in Figure 5.11b. By contrast, for $-k_F$ electrons, $T_n(B_n^-)$ is expected to increase with B_n^- for $B_n^- \leq B_T$ where

$$B_T = \hbar k_F / e \left(\frac{b}{2} + 3a_o\right) , \qquad (5.46)$$

and to decrease with B_n^- for $B_n^- \geq B_T$. Such variation is clearly observed in Figure 5.11b, which shows maximum $-k_F$ transmission being attained for $B_3^- \simeq 2$ T, in good agreement with the estimated value $B_T \simeq 2.2$ T.

The reason for this behaviour is easily understood. Equation (5.44) shows that for $B_n^- < \hbar k_F/e(b + 3a_o)$, the orbit centre X- is located on the RHS of the potential barrier. With increasing B_n^-(decreasing n), X- moves towards the RH barrier interface so that the effective barrier height is reduced and $T_n(B_n^-)$ rises. Maximum transmission is reached when $B_n^- \simeq B_T$, for which X- lies close to the centre of the barrier. With increasing $B_n^- > B_T$, X- moves further to the left of the barrier so that the effective barrier height rises and the transmission coefficient falls.

5.10.5 Field-dependence of the interfacial Landau state skipping frequencies $F_n(B)$ calculated for V = 25 mV

The semiclassical skipping frequencies $F_n(B)$ corresponding to the n = 0, 1, ... 9 interfacial Landau states are shown for V = 25 mV in Figure 5.11a. For this voltage, the tunnelling energy lies in the range 34 meV $\leq E_n(k_y) \leq$ 42 meV and therefore varies only slowly with magnetic field as the intersection point $k_y(n)$ moves through the 2DEG parabola. The orbital speed $v_n = (2E_n(k_y(n))/\overline{m^*_L})^{\frac{1}{2}}$ is thus almost identical for all interfacial electrons, regardless of field or index. It follows that variations in the skipping frequency (4.55) are due primarily to changes in the skipping arclength $S_n = 2R_n \cos^{-1} u_o$ (see Figure 4.5). With increasing field (and decreasing $k_y'(n)$), the orbit centre $X_{k_y} = -(b+3a_o) - (\hbar k_y'/Be)$ of the n^{th} interfacial Landau state moves along the x-axis. As can be seen from Figure 4.5, this shift tends to increase the skipping arclength S_n. However, this effect is small compared with the contraction of the orbital radius R_n which, from equation (4.48), falls as B^{-1}, leading to a nett reduction of S_n. Since the orbital speed remains approximately constant, the skipping frequency $F_n(B)$ increases with field as shown in Figure 5.11a.

The calculated field-dependence of the angle of incidence $\theta_n = \cos^{-1} u_o$ (see Figure 4.5) of the skipping electrons, shown in Figure 5.13, confirms this interpretation. For given n, $\cos^{-1}u_o$ rises sub-linearly with field so that the variation of the skipping frequency (4.55) is dominated by the linear increase in angular velocity $Be/\overline{m^*_L}$.

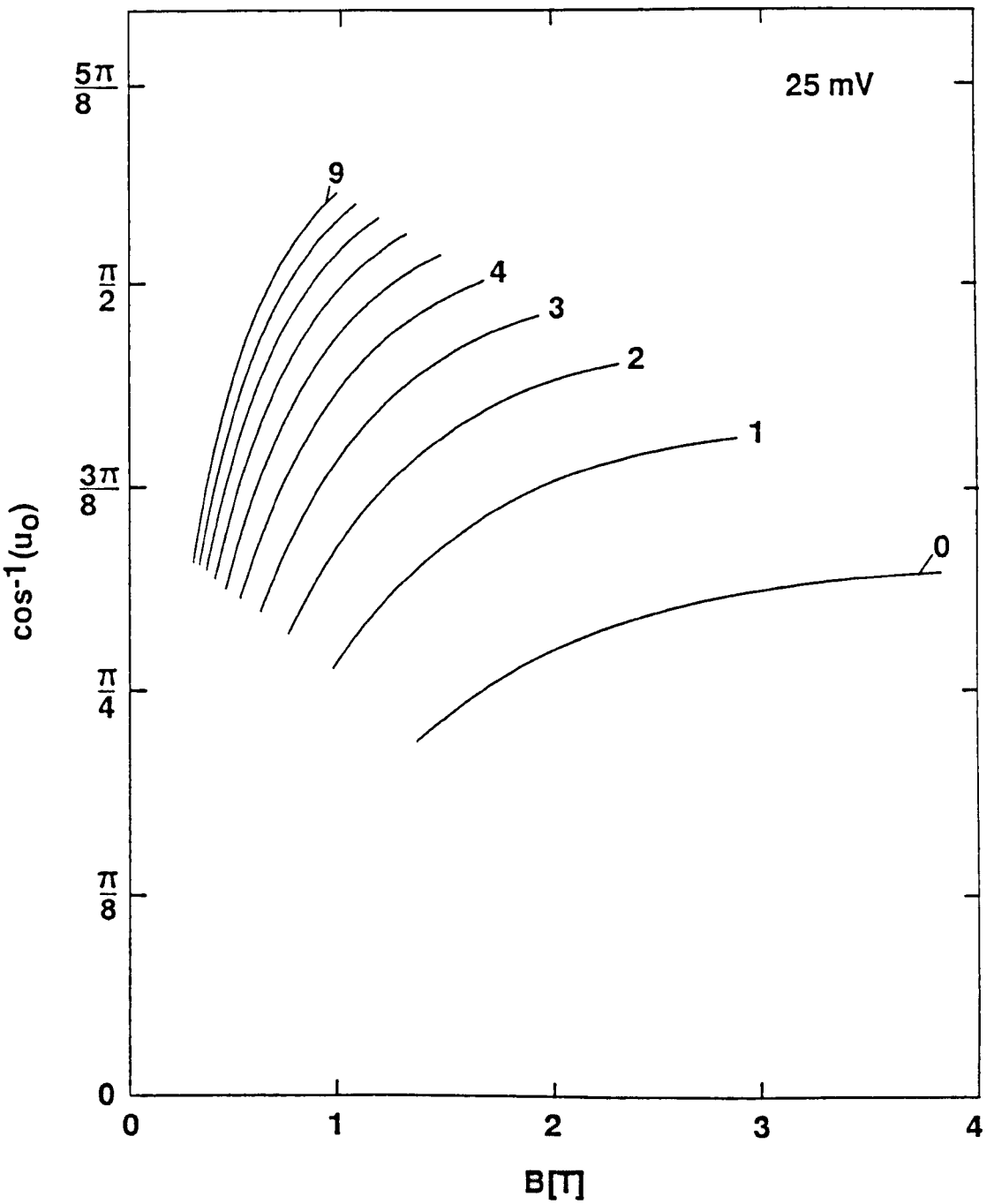

Figure 5.13 Angle of incidence $\theta_n = \cos^{-1}u_0$ of the skipping trajectories along the RH barrier interface corresponding to the n = 0, 1, ... 9 interfacial Landau states, calculated for V = 25 mV over the field ranges $B_n^+ \leq B \leq B_n^-$.

Figure 5.5 shows that for given field, lower-index interfacial Landau states are accessed by 2DEG electrons with higher transverse wavevector components $k_y(n)$, which therefore have orbit centres $X_{k_y(n)} = -\hbar k_y(n)/Be$ further to the left of the barrier. Since the orbital radii (4.48) and orbital speeds $(2\overline{m^*_L}E_n)^{\frac{1}{2}}$ vary slowly with n over the range 34 meV $\leq E_n \leq$ 42 meV of occupied 2DEG levels at V = 25 mV, electrons tunnelling into lower-index states traverse shorter skipping arclengths and thus have higher skipping frequencies $F_n(B)$ as shown in Figure 5.11a.

Figure 5.13 shows that the angle of incidence $\cos^{-1}u_o$ of both $+k_F$ and $-k_F$ electrons decreases with increasing $B_n^{\pm}$. It follows from equation (4.55) that the skipping frequencies $F_n(B_n^{\pm})$ rise superlinearly as shown in Figure 5.11a. Physically the $\pm k_F$ skipping frequencies increase with field as the orbital radii and skipping arclengths contract, whilst the orbital speed $(2\overline{m^*_L}\ (eV + E_{FR}))^{\frac{1}{2}}$ remains the same.

5.10.6 Field-dependence of the normalised transition rates $W_n(B)$ calculated for V = 25 mV

From equations (5.38) and (5.41), the normalised transition rates $W_n(B)$ shown in Figure 5.10 are proportional to the product of the barrier transmission coefficients $T_n(B)$ and the interfacial state skipping frequencies $F_n(B)$. For given n, $W_n(B)$ generally increases with field, since $T_n(B)$ and $F_n(B)$ both rise. However, $W_n(B)$ also

reflects the slight reduction in transmission coefficient visible in Figure 5.11b as the field is raised just above B_n^+. It is clear from Figure 5.10 that the average transition rate into the n^{th} interfacial Landau state, evaluated over the field range $B_n^+ \leq B \leq B_n^-$, increases with decreasing quantum number n. Figure 5.11 shows that this increase is entirely due to the higher skipping frequencies of the lower-index interfacial states, since the average transmission coefficient decreases with n, owing to the increased contribution of the magnetic potential to the effective barrier height.

5.10.7 Interpretation of the field-dependence of the current contributions $I_n(B)$ calculated for V = 25 mV

Comparison of Figures 5.9 and 5.10 shows that for V = 25 mV, the transition rates $W_n(B)$ and density of states terms $D_n(B)$ vary slowly with field compared with the factors $N_n(B)$. These factors increase rapidly from zero when $B = B_n^{\pm}$, to a maximum value of $+k_F$ at the field values B_n° for which $k_y'(n) = 0$. These rapidly-varying terms therefore determine the shape of the current contributions $I_n(B)$ which, as shown in Figure 5.6, attain maximum values I_n^{MAX} when $B \simeq B_n^\circ$. Since $N_n(B_n^\circ) = +k_F$ for all n, these maximum current contributions depend approximately on the values of $D_n(B_n^\circ)$, $T_n(B_n^\circ)$ and $F_n(B_n^\circ)$, marked by open circles in Figures 5.9 and 5.11.

By definition, $k_y'(n) = 0$ when $B = B_n^\circ$ so that $k_y(n) = k_0$ and the orbit centre $X_{k\,o} = -(b + 3a_o)$ is fixed at the mean stand-off position of the 2DEG. Consequently, the mean magnetic potential in the barrier region and the total effective barrier height, both increase with B_n°, as shown in Figure 5.14, leading to the diminished transmission coefficients $T_n(B_n^\circ)$ shown in Figure 5.11b. The values of $D_n(B_n^\circ) = (dE_n/dk_y)^{-1}$ shown in Figure 5.9b also decrease slowly as the gradients of the interfacial state dispersion curves increase with B_n°. Both of these effects are small, however, compared with the dramatic increase of the skipping frequencies $F_n(B_n^\circ)$ which occurs as the orbital radii and skipping arclengths (4.53) contract with increasing B_n°, whilst the orbital speed $v_n = (2E_{bo}'/\overline{m^*_L})^{\frac{1}{2}}$ remains constant. This trend is clearly reflected in the increasing transition rates $W_n(B_n^\circ)$ shown in Figure 5.10, and is entirely responsible for the higher peak currents I_n^{MAX} resulting from transitions into lower-index interfacial states.

Figure 5.14 shows the magnetic potential energy experienced by 2DEG electrons tunnelling at the field values B_1° and B_0° ($> B_1^\circ$), when V = 25 mV. Quantum-mechanically, increased magnetic confinement ($w_0 < w_1$) at the higher field B_1° raises the amplitude of the magneto-quantised interfacial state wavefunction at the RH barrier interface ($\psi_0(0_+) > \psi_1(0_+)$), despite the accompanying increase of the mean magnetic potential energy (MPE) in the barrier region (Fromhold et al., 1990). At low voltages, this mean MPE has little effect on the degree of wavefunction penetration (see Section 5.13). From

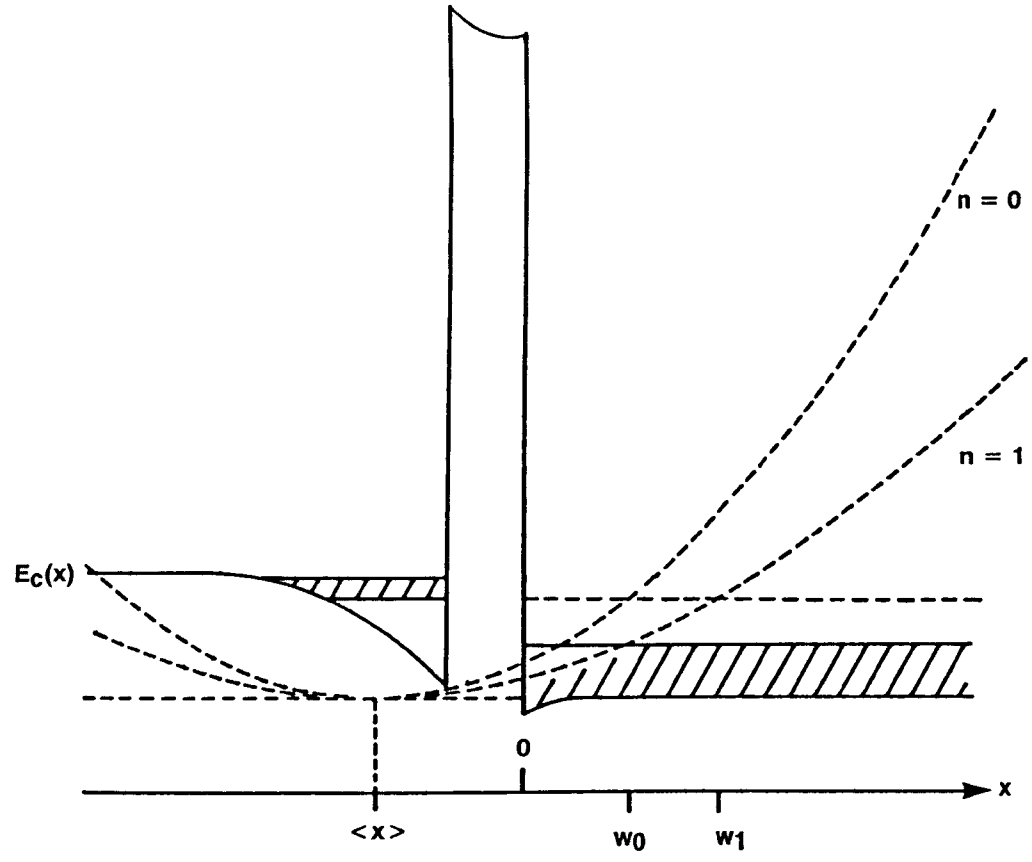

Figure 5.14 Conduction band profile $E_c(x)$ and magnetic potential energy (broken curves) experienced by electrons with $k_y' = 0$ tunnelling into the n = 1 (0) interfacial Landau state when B_n° = 1.6 T (2.2 T) and V = 25 mV. Both magnetic potential orbit centre positions coincide with the mean 2DEG stand-off position <x>. The turning points w_n of the classical skipping orbits are also shown. For clarity of illustration, the effective mass is taken to be m_L^* throughout the device.

equation (5.38), the higher wavefunction amplitude $\psi_0(0_+)$ leads to faster transitions into the n = 0 interfacial state so that the peak current contribution $I_0^{MAX} > I_1^{MAX}$ as shown in Figure 5.6.

5.10.8 The effect of increasing voltage on the factors $N_n(B)$, $D_n(B)$, $W_n(B)$, $F_n(B)$ and $T_n(B)$

Figures 5.15, 5.16 and 5.17 show the field-dependence of the factors of $I_n(B)$ calculated for V = 125 mV. The most dramatic effect of increasing the voltage is on the barrier transmission coefficients $T_n(B)$. Comparison of Figures 5.11b and 5.17b shows that these transmission coefficients are at least one order of magnitude higher for V = 125 mV than for V = 25 mV, because the higher electric field in the barrier region significantly reduces the mean effective barrier height. In addition, for given n, $T_n(B)$ rises more rapidly with field at the higher voltage.

As discussed in Section 5.10.4 for the case V = 25 mV, the orbit centre of the magnetic potential energy moves closer to the barrier as the field is increased from B_n^+ to B_n^-. Consequently, the mean magnetic potential in the barrier region ($\bar{E}_{MAG}$) falls and $T_n(B)$ rises as shown in Figure 5.17b. However, because the mean zero-field barrier height is much lower at the higher voltage V = 125 mV, a comparable reduction in $\bar{E}_{MAG}$ produces a greater percentage decrease in the total effective barrier height, leading to a more dramatic rise in transmission coefficient. This effect is considered in more

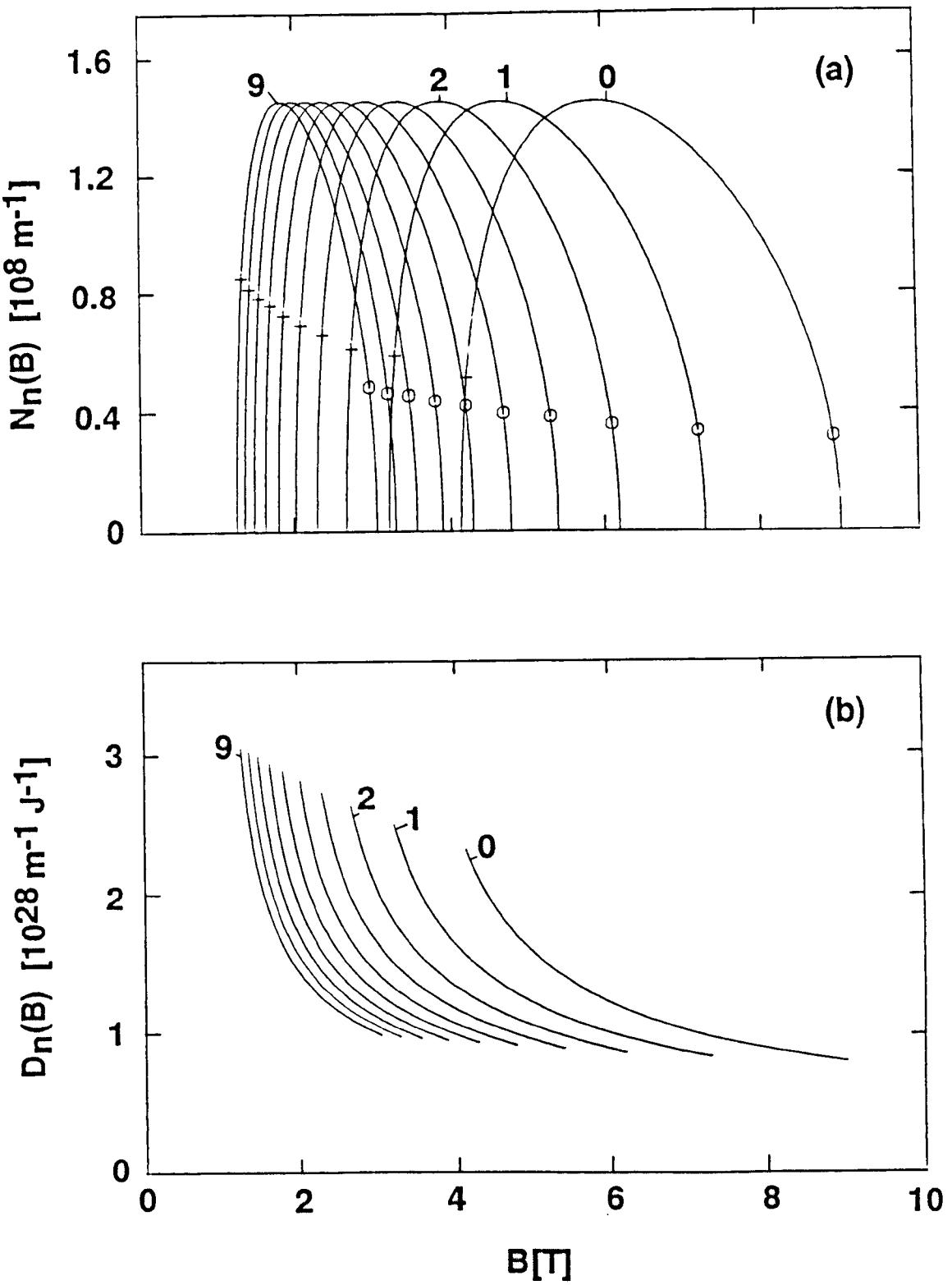

Figure 5.15 The factors (a) $N_n(B)$ and (b) $D_n(B)$, n = 0, 1, .. 9, calculated for V = 125 mV over the field ranges $B_n^+ \leq B \leq B_n^-$. The crosses (open circles) in (a) show the mean values $\bar{N}_n^{\pm}$.

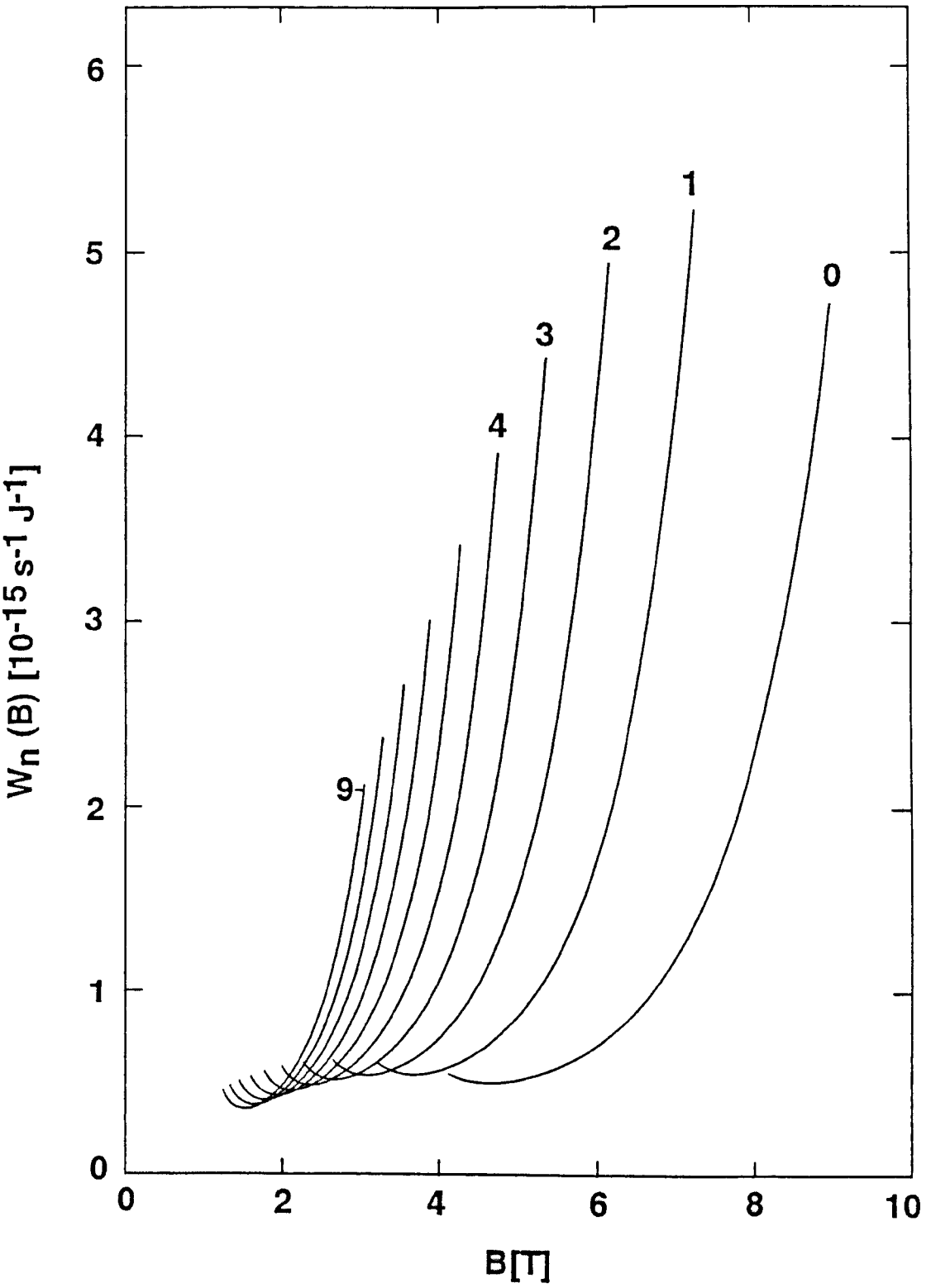

Figure 5.16 Normalised transition rates $W_n(B)$, n = 0, 1, ... 9, calculated for V = 125 mV over the field ranges $B_n^+ \leq B \leq B_n^-$.

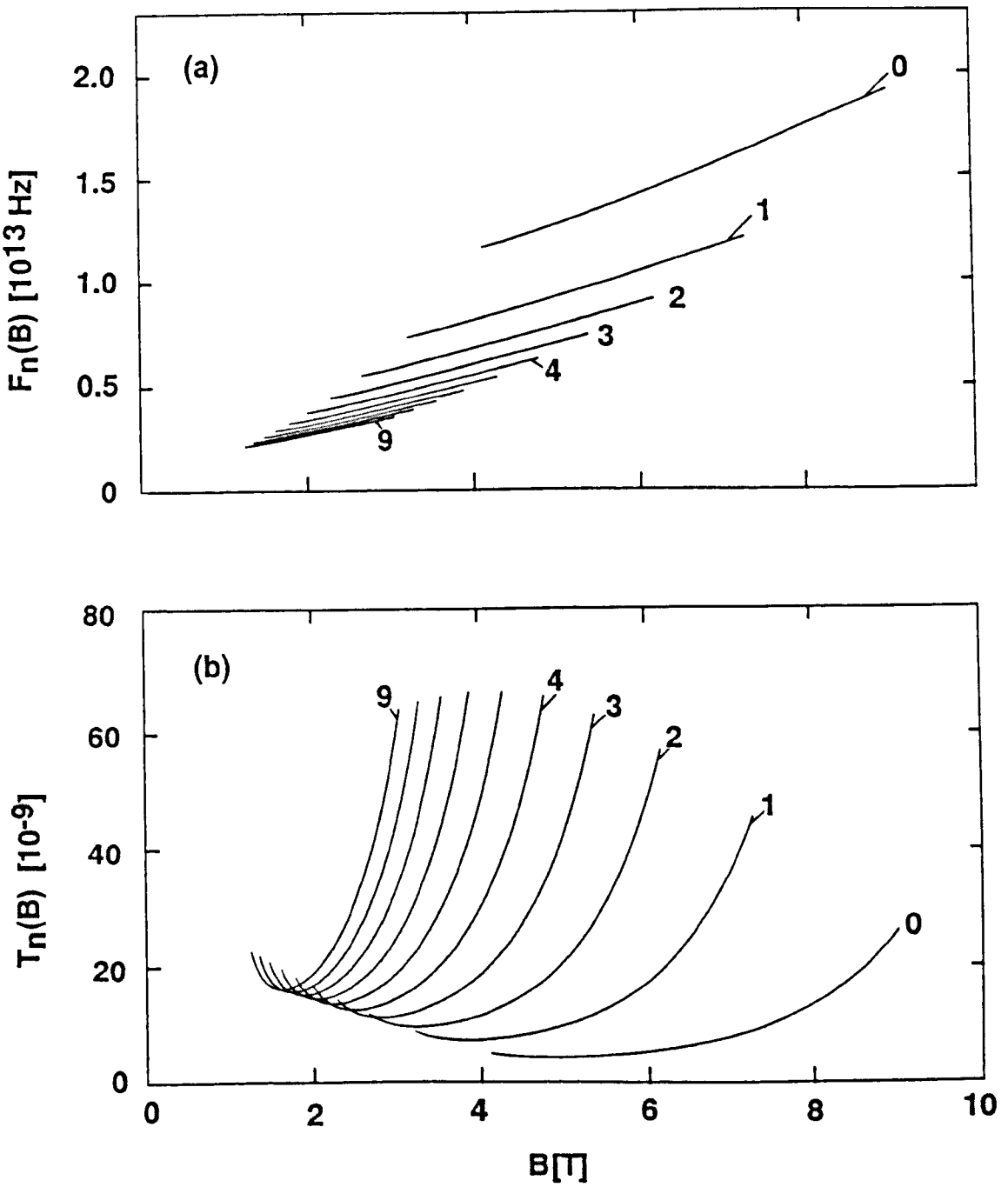

Figure 5.17 (a) Semiclassical interfacial state skipping frequencies $F_n(B)$ and, (b) barrier transmission coefficients $T_n(B)$, $n = 0, 1, .. 9$, calculated for $V = 125$ mV over the field ranges $B_n^+ \leq B \leq B_n^-$.

detail in Section 5.13. For given n, $T_n(B)$ increases so rapidly with field when V = 125 mV that it has a visible effect on the shape of the $I_n(B)$ curves shown in Figure 5.8.

The qualitative field-dependence of the $-k_F$ transmission coefficients $T_n(B_n^-)$ was explained in Section 5.10.4 for V = 25 mV. For V = 125 mV, equation (5.46) predicts maximum transmission of $-k_F$ electrons when $B_n^- \cong B_T = 4$ T. This estimate is in good agreement with the position of the maximum calculated $-k_F$ transmission coefficient $T_5(B_5^-)$ shown in Figure 5.17b.

The reduction of $T_n(B_n^-)$ which occurs with increasing $B_n^- \geq 4$ T, is generally slow compared with the rapid increase of the corresponding skipping frequencies $F_n(B_n^-)$ shown in Figure 5.17a. This increase therefore dominates the field-dependence of the transition rates $W_n(B_n^-)$ shown in Figure 5.16. However, at the highest fields, the mean magnetic potential energy in the barrier region makes a large contribution to the total effective barrier height. Consequently, the barrier transmission coefficient falls rapidly and, as shown in Figure 5.17b, $T_0(B_0^-) \cong 0.5\ T_1(B_1^-)$. This dramatic reduction in transmission coefficient more than compensates for the comparatively small increase in skipping frequency ($F_0(B_0^-) \cong 1.5\ F_1(B_1^-)$), leading to the diminished value of $W_0(B_0^-)$, clearly revealed in Figure 5.16.

This effect is central to the explanation given in Section 5.13.2 for the observed weakening of the $-p_F$ series at high fields and bias voltages.

5.11 Simulation of the Magneto-current Derivatives dI/dB and d^2I/dB^2

5.11.1 Unaveraged derivatives

Figure 5.18 shows the first derivative of the magneto-current curve 5.6, calculated for V = 25 mV. The current contributions $I_n(B)$ n = 0, 1, ...9 are also shown. As predicted by equation (A.2) of Appendix 1, maxima (minima) in dI/dB originate from the opening (closure) of conduction channels whenever $B = B_n^+$ (B_n^-). The oscillatory amplitudes are not, of course, infinite since the calculated derivative is equal to the linear gradient between adjacent data points with finite field and current values.

Generally, the amplitudes of both the $\pm p_F$ series of oscillations increase with field. In addition, for $B \leq B_o^+$, the $-p_F$ minima are of much smaller magnitude than adjacent $+p_F$ maxima. Although these trends are in reasonable qualitative agreement with the observed features (Figure 5.3), the simulated oscillatory structure is unrealistically sharp, because the experimental derivatives were obtained using an averaging routine intended to smooth out noise.

For comparison with experiment, theoretical derivatives must be calculated using the same smoothing procedure, which is described in Section 5.11.2.

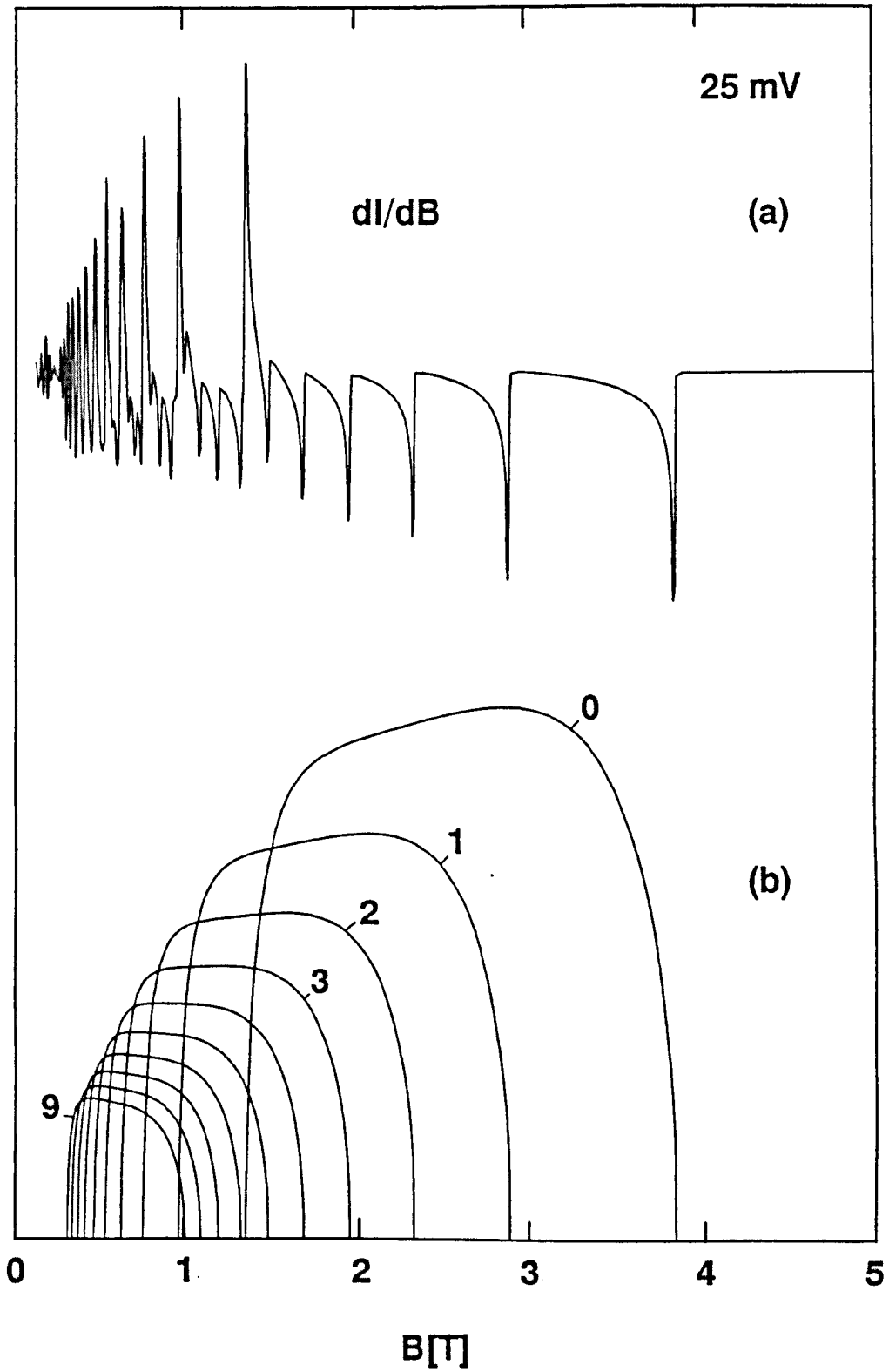

Figure 5.18 (a) Magneto-current derivative, dI/dB, calculated for V = 25 mV, (b) Individual current contributions $I_n(B)$, n = 0, 1, .. 9. Maxima (minima) in dI/dB originate from the opening (closure) of these tunnelling channels.

An additional advantage of calculating smoothed derivatives in this way is that approximate analytical expressions can be obtained which directly relate the extremal values of the averaged first derivatives to the factors $D_n(B_n^{\pm})$ and $W_n(B_n^{\pm}) \propto F_n(B_n^{\pm})\, T_n(B_n^{\pm})$, appropriate to $\pm k_F$ transitions. The field-dependence of the oscillatory amplitudes can thus be understood physically by considering the effect of the field on the barrier transmission coefficient and interfacial state skipping frequencies.

5.11.2 Description of the averaging procedure used to obtain the experimental magneto-current derivatives

Suppose that N discrete current measurements $I(B_i)$ $i = 1, 2, \ldots N$ are made at the equally-spaced field values B_i. To obtain the averaged first derivative of this set of data, the mean field and current values $(\overline{B_1}, \overline{I_1})$ of the first A data points are calculated, and also those of the adjacent A points, starting from the $A + 1^{th}$ point. The value of the averaged first derivative at the mean field value $B_1' = B_1 + (A - \frac{1}{2})\delta B$ of both sets of data is defined to be

$$\left\langle\frac{dI}{dB}\right\rangle_{B=B_1'} = (\overline{I}_2 - \overline{I}_1)/(\overline{B}_2 - \overline{B}_1) = (\overline{I}_2 - \overline{I}_1)/A\delta B \quad . \qquad (5.47)$$

The two sets of A points are then stepped, one data point at a time, through the whole data set, repeating the calculation of the gradient at each step. Thus, at the field value $B_\ell' = B_\ell + (A - \frac{1}{2})\delta B$ ($\cong B_{\ell+A}$ for $A \gg 1$) the averaged first derivative is

$$\left\langle \frac{dI}{dB} \right\rangle_{B=B_{\ell}'} = \frac{\sum_{i=\ell+A}^{\ell+2A-1} I(B_i) - \sum_{i=\ell}^{\ell+A-1} I(B_i)}{A^2 \delta B} \quad . \tag{5.48}$$

The averaged second derivative is calculated in the same way, from the averaged first derivative data points.

When A = 1, this differentiation procedure simply gives the linear gradient between adjacent data points. For larger A, more points are averaged, so that high-frequency oscillatory components are smoothed from the derivative curves. When calculating theoretical derivatives, A is chosen so that current averaging is performed over the same range of field $\Delta B = (A - 1)\delta B \cong 0.2$ T (Snell, 1987a), used to obtain the measured curves.

5.11.3 Relation between the extremal values of the averaged first derivative <dI/dB> and the factors $D_n(B_n\pm)$, $T_n(B_n\pm)$ and $F_n(B_n\pm)$

The aim of this section is to obtain approximate analytical expressions for the extremal values of <dI/dB> attained close to the resonant fields $B_n^{\pm}$.

Using equation (5.11) in equation (5.48) and introducing the dummy variable $j = \ell + A$ gives, for $A >> 1$

$$\left\langle \frac{dI}{dB} \right\rangle_{B=B_j} = \frac{\sum_n \left(\sum_{i=j}^{j+A-1} I_n(B_i) - \sum_{i=j-A}^{j-1} I_n(B_i) \right)}{A\Delta B} \quad , \qquad (5.49)$$

where $\Delta B = (A - 1)\delta B \cong A\delta B$ is the field range over which current averaging is performed. Figure 5.18 shows that if $B_j \cong B_n^{\pm}$, and the separation between $B_n^{\pm}$ and adjacent resonant fields greatly exceeds ΔB ($\cong 0.2$ T), the n^{th} current contribution varies most rapidly over the field range $B_j - \Delta B \leq B \leq B_j + \Delta B$. Consequently, for $B_j \cong B_n^{\pm}$, equation (5.49) is dominated by the n^{th} term and may be written, to good approximation

$$\left\langle \frac{dI}{dB} \right\rangle_{B_j} \cong \left\langle \frac{dI_n}{dB} \right\rangle_{B_j} = \frac{\bar{I}_R - \bar{I}_L}{\Delta B} \quad , \qquad (5.50)$$

where

$$\bar{I}_R = \sum_{i=j}^{j+A-1} \frac{I_n(B_i)}{A} \quad \text{and} \quad \bar{I}_L = \sum_{i=j-A}^{j-1} \frac{I_n(B_i)}{A} \quad .$$

Figure 5.19 shows the schematic field-dependence of the discrete data points $\{B_i, I_n(B_i)\}$ close to the resonant field B_n^+, which is taken to lie between B_K and B_{K+1}. The data points $\{(B_i, I_n(B_i))\ i = j, j + 1, \ldots j + A - 1\}$ which lie on or within the ordinates $B = B_j$ and $B = B_{j+A-1}$ are collectively referred to as the RH data bin. An expression for the average current value $\bar{I}_R$ of these points is given in equation (5.50). Similarly, $\bar{I}_L$ is the average current value of the LH data bin which, as shown in Figure 5.19, comprises all data points lying on or within the lines $B = B_{j-A}$ and $B = B_{j-1}$. Equation (5.50)

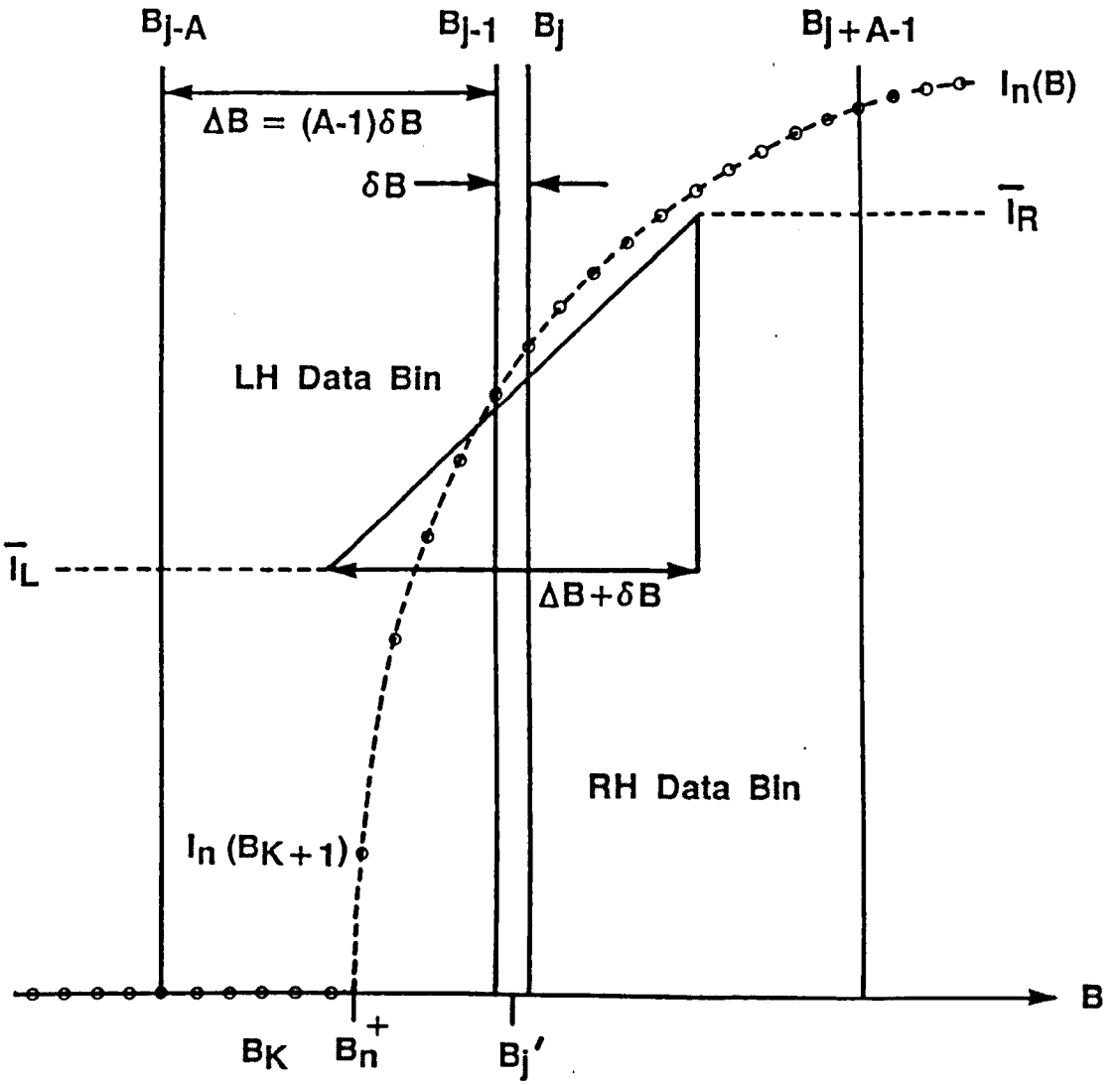

Figure 5.19 Schematic variation of the discrete data points $(B_i, I_n(B_i))$, close to the resonant field B_n^+, which lies between B_K and B_{K+1}. The 'averaged' derivative $\langle dI/dB \rangle_{B_j'}$, at the field value $B_j' = 0.5(B_{j-1} + B_j) \equiv B_j$ close to B_n^+, is approximately equal to the difference between the mean current values $\bar{I}_R$ and $\bar{I}_L$ of the RH and LH data bins (comprising the A data points above or below B_j), divided by the corresponding difference $\Delta B + \delta B$ in mean field values. For the simulated derivatives, A is chosen so that current averaging is performed over the same field range as the measured curves.

therefore asserts that the averaged first derivative at the field value B_j, is proportional to the difference between the mean current values $\bar{I}_R$ and $\bar{I}_L$ of the RH and LH data bins.

It is clear from Figure 5.19 that if $B_{j+A-1} < B_{K+1} \equiv B_n^+$, the average current in each bin vanishes and $\langle dI_n/dB \rangle_{B_j} = 0$. In this case, the series expression (5.49) is not dominated by the n^{th} term, and equation (5.50) is clearly inaccurate. As the data bins are steppped, one data point at a time to higher fields, $\langle dI_n/dB \rangle_{B_j}$ remains zero until $B_{j+A-1} = B_{K+1}$ when, as can be seen from Figure 5.19, the RH data bin contains one positive current value $I_n(B_{K+1})$, so that $\langle dI_n/dB \rangle_{B_{K-A+2}} > 0$. As the data bins are moved to yet higher fields, more data points with finite current values are included in the RH bin and $\bar{I}_R$ increases rapidly. Provided B_{j-1} remains less than B_{K+1} so that $\bar{I}_L = 0$, $\langle dI_n/dB \rangle_{B_j}$ also increases rapidly and soon dominates the series expansion (5.49), which is then given to reasonable approximation by equation (5.50).

The maximum value of $\langle dI_n/dB \rangle_{B_j}$ is attained when the difference

$$\left\langle \frac{dI_n}{dB} \right\rangle_{B_{j+1}} - \left\langle \frac{dI_n}{dB} \right\rangle_{B_j} = \frac{1}{A}\left(I_n(B_{j+A}) - 2I_n(B_j) + I_n(B_{j-A})\right) \tag{5.51}$$

$$\cong \frac{1}{A}\left(I_n(B_j + \Delta B) + I_n(Bj - \Delta B) - 2I_n(B_j)\right)$$

between adjacent averaged derivative values is closest to zero.

Assuming that this maximum is attained for some $B_j \leq B_n^+ + \Delta B$, so that $I_n(B_j - \Delta B) = 0$, the value of B_j can be found graphically by looking for intercepts between the curves $I_n(B + \Delta B)$ and $2I_n(B)$. However, it is clear from inspection of Figures 5.20, 5.21 and 5.22 that the maximum value of $\langle dI/dB \rangle$ is attained when $B_j \cong B_n^+ \cong B_K$ and thus, from equation (5.50) is given approximately by

$$\left\langle \frac{dI}{dB} \right\rangle_n^+ \cong (A\Delta B)^{-1} \sum_{i=K}^{K+A-1} I_n(B_i) \quad . \tag{5.52}$$

A similar analysis shows that if the $-p_F$ resonant field B_n^- lies between the discrete field values B_{L-1} and B_L, the associated minimum value of $\langle dI/dB \rangle$ is approximately

$$\left\langle \frac{dI}{dB} \right\rangle_n^- \cong -(A\Delta B)^{-1} \sum_{i=L-A+1}^{L} I_n(B_i) \quad . \tag{5.53}$$

For the simulated derivatives, the number of points averaged $A \cong 15 >> 1$, so that the extremal values (5.52) and (5.53) may be written in the integral form

$$\left\langle \frac{dI}{dB} \right\rangle_n^{\pm} \cong \pm(\Delta B)^{-1} \, \bar{I}_n^{\pm} \quad , \tag{5.54}$$

where the mean current values

$$\bar{I}_n^{\pm} = \pm(\Delta B)^{-1} \int_{B_n^{\pm}}^{B_n^{\pm} \pm \Delta B} I_n(B) \, dB \quad .$$

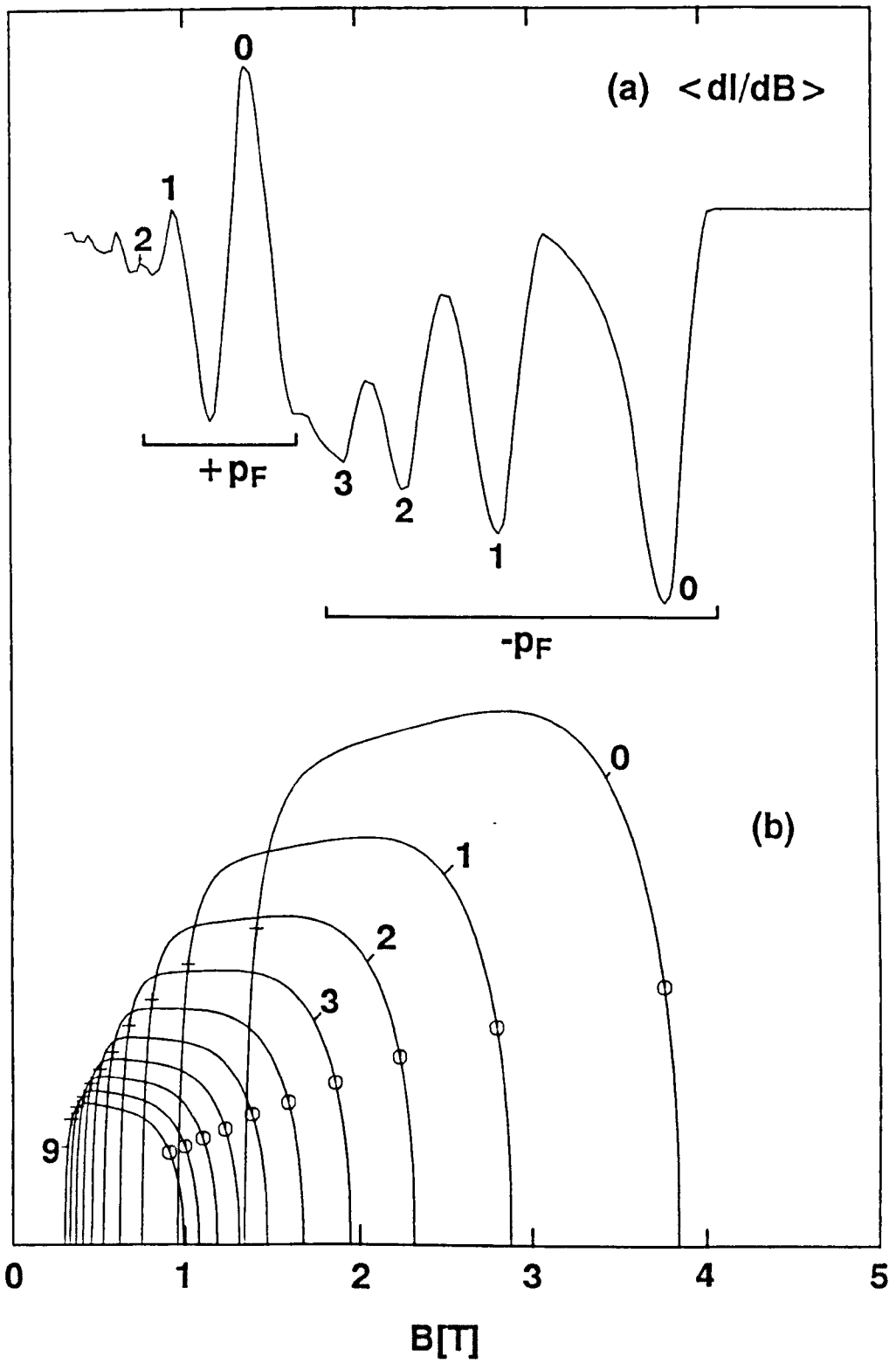

Figure 5.20 (a) Averaged magneto-current derivative <dI/dB> calculated for V = 25 mV, taking ΔB = 0.2 T. The $\pm p_F$ series of oscillations, originating from the opening and closure of the indicated tunnelling channels are distinguished by horizontal brackets. (b) The current contributions $I_n(B)$, n = 0, 1, ... 9. The mean current values $\bar{I}_n^+(\bar{I}_n^-)$ are shown by crosses (open circles).

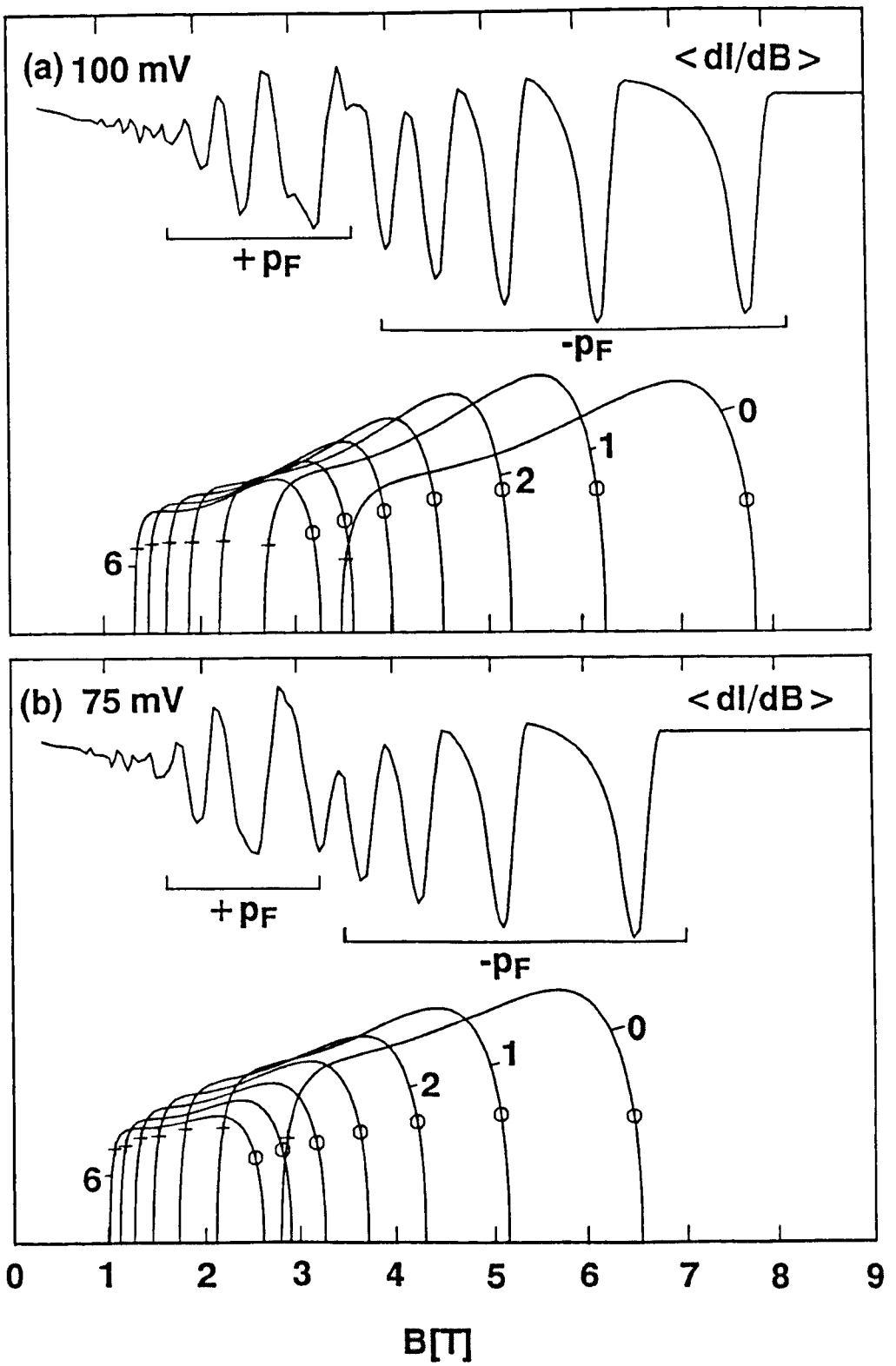

Figure 5.21 Averaged derivative <dI/dB> and current contributions $I_n(B)$, n = 0, 1, ... 6, calculated for (a) 100 mV and (b) 75 mV, taking $\Delta B = 0.2$ T. The $\pm p_F$ series of oscillations are distinguished by horizontal brackets and the mean current values $\bar{I}_n^+$ ($\bar{I}_n^-$) are marked by crosses (open circles).

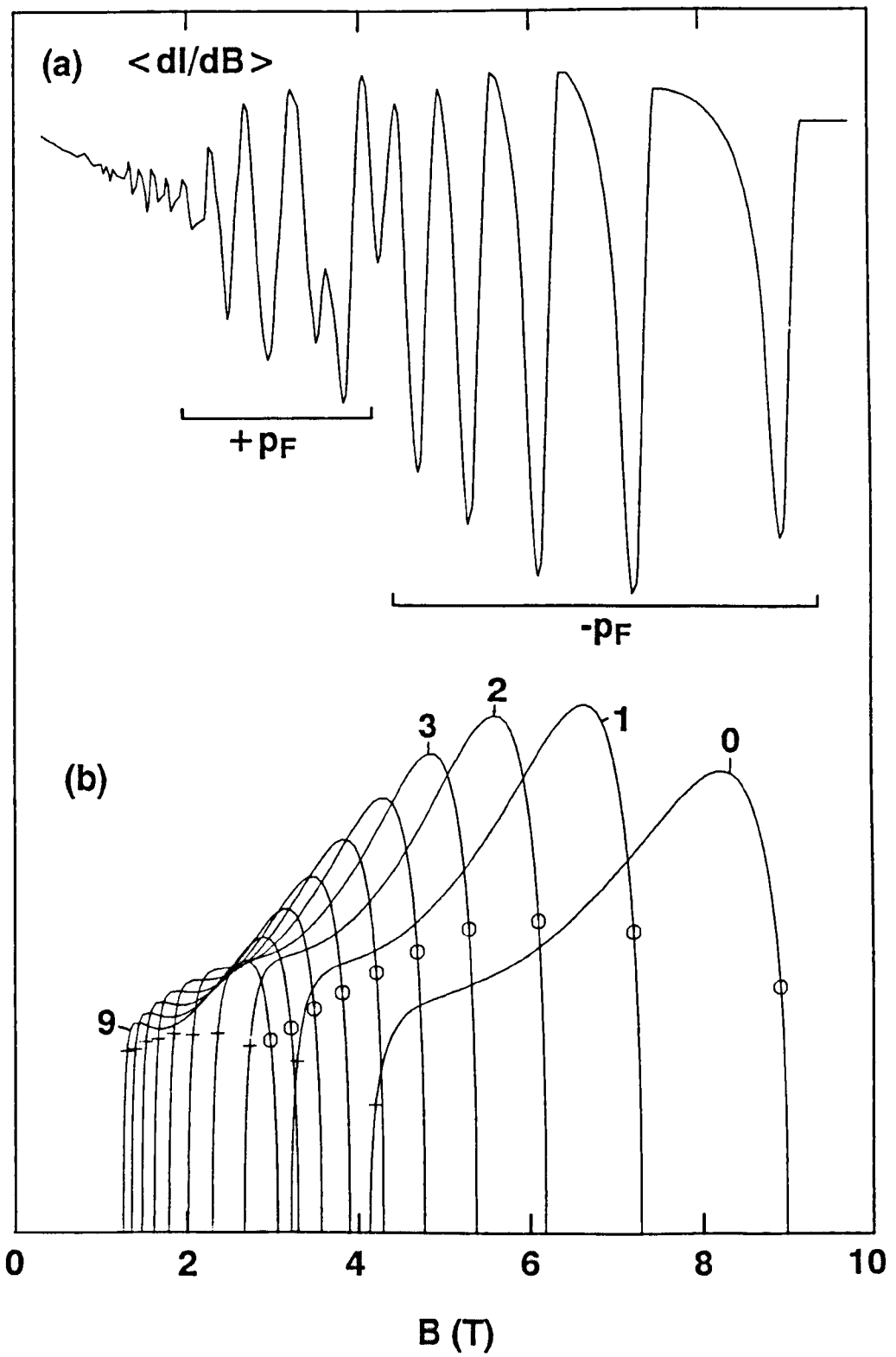

Figure 5.22 (a) Averaged derivative <dI/dB> calculated for V = 125 mV, taking ΔB = 0.2 T. The $\pm p_F$ series of oscillations are distinguished by horizontal brackets. (b) The current contributions $I_n(B)$, n = 0, 1, .. 9. The mean current values $\bar{I}_n^+$ ($\bar{I}_n^-$) are marked by crosses (open circles).

Figures 5.9, 5.10, 5.15 and 5.16 show that the factors $N_n(B)$ vary rapidly over the field ranges $B_n^+ \leq B \leq B_n^+ + \Delta B$ and $B_n^- - \Delta B \leq B \leq B_n^-$ compared with the transition rates $W_n(B)$ and density of states factors $D_n(B)$. Equation (5.54) may therefore be written, to good approximation

$$\langle \frac{dI}{dB} \rangle_n^{\pm} \cong \pm(\Delta B)^{-1} \bar{I}_n^{\pm} \cong \pm(\Delta B)^{-1} D_n(B_n^{\pm}) W_n(B_n^{\pm}) \bar{N}_n^{\pm}$$

$$\propto D_n(B_n^{\pm}) F_n(B_n^{\pm}) T_n(B_n^{\pm}) \bar{N}_n^{\pm} \quad , \tag{5.55}$$

where the mean values

$$\bar{N}_n^{\pm} = \pm(\Delta B)^{-1} \int_{B_n^{\pm}}^{B_n^{\pm} \pm \Delta B} N_n(B) dB \quad .$$

Thus equation (5.55) predicts direct proportionality between the extremal values $\langle dI/dB \rangle_n^{\pm}$ and the factors $D_n(B_n^{\pm})$, $W_n(B_n^{\pm})$ describing $\pm k_F$ transitions into the n^{th} interfacial Landau state.

5.11.4 Comparison between the simulated and measured magneto-current derivatives

First derivative curves calculated following the averaging procedure described in Section 5.11.2, taking $\Delta B = 0.2$ T, are shown for a variety of bias voltages in Figures 5.20, 5.21 and 5.22. The individual current contributions $I_n(B)$ are also shown. Comparison of Figures 5.18 and 5.20 reveals that the averaging process smoothes out the small $-p_F$ minima which are visible at low fields in the unaveraged curve. For each voltage, this results in clear separation of the $\pm p_F$ series, as observed experimentally.

In general, both $\pm p_F$ series of oscillations grow stronger with field, except for the final (high field) $-p_F$ oscillations calculated for V = 100 mV, and V = 125 mV.

The field-dependence of the $\pm p_F$ oscillatory structure revealed in the simulated $\langle d^2I/dB^2 \rangle$ curves 5.23 and 5.24 clearly reflects that of the first derivatives. Both the measured (Figures 5.1 and 5.3) and simulated $\langle d^2I/dB^2 \rangle$ curves reveal distinct $\pm p_F$ series which generally strengthen with increasing field. The diminished $-p_F$ oscillatory amplitudes observed at high fields when V = 100 mV (Figure 5.1) are also reproduced in the simulated second derivative 5.24b.

Weakening of the $+p_F$ series relative to the $-p_F$ series is apparent with increasing voltage in both the theoretical and

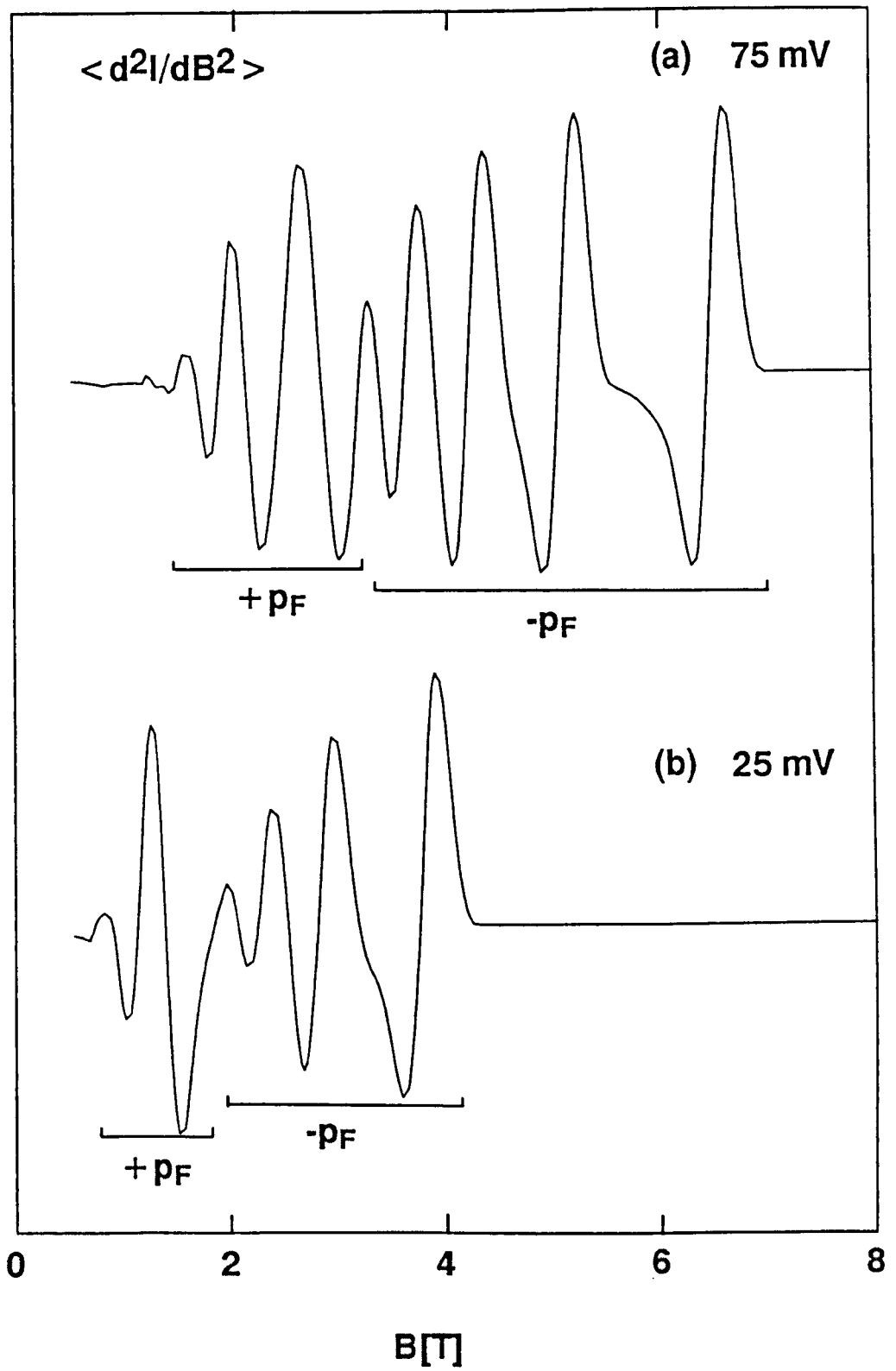

Figure 5.23 Averaged second derivative $\langle d^2I/dB^2 \rangle$ calculated for (a) 75 mV, (b) 25 mV, taking $\Delta B = 0.2$ T. The $\pm p_F$ series of oscillations are distinguished by horizontal brackets.

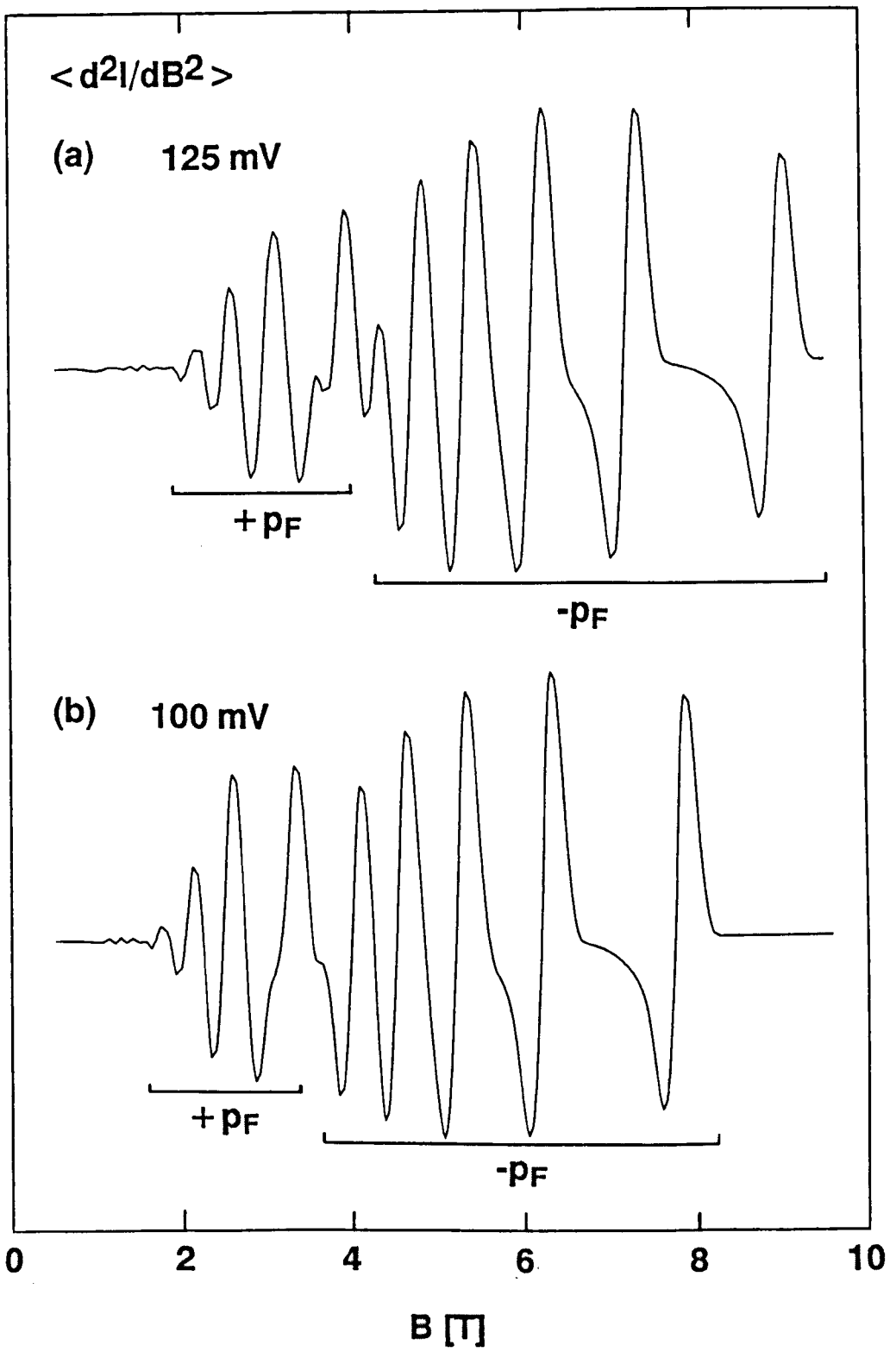

Figure 5.24 Averaged second derivatives $\langle d^2I/dB^2 \rangle$ calculated for (a) 125 mV, (b) 100 mV, taking $\Delta B = 0.2$ T. The $\pm p_F$ series of oscillations are distinguished by horizontal brackets.

experimental $\langle d^2I/dB^2 \rangle$ curves. This effect is explained in Section 5.13.3.

The predicted positions of the $+p_F$ oscillations, and the field values corresponding to the transition between the $\pm p_F$ series, compare reasonably with experiment. By contrast, the predicted $-p_F$ resonant fields B_n^- are generally much lower than observed. This discrepancy is not surprising since the predicted values of B_n^- depend on the perturbed 2DEG and WKB interfacial Landau levels, which are both less accurate at the higher fields for which the $-p_F$ series is observed. However, despite this lack of quantitative accuracy, all the qualitative features of the measured $\langle d^2I/dB^2 \rangle$ curves are clearly reproduced in the simulated derivatives.

5.11.5 Verification of the predicted correlation between $\bar{I}_n^{\pm}$ and $\langle dI/dB \rangle_n^{\pm}$

Equation (5.54) predicts that provided the separation between adjacent resonant fields greatly exceeds $\Delta B = 0.2$ T, the extremal values of $\langle dI/dB \rangle$ are directly proportional to the corresponding mean current values $\bar{I}_n^{\pm}$ shown, for 25 mV, in Figure 5.20. Owing to the large separation $B_{n-1}^- - B_n^-$ at high fields, equation (5.54) accurately predicts the field-dependence of the visible $-p_F$ minima $\langle dI/dB \rangle_n^-$, which increase in magnitude with increasing field at approximately the same rate as the mean current values $\bar{I}_n^-$.

However, the $-p_F$ oscillatory amplitudes increase even faster than these minima owing to the greater separation, $B_{n-1}^{-} - B_n^{-}$, between lower-index $-p_F$ resonant fields. For example, Figure 5.20 shows that soon after <dI/dB> begins to rise following closure of the n = 3 channel, $I_2(B)$, and consequently <dI/dB>, decrease rapidly so that the amplitude of the n = 3 - p_F oscillation remains small. By contrast, <dI/dB> rises almost to zero following closure of the n = 1 channel, before $I_0(B)$ drops rapidly. Thus the amplitude of the n = 1 $-p_F$ oscillation is almost equal to the minimum value $\langle dI/dB \rangle_1^{-}$.

Although the separation between adjacent $+p_F$ resonant fields is not sufficiently large when V = 25 mV for equation (5.54) to be of quantitative accuracy, the increase of the $+p_F$ maxima $\langle dI/dB \rangle_n^{+}$ visible with increasing field in Figure 5.20 is broadly consistent with the higher mean current values $\bar{I}_n^{+}$ of the lower-index channels. Just as for the $-p_F$ series, the strengthening of the $+p_F$ oscillations is also partly due to the increased separation $B_{n-1}^{+} - B_n^{+}$ between higher $+p_F$ resonant fields, which reduces the smoothing effect of the averaging procedure.

Figure 5.20 shows that the mean current values corresponding to adjacent resonant fields $B_n^{+} \simeq B_m^{-} < B_0^{+}$ satisfy $\bar{I}_n^{+} > \bar{I}_m^{-}$. It follows from equation (5.54) that the $+p_F$ series will dominate the oscillatory structure at low fields. This dominance is further enhanced by the averaging routine used to calculate the derivatives, which smoothes out the small $-p_F$ minima visible in the unaveraged curve 5.18. In Section 5.12.2, this smoothing procedure is shown to

simulate the effect of interfacial Landau level broadening, which prevents resolution of the more closely-spaced interfacial Landau levels, near the $-k_F$ extremity of the 2DEG parabola (see Figure 5.5).

5.12 Physical Explanation for the Field-dependence of the Oscillatory Amplitudes of $\langle dI/dB \rangle$ and $\langle d^2I/dB^2 \rangle$ when V = 25 mV

5.12.1 Introduction

The field dependence of $\overline{I}_n^{\pm}$ and consequently of the extremal values $\langle dI/dB \rangle_n^{\pm}$, is most easily understood physically by considering the factors of $I_n(B)$ shown for V = 25 mV in Figures 5.9, 5.10 and 5.11. Comparison of Figures 5.9 and 5.10 shows that the mean values $\overline{N}_n^{\pm}$ defined in equation (5.55) vary slowly with n compared with $W_n(B_n^{\pm})$ and $D_n(B_n^{\pm})$. Equation (5.55) therefore predicts, to reasonable approximation

$$\langle \frac{dI}{dB} \rangle_n^{\pm} \propto D_n(B_n^{\pm})\, W_n(B_n^{\pm}) \propto D_n(B_n^{\pm})\, F_n(B_n^{\pm})\, T_n(B_n^{\pm}) , \qquad (5.56)$$

which directly relates the extremal values of the averaged first derivative to the density of states factors, barrier transmission coefficients, and interfacial skipping frequencies associated with $\pm k_F$ transitions into the n^{th} interfacial Landau state.

5.12.2 Explanation for the clear separation of the $\pm p_F$ series

Figure 5.10 shows that the transition rates $W_n(B_n^+)$ and $W_m(B_m^-)$ of $\pm k_F$ electrons tunnelling at adjacent resonant fields $B_n^+ \cong B_m^-$ (for example B_0^+ and $B_6^- \cong 1.3$ T) are approximately equal. However, Figure 5.9b shows that the corresponding density of states terms satisfy $D_n(B_n^+) \cong 3D_m(B_m^-)$, primarily because of the opposite slopes at either extremity of the 2DEG parabola (see Section 5.10.3). Consequently equation (5.56) predicts $\langle dI/dB \rangle_n^+ \cong 3 \left| \langle dI/dB \rangle_m^- \right|$. This disparity is clearly revealed in the unaveraged derivative shown in Figure 5.18 and partly explains why the $+p_F$ series dominates the oscillatory structure at low fields. However, the complete separation of the $\pm p_F$ series in the averaged derivative 5.20 is a consequence of the averaging procedure which smoothes out small high-frequency $-p_F$ oscillations at low fields. Physically this averaging process simulates the effect of interfacial Landau level broadening for the following reasons.

The high rate of channel closure at low fields originates from the high energy density of interfacial states close to the $-k_F$ extremity of the 2DEG parabola, as compared to the $+k_F$ extremity (see Figure 5.5).

Quantised energy levels are only resolved provided the separation between adjacent levels exceeds the lifetime broadening. The dominant scattering mechanism of hot electrons in III-V materials at 4.2 K is LO phonon emission (see, for example, Ridley, 1988).

Thus, for given k_y, the n^{th} interfacial Landau level can only be resolved provided

$$E_{n+1}(k_y) - E_n(k_y) >> \hbar W_{LO} \tag{5.57}$$

where $W_{LO} \cong 10^{13}\ s^{-1}$ (Lobentanzer et al., 1987) is the approximate LO phonon emission rate of hot electrons in (InGa)As.

In the limit of large n inequality (5.57) is, from the correspondence principle (see, for example, Merzbacher, 1970), equivalent to the semiclassical requirement

$$F_n(B) >> \frac{W_{LO}}{2\pi} \tag{5.58}$$

that the interfacial electrons complete at least one skipping orbit before scattering.

The value of $W_{LO}/2\pi \cong 1.6 \times 10^{12}\ s^{-1}$ appropriate to (InGa)As is indicated by the broken line in Figure 5.11a. It is clear from this figure that inequality (5.58) predicts no visible $-p_F$ oscillations for $B < B_5^- \cong 1.5$ T. Since the highest $+p_F$ resonant field $B_0^+ < B_5^-$, it follows that no interference is expected between the $\pm p_F$ series. In addition, $F_n(B_n^+) \leq W_{LO}/2\pi$ for all $B_n^+ \leq 1$ T. Consequently, the $+p_F$ series is expected to vanish for $B < 1$ T, in reasonable agreement with the measured threshold field shown in Figure 5.3. Thus, the smoothing procedure simulates the predicted

effects of level broadening at low fields since it removes all but the $n = 0$ and $n = 1$ $^{+}p_F$ oscillations, which are the only ones to satisfy the energy level resolution requirement (5.58).

5.12.3 Field-dependence of the $^{\pm}p_F$ oscillatory amplitudes

Figure 5.9b shows that for $V = 25$ mV, the values of $D_n(B_n^+)$ are almost independent of n. Similarly, the values of $D_n(B_n^-)$ vary only slowly with n. Equation (5.56) therefore predicts that the extremal values $\langle dI/dB \rangle_n^{\pm}$ of the $\pm p_F$ oscillations will increase with field following the normalised transition rates $W_n(B_n^{\pm}) \propto F_n(B_n^{\pm})$ $T_n(B_n^{\pm})$ shown in Figure 5.10. Semiclassically the values of $W_n(B_n^{\pm})$ increase with field owing to contraction of the orbital radius R_n which reduces the arclength (4.53) traversed between successive collisions with the RH barrier interface (see Section 5.10.5), thereby increasing the skipping frequencies $F_n(B_n^{\pm})$, as shown in Figure 5.11a.

This rapid increase of $F_n(B_n^{\pm})$ more than compensates for the decreasing transmission coefficients $T_n(B_n^{\pm})$ shown in Figure 5.11b (see Section 5.10.4), and is thus reflected in the higher transition rates $W_n(B_n^{\pm})$ and increased extremal values $\langle dI/dB \rangle_n^{\pm} \propto \bar{I}_n^{\pm}$ of Figure 5.20.

Quantum-mechanically, the extremal values $\langle dI/dB \rangle_n^{\pm}$ increase with $B_n^{\pm}$ owing to increased magnetic confinement in the n^+ contact, which raises the amplitudes $\psi_n(0_-)$ of the interfacial state wavefunctions at the RH barrier interface, and thus, from equations (3.25) and (5.38), the transition rates $W_n(B_n^{\pm})$.

Figure 5.20 shows that the $\pm p_F$ oscillatory amplitudes increase more rapidly with field than the extremal values $\langle dI/dB \rangle_n^{\pm}$, since increased separation $B_{n-1}^{\pm} - B_n^{\pm}$ between adjacent lower-index resonant fields reduces the smoothing effect of the averaging procedure. This has particular influence on the more closely-spaced $+p_F$ oscillations and is largely responsible for the dramatic strengthening of the $+p_F$ series revealed in Figure 5.20.

The reduced smoothing of more widely-spaced oscillations at higher fields simulates the physical effect of increased interfacial Landau level separation which, for large n, is equivalent to the enhanced semiclassical skipping frequencies $F_n(B_n^{\pm})$ at higher fields shown in Figure 5.11a and explained in Section 5.10.5. Increased resolution of the interfacial Landau levels at higher fields gives rise to more pronounced oscillatory structure as, semiclassically, a greater fraction of the tunnelling electrons complete entire skipping orbits before scattering.

The higher skipping frequencies of $\pm k_F$ electrons tunnelling at higher fields therefore gives rise to stronger $\pm p_F$ oscillatory structure for two distinct reasons.

Firstly, the associated rise in the transition rates $W_n(B_n^{\pm}) \propto F_n(B_n^{\pm})$ increases the extremal values $\langle dI/dB \rangle_n^{\pm}$ predicted by equation (5.56). Secondly, the oscillatory amplitudes become more pronounced as a greater fraction of the tunnelling electrons complete whole skipping orbits before scattering.

5.13 The Effect of Increasing Voltage on the Oscillatory Structure

5.13.1 The effect of increasing voltage on the relative amplitudes of adjacent $\pm p_F$ oscillations

Comparison of Figures 5.20 and 5.22 shows that the ratio $\bar{I}_m^-/\bar{I}_n^+$ of mean current values corresponding to adjacent resonant fields $B_m^- \simeq B_n^+$ increases with voltage and is close to unity for V = 125 mV. Equation (5.54) therefore predicts that for V = 125 mV, adjacent $\pm p_F$ extrema in $\langle dI/dB \rangle$ will be of comparable magnitude. The clear separation of the $\pm p_F$ series in the derivative curves 5.22 and 5.24a calculated for V = 125 mV is thus entirely due to smoothing of the higher-frequency $-p_F$ oscillations at low fields, which simulates the poor resolution of interfacial Landau levels close to the $-k_F$ extremity of the 2DEG parabola, as compared with the $+k_F$ extremity (see Figure 5.5). The increased resolution of interfacial Landau levels close to the $+k_F$ extremity corresponds, for large n, to the higher $+k_F$ skipping frequencies $F_n(B_n^+) > F_m(B_m^-)$ shown in Figure

5.17a. Thus, semiclassically, the $+p_F$ series is expected to dominate the oscillatory structure at low fields and high voltages, entirely because a greater fraction of $+k_F$ tunnelling electrons complete whole skipping orbits in the n^+ contact before scattering.

Figures 5.9a and 5.15a show that the mean values $\bar{N}_n^{\pm}$ defined in equation (5.55) vary slowly with n and are of comparable magnitude for V = 25 mV and V = 125 mV. It follows from equation (5.55) that the voltage-dependence of $\bar{I}_m^-/\bar{I}_n^+$ can be explained physically by considering that of the ratios $D_m^-(B_m^-)/D_n^+(B_n^+)$, $F_m(B_m^-)/F_n(B_n^+)$ and $T_m(B_m^-)/T_n(B_n^-)$ where $B_m^- \cong B_n^+$. Comparison of Figure 5.9b with 5.15b and 5.11a with 5.17a shows that for both voltages, $D_m^-(B_m^-)/D_n(B_n^+) \cong 1/3$ and $F_m(B_m^-)/F_n(B_n^+) \cong 1/2$. Consequently, $\bar{I}_m^-/\bar{I}_n^+ \propto T_m(B_m^-)/6T_n(B_n^+)$ is expected to increase from approximately one third to unity as the voltage is increased from V = 25 mV to 125 mV, and the transmission coefficient ratio $T_m(B_m^- \cong B_n^+)/T_n(B_n^+)$ rises from ≅2 to ≅6, as shown in Figures 5.11b and 5.17b. These predicted mean current ratios are in reasonable agreement with the calculated values shown in Figure 5.20 and 5.22.

Provided the mean magnetic potential energy in the barrier region $\bar{E}_{MAG}^{\pm}$ experienced by $\pm k_F$ electrons tunnelling at adjacent resonant fields $B_n^+ \cong B_m^-$, is small compared with the mean zero-field barrier height $\bar{E}_0$ measured from the Fermi level of the 2DEG, expansion of the exponential term in equation (1.53) predicts

$$\frac{T_m(B_m^-)}{T_n(B_n^+)} \cong \exp\left(\left[(2m^*)^{\frac{1}{2}} b/\hbar\right]\left[(\bar{E}_{MAG}^{+} - \bar{E}_{MAG}^{-})/\bar{E}_0^{\frac{1}{2}}\right]\right) \quad . \qquad (5.59)$$

The voltage-dependence of this ratio can be understood by comparing Figures 5.25a and 5.25b which show the conduction band and magnetic potential energy profiles experienced by $\pm k_F$ electrons tunnelling when (a) V = 25 mV and B = 1.3 T $\cong B_0^+ \cong B_6^-$ and (b) V = 125 mV and B = 4.1 T $\cong B_0^+ \cong B_5^-$. For both voltages $X_+ < X_-$ so that the mean total effective barrier height is higher for $+k_F$ electrons ($\bar{E}^+_{MAG^+} E_0 > \bar{E}^-_{MAG^+} \bar{E}_0$) which therefore have lower transmission coefficients as shown in Figures 5.11b and 5.17b. However, it is clear from Figure 5.25 that the mean zero-field barrier height $\bar{E}_0$ decreases with increasing voltage. Consequently, at higher voltages, a given difference $\bar{E}^+_{MAG} - \bar{E}^-_{MAG}$ between the mean magnetic potential energies (MPE) experienced by $\pm k_F$ electrons produces a greater percentage difference in the total effective barrier heights, thereby increasing the transmission coefficient ratio (5.59).

Since the resonant fields generally increase with voltage (see Figures 5.6, 5.7 and 5.8), the mean MPE difference $\bar{E}^+_{MAG} - \bar{E}^-_{MAG}$ also increases as shown in Figure 5.25, thus further enhancing the transmission coefficient ratio (5.59). This ratio, and from equation (5.55), the mean current ratio $\bar{I}^-_m/\bar{I}^+_n$, are therefore expected to increase continuously with voltage, thereby increasing the ratio $\langle dI/dB\rangle^-_m/\langle dI/dB\rangle^+_n$ of adjacent $\pm p_F$ extrema predicted by equation (5.55). For precisely this reason, no $+p_F$ oscillatory structure is observed in the I(B) characteristics and derivatives of GaAs/(AlGa)As single-barrier structures measured at comparatively high ($V \geq 240$ mV) forward-bias voltages (see Chapter 6).

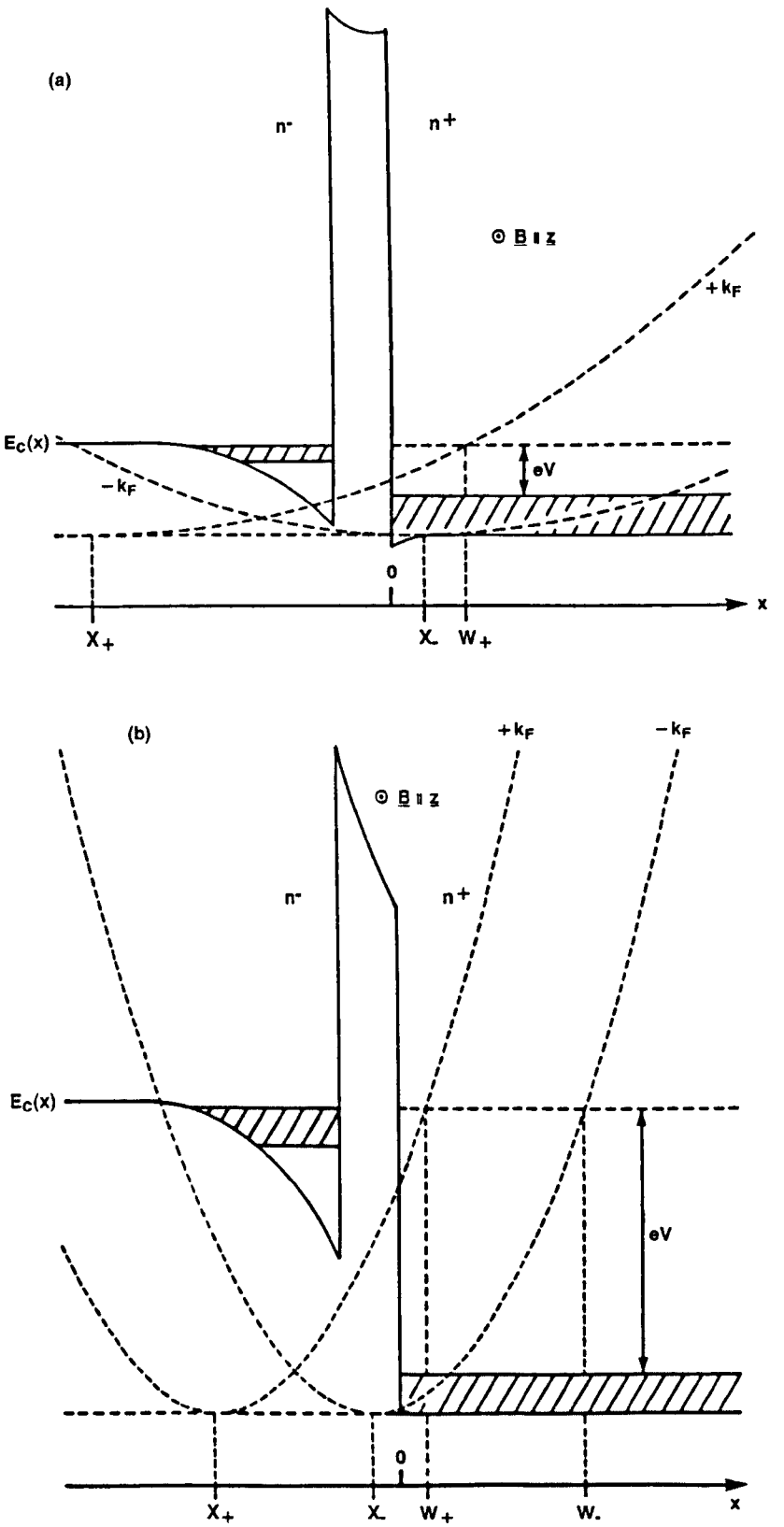

Figure 5.25 Conduction band profile $E_C(x)$ and magnetic potential energy (broken curves) experienced by $\pm k_F$ electrons tunnelling when (a) V = 25 mV and B = 1.3 T $\cong B_0^+ \cong B_6^-$ and (b) V = 125 mV and B = 4.1 T $\cong B_0^+ \cong B_5^-$. The $\pm k_F$ orbit centres $X_\pm$ and interfacial state turning points $w_\pm$ are also shown. For illustration, the effective mass is taken to be m_L^* throughout the device. A conduction band offset of 230 meV is assumed.

5.13.2 The effect of increasing voltage on the field-dependence of the $\pm p_F$ oscillatory amplitudes

As explained in Section 5.10.5, the $\pm k_F$ skipping frequencies $F_n(B_n^{\pm})$ increase with $B_n^{\pm}$ because the skipping arclength decreases, whilst the orbital speed remains the same. By contrast, the transmission coefficients $T_n(B_n^{\pm})$ generally decrease as the mean magnetic potential energy in the barrier $\bar{E}_{MAG}^{\pm}$, and consequently the effective barrier height both increase with $B_n^{\pm}$.

At higher voltages, a given change in $\bar{E}_{MAG}^{\pm}$ produces a greater fractional change in the total effective barrier height, and consequently in $T_n(B_n^{\pm})$. Figure 5.17b shows that in contrast to the lower voltage V = 25 mV (see Section 5.10.4), when V = 125 mV, the values of $T_n(B_n^{+})$ decrease with B_n^{+} at approximately the same rate as the skipping frequencies $F_n(B_n^{+})$ increase. Consequently the transition rates $W_n(B_n^{+}) \propto T_n(B_n^{+})F_n(B_n^{+})$ vary only slowly with B_n^{+}, as shown in Figure 5.16. Since the values of $D_n(B_n^{+})$ also vary slowly with B_n^{+} (Figure 5.15b) equation (5.55) predicts that the extremal values $\langle dI/dB \rangle_n^{+}$ will be almost identical for all n. The strengthening of the $+p_F$ series apparent with increasing field in Figures 5.22 and 5.24a is therefore entirely due to reduced smoothing of the more widely-spaced $+p_F$ oscillations at higher fields. Physically, this simulates the effect of increased separation between adjacent interfacial Landau levels at higher fields which, for large n, corresponds to the higher skipping frequencies $F_n(B_n^{+})$ shown in Figure 5.17a. Semiclassically then, the $+p_F$ oscillatory structure

becomes more pronounced at higher fields as a greater fraction of the tunnelling electrons complete whole skipping orbits before scattering.

Figure 5.17a shows that in general, the $-k_F$ skipping frequencies $F_n(B_n^-)$ increase with B_n^- at a faster rate than the decreasing transmission coefficients $F_n(B_n^-)$. Consequently, in general, the $-k_F$ transition rates $W_n(B_n^-) \propto T_n(B_n^-)\ F_n(B_n^-)$ also increase with field as shown in Figure 5.16. The $-p_F$ oscillatory amplitudes are therefore expected to increase with field, as shown in Figure 5.22, partly owing to the increased minima $\langle dI/dB \rangle_n^- \propto W_n(B_n^-) \propto F_n(B_n^-)$ predicted by equation (5.55), and partly because as $F_n(B_n^-)$ rises, a greater fraction of the tunnelling electrons complete whole skipping orbits before scattering, thereby giving rise to more pronounced oscillatory structure.

It should be noted that the transmission coefficient falls so rapidly at the highest $-p_F$ resonant fields ($T_0(B_0^-) \simeq 0.5\ T_1\ (B_1^-)$ in Figure 5.17b) that the transition rate also falls ($W_0(B_0^-) < W_1(B_1^-)$ in Figure 5.16). Despite the increased fraction of tunnelling electrons which, at the higher field, complete whole skipping orbits before scattering ($F_0(B_0^-) > F_1(B_1^-)$), the reduced minimum value $|\langle dI/dB \rangle_0^-| < |\langle dI/dB \rangle_1^-|$ predicted by equation (5.55) as a consequence of the lower transition rate $W_0(B_0^-)$, is reflected in the diminished $n = 0 - p_F$ oscillatory amplitude, clearly revealed in Figure 5.22. Weakening of the $-p_F$ series as the decreasing transmission coefficients $T_n(B_n^-)$ dominate the transition rate at

high voltages and magnetic fields, is apparent in the second derivative curve 5.1 measured for V = 100 mV, and is also clearly reproduced in the derivatives 5.21a, 5.22 and 5.24 calculated for V = 100 mV and V = 125 mV.

5.13.3 The effect of increasing voltage on the relative strengths of the $\pm p_F$ series

Comparison of Figures 5.11b and 5.17b shows that for given n, $T_n(B)$ increases more rapidly with field at higher voltages. The barrier transmission increases as the orbit centre X_{k_y} moves closer to the barrier with increasing field, thereby reducing the mean magnetic potential energy in the barrier region and the total effective barrier height (see Section 5.10.4). At higher voltages, the mean zero-field barrier height is lower (see Figure 5.25) so that a given reduction in mean magnetic potential energy produces a greater fractional reduction in the total effective barrier height, which results in a more dramatic increase in the transmission coefficient $T_n(B)$. The rapid increase of $T_n(B)$ for V = 125 mV is reflected in the shapes of the current contributions $I_n(B)$ which are less symmetrical than for lower voltages (Figures 5.6 and 5.8).

Equation (5.56) predicts that since $D_n(B_n^-)/D_n(B_n^+) \simeq 1/3$ and $F_n(B_n^-)/F_n(B_n^+) \simeq 2$ over the voltage range 25 mV → 125 mV (Figures 5.9b, 5.11a, 5.15b and 5.17a), the ratio of $\pm p_F$ extrema arising from the opening and closure of the n^{th} tunnelling channel is approximately

$$\frac{\langle dI/dB\rangle_n^-}{\langle dI/dB\rangle_n^+} = \frac{T_n(B_n^-)}{T_n(B_n^+)} \quad . \qquad (5.60)$$

It follows that at higher voltages, the increased transmission coefficient ratio $T_n(B_n^-)/T_n(B_n^+)$ will cause the $+p_F$ series of oscillatory structure to diminish relative to the $-p_F$. Such weakening of the $+p_F$ series with increasing voltage is visible in both the measured derivatives 5.1 and 5.3 and the corresponding simulated curves shown in Figures 5.20, 5.21, 5.22, 5.23 and 5.24.

5.14 Summary

The current $\underline{I}$ which flows as a result of tunnelling transitions from perturbed 2DEG states in the LH (emitter) contact into magneto-quantised interfacial states in the RH (collector) contact of asymmetrically-doped (InGa)As/InP single-barrier structures under forward bias and with $\underline{B} \perp \underline{I}$, has been calculated within the transfer-Hamiltonian formalism. In this transverse field geometry, the requirements of total energy and transverse wavevector conservation gives rise to two distinct ($\pm p_F$) series of oscillations in the simulated I(B) characteristics and derivatives. These oscillations occur at the resonant fields $B_n^{\pm}$ for which 2DEG electrons with transverse momentum $m_L^*\langle v_y\rangle = p_y' = \pm\hbar k_F$ tunnel into the n^{th} interfacial state. Good agreement is obtained between the measured fundamental fields $B_{F\pm}(V)$, equal to the inverse periodicities of the

$\pm p_F$ series plotted as a function of 1/B, and theoretical values calculated using WKB interfacial Landau levels, in the limit of an infinite conduction band offset, and taking the nonparabolicity parameter of (InGa)As to be $\alpha = 1.3\ eV^{-1}$. The fundamental fields predicted for $\pm k_F$ transitions into bulk Landau levels cannot be reconciled with the data for any reasonable value of α. This is not surprising, however, since the Fermi energy of the 2DEG is insufficient to allow such transitions into bulk Landau states.

The simulated I(B) characteristics reproduce all the qualitative features of the measured curves. In particular, quenching of the current is predicted for field values $B \geq B_0^-(V)$, above which there are no intercepts in the E-k_y plane between the occupied 2DEG and interfacial Landau state dispersion curves. The predicted values of $B_0^-(V)$ are, however, generally lower than observed owing to inaccuracies of the WKB interfacial Landau levels in the quantum limit n = 0, and also, at high fields, in the perturbation calculation of the 2DEG energy levels.

Approximate analytical expressions can be obtained for the extremal values of magneto-current derivatives <dI/dB>, calculated using the same averaging procedure as the measured curves. These extremal values $\langle dI/dB \rangle_n^{\pm}$ are directly proportional to the density of states factors $D_n(B_n^{\pm})$, interfacial skipping frequencies $F_n(B_n^{\pm})$ and

barrier transmission coefficients $T_n(B_n^{\pm})$, of 2DEG electrons with $k_y'(n) = \pm k_F$. Thus, the field-dependence of the oscillatory amplitudes gives information about the effect of the field on electronic motion in the n^+ layer and also on the barrier transmission coefficient.

High skipping frequencies correspond, for large n, to widely spaced, well resolved, interfacial Landau levels. The averaging procedure simulates the effect of level broadening by suppressing high frequency oscillatory structure ($B_n^{\pm} - B_{n-1}^{\pm}$ small) originating from closely spaced interfacial Landau levels.

Both the $\pm p_F$ series of oscillations are visible in the simulated derivatives over clearly separated field ranges, in good agreement with experiment. The $+p_F$ series dominates the oscillatory structure at low fields ($B \leq B_0^+$) because the difference in orbit centre positions, $X_+ < X_-$, ensures that the skipping frequency $F_n(B_n^+)$ of $+k_F$ interfacial electrons exceeds that of $-k_F$ electrons tunnelling at a comparable magnetic field $B_m^- \simeq B_n^+$. Since $F_n(B_n^+ \simeq B_m^-) > F_m(B_m^-)$, a greater fraction of the $+k_F$ electrons complete whole cyclotron orbits before scattering, thereby giving rise to more pronounced oscillatory structure. In addition, the absolute change Δv, in the mean y-component of velocity is smaller for the $+k_F$ electrons. The density of states factor $D_n(B) \propto \Delta v^{-1}$ is therefore higher for $+k_F$ transitions, which, from equation (5.55), also contributes to the dominance of the $+p_F$ series at low fields.

In general, both the simulated and measured $\pm p_F$ series of oscillations strengthen with increasing field. This trend reflects that of the skipping frequencies $F_n(B_n^{\pm})$, which increase with field as the skipping arclength contracts whilst the orbital speed remains the same. At low voltages, the $\pm k_F$ skipping frequencies rise so rapidly with field that the transition rates, and consequently the extremal values $\langle dI/dB \rangle_n^{\pm}$ also increase.

In addition, a greater fraction of the tunnelling electrons complete whole skipping orbits before scattering, thereby giving rise to more pronounced oscillatory structure.

At higher voltages however, the magnetic potential makes a greater percentage contribution to the total effective barrier height, so that the rapid decrease in barrier transmission which occurs at high fields, is reflected in reduced transition rates and ultimately in diminished $-p_F$ oscillatory amplitudes of both the measured and simulated derivatives.

The transmission coefficient ratio $T_m(B_m^-)/T_n(B_n^+)$ of $\pm k_F$ electrons tunnelling at adjacent resonant fields $B_n^+ \simeq B_m^-$, increases with voltage as the difference in mean magnetic potential experienced by the $\pm k_F$ electrons produces a greater percentage difference in the total effective barrier heights. This effect gives rise to visible weakening of both the simulated and measured $+p_F$ oscillations with

increasing voltage, and is central to the explanation, given in Chapter 6, for the absence of $+p_F$ structure in the I(B) characteristics of similar GaAs/(AlGa)As structures, measured at high voltages ($V \geq 200$ mV).

Gueret et al. (1987) accurately described transverse magneto-tunnelling phenomena in devices containing low and wide barriers by considering the effect of the field on the barrier height and transmission coefficient only.

Within this approximation, equation (5.56) predicts that both the $\pm p_F$ oscillatory amplitudes will decrease with increasing field, as the mean magnetic potential energy in the barrier region increases, and the transmission coefficient falls. In addition, the $-k_F$ electrons have higher transmission coefficients, and are therefore expected to give rise to dominant oscillatory structure at low fields ($\leq B_0^+$). Thus, the measurements of Snell et al. (1987) on structures containing a high and narrow barrier can only be explained if the effect of the magnetic field on both the effective barrier height, and on the amplitudes $\psi_n(0_+)$ of the magneto-quantised wavefunctions (or equivalently the semiclassical skipping frequencies), is considered (Fromhold et al., 1990).

CHAPTER SIX

TRANSVERSE MAGNETOTUNNELLING IN ASYMMETRICALLY-DOPED GaAs/(AlGa)As SINGLE-BARRIER HETEROSTRUCTURES

6.1 Introduction

The first experimental investigation of transverse magneto-tunnelling in asymmetrically-doped single-barrier structures was reported by Hickmott (1987) for GaAs/($Al_{0.3}Ga_{0.6}$)As-based samples. Under forward-bias, a single series of oscillatory structure is observed in both the I(V) (Hickmott, 1987) and I(B) (Hickmott, 1988) characteristics, and more clearly in their derivatives. Hickmott (1987) attributed the origin of these oscillations to electrons at the Fermi level in the 2DEG tunnelling into bulk Landau levels in the n^+ collector, although the oscillatory periodicities predicted by this model are in poor agreement with experiment (see Section 6.5.2)

However, in Section 6.4, the observation of only one ($-p_F$) series of oscillatory structure in the I(B) curves and derivatives is shown to be fully consistent with the model of tunnelling into interfacial Landau states developed in Chapter 5. The absence of the $+p_F$ series of oscillations is due to the comparatively high voltages ($V \geq 200$ mV) required to obtain a measurable tunnel current in the GaAs/ (AlGa)As structures, which contain higher and wider potential barriers than the (InGa)As/InP samples considered in Chapter 5.

In Section 6.5.2, the periodicity of the single ($-p_F$) series of oscillations revealed in the simulated LnI(V) characteristics of the GaAs/(AlGa)As structures is also shown to be in good agreement with experiment.

6.2 Sample Construction

The composition of the GaAs/(AlGa)As single-barrier structures is described generally in Chapter 2 and is similar to that of the (InGa)As/InP samples specified in Section 5.2.

The nominal doping concentrations of the n^- emitter and n^+ collector contacts are 1.7×10^{21} m^{-3} and 9×10^{23} m^{-3} respectively.

Taking the conduction band-edge effective mass and non-parabolicity factor of GaAs to be $m^*_L = 0.067\ m_o$ and $\alpha = 0.834$ eV^{-1} respectively (Heiblum et al., 1987), the Fermi energy of the 3DEG formed in the n^+ contact is, from equation (2.1), $E_{FR} \cong 44$ meV. The width of the (AlGa)As barrier layer is 230 Å and the conduction band offset is approximately 300 meV (Hickmott et al., 1985). The conduction band-edge mass of (AlGa)As is taken to be $m^*_B = 0.1\ m_o$.

For forward-bias voltages $V \geq 100$ mV, the measured differential capacitance per unit area is approximately constant and equal to $C \cong 2.93 \times 10^{-3}$ F m^{-2} (Hickmott, 1988).

The 2DEG sheet electron concentration $n_s(V)$ is obtained using this value of C in equation (2.27), together with the measured flat-band voltage V_{FB} = 30 mV (Hickmott, 1988), which reveals the existence of negative space charge in the barrier region. The conduction band profile $E_c(x)$ is determined for given $n_s(V)$ by solving Poisson's equation throughout the device, as described in Chapter 2.

It should be noted that owing to the higher applied voltages, band bending in the n^+ layer of the GaAs/(AlGa)As structures is likely to be more pronounced than in the (InGa)As/InP structures. This band bending is further enhanced by the existence of negative space charge in the (AlGa)As barrier region (Hickmott, 1988), which increases the electric field and electrostatic potential energy at the RH barrier interface. By contrast, positive space charge in the InP barriers reduces band bending in the n^+ layer. Thus, the interfacial Landau levels and associated wavefunctions, which are calculated assuming $E_c(x)$ = 0 throughout the n^+ layer, are expected to be less accurate for the GaAs/(AlGa)As structures. It follows that the calculated tunnel current, which depends implicitly on the interfacial Landau levels, will also be less accurate for the GaAs/(AlGa)As structures.

6.3 Features of the Measured I(B) and d^2I/dB^2 Curves

Figure 6.1 shows normalised I(B) characteristics of the GaAs/(AlGa)As structures measured for a range of forward-bias voltages. Just as for the (InGa)As/InP samples, the tunnel current falls rapidly, almost to zero, with increasing magnetic field. For B $\geq$ 7 T, weak oscillatory structure is observed superimposed on this fall off, which is more clearly revealed in the second derivative curves shown in Figure 6.2. Only one series of oscillations is present, which is notably weaker than for the (InGa)As/InP structures (Figures 5.1 and 5.3).

6.4 Calculation of the Current-field Characteristics and Interpretation of the Oscillatory Structure revealed in the Simulated Derivative Curves

6.4.1 Simulation of the I(B) curves and derivatives

As for the (InGa)As/InP samples, tunnelling into bulk Landau levels does not occur because the electrons in the 2DEG have insufficient transverse momentum (small k_F). This is easily proven by showing that the device parameters given in Section 6.2 lead to violation of inequality (5.22).

Equation (5.11) gives the current flowing in transitions from the 2DEG into interfacial Landau states in the n^+ collector. Care must be taken when evaluating this current for the comparatively high

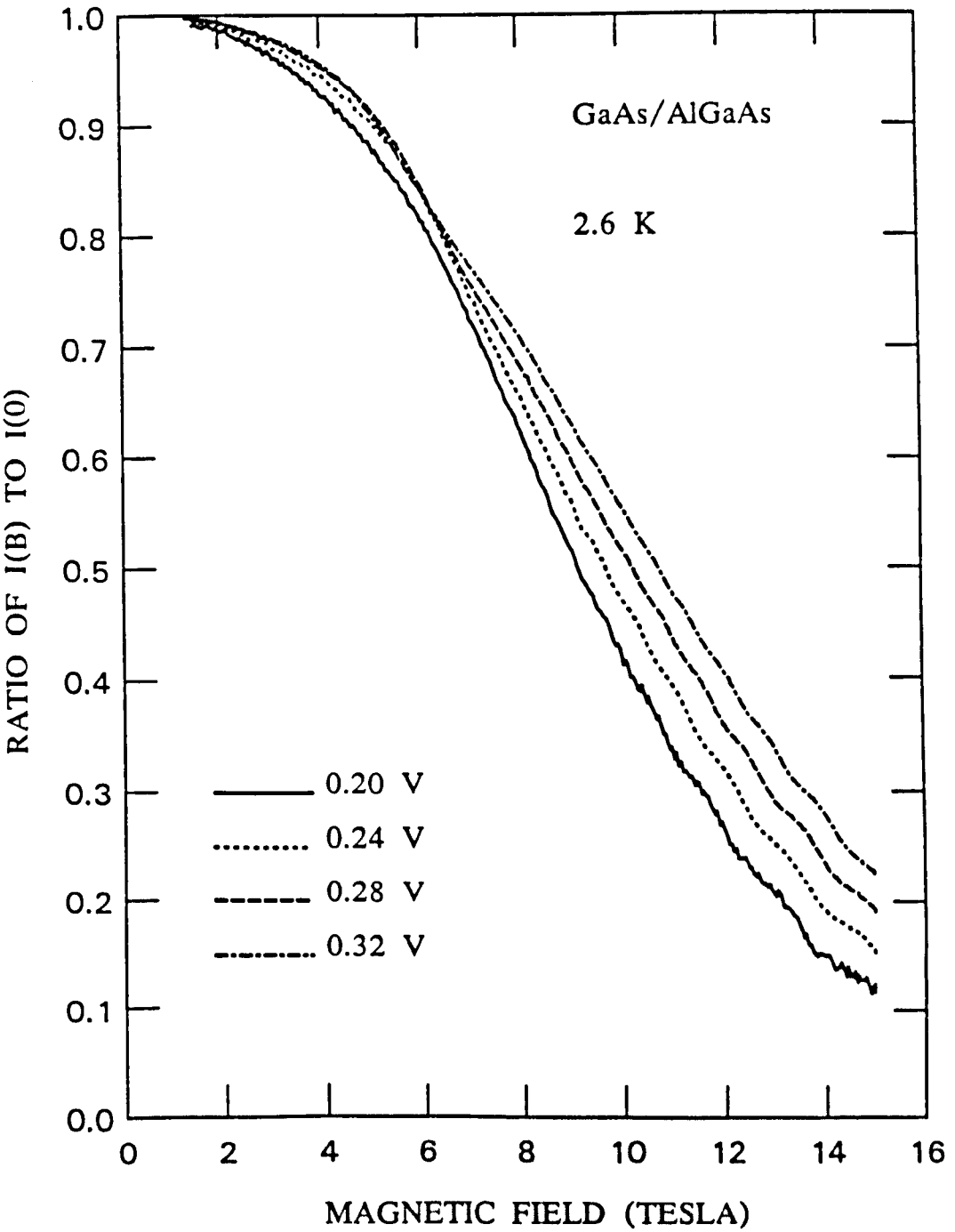

Figure 6.1 Current-field characteristics of the GaAs/(AlGa)As single-barrier structures measured for a variety of forward-bias voltages (Hickmott, 1988).

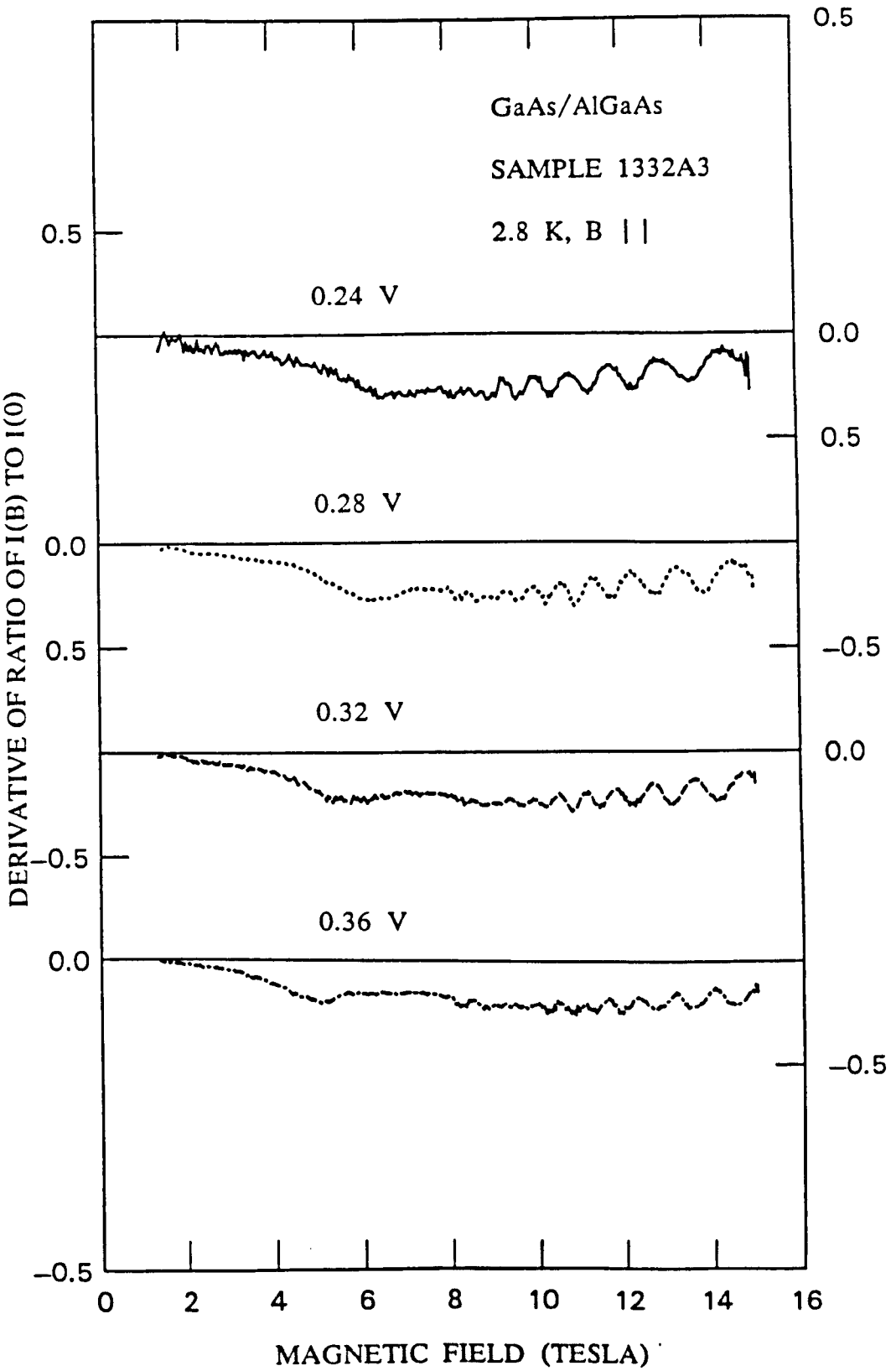

Figure 6.2 Second derivative curves d^2I/dB^2 of the GaAs/(AlGa)As single-barrier structures measured for a variety of forward-bias voltages (Hickmott, 1988).

bias voltages used in the experiments of Hickmott since, for $V \geq 260$ mV, $E_c(0-) < eV + E_{FR}$ so that electrons close to the Fermi level of the 2DEG may tunnel into travelling wave states above the top RHS of the potential barrier (Fowler and Nordheim, 1928). To avoid problems associated with imaginary values of the decay function $\mu_{n1}(0-)$ in this high-voltage regime, the interfacial Landau levels are calculated from equation (4.43) within the infinite barrier approximation $\mu_{n1}(0-) \to \infty$, which is reasonably accurate for large n.

In addition, the squared transition matrix elements $|M_n(k_y)|^2$ are calculated for $V \geq 260$ mV by assuming that the electrons tunnel through a rectangular potential barrier of width $b + \ell$ where ℓ is the classical turning point in the barrier region given by

$$E_c(\ell) + \frac{B^2e^2}{2m_B^*}\left(\ell + \frac{\hbar k_y}{Be}\right)^2 = E_n(k_y) \quad . \qquad (6.1)$$

The (constant) effective barrier height is taken to be the mean potential energy between $x = -b$ and $x = \ell$. This simplification retains the essential physics and avoids problems arising from otherwise divergent WKB wavefunctions (4.32).

Figure 6.3 shows theoretical I(B) curves calculated from equation (5.11) for a variety of forward-bias voltages. The shapes of these curves are in good qualitative agreement with the measured characteristics shown in Figure 6.1. The superimposed oscillatory

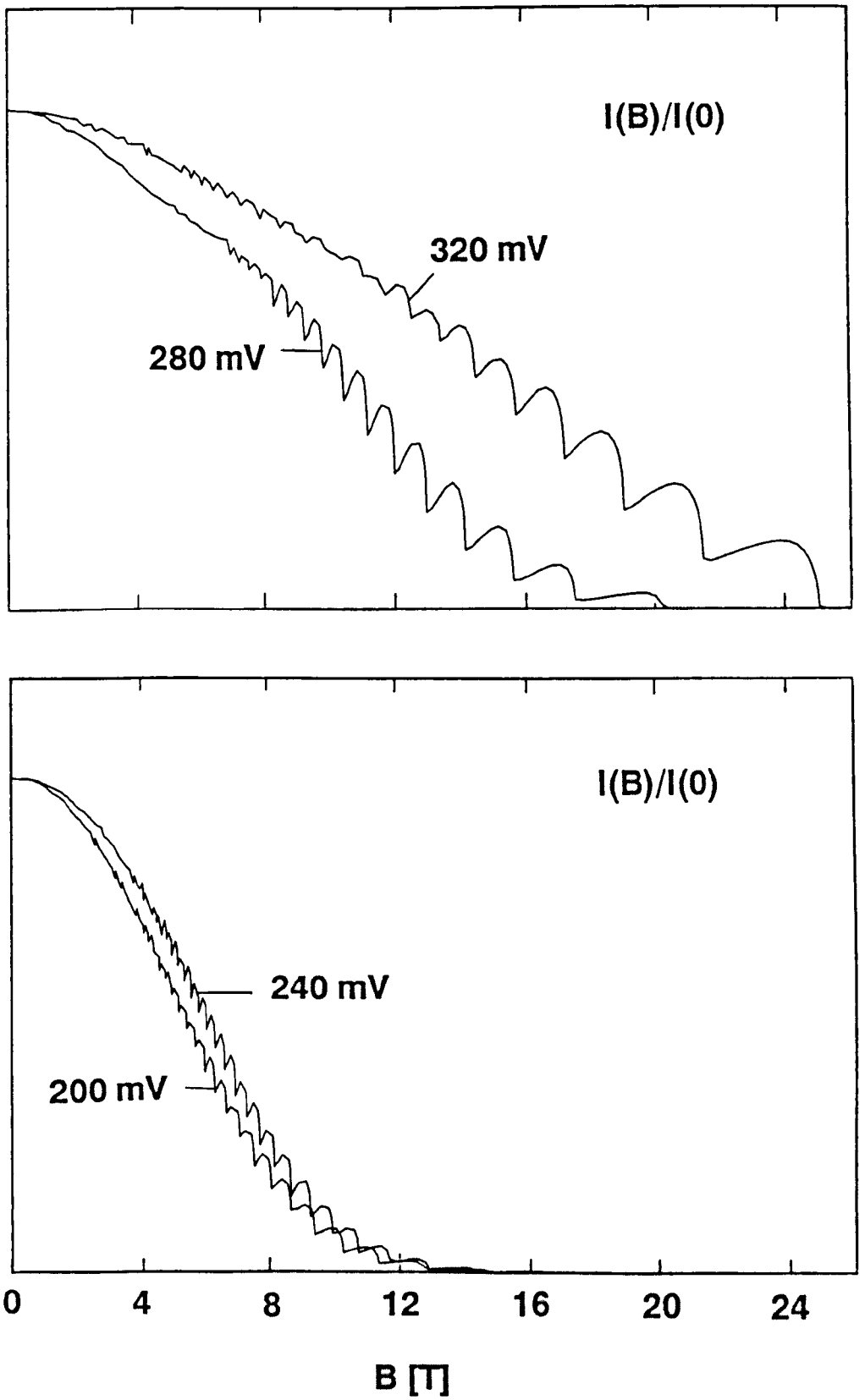

Figure 6.3 Current-field characteristics of the GaAs/(AlGa)As single-barrier structures calculated for several foward-bias voltages, taking the conduction band nonparabolicity parameter of GaAs to be $\alpha = 1.1\ eV^{-1}$.

structure is emphasised in the second derivative curves shown in Figure 6.4. These derivatives are calculated following the averaging procedure described in Section 5.11.2, taking $\Delta B = 0.2$ T.

The qualitative field-dependence of the extremal values of $\langle d^2I/dB^2 \rangle$ reflects that of the averaged first derivative curve $\langle dI/dB \rangle$, shown for V = 240 mV in Figure 6.5, together with the individual current contributions $I_n(B)$. This first derivative is calculated using exact interfacial Landau levels and transition matrix elements (5.38), since V = 240 mV is below the threshold for Fowler-Nordheim tunnelling.

Each current contribution $I_n(B)$ increases dramatically over the field range $B_n^+ \leq B \leq B_n^-$, reflecting the behaviour of the corresponding transmission coefficient $T_n(B)$ shown for V = 240 mV in Figure 6.6b.

As explained in Section 5.13.3, the application of a high forward-bias voltage, reduces the mean zero-field barrier height. Consequently, the reduction in mean magnetic potential in the barrier region which occurs as the orbit centre moves towards the barrier with increasing field $> B_n^+$ (see Section 5.10.4), produces a large percentage reduction in the total effective barrier height, causing the dramatic increase of both $T_n(B)$ and $I_n(B)$.

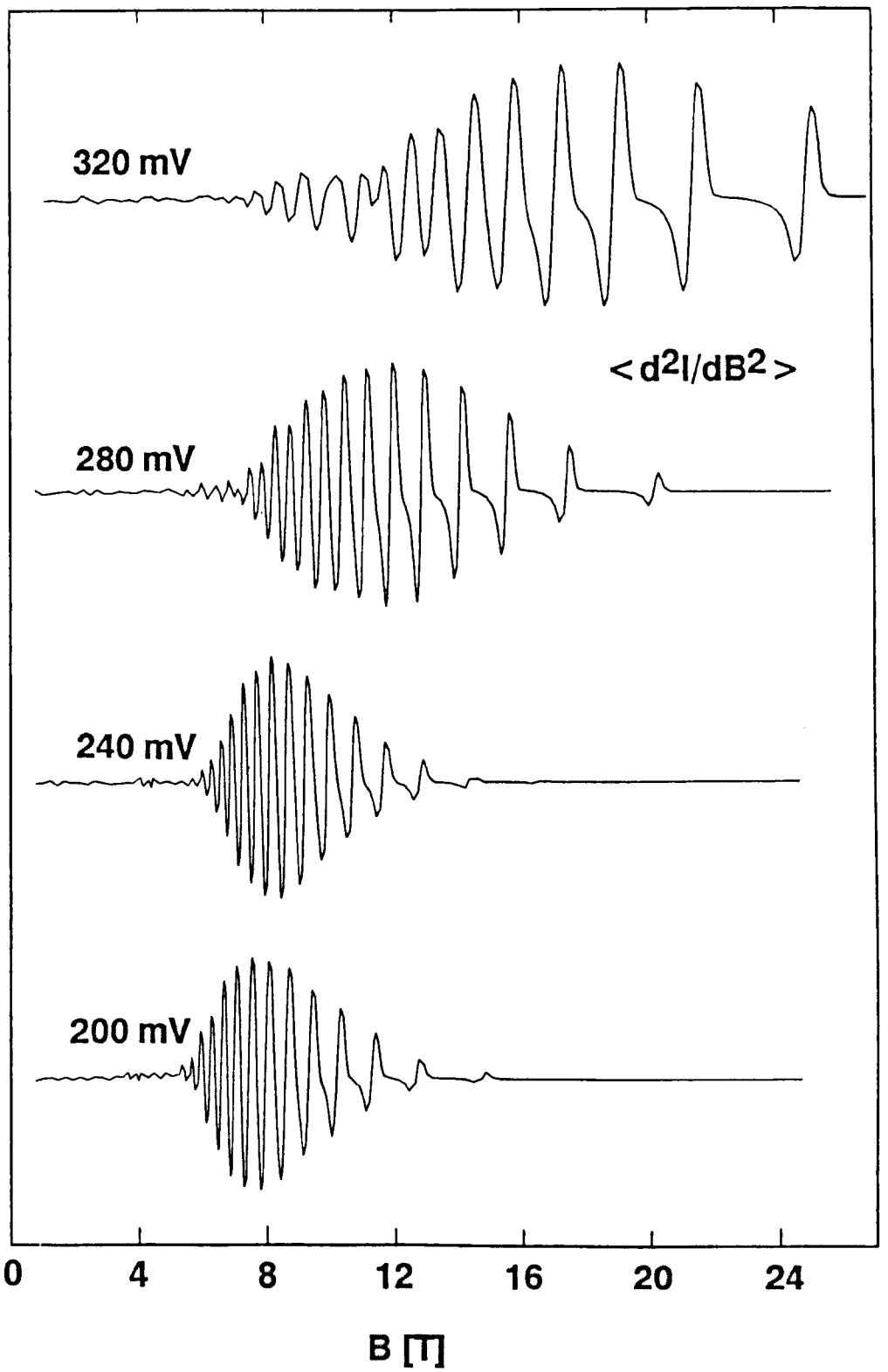

Figure 6.4 Simulated $\langle d^2I/dB^2 \rangle$ characteristics of the GaAs/(AlGa)As single-barrier structures, calculated for several forward-bias voltages taking $\alpha = 1.1\ eV^{-1}$. Only one ($-p_F$) series of oscillations is revealed in each curve.

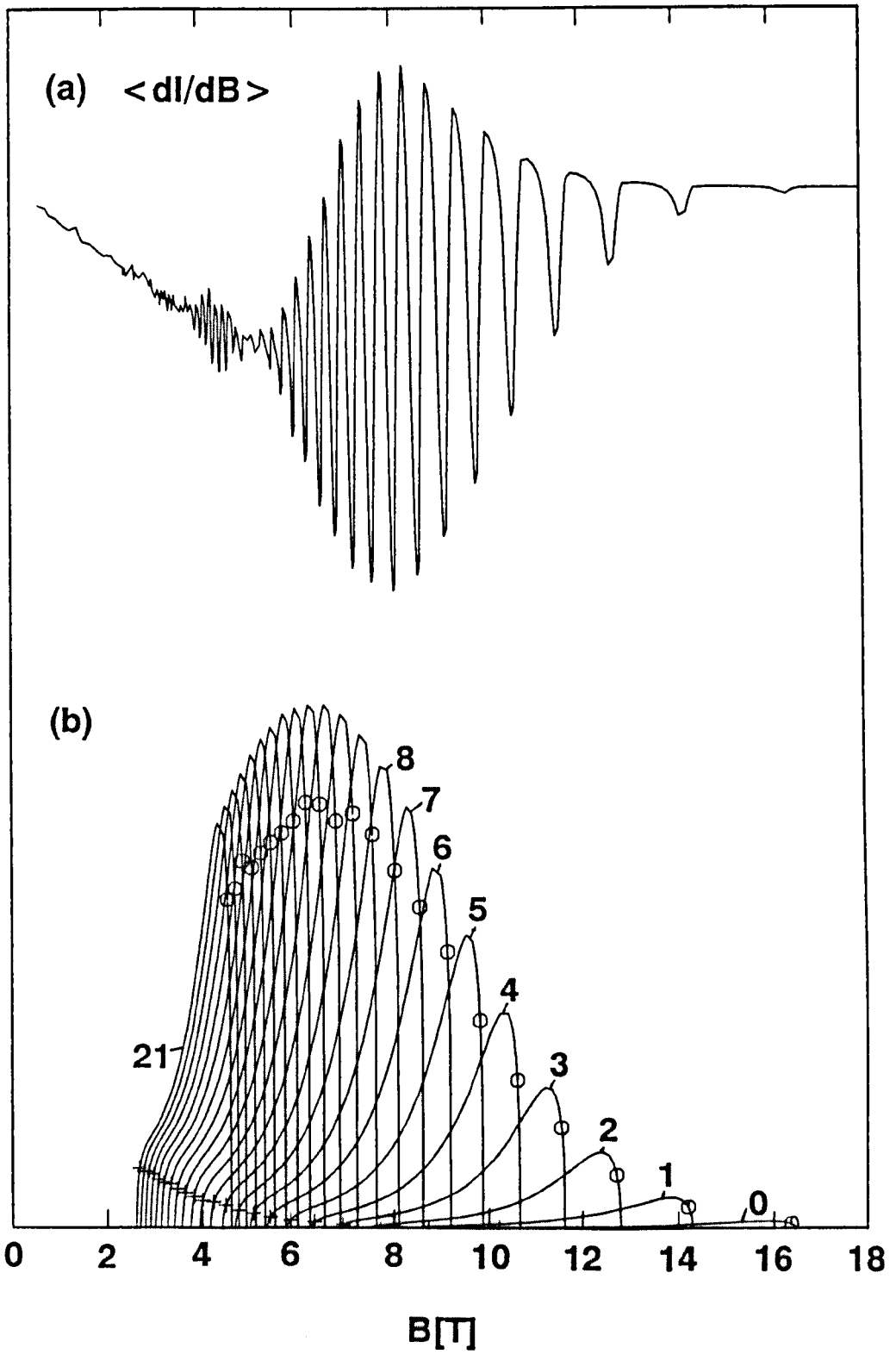

Figure 6.5 (a) Simulated <dI/dB> characteristic of the GaAs/(AlGa)As single-barrier structures calculated for V = 240 mV, taking $\alpha = 1.1\ eV^{-1}$ and $\Delta B = 0.2$ T. Only one ($-p_F$) series of oscillatory structure is revealed. (b) Individual current contributions $I_n(B)$, n = 0, 1, ... 21, calculated over the field ranges $B_n^+ \leq B \leq B_n^-$. The mean current values $\bar{I}_n^+$ ($\bar{I}_n^-$) are indicated by crosses (open circles).

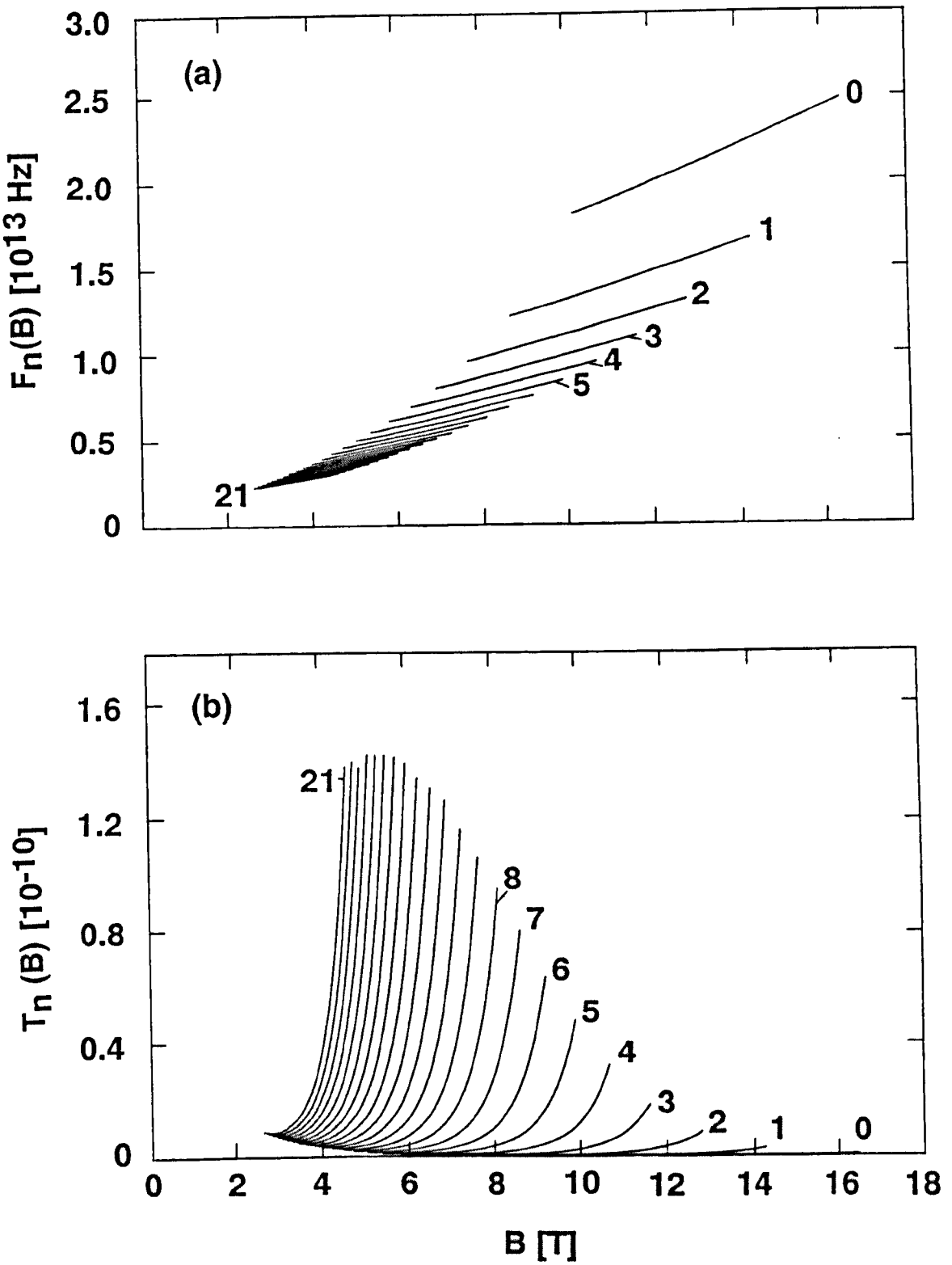

Figure 6.6 (a) Semiclassical skipping frequencies $F_n(B)$, and (b) Barrier transmission coefficients $T_n(B)$, n = 0, 1, ... 21, of the GaAs/(AlGa)As structures calculated for V = 240 mV over the field ranges $B_n^+ \leq B \leq B_n^-$.

6.4.2 Verification of the predicted correlation between the $-p_F$ extrema $\langle dI/dB\rangle_n^-$ and the mean current values $\bar{I}_n^-$

It is clear from Figure 6.5 that the oscillatory structure in $\langle dI/dB\rangle$ originates from the closure of tunnelling channels, which gives rise to a series of $-p_F$ minima whenever $B = B_n^-$.

Provided the separation between adjacent resonant fields greatly exceeds the averaging bin width $\Delta B = 0.2$ T (which for 240 mV is the case for $B \geq 7$ T), equation (5.54) predicts direct proportionality between the extremal values $\langle dI/dB\rangle_n^\pm$ of $\langle dI/dB\rangle$ and the corresponding mean values $\bar{I}_n^\pm$ of $I_n(B)$, evaluated over the field ranges $B_n^\pm \rightarrow B_n^\pm \pm \Delta B$.

The predicted correlation $\langle dI/dB\rangle_n^- \propto \bar{I}_n^-$ is clearly revealed in Figure 6.5, with both sets of values attaining a maximum for $B \cong 8$ T. Below 8 T, the oscillatory amplitudes in $\langle dI/dB\rangle$ decrease with field, partly reflecting the diminished values of $\bar{I}_n^-$, and also partly because reduced separation between adjacent $-p_F$ resonant fields leads to increased smoothing.

Owing to the slow increase of each current contribution $I_n(B)$ with increasing field just above B_n^+, the values of $\bar{I}_n^+$ are much lower than $\bar{I}_m^-$, for all $B \leq B_0^+$. Equation (5.54) therefore predicts that $+p_F$ oscillatory maxima in $\langle dI/dB\rangle$, associated with the opening of new tunnelling channels, will be small compared with $-p_F$ minima resulting

from channel closure. In fact, no $^{+}p_F$ oscillatory structure is present in the simulated <dI/dB> curve 6.5a, in good agreement with experiment.

6.4.3 Physical explanation for the absence of $^{+}P_F$ oscillations

The variation of $\bar{I}_n^{\pm}$, and consequently of the extremal values $\langle dI/dB\rangle_n^{\pm}$, is most easily understood in physical terms by considering the factors $N_n(B) = (k_F^2 - k_y'^2(n))^{\frac{1}{2}}$, $D_n(B) = |\hbar^2 k_y'/m^*_L - dE_n/dk_y|^{-1}$ and $W_n(B) = 2\pi|M_n(k_y)|^2/\hbar$ of $I_n(B)$, which are shown for V = 240 mV in Figures 6.7 and 6.8. The normalised transition rates $W_n(B)$ are proportional to the product of the barrier transmission coefficients $T_n(B)$ and the interfacial state skipping frequencies $F_n(B)$ which are shown for V = 240 mV in Figure 6.6. The qualitative features of each set of curves were explained in Section 5.10 with reference to the (InGa)As/InP structures.

Equation (5.55) predicts that the magnitudes of $\bar{I}_n^{\pm}$ and $\langle dI/dB\rangle_n^{\pm}$ are proportional to the product of the mean values $\bar{N}_n^{\pm}$, the density of states factors $D_n(B_n^{\pm})$ and the normalised transition rates $W_n(B_n^{\pm})$ of 2DEG electrons with transverse momentum $p_y' = \pm p_F$. Since the values of $\bar{N}_n^{\pm}$ shown in Figure 6.7a vary slowly with n, this relation may be written

$$\langle dI/dB\rangle_n^{\pm} \propto \bar{I}_n^{\pm} \propto D_n(B_n^{\pm})\, W_n(B_n^{\pm}) \propto D_n(B_n^{\pm})\, F_n(B_n^{\pm})\, T_n(B_n^{\pm}) \qquad (6.2)$$

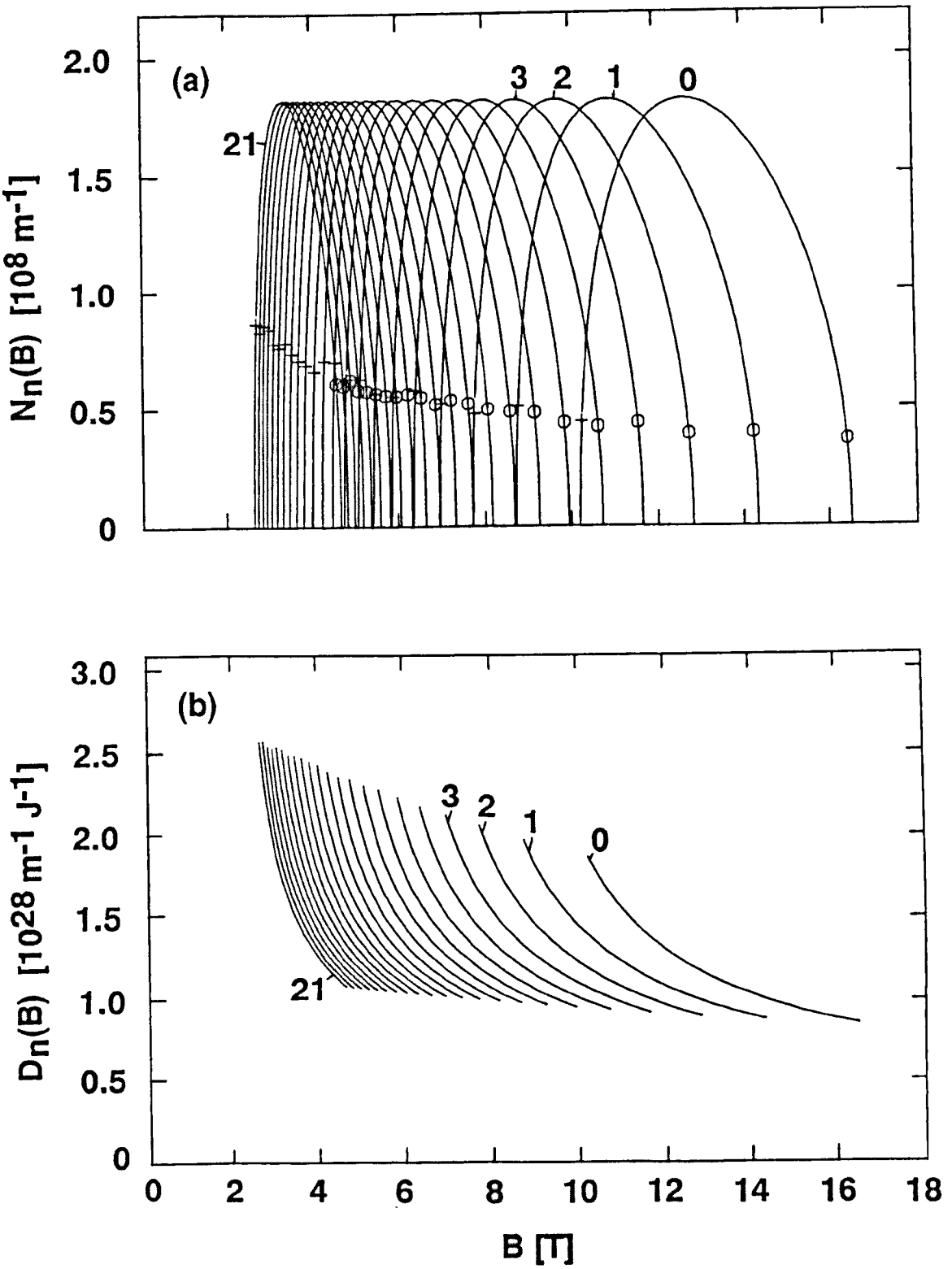

Figure 6.7 The factors (a) $N_n(B)$ and (b) $D_n(B)$, n = 0, 1, ... 21, calculated for V = 240 mV over the field ranges $B_n^+ \leq B \leq B_n^-$. The mean values $\bar{N}_n^+$ ($\bar{N}_n^-$) are indicated by crosses (open circles).

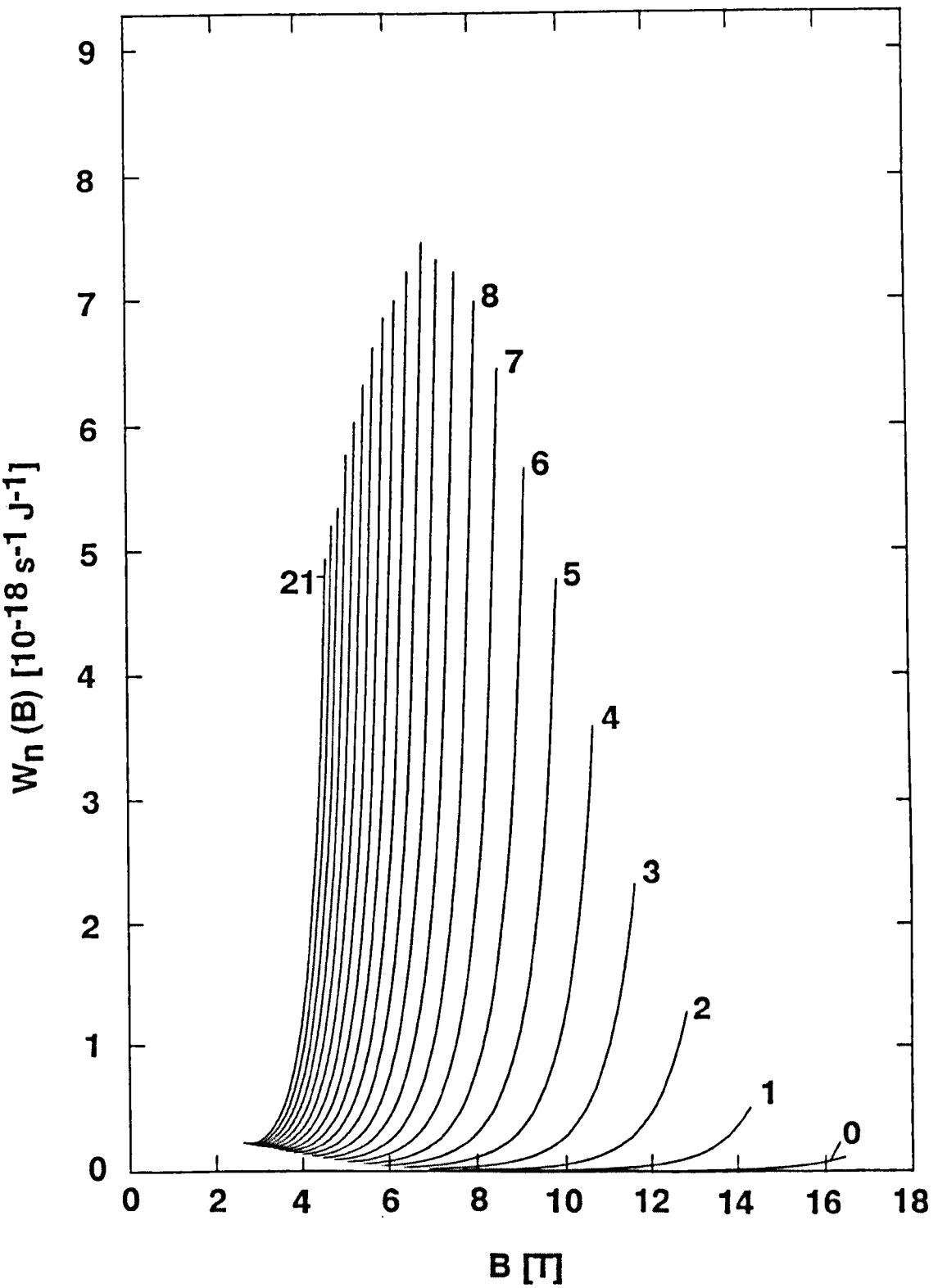

Figure 6.8 The normalised transition rates $W_n(B)$, n = 0, 1, ... 21, of the GaAs/(AlGa)As structures calculated for V = 240 mV over the field ranges $B_n^+ \leq B \leq B_n^-$.

Figure 6.7b shows that for adjacent resonant fields $B_n^+ \cong B_m^-$, $D_n(B_n^+) \cong 2D_m\,(B_m^-)$, the difference being primarily due to the opposite slopes at either extremity of the 2DEG parabola. This disparity is, however, small compared to that of the corresponding transition rates; Figure 6.8 shows that $W_m(B_m^-) >> W_n(B_n^+)$ for all $B_n^+ \cong B_m^-$. Equation (6.2) therefore predicts $\bar{I}_m^- >> \bar{I}_n^+$, as observed in Figure 6.5, and also

$$\langle dI/dB \rangle_m^- >> \langle dI/dB \rangle_n^+ \quad , \tag{6.3}$$

so that the $-p_F$ series is expected to totally dominate the oscillatory structure.

By contrast, in the (InGa)As/InP structures the $\pm k_F$ transition rates are of comparable magnitude (see Figures 5.10 and 5.16). Thus, in these samples, the $+p_F$ series dominates the oscillatory structure at low fields owing to the favourable density of states factors $D_n(B_n^+) \cong 2D_n(B_m^-)$ and skipping frequencies $F_n(B_n^+) \cong 2F_m(B_m^-)$.

Comparison of Figures 5.11a, 5.17a and 6.6a reveals that $F_n(B_n^+ \cong B_m^-) \cong 2F_m(B_m^-)$ for both the (InGa)As/InP and the GaAs/(AlGa)As samples, independent of voltage. Since $W_n(B_n^\pm) \propto F_n(B_n^\pm)\, T_n(B_n^\pm)$, it follows that the ratio $W_m(B_m^-)/W_n(B_n^+)$ of $\pm k_F$ transition rates is higher for the GaAs/(AlGa)As structures simply

because the transmission coefficient ratio $T_m(B_m^-)/T_n(B_n^+)$ is also higher (see Figures 5.11b, 5.17b and 6.6b). This ratio is so much higher for the GaAs/(AlGa)As samples because they are measured at higher voltages. Consequently, the mean zero-field barrier height is lower, so that the difference between the mean magnetic potential energies $\bar{E}^{\pm}_{MAG}$ experienced by $\pm k_F$ electrons tunnelling at comparable magnetic fields produces a greater fractional difference in the total effective barrier heights and transmission coefficients (see Section 5.13.1).

This can be seen by comparing the conduction band and magnetic potential energy profiles experienced by $\pm k_F$ electrons tunnelling at adjacent resonant fields in the (InGa)As/InP structures (Figure 5.25) and GaAs/(AlGa)As structures (Figure 6.9). The mean zero-field barrier height $\bar{E}_o$ in the (InGa)As/InP structures is ≈ 190 meV for V = 25 mV and 120 meV for V = 125 mV, and in the GaAs/(AlGa)As structures is ≈ 100 meV for V = 240 mV. In addition, the resonant fields generally increase with voltage, so that for the (InGa)As/InP structures $\bar{E}^{+}_{MAG} - \bar{E}^{-}_{MAG} \approx 25$ meV when V = 25 mV and ≈80 meV when V = 125 mV. For the GaAs/(AlGa)As structures $\bar{E}^{+}_{MAG} - \bar{E}^{-}_{MAG} \approx$ 110 meV when V = 240 mV. Thus, equation (5.59) predicts that $T_m(B_m^-)/T_n(B_n^+)$ will be much higher for the GaAs/(AlGa)As structures. The thicker barrier (230 Å compared with 170 Å), and higher effective mass m_B^* (0.1 m_o compared with 0.077 m_o) of the GaAs/(AlGa)As structures also contributes to the increased transmission coefficient ratio (5.59). The absence of $+p_F$ oscillations in the I(B) curves of the GaAs/(AlGa)As structures is therefore partly due to unfavourable barrier parameters.

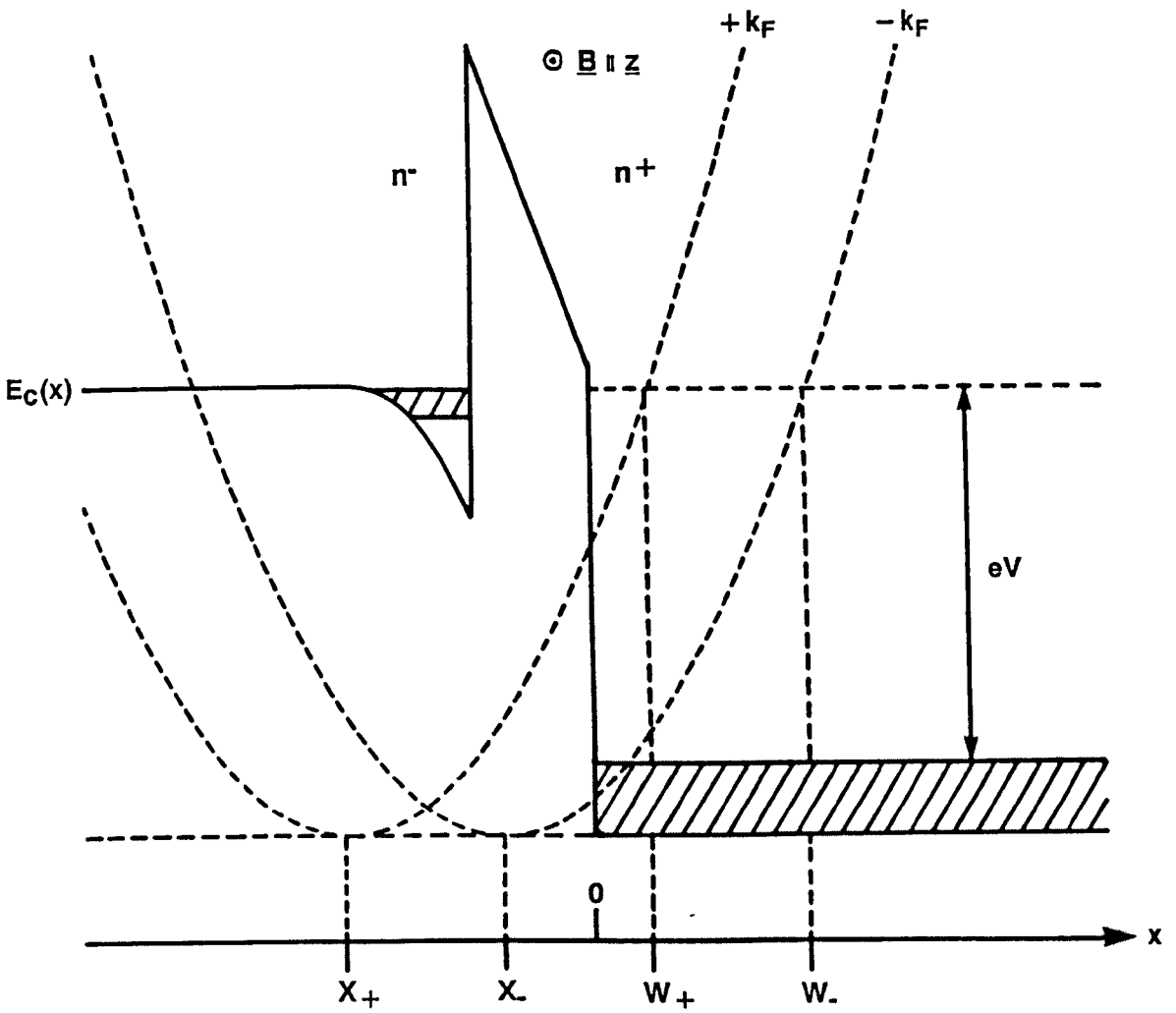

Figure 6.9 Conduction band profile $E_C(x)$ and magnetic potential energy (broken curves) experienced by $\pm k_F$ electrons tunnelling in the GaAs/(AlGa)As structures when V = 240 mV and B = 7.8 T ≅ B_2^+ ≅ B_9^-. The conduction band offset is taken to be 300 meV.

For voltages $V \leq 50$ mV, the $\pm k_F$ transmission coefficients do not dominate the transition rates and simulated derivatives do reveal the ^+p_F series of oscillations (Fromhold et al., 1990a). However, this oscillatory structure has not yet been observed in GaAs/(AlGa)As devices because, owing to the high and wide barriers, the current for $V \leq 100$ mV is below the experimental noise level (Hickmott, 1987).

6.4.4 Predicted field-dependence of the $^-$PF oscillatory amplitudes

Figure 6.7b shows that the density of states factors $D_n(B_n^-)$ vary slowly with n. Equation (6.2) therefore predicts direct proportionality between the oscillatory minima $\langle dI/dB \rangle_n^-$ and the $-k_F$ transition rates $W_n(B_n^-)$. This correlation is clearly revealed in Figures 6.5a and 6.8, with both sets of values reaching a maximum at $B \cong 7$ T.

For fields below 5 T, no oscillatory structure is present in either the simulated or measured derivatives. This is due to conduction band nonparabolicity in the n^+ contact, which leads to closely spaced, and therefore poorly resolved interfacial Landau levels at the high injection energies of ~ 300 meV.

Figure 6.6b shows that the $-k_F$ transmission coefficients $T_n(B_n^-)$ vary slowly over the field range $5 \text{ T} \leq B \leq 7$ T. This is because for this range of field, the orbit centre X_{k_y} lies within the

barrier (see Section 5.10.4) so that the magnetic potential has little effect on the total effective barrier height and transmission coefficient. Over this field range the transition rates $W_n(B_n^-)$ and, from equation (6.2), the oscillatory minima $\langle dI/dB \rangle_n^-$ shown in Figure 6.5 therefore reflect the variation of the skipping frequencies $F_n(B_n^-)$ which, as shown in Figure 6.6a, increase with field owing to contraction of the orbital radius (see Section 5.10.5). Above 7 T, Figures 6.6 and 6.8 show that the variation of the transition rates $W_n(B_n^-)$ is dominated by the rapidly decreasing transmission coefficients, so that the oscillatory minima $\langle dI/dB \rangle_n^-$ also decrease as shown in Figure 6.5.

Although the observed oscillatory structure does not weaken at high fields, as in the simulated derivatives, the predicted threshold fields $\simeq$ 5 T, below which no oscillations are observed are in reasonable agreement with the measured values.

6.4.5 Comparison with other models

Brey et al. (1988a, 1988b), Schulz and Tejedor (1989), and Platero et al. (1990) have also used a transfer-Hamiltonian approach to calculate the I(B) characteristics of the GaAs/(AlGa)As structures measured by Hickmott.

These simulations are based on a calculation of the energy levels $E_n(k_y)$ of the entire structure, rather than the left- and right-hand subsystems. However, self-consistent calculation of these

energy levels, taking into account electrostatic screening by the 2DEG was not attempted. Such screening effects are more easily incorporated in calculations of separate left-hand eigenvalues by using the Fang-Howard wavefunction to model the potential variation throughout the accumulation layer (see Section 4.2).

Allowed transitions between degenerate left- and right-hand eigenstates with the same k_y value are identified by looking for intercepts between the corresponding dispersion curves, as described in Section 5.4. Owing to the repulsion of degenerate levels (see, for example, Merzbacher, 1970), these intercepts appear as anti-crossings in the E-k_y relation of the whole structure. Each anti-crossing corresponds to an allowed tunnelling channel since the amplitude of the associated wavefunctions is appreciable on both sides of the barrier, (Helm et al., 1989, Peeters et al., 1989).

Theoretical I(B) and d^2I/dB^2 curves calculated for V = 400 mV by Schulz and Tejedor (1989) reveal a single series of oscillatory structure, periodic in 1/B, over the field range 10 T $\leq$ B $\leq$ 18 T. This structure originates as anti-crossings in the energy spectrum $E_n(k_y)$ of the entire system rise above the Fermi level in the emitter contact, with increasing field. These oscillations are thus equivalent to the $-p_F$ series described in Section 6.4, which occur as intercepts are lost from the $-k_F$ extremity of the 2DEG parabola. However, owing to the neglect of nonparabolicity in the n^+ contact, and electrostatic screening by the 2DEG on the energy levels of the system, the oscillatory periodicities predicted by Schulz and Tejedor are not in good agreement with the measured values. In

addition, no explanation is given for the field-dependence of the oscillatory amplitudes, which is more easily understood in physical terms using the semiclassical model described in Chapters 5 and 6 of this thesis.

6.5 Analysis of the Oscillatory Structure Observed in the Forward-bias I(V) Characteristics of GaAs/(AlGa)As Single-barrier Structures in a Transverse Magnetic Field

6.5.1 Experimental data

In the previous section, the observation of only one series of oscillatory structure in the I(B) and d^2I/dB^2 characteristics of GaAs/(AlGa)As single-barrier structures measured for $V \geq 200$ mV was shown to be consistent with the model of tunnelling into interfacial Landau states described in Chapter 5.

Hickmott (1987) also observed a single series of oscillations in the current-voltage characteristics of these devices when a uniform transverse magnetic field is applied.

Figure 6.10a shows the logarithm of the difference I(V,B) -I(V,0) between the tunnel current measured for B = 13 T and B = 0 T, as a function of applied foward bias. The first derivative of this curve, shown in Figure 6.10b, clearly reveals a single series of

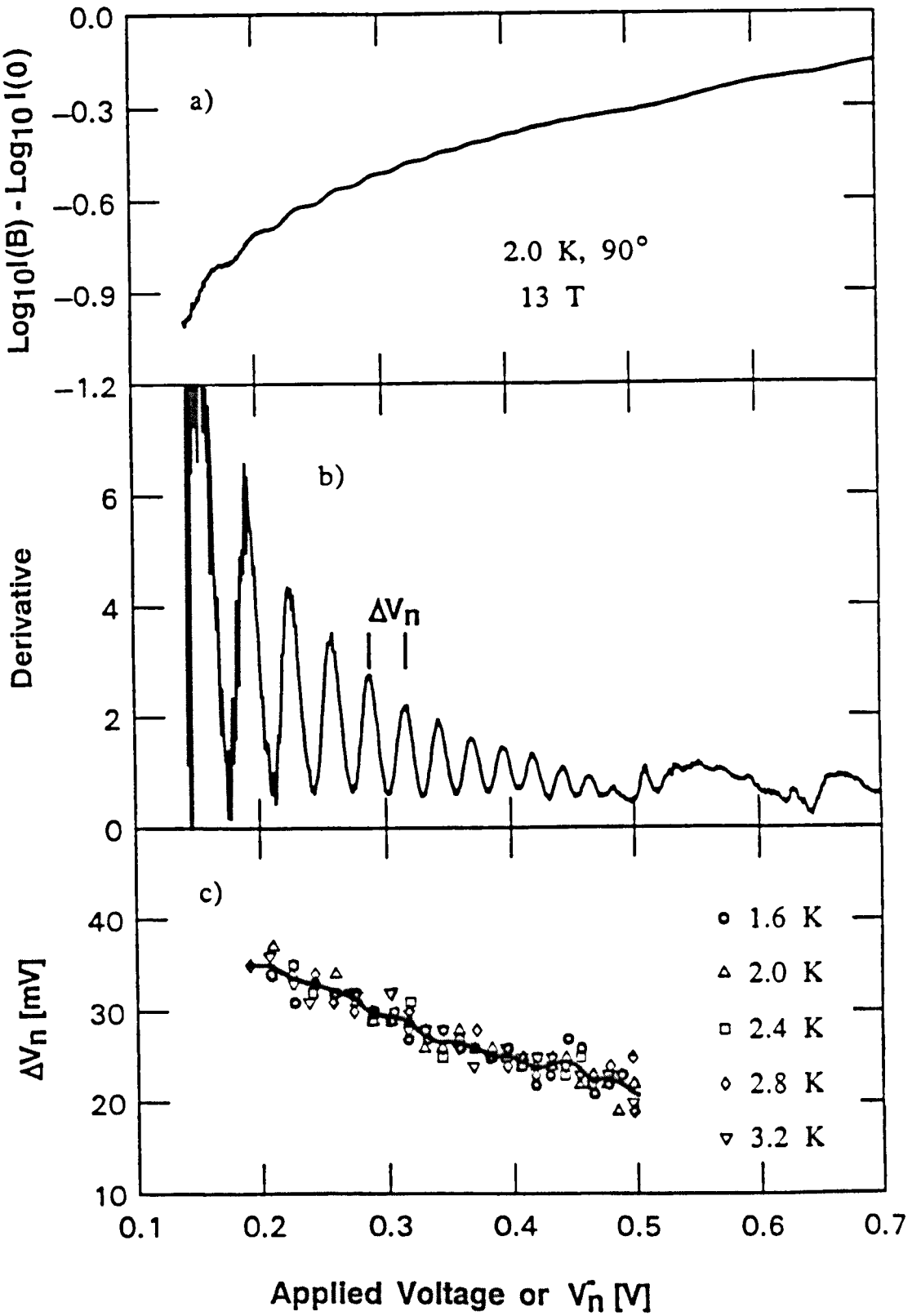

Figure 6.10 (a) Difference between $\log_{10}I$ at 13 T ($\underline{B} \perp \underline{I}$) and $\log_{10}I$ at 0 T as a function of applied voltage. (b) Derivative of difference of $\log_{10}I$ as a function of applied voltage. (c) Separation $\Delta V_n = V_n^- - V_{n-1}^-$ between adjacent maxima in the derivative curve, as a function of V_n^- at different temperatures. Solid line shows the average of the points at each V_n^- (Hickmott, 1987).

oscillatory structure which becomes more closely spaced and decreases in amplitude with increasing voltage.

The separation $\Delta V_n = V_n^- - V_{n-1}^-$ between adjacent maxima in this derivative is plotted in Figure 6.10c as a function of V_n^-, and for a variety of temperatures. The solid line gives the average value of ΔV_n at each V_n^- and shows that the separation between adjacent maxima falls almost linearly with increasing voltage.

6.5.2 Simulation of the I(V) Characteristics

The voltage-dependence of the tunnel current (5.11) flowing into interfacial Landau states arises from changes in the 2DEG and interfacial Landau state dispersion curves, and consequently of the allowed transverse wavevector components $\{k_y(n)\}$.

Changing the voltage modifies the interfacial Landau state wavefunctions through its influence on the electrostatic potential in the barrier region. However, this has little effect on the associated energy levels, particularly those with high n which, from equation (4.43), are fairly insensitive to changes in barrier penetration.

Both the highest ($eV + E_{FR}$) and lowest ($\cong E_{bo}$) occupied 2DEG levels increase almost linearly with voltage so that the 2DEG parabola is shifted to higher energies in the E-k_y plane. In

addition, the mean stand-off distance $3a_0$, and consequently the mean k_y value $k_0 = Be\,(b + 3a_0)/\hbar$ of the occupied 2DEG states both decrease with increasing voltage. It is easily seen from Figure 5.5 that shifting the occupied 2DEG states to higher energies and lower k_y values causes the $-k_F$ extremity of the 2DEG parabola to make successive intersections with higher-index interfacial Landau dispersion curves, resulting in the opening of new conduction channels whenever $V = V_n^-$ and $k_y'(n) = -k_F$.

As the voltage is raised above V_n^-, the intersection with the n^{th} interfacial state dispersion curve moves towards the $+k_F$ extremity of the 2DEG parabola, resulting in closure of the n^{th} tunnelling channel when $V = V_n^+$ and $k_y'(n) = +k_F$. Thus, with increasing voltage, the intersection points move through the 2DEG parabola in the opposite direction as for increasing magnetic field.

It can be shown, using a similar analysis to that given in Appendix 1, that equation (5.11) predicts $dI/dV \to \pm\infty$ whenever $k_y'(n) = \mp k_F$ and $V = V_n^{\mp}$. Consequently the successive opening and closure of tunnelling channels is expected to give rise to two sets of oscillatory structure in dI/dV.

The broken curve in Figure 6.11a shows the natural logarithm of the tunnel current $I(V)$ calculated for $B = 13$ T from equation (5.11), taking the nonparabolicity factor of the n^+ GaAs layer to be $\alpha = 1.1\ eV^{-1}$. This curve is not intended for direct comparison with the experimental curve of Figure 6.10a which shows the logarithm of

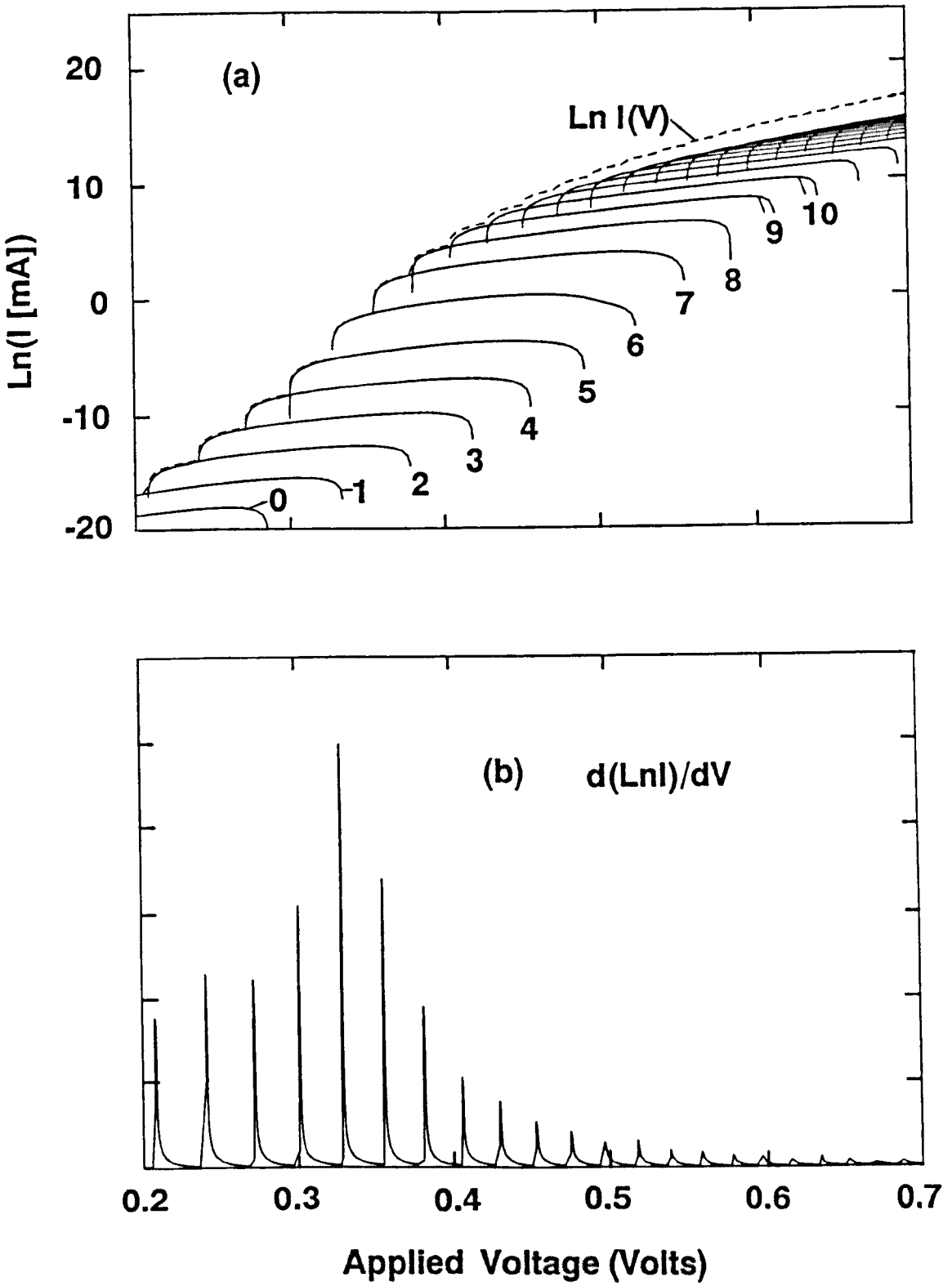

Figure 6.11 (a) Broken curve shows the natural logarithm of the tunnel current LnI calculated as a function of applied voltage when $\underline{B} \perp \underline{I}$ = 13 T, taking α = 1.1 eV^{-1}. The solid curves show the natural logarithm of the individual current contributions $I_n(V)$ n = 0, 1, ... 23, over the field ranges $V_n^- \leq V \leq V_n^+$. (b) Derivative of LnI(V) showing the single ($-p_F$) series of oscillatory maxima which occur when $V = V_n^-$.

the difference between the tunnel current measured in finite and zero magnetic fields. The solid curves in Figure 6.11a show the logarithms of the individual current contributions $I_n(V)$ for $V_n^- \leq V \leq V_n^+$.

In the Fowler-Nordheim tunnelling regime ($V \geq 260$ mV), the current is calculated within the approximations described in Section 6.4.1, to avoid problems arising from imaginary values of the decay function $\mu_{n1}(0-)$.

Oscillatory structure in the Ln I(V) curve is observed at the voltages V_n^- for which 2DEG electrons with transverse momentum $p_y' = -p_F$ tunnel into the n^{th} interfacial Landau state. This structure is more clearly revealed in the first derivative <dLnI(V)/dV> shown in Figure 6.11b, which is calculated following the averaging procedure described in Section 5.11.2, using an averaging bin width $\Delta V = 5$ mV.

No oscillatory structure associated with the closure of tunnelling channels is observed in either the LnI(V) curve or its derivative.

It was shown in Section 6.4.3 that at high applied biasses, the transition rates from the 2DEG into interfacial Landau states depend mainly on the corresponding transmission coefficients, determined by the magnetic potential energy in the barrier region. For given voltage and field, this magnetic potential energy depends only on the transverse wavevector component $k_y(n)$ of the tunnelling

electrons, which determines the orbit centre position. Electrons with the smallest positive value of $k_y(n)$ have orbit centres $X_{k_y} = -\hbar k_y(n)/Be$ which lie closest to the potential barrier, and therefore have the highest transmission coefficient. At high biasses, these electrons also have the fastest transition rates and therefore dominate the tunnel current. Figure 6.11a shows that for given V, the maximum current contribution arises from transitions into the highest-index interfacial state which, from Figure 5.5 is accessed by 2DEG electrons with the lowest of the allowed wavevector components $\{k_y(n)\}$.

When V is just above V_i^-, the lowest value of $\{k_y(n)\}$ is $k_y(i) = k_o - k_F$ so that the current contribution $I_i(V)$ due to the newly-opened i^{th} tunnelling channel, soon dominates the total tunnel current as shown in Figure 6.11a. Consequently, the opening of new channels produces visible $-p_F$ oscillatory structure in LnI(V) and its derivative.

As the voltage is increased from V_i^-, $k_y(i)$ also increases so that the orbit centre $X_{k_y} = -\hbar k_y(i)/Be$ moves further left, thereby raising the magnetic potential energy in the barrier region and the total effective barrier height. This increase is so large that despite the increased electrostatic trimming of the potential barrier, the value of Ln $I_i(V)$ close to V_i^+ is smaller than that close to V_i^-.

As the voltage is raised from V_i^- to V_i^+, additional higher-index tunnelling channels are opened, which are accessed by 2DEG electrons with lower values of $k_y(n)$, and therefore dominate the current. Consequently, when V reaches V_i^+, 2DEG electrons tunnelling into the i^{th} interfacial Landau state contribute only a small fraction of the total current, and closure of the channel has no visible effect on either LnI or its derivative.

Weakening of the oscillatory structure in d(LnI)/dV, is clearly visible with increasing voltage $\geq$ 330 mV in Figure 6.11b. This is due to nonparabolicity in the n^+ contact which causes the density of interfacial Landau levels to increase with energy. Consequently, at higher voltages, more tunnelling channels are open, as shown in Figure 6.11a, so that the separation between the allowed wavevector components $\{k_y(n)\}$ is reduced. It follows that the difference between the orbit centre positions and transition rates of electrons tunnelling into the n^{th} and $n\text{-}1^{th}$ interfacial states is also reduced. Because the number of open tunnelling channels increases with voltage and the difference between the transition rates into higher-index channels is reduced, the highest-index current contribution is a smaller fraction of the total current. This can be seen from Figure 6.11a which shows that the difference between the logarithm of the total tunnel current and that of the highest-index contribution increases with voltage. At higher voltages the opening of new tunnelling channels therefore produces a smaller fractional increase in the total current so that the oscillatory 'ripples' in LnI become less pronounced leading to diminished oscillatory amplitudes in d(LnI)/dV.

The solid curve in Figure 6.12 shows the voltage-dependence of the separation ΔV_n between adjacent maxima in the first derivative curve dLnI/dV. The reduction in ΔV_n with increasing voltage is primarily due to nonparabolicity in the n^+ collector, which reduces the energy separation between high-lying interfacial Landau levels.

Taking the nonparabolicity factor of GaAs to be $\alpha = 1.1\ eV^{-1}$, which is comparable to that measured by Heiblum et al. (1987), the predicted values of ΔV_n lie within the experimental limits over the entire voltage range. Similar results were obtained by Sheard et al. (1988), but the use of a voltage-independent stand-off distance $3a_0 \sim 8$ nm gave rise to discrepancies at bias voltages $V \lesssim 300$ mV. It should be noted that the values of ΔV_n expected for tunnelling into bulk Landau levels shown by the broken curve in Figure 6.12, cannot be reconciled with the experimental data for any reasonable choice of α.

6.6 Summary

The observation of a single series of oscillations in the current-voltage and current-field characteristics of GaAs/ (AlGa)As single-barrier structures is fully consistent with the model of tunnelling into interfacial Landau states developed in Chapter 5. Tunnelling into bulk Landau levels does not occur due to the low Fermi momentum $p_F = \hbar k_F$ of the 2DEG formed in these samples.

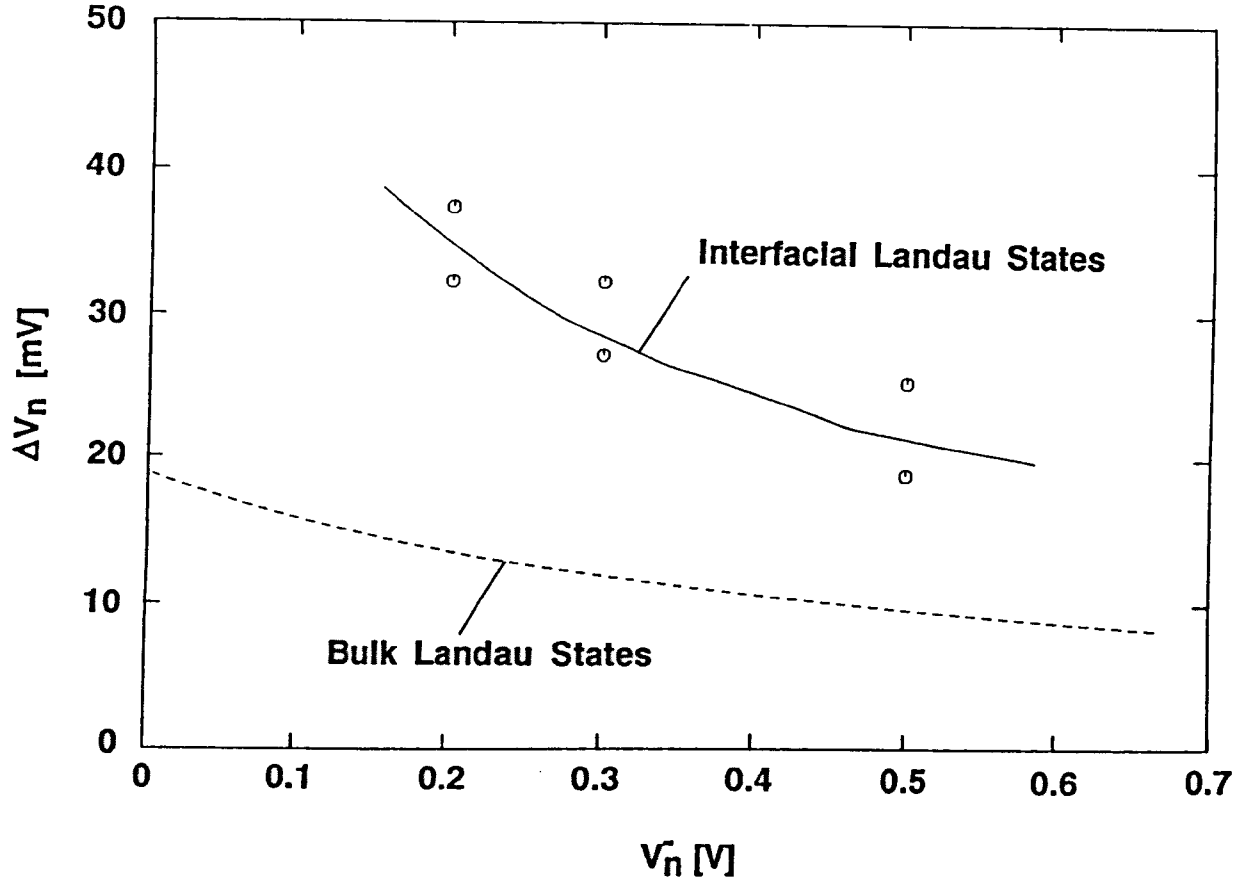

Figure 6.12 Solid curve shows the separation $\Delta V_n = V_n^- - V_{n-1}^-$ between adjacent maxima in the simulated derivative curve 6.11b, as a function of V_n^-, calculated for $\underline{B} \perp \underline{I}$ = 13 T, taking α = 1.1 eV^{-1}. Broken curve shows ΔV_n predicted for transitions into bulk Landau levels taking the same value of α. The circles indicate the range of measured values, taken from Figure 6.10c.

The absence of any $+p_F$ oscillations is attributed to the high applied bias voltages (240 mV - 700 mV). Over this range of bias, the magnetic potential energy makes a large contribution to the total effective barrier height and greatly affects the barrier transmission coefficient. Owing to the different orbit centre positions $X_+ < X_-$, the potential barrier experienced by 2DEG electrons with $k_y'(n) = +k_F$ is significantly higher than for $-k_F$ electrons tunnelling at similar voltages and fields. Consequently, the transmission coefficients and normalised transition rates are several orders of magnitude lower for the $+k_F$ electrons (Figures 6.6b and 6.8). Equation (6.2) therefore predicts that the $-p_F$ series will dominate the oscillatory structure observed in $\langle dI/dB \rangle$ and $\langle d^2I/dB^2 \rangle$.

Taking the nonparabolicity factor of GaAs to be $\alpha = 1.1\ eV^{-1}$, the periodicities of the single series of $-p_F$ oscillations revealed in both the simulated and measured dLnI/dV curves are in good agreement over the entire voltage range.

CHAPTER SEVEN

TRANSVERSE MAGNETOTUNNELLING IN WIDE-WELL DOUBLE-BARRIER RESONANT-TUNNELLING STRUCTURES (DBRTS)

7.1 Introduction

In Chapters 5 and 6, oscillatory structure observed in the current-field and current-voltage characteristics of asymmetrically-doped single-barrier structures under forward-bias conditions and in the presence of a transverse magnetic field, was shown to originate from 2DEG electrons with transverse momentum $p_y' = \pm p_F$ tunnelling into magneto-quantised interfacial states in the n^+ contact.

In this geometry, similar oscillations have also been observed in the I(B) and I(V) characteristics of GaAs/(AlGa)As DBRTS containing a wide quantum well (600 Å - 1800 Å) and a lightly n-doped emitter contact in which a 2DEG is formed under bias (Eaves et al., 1988; Alves et al., 1989; Henini et al., 1989; Leadbeater et al., 1989).

The origin of this oscillatory structure has been attributed to electrons at the Fermi level in the 2DEG tunnelling into hybrid magneto-electric states in the quantum well (Eaves et al., 1988).

In this chapter, a model of transverse magnetotunnelling in wide-well DBRTS is developed and used to calculate the current-field characteristics and derivatives of the 1200 Å well GaAs/(AlGa)As DBRTS used in the experiments of Leadbeater et al. (1989).

Just as for the single-barrier structures, the oscillatory amplitudes of the simulated <dI/dB> curve are shown to be proportional to the transmission coefficient of the LH (emitter) barrier and the frequency of the semiclassical collisions between each $\pm k_F$ electron in the well and the emitter barrier.

Because most of the applied voltage is dropped across the wide quantum well, the emitter-barrier transmission coefficient is only weakly field-dependent (see Section 7.12.3). The field-dependence of the oscillatory amplitudes therefore primarily reflects that of the collision frequencies of electrons with the interfaces bounding the well.

Consequently, these wide-well structures are ideal for investigating the effect of the magnetic field on the semiclassical dynamics of electrons in the well. In particular, the diminished oscillatory amplitudes observed in <dI/dB> and $\langle d^2I/dB^2 \rangle$ over the field range corresponding to the transition from traversing states which interact with both barriers, to cycloidal skipping states which interact with the emitter barrier only, are shown to originate from the low collision frequencies characteristic of this transition region.

Previous theoretical studies of resonant tunnelling in a transverse magnetic field have concentrated on explaining the shift of the negative-differential-resistance regions to higher voltages, which is generally observed with increasing field (Ben Amor et al., 1988; England et al., 1989a, 1989b).

7.2 Device Construction

The DBRTS used in the experiments of Leadbeater et al. (1989) were grown by molecular beam epitaxy on GaAs substrates heavily doped with Si (electron carrier concentration $n = 2 \times 10^{24}$ m^{-3}) and comprised the following layers, in order of growth from the substrate (i) a 2 μm thick buffer layer of GaAs doped at $n = 2 \times 10^{24}$ m^{-3}; (ii) 500 Å of GaAs, $n = 2 \times 10^{22}$ m^{-3}; (iii) a spacer layer of undoped GaAs, $\ell = 25$ Å; (iv) an undoped $(Al_{0.4}Ga_{0.6})As$ barrier, $b = 56$ Å; (v) an undoped GaAs quantum well of width $w = 600$ Å or 1200 Å; (vi) an undoped $(Al_{0.4}Ga_{0.6})As$ barrier, $b = 56$ Å; (vii) a spacer layer of undoped GaAs, $\ell = 25$ Å; (viii) 500 Å of GaAs, $n = 2 \times 10^{22}$ m^{-3}; (ix) a 0.5 μm top contact layer of GaAs, $n = 2 \times 10^{24}$ m^{-3}. Only the 1200 Å well structures are considered in this chapter.

The graded doping of the n-type contact layers and the inclusion of undoped spacer layers adjacent to the barriers is intended to improve the performance of the device by limiting dopant diffusion into the barrier region. This reduces the elastic scattering of tunnelling electrons by ionised impurities, which has

been shown to have an adverse effect on the electrical properties of resonant tunnelling devices (Leadbeater et al., 1989).

Taking the nonparabolicity parameter of GaAs to be $\alpha = 1\ eV^{-1}$ (Heiblum et al., 1987), the Fermi energy (2.1) of the 3DEG formed in the n^+ contact regions, is $E_{FR} \cong 73$ meV.

7.3 Nonequilibrium Electrostatics

Figure 7.1 shows the schematic conduction band profile of the DBRTS used in the experiments of Leadbeater et al. (1989), under an applied voltage V. The co-ordinate system referred to throughout this chapter is also shown.

A quasi-2DEG is formed in the accumulation layer, adjacent to the emitter barrier. Most of the applied voltage is dropped across the wide undoped well region so that the mean height of the emitter barrier is approximately equal to the conduction band offset ΔE_c. The transmission coefficient of this barrier is therefore sufficiently low that the average lifetime (~ 1 ns) of an electron in the accumulation layer, given by the reciprocal of the transition rate into the well region, is long compared to the energy relaxation time due to acoustic phonon emission (~ 0.1 ns). Consequently, the 2DEG is degenerate at liquid helium temperatures. Assuming, in addition, that the conductivity of the lightly-doped emitter contact is sufficiently large, a uniform Fermi level is maintained throughout

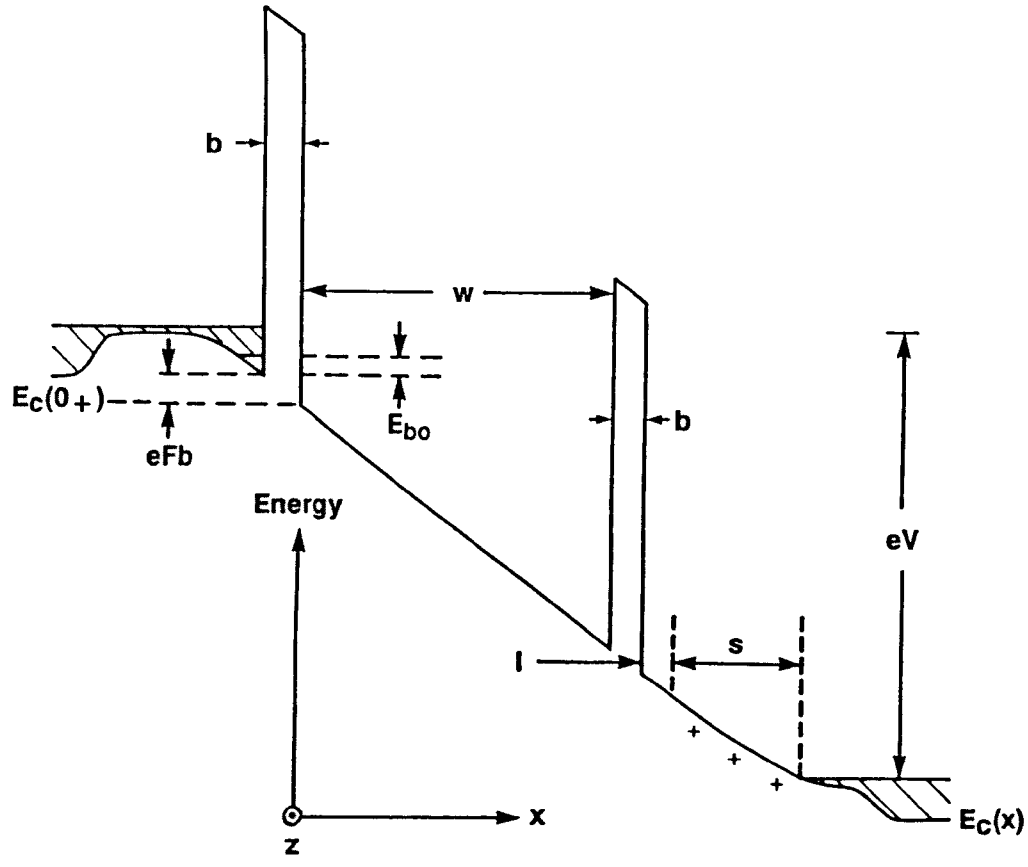

Figure 7.1 Schematic conduction band profile $E_c(x)$ of a wide-well DBRTS under bias, showing the formation of a quasi 2DEG in the lightly-doped emitter contact. A uniform electric field F extends throughout the barrier and well regions, and the undoped spacer layer (of length ℓ) adjacent to the collector barrier. This electric field is screened by a depletion region of length s in the lightly-doped part of the collector contact.

the doped region of the emitter contact and the 2DEG, which are thus in approximate equilibrium.

The doping concentration in the n^- region of the emitter contact is sufficiently high that the Fermi level lies just above the conduction band edge. There are thus a small number of extended states in the emitter contact which contribute to the tunnel current. However, the main contribution is due to the two-dimensional electrons in the accumulation layer.

The electronic potential energy variation throughout the accumulation layer is given, within the Fang-Howard approximation by equation (2.15). Just as for the single-barrier structures, the 2DEG sheet electron concentration is determined for each bias voltage from the periodicity of maxima observed in the first derivative of the tunnel current I, measured as a function of longitudinal magnetic field $\underline{B} \parallel \underline{I}$ (see Section 2.5). This sheet electron density is approximately (Leadbeater, 1990)

$$n_s(V) = 2.9 \times 10^{15} V \qquad [m^{-2}] \quad . \tag{7.1}$$

Resonant tunnelling occurs when the energies of the bound states in the emitter 2DEG and quantum well coincide (see Section 1.9). The associated buildup of negative space charge in the well can modify the potential profile and, if sufficiently large, can give rise to a bistable region in the I(V) characteristics (Sheard and

Toombs, 1988). On resonance, the charge in the well is given by $Q_W = Q_S T_L/(T_L + T_R)$, where Q_S is the 2DEG charge and T_L, T_R are the transmission coefficients of the emitter and collector barriers. Figure 7.1 shows that most of the voltage is dropped across the wide well, so that the top of the collector barrier is approximately eV below that of the emitter barrier. Hence $T_R >> T_L$ and Q_W is small.

Provided that the space charge associated with ionised impurities is also small, and neglecting the difference between the dielectric constants of GaAs and (AlGa)As, the electric field $\underline{F} = -(n_S\, e/\varepsilon_0\varepsilon_{rL})\underline{x}$ created by the 2DEG, extends throughout both barriers, the well region, and the undoped spacer layer adjacent to the collector barrier. The electronic potential energy in these regions is thus approximately

$$-e\phi(x) = -e\phi(-b) - \frac{n_S e^2(x + b)}{\varepsilon_0\varepsilon_{rL}} \; ; \; -b \leq x \leq b + w + \ell \quad , \quad (7.2)$$

where ε_{rL} is the dielectric constant of GaAs and ℓ is the width of the undoped spacer layer. The electric field F is screened by a depletion region of length s in the lightly-doped part of the collector contact (see Figure 7.1). The electronic potential energy throughout this depletion region is

$$-e\phi(x) = E_{FR} + \frac{N_L e^2}{2\varepsilon_o \varepsilon_{rL}} (x^2 - (b + w + \ell + s)^2)$$

$$- \frac{e^2}{\varepsilon_o \varepsilon_{rL}} (N_L (b + w + \ell) + n_s)(x - (b + w + \ell + s))$$

$$; b + w + \ell \leq x \leq b + w + \ell + s \quad , \qquad (7.3)$$

where N_L is the n^- donor density, and the small potential dropped across the undepleted part of the n^- region is neglected so that $-e\phi(b + w + \ell + s) = E_{FR}$.

The depletion length s is determined from the requirement that the sum of the potentials dropped across the accumulation layer, the barrier and well regions, and the collector contact equals $V + E_{FR}/e$.

The conduction band profile is related to the electrostatic potential by

$$E_c(x) = \begin{cases} -e\phi(x) \; ; \; x < -b \; ; \; 0 < x < w \; ; \; x > w + b \\ -e\phi(x) + \Delta E_c ; \; -b \leq x \leq 0 \; ; \; w \leq x \leq w + b \end{cases} \qquad (7.4)$$

where $\Delta E_c \cong 330$ meV is the conduction band offset.

7.4 Features of the Measured Transverse Magneto-current

Figure 7.2 shows typical I(B) and d^2I/dB^2 curves ($\underline{B} \perp \underline{I}$), measured at T = 4.2 K for V = 600 mV. The current falls rapidly to zero with increasing field. Three distinct series of oscillations are observed, labelled t+, t- and s-. None of the series is periodic in 1/B, which would be the case for tunnelling into bulk Landau levels. The t- and s- series are separated by a field range ≈ 2 T over which no oscillatory structure is observed. The amplitudes of both the t- and s- series decrease rapidly to zero as the field approaches this transition region.

Similar oscillatory structure is observed over a range of bias voltages. Although the positions of the extrema are strongly voltage-dependent, suggesting close association with the tunnelling process itself, the qualitative field-dependence of the oscillatory amplitudes is unchanged (Leadbeater, 1990).

7.5 The Transfer-Hamiltonian Formalism of Resonant Tunnelling

The first time-dependent picture of resonant tunnelling was proposed by Luryi (1985), who suggested that the process can be considered as two sequential transitions; first from the LH emitter contact into a bound state in the quantum well, and subsequently from the well into the RH collector contact.

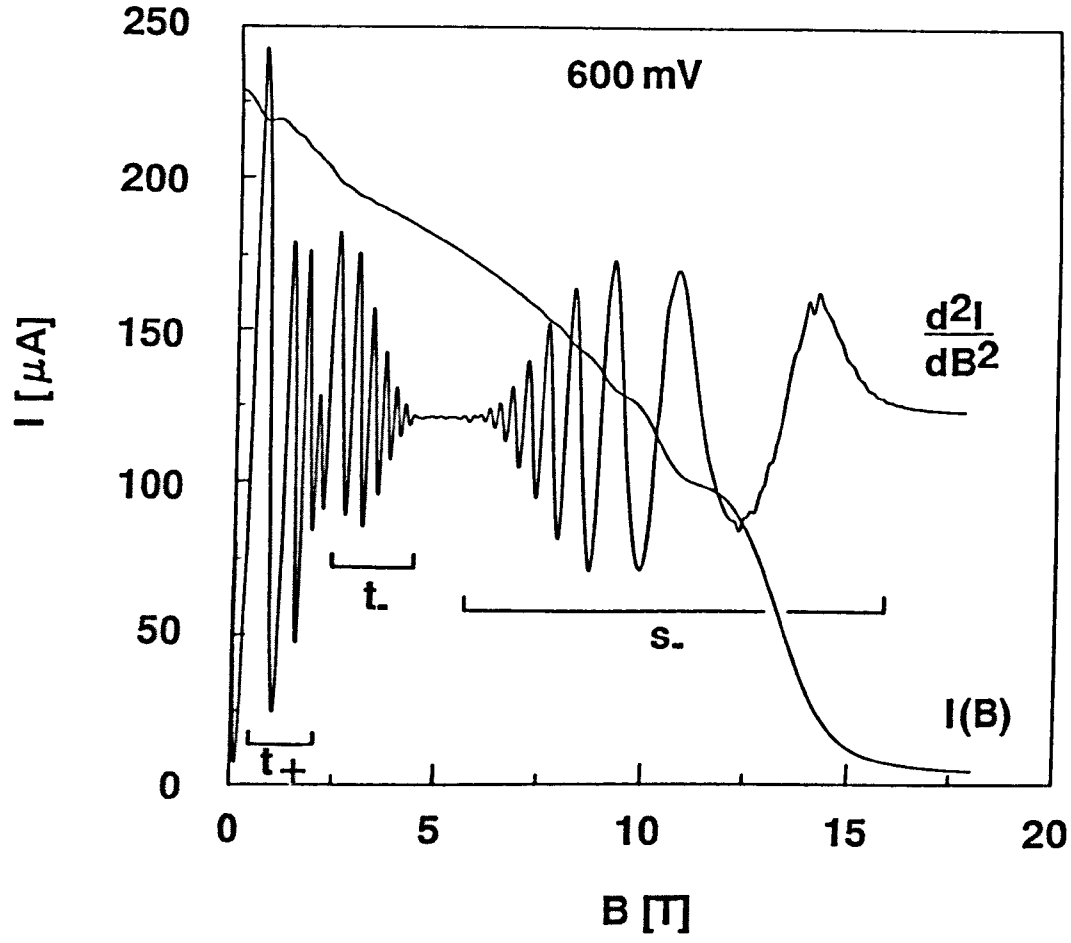

Figure 7.2 I(B) and d^2I/dB^2 characteristics of a GaAs/(AlGa)As DBRTS containing a 1200 Å quantum well, measured at V = 600 mV and T = 4 K. The current is quenched at high fields. Three series of oscillatory structure are observed in the second derivative curve, distinguished by horizontal brackets. (After Leadbeater et al., 1989).

Payne (1986), used the transfer-Hamiltonian approach to formulate a model of sequential tunnelling in symmetric DBRTS with heavily n-doped contacts. Within this formalism, left-hand, quantum well, and right-hand subsystems are defined by suitably extending the emitter and collector barrier potentials, as shown in Figure 7.3. The LH and RH subsystems each contain potential steps, whereas the well subsystem contains a single isolated quantum well, which is assumed to support at least one bound state.

The rates of allowed transitions between each subsystem are given by equation (3.25), where the subscripts ℓ and r refer to the initial and final states respectively. To account for the finite occupancy $f(E_w)$ of the well states, which describes resonant space-charge buildup, the transition rate (3.25) is multiplied by $1-f(E_w)$ when considering transitions into the well, and by $f(E_w)$ when considering transitions from the well into the collector contact. The value of $f(E_w)$ is determined from the current continuity requirement that the total number of transitions per second from all LH eigen-states into the well equals that from the well into all RH eigen-states. Since most of the applied voltage is dropped across the wide well, $T_L/T_R \ll 1$, so that the transition rates from the LH contact into the well are much lower than from the well into the RH contact. Consequently $f(E_w) \cong 0$. Within this approximation, the current flowing through the device depends only on the tunnelling transition rate from the emitter contact into the bound states of the well.

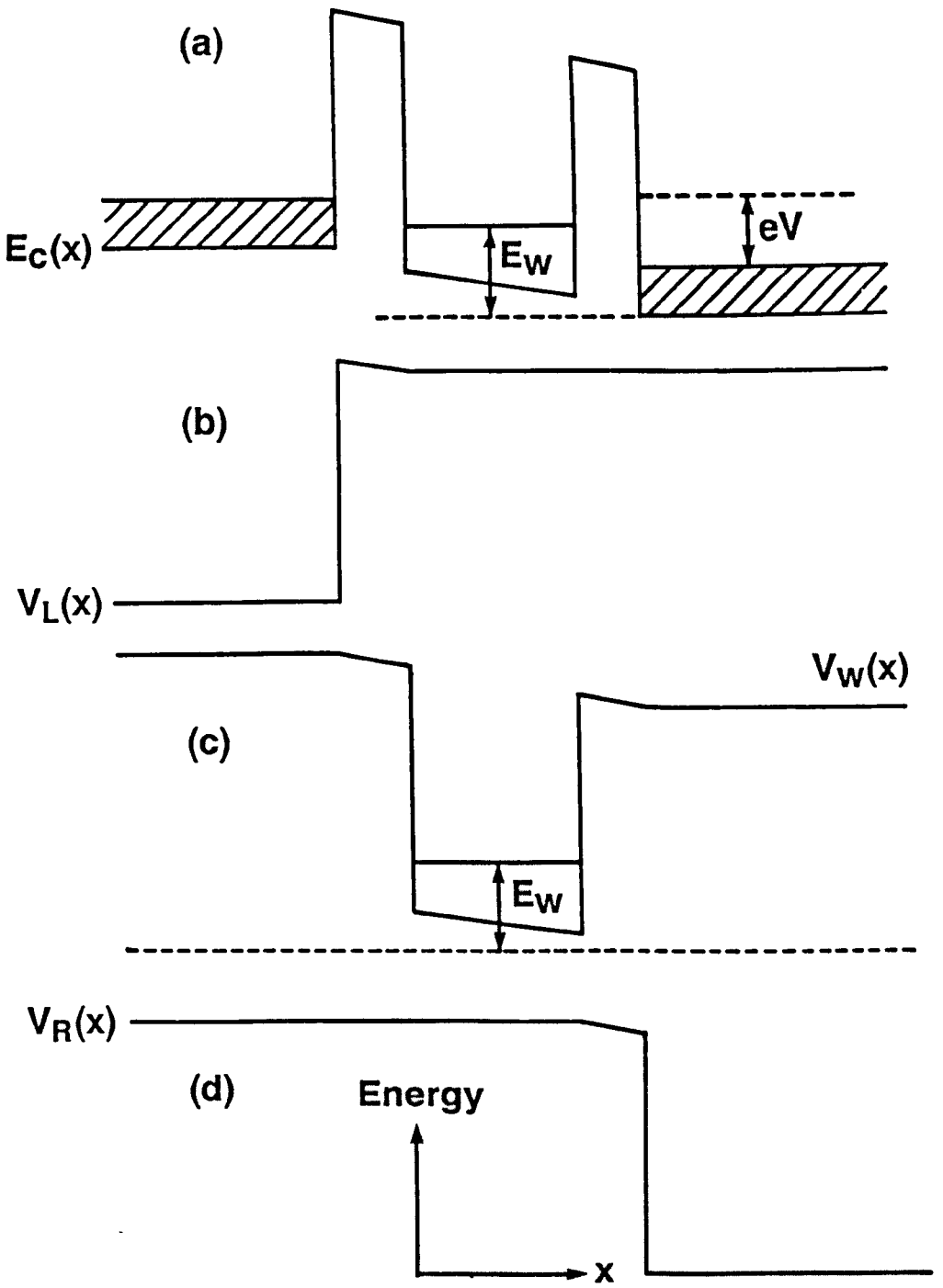

Figure 7.3 (a) Conduction band profile $E_c(x)$ of a symmetrical DBRTS with heavily n-doped contacts. The effective 1D potential energy profiles of (b) the LH subsystem, (c) the well subsystem and (d) the RH subsystem are also shown.

7.6 Calculation and Interpretation of the LH and Quantum Well Eigenstates of the Wide-well Structures in the Presence of a Transverse Magnetic Field

7.6.1 LH Eigenstates

When a transverse magnetic field $\underline{B} \parallel \underline{z}$ is applied, the conduction band effective-mass Hamiltonian H_T is given by equation (3.2) in which $E_c(x)$ is determined from equations (2.15), (7.2), (7.3) and (7.4).

From the definition (3.5), the LH subsystem comprises the accumulation layer and emitter-barrier regions and is thus identical to that of the single-barrier structures described in Section 4.2. It follows that the LH eigenvalues are simply the perturbed 2DEG levels (4.14).

7.6.2 Qualitative discussion of the quantum well states

Within the approximations of Section 4.3.1, the x-dependent wavefunction $\psi_n(x)$ of the n^{th} bound state in the well satisfies

$$\left[-\frac{\hbar^2}{2} \frac{d}{dx} \left(\frac{1}{m^*(x)} \right) \frac{d}{dx} + E_{EFF}(x, k_y) \right] \psi_n(x)$$

$$= \left(E_W(k_y, k_z) - \frac{\hbar^2 k_z^2}{2m_L^*} \right) \psi_n(x) = E_n(k_y)\, \psi_n(x) \quad , \tag{7.5}$$

$$m_B^* \; ; \; x \leq 0 \; ; \; x \geq w$$

where $m^*(x) = \{$

$$m_L^* \, (1 + \alpha(E_n - E_c(x))); \; 0 < x < w \, ,$$

$$E_c(x) + \frac{B^2e^2}{2m^*(x)} \left(x + \frac{\hbar k_y}{Be}\right)^2 \; ; \; -b < x < w + b$$

$$E_{EFF}(x, k_y) = \{ \; E_c(-b_+) + \frac{B^2e^2}{2m_B^*} \left(-b + \frac{\hbar k_y}{Be}\right)^2 \; ; \; x \leq -b$$

$$E_c((b + w)_-) + \frac{B^2e^2}{2m_B^*} \left(b + w + \frac{\hbar k_y}{Be}\right)^2 ; \; x \geq b + w ,$$

$E_w(k_y, k_z)$ is the total energy, and $E_n(k_y)$ that associated with motion perpendicular to the magnetic field.

Equation (7.5) is similar to the effective-mass equation (4.22) for the RH subsystem of the single-barrier structures, except that electron motion is further constrained by the collector barrier. The energy level spectrum is also modified by the large electric field in the well which, in contrast to the single-barrier structures, gives rise to a spatially-varying effective mass.

Using equations (7.2) and (7.4) to determine $E_c(x)$ in the well and barrier regions, equation (7.5) may be written in the form

$$\left[-\frac{\hbar^2}{2} \frac{d}{dx} \left(\frac{1}{m^*(x)}\right) \frac{d}{dx} + V(x)\right] \psi_n(x) = E_n(k_y) \; \psi_n(x) \quad . \qquad (7.6)$$

where the effective 1D potential energy is

$$\frac{B^2e^2(x - X')^2}{2m^*(x)} - eFX' + U(x) + \frac{m^*(x)F^2}{2B^2} \quad ; \; -b < x < w + b$$

$$V(x) = \begin{cases} V(-b_+) & ; \; x \leq -b \\ V((w + b)_-) & ; \; x \geq w + b \end{cases} ,$$

in which

$$X'(x) = -\frac{\hbar k_y}{Be} + \frac{m^*(x)F}{eB^2} ,$$

and

$$U(x) = \begin{cases} \Delta E_c - e\phi(0) & ; \; x \geq w \; ; \; x \leq 0 \\ -e\phi(0) & ; \; 0 < x < w \end{cases} .$$

Neglecting the x-dependence of the effective mass, the first term in V(x) describes the potential energy of a simple harmonic oscillator with orbit centre X' and angular frequency ω_c. The second term is the electrostatic potential energy at the orbit centre. The third term, U(x), describes the rectangular potential well formed by

the conduction band discontinuity between the high-and low-gap materials. The final term is the mean kinetic energy of an electron in bulk GaAs associated with motion perpendicular to crossed electric and magnetic fields (see Section 1.5).

Figure 7.4 illustrates V(x) for the case of parabolic bands, so that the effective mass is independent of position within each layer. If nonparabolicity is taken into account, the effective mass varies continuously throughout the well region and V(x) is no longer parabolic. In addition, $E_n(k_y)$ and V(x) are coupled through the energy-dependent effective mass and must be calculated self-consistently.

Distinct types of well state can, however, be classified quite generally, irrespective of conduction band nonparabolicity. If $V(0_+) < V(w_-)$ for given k_y, three kinds of bound state may exist, labelled r, s and t in Figure 7.4. These states are distinguished by the nature of their classical turning points and therefore correspond to distinct types of classical trajectory.

Type r states for which $E_n(k_y) < V(0_+)$ and $E_n(k_y) < V(w_-)$, correspond to classical bulk cycloidal trajectories (see Section 1.5), which are bounded by soft turning points and do not intersect with either barrier. Within the WKB approximation, the energy levels of these states depend only on the potential energy between the turning points and are given by equation (1.24).

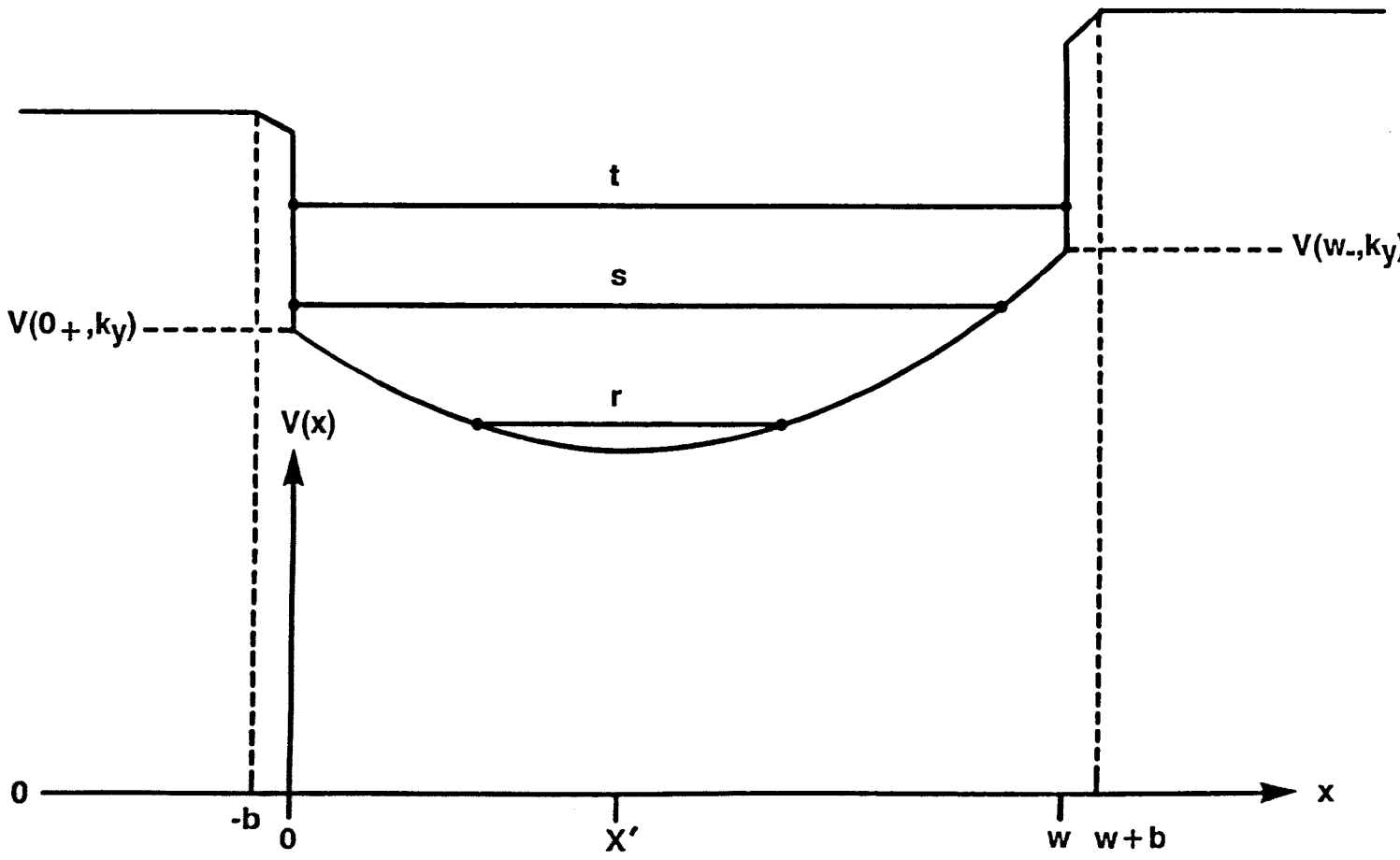

Figure 7.4 Effective potential energy variation V(x) throughout the well subsystem of a wide-well DBRTS under bias and in the presence of a transverse magnetic field $\underline{B} \parallel \underline{z}$. If $V(0_+, k_y) < V(w_-, k_y)$, three distinct types of bound state may exist, labelled r, s and t. Type r states correspond to classical bulk cycloidal motion, type s states to cycloidal skipping orbits along the emitter barrier, and type t states to traversing orbits, which intersect with both barriers.

Type s states for which $V(0_+) \leq E_n(k_y) \leq V(w_-)$ correspond to classical skipping trajectories which intersect with the emitter barrier only. These states are referred to as cycloidal skipping states, since between collisions with the emitter barrier, the electron executes cycloidal motion.

The classical trajectories corresponding to type t states for which $E_n(k_y) > V(0_+)$ and $E_n(k_y) > V(w_-)$ extend throughout the well region and are bounded by hard turning points at the barrier interfaces. The electrons are repeatedly reflected from each interface and execute classical traversing orbits. In zero magnetic field all eigenstates of the quantum well subsystem correspond to these traversing orbits.

If $V(0_+) > V(w_-)$, a fourth type of bound state may exist corresponding to cycloidal skipping motion along the collector barrier. However, since transitions from the 2DEG into all well states with soft LH turning points are forbidden (see Section 7.7), these states are not considered in detail.

7.6.3 Calculation of the traversing and cycloidal skipping state dispersion relations

The WKB energy quantisation condition (4.37) and effective-mass wavefunctions (4.32) derived for interfacial skipping states in single-barrier structures are applicable, quite generally, to all bound eigenstates with hard LH and soft RH turning points. In particular, taking

$$\alpha_n(x) = [2m^*(x)(E_n(k_y) - V(x))]^{\frac{1}{2}} /\hbar \ , \qquad (7.7)$$

$$\mu_{n1}(x) = [2m_B^*(V(x) - E_n(k_y))]^{\frac{1}{2}} /\hbar \ , \qquad (7.8)$$

and $$\alpha_n(w_n) = 0 \ , \qquad (7.9)$$

equations (4.37) and (4.32) give the cycloidal skipping state dispersion relations and envelope wavefunctions.

Piecewise WKB solutions of equation (7.6) appropriate to traversing states in the well are

$$\psi_n(x) = \begin{cases} C_n \mu_{n1}^{-\frac{1}{2}}(x)\, e^{-Q(x)} & ; \ x \leq 0 \quad (a) \\ D_n \alpha_n^{-\frac{1}{2}}(x) \sin[T(x) + \delta_n] & ; \ 0 \leq x \leq w \quad (b) \\ G_n \mu_{n1}^{-\frac{1}{2}}(x)\, e^{-Z(x)} & ; \ x \geq w \quad (c) \end{cases} \qquad (7.10)$$

where the integral functions Q(x), T(x) and Z(x) are defined in equation (4.26). The traversing state energy quantisation condition, obtained by imposing the matching conditions (1.39) and (1.40) at each barrier interface is

$$\int_o^w \alpha_n(x)\, dx = (n + 1)\pi - \tan^{-1}\left(\frac{m_B^* \alpha_n(0_+)}{m^*(0_+)\mu_n(0_-)}\right) - \delta_n \qquad (7.11)$$

$$; n = 0, 1, \ldots ,$$

where $\delta_n = \tan^{-1}\left(\frac{m_B^* \alpha_n(w_-)}{m^*(w_-)\ \mu_n(w_+)}\right)$.

Implicit expressions for the traversing and cycloidal skipping state dispersion relations can be found from equations (4.37) and (7.11) by evaluating the phase change integral.

$$\int_o^a \alpha_n(x)\, dx \quad ; n = 0, 1, \ldots , \qquad (7.12)$$

where a = w for traversing states and, for the n^{th} cycloidal skipping state, equals the soft RH turning point w_n.

Using the expressions for $\alpha_n(x)$ and V(x) given in equations (7.6) and (7.7), equation (7.12) may be written in the form

$$\int_o^a \alpha_n(x)\, dx = \hbar^{-1} \int_o^a [\gamma - \beta(x - \bar{X})^2]^{\frac{1}{2}}\, dx , \qquad (7.13)$$

where

$$\gamma = \hbar^2\alpha_n^2(0+) + \beta\bar{X}^2 = 2m^*(0+)(E_n(k_y) - E_c(0+)) - \hbar^2k_y^2 + \beta\bar{X}^2,$$

$$\beta = B^2e^2 - 2m_L^*\,\alpha e^2F^2 ,$$

$$\bar{X} = [m^*(0_+)eF + m_L^*\alpha eF(E_n - E_c(0+)) - \hbar k_yBe]/\beta ,$$

and α is the nonparabolicity parameter of the well material. The form of this integral depends on the sign of β and consequently on the relative magnitude of the electric and magnetic fields. However, evaluation of (7.13) can be simplified using the following physical argument which shows that $\gamma/\beta > 0$ for all B.

In the absence of confining barriers, an electron with energy $E_n(k_y)$ associated with motion perpendicular to the magnetic field, executes bulk cycloidal motion between the turning points

$$w_n = \bar{X} + R , \tag{7.14}$$

and

$$w_n^L = \bar{X} - R , \tag{7.15}$$

where $R = (\gamma/\beta)^{\frac{1}{2}}$ is the orbital radius.

In order that these turning points are real, the inequality

$$(\gamma/\beta) > 0 \tag{7.16}$$

must always be satisfied. It follows that if $B > (2m_L{}^*\alpha)^{\frac{1}{2}}F$ so that $\beta > 0$, equation (7.13) may be written

$$\int_0^a \alpha_n(x)\, dx = \hbar^{-1}\, \gamma\, \beta^{-\frac{1}{2}} \int_{u_0}^{u_1} (1 - u^2)^{\frac{1}{2}}\, du\ , \tag{7.17}$$

where

$$u(x) = (\beta/\gamma)^{\frac{1}{2}}\, (x - \bar{X})\ , \tag{7.18}$$

$$u_0 = u(0)\ ,$$

and $$u_1 = u(a)\ .$$

The integral on the RHS of (7.17) is evaluated using the results of Section 4.3.3, giving

$$\int_0^a \alpha_n(x)\, dx = \hbar^{-1}\, \gamma\, \beta^{-\frac{1}{2}}\, [f(u_1) - f(u_0)]\ , \tag{7.19}$$

where $f(x)$ is defined in equation (4.42).

For cycloidal skipping states $a = w_n$ whence, combining equations (7.14) and (7.18), $u_1 = 1$ so that, from equation (4.42), $f(u_1) = \pi/2$.

It follows from inequality (7.16) that if $\beta < 0$, equation (7.13) may be written in the form

$$\int_0^a \alpha_n(x)\, dx = -\hbar^{-1}\, \gamma(-\beta)^{-\frac{1}{2}} \int_{u_0}^{u_1} (u^2 - 1)^{\frac{1}{2}}\, du \quad . \qquad (7.20)$$

The integral on the RHS of this equation is easily evaluated giving

$$\int_0^a \alpha_n(x)\, dx = -\hbar^{-1}\, \gamma\, (-\beta)^{-\frac{1}{2}} [g(u_1) - g(u_0)] \, , \qquad (7.21)$$

where

$$g(u) = \frac{u}{2} (u^2 - 1)^{\frac{1}{2}} - \frac{1}{2} \mathrm{Ln} \left| u + (u^2 - 1)^{\frac{1}{2}} \right| \, .$$

For cycloidal skipping states, $u_1 = 1$ so that $g(u_1) = 0$. Provided the field value $B = (2m_L{}^*\alpha)^{\frac{1}{2}} F$ is avoided in all simulations, it is not necessary to evaluate the phase change integral on the LHS of equation (7.13) for the case $\beta = 0$.

Combining equations (4.37), (7.19) and (7.21), the cycloidal skipping state energy levels $E_n(k_y)$ are implicit solutions of

$$\left(n + \frac{3}{4}\pi\right) - \tan^{-1}\left(\frac{m_B{}^*\, \alpha_n(0_+)}{m^*(0_+)\, \mu_{n1}(0_-)}\right)$$

$$= \begin{cases} \hbar^{-1}\, \gamma\, \beta^{-\frac{1}{2}} \left[\frac{\pi}{2} - f(u_0)\right] \, ; \, \beta > 0 \\ \\ \hbar^{-1}\, \gamma\, (-\beta)^{-\frac{1}{2}}\, g(u_0) \, ; \, \beta < 0 \quad . \end{cases} \; ; \; n = 0, 1, \ldots$$

(7.22)

Similarly, from equations (7.11), (7.19) and (7.21), the traversing state energy levels satisfy

$$(n+1)\pi - \tan^{-1}\left(\frac{m_B^*\,\alpha_n(0_+)}{m^*(0_+)\,\mu_{n1}(0_-)}\right) - \tan^{-1}\left(\frac{m_B^*\,\alpha_n(w_-)}{m^*(w_-)\,\mu_n(w_+)}\right)$$

$$\hbar^{-1}\,\gamma\,\beta^{-1}\,[f(u_1) - f(u_0)] \qquad ;\ \beta > 0$$

$$= \Big\{ \qquad\qquad\qquad\qquad\qquad\qquad \Big\}\ ;\ n = 0,\ 1,..$$

$$-\hbar^{-1}\,\gamma\,(-\beta)^{-\frac{1}{2}}[g(u_1) - g(u_0)]\ ;\ \beta < 0 \quad .$$

(7.23)

For parabolic bands in zero magnetic field, the (traversing state) dispersion curves $E_n(k_y)$ form a set of parabolas in the E-k_y plane, with minima at $k_y = 0$ equal to the bound state energies in the well.

Figure 7.5 shows the dispersion curves of traversing states in the 1200 Å well GaAs/(AlGa)As DBRTS, calculated from equation (7.23) for V = 600 mV and B = 0.5 T. This comparatively small field acts as a perturbation which distorts the zero-field parabolic dispersion curves. The conduction band nonparabolicity factor of GaAs is taken to be 2 eV^{-1}. This is higher than the value $\alpha \simeq 0.85$ eV^{-1} predicted by $\underline{k}.\underline{p}$ theory and measured by Heiblum et al. (1987), to account for increased nonparabolicity at the high-lying levels (≈ 350 meV above the band-edge position at the centre of the well) into which the 2DEG electrons are injected (Blakemore, 1982).

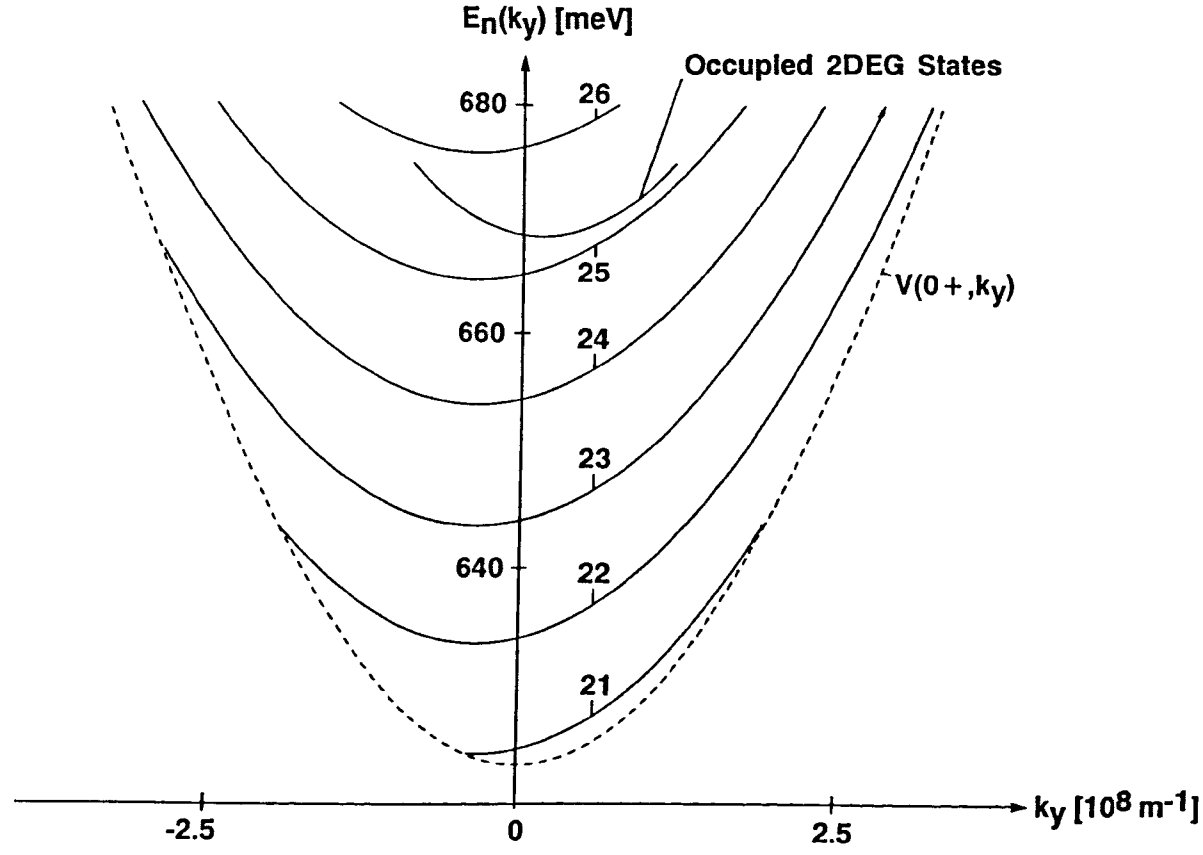

Figure 7.5 Plot of the WKB energy eigenvalues of the n = 21, 22, ... 26 traversing states in the 1200 Å GaAs quantum well, calculated for V = 600 mV, B = 0.5 T and taking $\alpha = 2\ eV^{-1}$. The energies of the occupied 2DEG states in the emitter contact are also shown. The broken curve shows the effective potential energy at the LHS of the quantum well, as a function of k_y.

The broken curve in Figure 7.5 shows the k_y-dependence of the effective potential energy $V(0_+)$ close to the LHS of the quantum well. Energy levels below this curve are not shown since they correspond to eigenstates with soft LH turning points which are inaccessible in tunnelling transitions from the 2DEG (see Section 7.7).

Figure 7.6 shows the dispersion curves $E_n(k_y)$ of well states with hard LH turning points, and of the occupied 2DEG states, calculated for V = 600 mV and B = 5 T, taking $\alpha = 2\ eV^{-1}$. The broken curves show the effective potential energy V(x) at either side of the quantum well, as a function of k_y. Energy levels $E_n(k_y) < V(w_-, k_y)$ in region s correspond to classical skipping trajectories along the emitter barrier (inset right). Energy levels $E_n(k_y) > V(w_-, k_y)$ in region t correspond to classical traversing orbits (inset left). Energy levels in regions r and q correspond to bulk cycloidal trajectories and cycloidal skipping orbits which intersect with the collector barrier only.

To avoid discontinuities in the WKB dispersion curves at the boundary between regions s and t, the constant phase factor of unity on the LHS of the traversing state quantisation condition (7.23) is replaced by 3/4. This approximation avoids problems otherwise encountered when evaluating the tunnel current, due to gaps in the energy spectrum, and is reasonably accurate for the high-index traversing states ($n \geq 10$) which are accessed in transitions from the 2DEG.

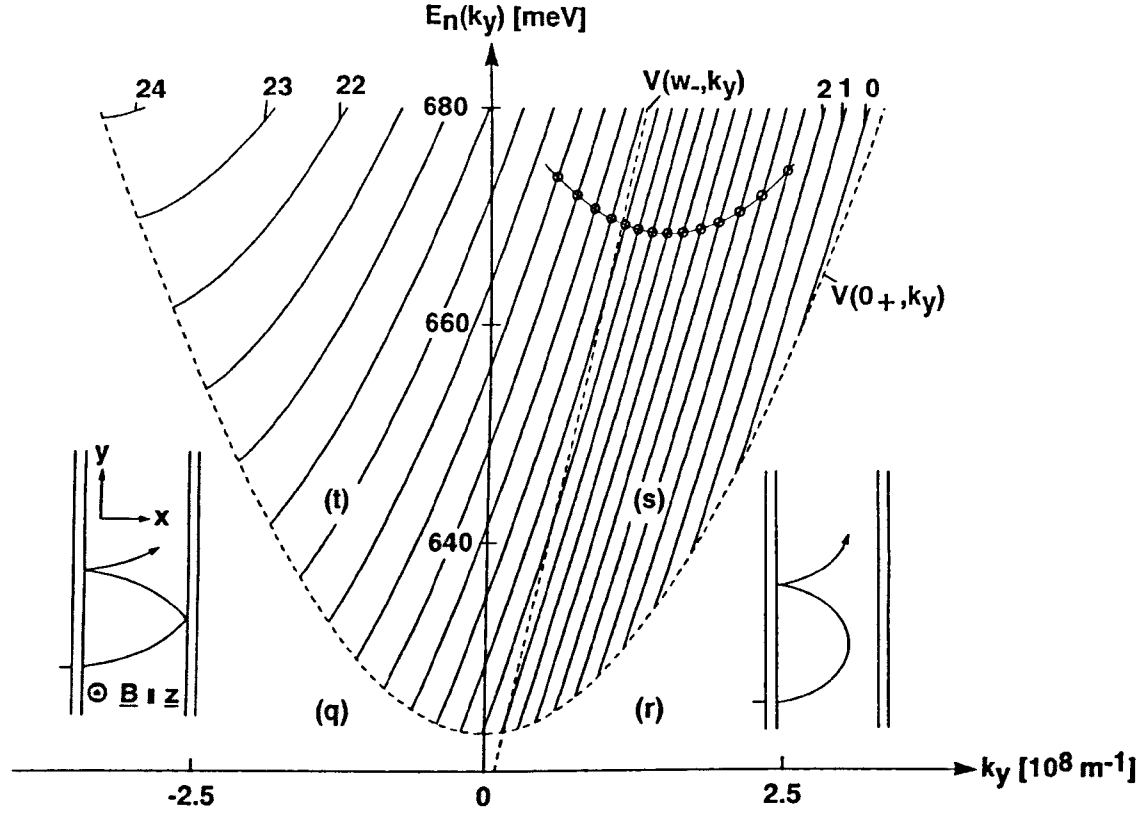

Figure 7.6 Plot of the WKB energy levels $E_n(k_y) > V(0_+, k_y)$; n = 0, 1, ...24 of the 1200 Å GaAs quantum well for V = 600 mV, B = 5 T and taking $\alpha = 2\ eV^{-1}$. The broken curves show the effective potential energy at the LH and RH sides of the well, as a function of k_y, and mark the transition between the distinct types of well state. Energy levels in region t correspond to classical traversing orbits (inset left), and those in region s to emitter-bound cycloidal skipping trajectories (inset right). Intercepts with the 2DEG dispersion curve are marked by open circles and correspond to allowed tunnelling channels. The collector-bound cycloidal skipping states and bulk cycloidal statesin regions q and r are inaccessible via transitions from the 2DEG.

Neglecting the increase in effective mass which occurs as electrons are injected into the well region, the requirements that both the total energy and the transverse wavevector be conserved in tunnelling transitions may be expressed in the single equation (5.8). As for the single-barrier case, this condition can be interpreted by looking for intercepts in the E-k_y plane between the 2DEG and well-state dispersion curves. For V = 600 mV and B = 5 T, each intercept is marked by an open circle in Figure 7.6, and corresponds to a group of 2DEG electrons which makes allowed transitions into either traversing states, or cycloidal skipping states which interact with the emitter barrier only. In the next section, transitions into all other types of well state are shown to be forbidden.

7.7 $\pm k_F$ Transitions into Well States with Soft LH Turning Points Do Not Occur

Transitions into bulk cycloidal states or cycloidal skipping states which interact with the collector barrier, occur only if the soft LH turning point (7.15) lies to the right of the emitter barrier. This is equivalent to the requirement

$$\bar{X} > R \ , \tag{7.24}$$

that the distance from the emitter barrier to the orbit centre exceeds the classical orbital radius. Using the forms of $\bar{X}$ and R given in equations (7.13) and (7.15) appropriate to parabolic bands, inequality (7.24) becomes

$$\frac{m_L^*F}{B^2e} - \frac{\hbar k_y}{Be} > \left[2m_L^*(E_n - E_c(0_+)) + \frac{m_L^*F^2}{B^2} - \frac{2m_L^*F\hbar k_y}{B}\right]^{\frac{1}{2}}/Be \ , \tag{7.25}$$

where the RHS refers to the positive square root. This inequality is only satisfied provided

$$\frac{m_L^*F}{B^2e} - \frac{\hbar k_y}{Be} > 0 \tag{7.26a}$$

and then, squaring both sides, only if

$$\left(\frac{\hbar^2k_y^2}{2m_L^*}\right) > E_n(k_y) - E_c(0_+) \quad . \tag{7.26b}$$

For 2DEG electrons with $k_y = k_o \pm k_F$, $E_n(k_y) = eV + E_{FR}$ so that, as shown in Figure 7.1, the RHS of inequality (7.26b) is the potential energy $eF(b + 3a_o)$ dropped across the accumulation layer and emitter barrier. It follows that for $\pm k_F$ transitions, inequalities (7.26a) and (7.26b) may be written

$$\frac{m_L^*F}{B^2e} - \frac{\hbar (k_o \pm k_F)}{Be} > 0 \ , \tag{7.27a}$$

and

$$\frac{\hbar^2(k_o \pm k_F)^2}{2m_L^*} > eF\ (b + 3a_o) = E_1 \quad , \tag{7.27b}$$

where $k_o = Be(b + 3a_o)/\hbar$ and $F = n_s e/\varepsilon_o \varepsilon_{rL}$ is the electric field in the well.

For $-k_F$ transitions, if $k_F > k_o$,

$$\frac{\hbar^2(k_F - k_o)^2}{2m_L^*} < \frac{\hbar^2 k_F^2}{2m_L^*} = E_F < eF(b + 3a_o) \quad ,$$

so that inequality (7.27b) cannot be satisfied. From Appendix 2, if $k_F < k_o$, inequality (7.27a) is satisfied for $-k_F$ transitions only if

$$\frac{\hbar^2(k_o - k_F)^2}{2m_L^*} < eF(b + 3a_o) - (eFb + E_{bo} + E_F/2)/2 < eF(b + 3a_o) \quad .$$

Consequently, inequalities (7.27a) and (7.27b) cannot both be satisfied and $-k_F$ transitions into well states with soft LH turning points do not occur for any voltages or fields.

It follows directly from inequality (A2.3) of Appendix 2 that (7.27a) is satisfied for $+k_F$ transitions only if

$$\frac{\hbar^2(k_o + k_F)^2}{2m_L^*} < \frac{[E_F + Fe(b + 3a_o)]}{2} + \frac{\hbar^2 k_F}{4m_L^*}\left[k_F^2 + 4m_L^* eF(b + 3a_o)/\hbar^2\right]^{\frac{1}{2}}$$

$$= E_2$$

Thus, conditions (7.27a) and (7.27b) are both satisfied for $+k_F$ transitions only if

$$E_1 - E_2 < 0$$

or, substituting for E_1 and E_2, only if

$$p_1 - p_2 < 1 \tag{7.28}$$

where $$p_1 = \frac{eF(b + 3a_0)}{E_F[1 + 2Fe(b + 3a_0)/E_F]^{\frac{1}{2}}}$$

and $$p_2 = \frac{1}{[1 + 2Fe(b + 3a_0)/E_F]^{\frac{1}{2}}}$$

For V = 600 mV, $p_1 = 1.95$ and $p_2 = 0.24$ so that inequality (7.28) is violated and $+k_F$ transitions into well states with soft LH turning points do not occur for any field values.

Similar conclusions are reached when nonparabolicity in the well region is taken into account by using the appropriate forms of $\bar{X}$ and R in inequality (7.24).

7.8 Derivation and Interpretation of the Matrix Elements $|M_n(k_y)|^2$ for Transitions into Traversing and Cycloidal Skipping States in the Well

To calculate the transition matrix elements from equations (3.25) and (3.37), the well state wavefunctions $\psi_n(x)$ must be normalised.

Neglecting penetration into the classically forbidden regions and assuming, as in Section 5.8, that $\alpha_n(x)$ varies slowly over one local wavelength $2\pi/\alpha_n(x)$, normalisation of the WKB traversing and cycloidal skipping state wavefunctions (4.32) and (7.10b) requires

$$\frac{K_n^2 Z_n}{2} = 1 \quad , \tag{7.29}$$

where

$$Z_n = \int_o^a \alpha_n^{-1}(x)\, dx \ ,$$

$a = w$ and $K_n = D_n$ (defined in equation (7.10b)) for traversing states, and, for cycloidal skipping states, $a = w_n$ and $K_n = G_n(6/\pi)^{\frac{1}{2}}$, where G_n is defined in equation (4.32). Using equation (7.7) for $\alpha_n(x)$, Z_n may be written in the form

$$\hbar\,\beta^{-\frac{1}{2}} \int_{u_0}^{u_1} (1 - u^2)^{-\frac{1}{2}} du \qquad ; \beta > 0$$

$$Z_n = \{ \tag{7.30}$$

$$\hbar\,(-\beta)^{-\frac{1}{2}} \int_{u_0}^{u_1} (u^2 - 1)^{-\frac{1}{2}}\, du \; ; \; \beta < 0 \quad ,$$

where $u(x)$ is defined in equation (7.18).

Evaluation of the integrals in equation (7.30) is straightforward and gives

$$\hbar\,\beta^{-\frac{1}{2}} [\sin^{-1} u_1 - \sin^{-1} u_0] \qquad ; \beta > 0$$

$$Z_n = \{ \tag{7.31}$$

$$\hbar\,(-\beta)^{-\frac{1}{2}} \left(\mathrm{Ln} \left| \frac{u_1 + (u_1^2 - 1)^{\frac{1}{2}}}{u_0 + (u_0^2 - 1)^{\frac{1}{2}}} \right| \right) \; ; \; \beta < 0 \quad ,$$

where $u_1 = 1$ for cycloidal skipping states.

Expressed in terms of Z_n, the WKB cycloidal skipping state wavefunctions (4.32) and first derivatives are, in the limit $x \to 0_+$,

$$\psi_n(0_+) = \left(\frac{2}{Z_n \alpha_n(0_+)}\right)^{\frac{1}{2}} \cos\left[T(0_+) - \frac{\pi}{4}\right] \tag{7.32}$$

and

$$\frac{d\psi_n(0+)}{dx} = \left(\frac{2\alpha_n(0+)}{Z_n}\right)^{\frac{1}{2}} \sin\left[T(0+) - \frac{\pi}{4}\right] \tag{7.33}$$

where T(x) is defined in equation (4.26).

Similarly, the traversing state wavefunctions (7.10b) and derivatives satisfy

$$\psi_n(0+) = \left(\frac{2}{Z_n\alpha_n(0+)}\right)^{\frac{1}{2}} \sin\left[T(0+) + \delta_n\right] \quad , \tag{7.34}$$

and

$$\frac{d\psi_n(0+)}{dx} = -\left(\frac{2\alpha_n(0+)}{Z_n}\right)^{\frac{1}{2}} \cos\left[T(0+) + \delta_n\right] \quad . \tag{7.35}$$

Using the energy quantisation conditions (7.22) and (7.23) to obtain expressions for the sine and cosine terms in equations (7.32), (7.33), (7.34) and (7.35), the wavefunctions and derivatives of both traversing and cycloidal skipping states may be written, in the limit $x \to 0_+$,

$$\psi_n(0+) = \left(\frac{2\alpha_n(0+)}{Z_n}\right)^{\frac{1}{2}} \frac{(-1)^n\, m_B^*}{\left[\alpha_n^2(0+)m_B^{*2} + u_{n1}^2(0-)m^*(0+)^2\right]^{\frac{1}{2}}} \quad , \tag{7.36}$$

and

$$\frac{d\psi_n(0+)}{dx} = \left(\frac{2\alpha_n(0+)}{Z_n}\right)^{\frac{1}{2}} \frac{(-1)^n\, m^*(0+)\, \mu_{n1}(0-)}{[\alpha_n^2(0+)\, m_B^{*2} + \mu_{n1}^2(0-) m^*(0+)^2]^{\frac{1}{2}}} \quad . \tag{7.37}$$

Using the matching conditions (1.39) and (1.40) to determine $\psi_n(0-)$ and $d\psi_n(0-)/dx$, and using these expressions together with the modified Fang-Howard wavefunction (5.25) and derivative (5.26) in equation (3.37) gives

$$|M_n(k_y)|^2 = \hbar^2 \left[\frac{\hbar\, k(-b_-)}{2(5a_0)m_L^*}\right] \left[\frac{\hbar}{2m^*(0+)Z_n}\right] \tag{7.38}$$

$$\left[\frac{16\, m_B^{*2}\, \alpha_n(0+)\, \mu_{n1}(0-)\, k(-b-)\, e^{-2\int_{-b}^{0} \mu_{n1}(x)\, dx}}{m_L^* m^*(0+)\, \mu_{n1}(-b+)[(\alpha_n(0+)m_B^*/m^*(0+))^2 + \mu_{n1}^2(0-)]}\right]$$

Following the discussion of Section 5.8, the first bracketed term on the RHS of equation (7.38) is approximately equal to the frequency of the semiclassical collisions between each 2DEG electron and the emitter barrier, and the final bracketed term is the WKB emitter-barrier transmission coefficient (1.53).

Owing to the high electric field, the effective mass varies with x throughout the well region. Thus, by contrast to the single-barrier case, the semiclassical collision frequency

$$F_n = \frac{\hbar}{2\int_o^a \frac{m^*(x)}{\alpha_n(x)}\,dx} = \frac{\hbar}{2\left[m^*(0_+)Z_n + m_L^*\,\alpha Fe\int_o^a \frac{x\,dx}{\alpha_n(x)}\right]} \qquad (7.39)$$

of an electron in the well with the emitter barrier, is not exactly equal to the second bracketed term on the RHS of equation (7.38). However, provided the nonparabolicity parameter α is small, the difference between this term and F_n is also small, and can be neglected when interpreting the experimental data.

7.9 A Model for the Tunnel Current

Figure 7.6 shows that the 2DEG parabola makes only one intercept with each $E_n(k_y)$ curve. Thus, taking the occupancy of each well state to be zero as discussed in Section 7.5, the tunnel current $I_n(V, B)$ due to allowed transitions from the 2DEG into the n^{th} bound state of the well, is calculated as described in Section 5.4 for the single-barrier structures.

However it should be noted from Figure 7.13 that for V = 600 mV and B = 0 T, the top of the collector barrier lies below the bound state energy of the 2DEG. Consequently in zero field, transitions into bound eigenstates of the well subsystem do not occur. The tunnel current is thus only calculated for magnetic fields B $\geq$ 1.5 T which raise the top of the collector barrier above the Fermi level in the LH contact, thereby ensuring that all 2DEG electrons tunnel into

bound states in the well, with WKB dispersion relations given by equations (7.22) and (7.23).

The total current flowing through the DBRTS is then given by equation (5.11), in which $E_n(k_y)$ is the n^{th} bound state dispersion relation, and $|M_n(k_y)|^2$ is the squared matrix element (7.38) for transitions into traversing states if $E_n(k_y(n)) > V(w_-, k_y)$, or cycloidal skipping states if $E_n(k_y(n)) < V(w_-, k_y)$.

Electrons which occupy cycloidal skipping states are magnetically confined close to the emitter barrier. Current continuity is therefore maintained by scattering processes in the well which enable the electrons to diffuse between localised states with different orbit centres. These scattering processes are assumed to be sufficiently fast that the total transition rate from the well into the RH contact greatly exceeds that from the 2DEG into the well. Only if this condition is satisfied can the occupancy of the well states be taken as zero when a field is applied.

Changing the applied voltage or field causes intercepts with the well state dispersion curves $E_n(k_y)$ to be gained or lost from each extremity of the 2DEG parabola. Just as for the single-barrier structures, equation (A.2) of Appendix 1 predicts maxima (minima) in dI/dB whenever $k_y'(n) = + k_F(-k_F)$. However, by contrast, four distinct series of oscillations are expected for the DBRTS originating from $\pm k_F$ transitions into traversing states at low fields, and cycloidal skipping states at higher fields.

7.10 Simulation of the I(B) Characteristics and Derivatives

Figure 7.7 shows the current-field characteristics of the GaAs/(AlGa)As DBRTS calculated for V = 600 mV, taking the non-parabolicity factor of GaAs to be $\alpha = 2\ eV^{-1}$. The shape of the calculated I(B) curve is in reasonable agreement with the measured curve shown in Figure 7.2, although the calculated current is quenched when $B = B_o^- \cong 10.5$ T, which is considerably lower than the measured value ≅ 15 T. This discrepancy is not surprising however, since only qualitative accuracy is expected of the n = 0 WKB dispersion curve, and consequently the predicted value of B_o^-. The inclusion of nonparabolicity in the well region improves the agreement with experiment by lowering the energy levels $E_n(k_y)$ for each n and k_y, thereby raising the predicted value of B_o^-.

Figure 7.8 shows the averaged $\langle dI/dB \rangle$ curve calculated for V = 600 mV, following the procedure of Section 5.11.2, taking $\Delta B = 0.2$ T. The individual current contributions $I_n(B)$, n = 0, 1, ... 24 are also shown. The corresponding second derivative $\langle d^2I/dB^2 \rangle$ is shown in Figure 7.9.

The t+, t- and s- series of oscillations, are clearly revealed in both the measured and simulated derivatives, and are distinguished by horizontal brackets in Figures 7.2, 7.8 and 7.9. The field-dependence of the observed oscillatory structure (Figure 7.2) is clearly reproduced in both simulated derivatives. In particular, the s- series of oscillations grows stronger with increasing field,

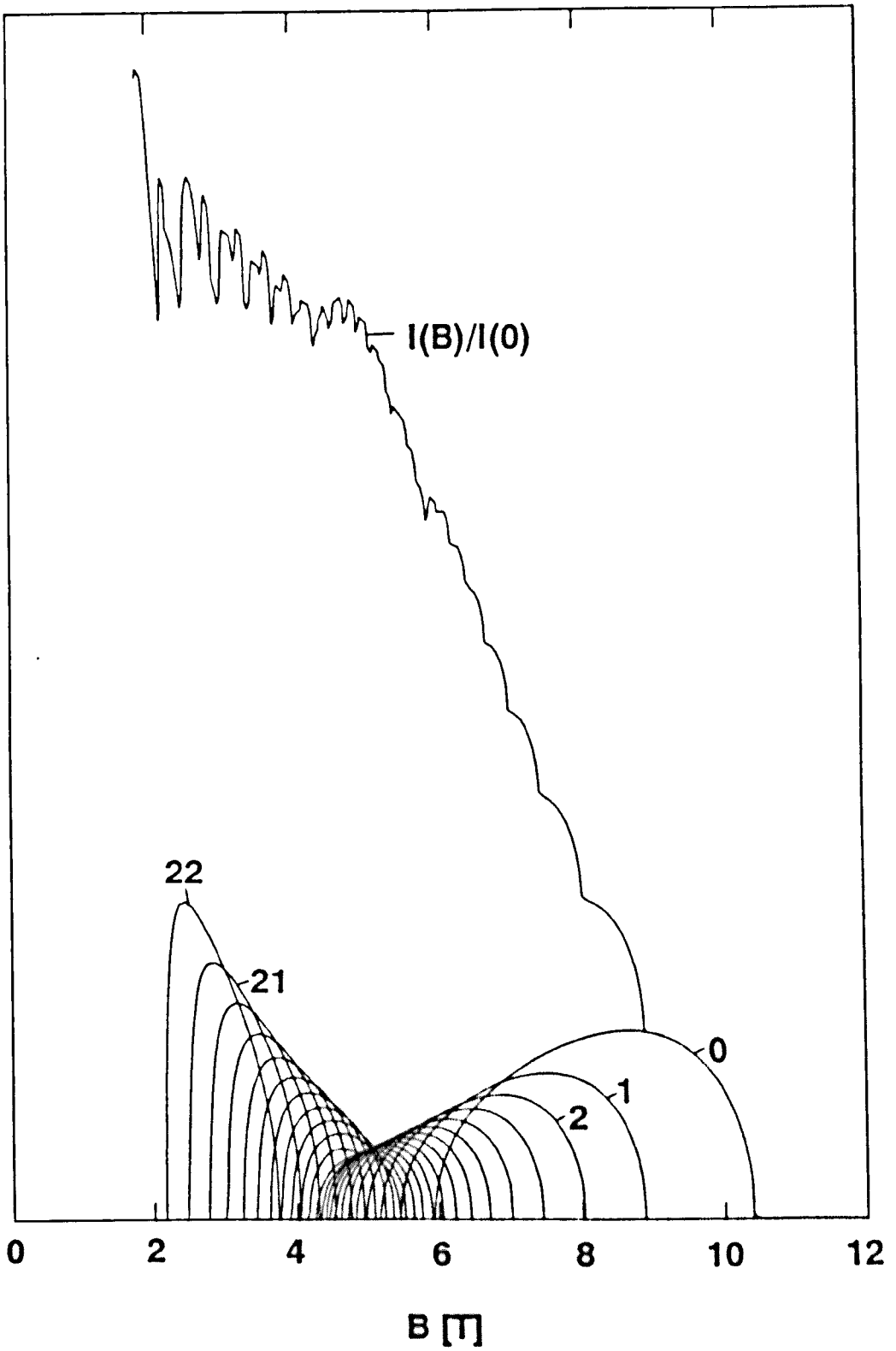

Figure 7.7 Simulated current-field characteristics of the GaAs/(AlGa)As DBRTS calculated for V = 600 mV, taking $\alpha = 2\ eV^{-1}$. The current contributions $I_n(B)$ are also shown over the field ranges $B_n^+ \leq B \leq B_n^-$.

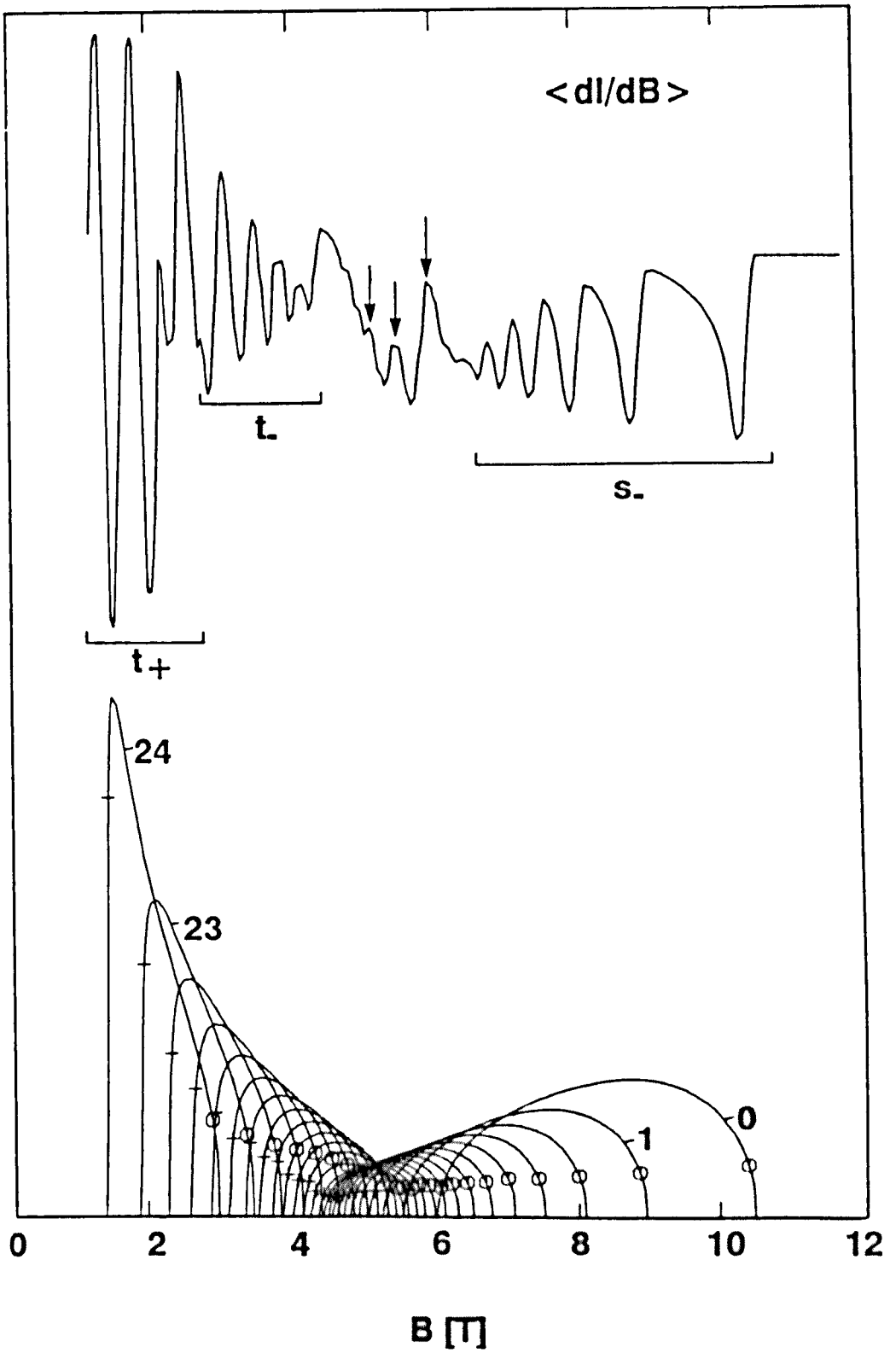

Figure 7.8 Simulated <dI/dB> curve of the GaAs/(AlGa)As DBRTS, calculated for V = 600 mV, taking $\alpha = 2\ eV^{-1}$. The current contributions $I_n(B)$ n = 0, 1, ... 24 are also shown. The mean current values $\bar{I}_n^+$ ($\bar{I}_n^-$) are indicated by crosses (circles). Three series of oscillations are revealed in <dI/dB> which are distinguished by horizontal brackets and originate from the opening and closure of tunnelling channels. The t- and s- series are separated by a field range 4 T ≤ B ≤ 6 T where only weak s^+ oscillations are observed, indicated by arrows.

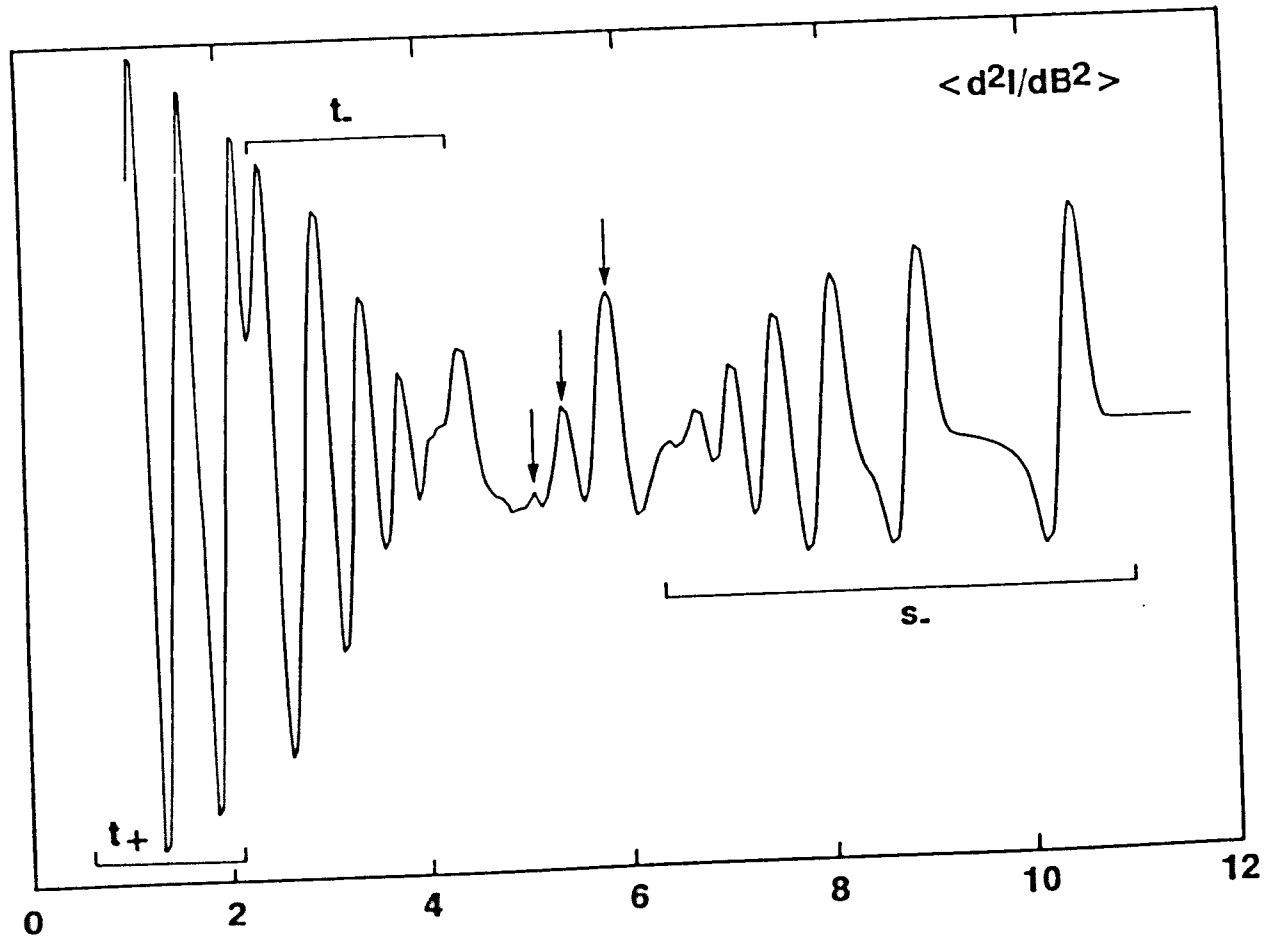

Figure 7.9 Simulated $\langle d^2I/dB^2 \rangle$ characteristic of the GaAs/(AlGa)As DBRTS, calculated for V = 600 mV, taking $a = 2\ eV^{-1}$. The t^+, t^- and s^- series, also present in the measured curve 7.2, are distinguished by horizontal brackets. The arrows indicate weak s^+ oscillations.

whereas the t+ and t- series both weaken. However, by contrast with the measured d^2I/dB^2 curve, s+ oscillatory structure is revealed in the simulated derivatives over the field range 4 T $\lesssim$ B $\lesssim$ 6.5 T separating the t- and s- series. This structure is indicated by arrows in Figures 7.8 and 7.9. Reasons for the experimental absence of s+ oscillations are given in Section 7.11.

The generally good qualitative agreement between the measured and simulated derivatives suggests that the observed oscillatory structure is indeed associated with the process of tunnelling through the emitter barrier. The absence of structure originating from transitions through the collector barrier indicates that the tunnel current is controlled by the emitter barrier, which dominates the resistance of the device. This in turn provides a posteriori justification for the assumption that tunnelling transition rates out of the well greatly exceed those into the well, and consequently that the occupancy of each well state is close to zero.

7.11 Explanation for the Origin of the Oscillatory Structure

Figure 7.6 shows that for V = 600 mV and B = 5 T, the intercepts between the 2DEG and well state dispersion curves lie in regions s and t, so that tunnelling transitions into both traversing and cycloidal skipping states are allowed. The changeover from resonances due to 2DEG electrons with $k_y'(n) = \pm k_F$ tunnelling into traversing states, to resonances due to $\pm k_F$ transitions into

cycloidal skipping states occurs as the 2DEG parabola passes from region t to region s of Figure 7.6, over the field range 4 T $\lesssim$ B $\lesssim$ 6 T. This transition region is characterised by diminished current contributions $I_n(B)$, as shown in Figure 7.8.

It is clear from Figure 7.8 that the t+ series of oscillatory maxima originates from the opening of tunnelling channels, as the $+k_F$ extremity of the 2DEG parabola intersects with lower-index traversing state dispersion curves. Closure of these channels gives rise to the t- minima, visible for B $\gtrsim$ 2.5 T.

The s- minima occur for B $\gtrsim$ 6.5 T as intercepts with the cycloidal skipping state dispersion curves are lost from the $-k_F$ extremity of the 2DEG parabola.

Eaves et al. (1988) showed that each s- resonant field B_n^- varies with voltage according to $(B_n^-)^{\frac{3}{2}} = C_nV$ where $\{C_n\}$ are constants. This linear variation of $(B_n^-)^{\frac{3}{2}}$ with V was explained using the WKB cycloidal skipping state dispersion relation (7.22), in the limit of an infinitely high emitter barrier, and neglecting non-parabolicity in the well region. Within these approximations, the predicted and measured values of C_n agree to within 15%, further supporting the interpretation of the s- oscillatory structure in terms of $-k_F$ transitions into cycloidal skipping well states.

By contrast with the measured derivative shown in Figure 7.2, s+ oscillatory structure originating from $+k_F$ transitions into cycloidal skipping states is revealed in the simulated derivatives,

indicated by arrows in Figures 7.8 and 7.9. The averaging procedure removes all other oscillatory structure associated with the rapid opening and closure of tunnelling channels over the field range separating the t- and s- series. This rapid opening and closure of tunnelling channels originates from the small separation between adjacent energy levels $E_n(k_y)$ in the transition region, which is, in part, due to conduction band nonparabolicity of the well material. Raising the nonparabolicity parameter of GaAs from $\alpha = 2$ eV^{-1} to $= 4$ eV^{-1} further reduces the separation between adjacent energy levels in the well. This in turn reduces the separation between adjacent resonant fields sufficiently that the weak s+ oscillations are totally removed by the averaging process. Semiclassically, raising α increases the effective mass in the well, thereby reducing the collision frequency F_n, which leads to diminished oscillatory structure as fewer tunnelling electrons complete whole orbits before scattering. Thus, the presence of s+ oscillatory structure in the simulated derivatives which is not observed experimentally, is possibly due to underestimating the electronic effective mass at high injection energies.

Ben Amor et al. (1990) have reported the observation of s+ oscillatory structure in similar (InGa)As/(AlIn)As wide-well DBRTS. Such structure is more likely to be seen in these samples, owing to the lighter mass of the (InGa)As well material ($m^* = 0.041$ m_0 compared with 0.067 m_0 for GaAs), which increases the separation and resolution of adjacent energy levels, and resonant fields.

7.12 Explanation for the Field-Dependence of the Factors $N_n(B)$, $D_n(B)$, $W_n(B)$, $T_n(B)$ and $F_n(B)$

7.12.1 Introduction

Equation (5.55) predicts that provided the separation between adjacent resonant fields greatly exceeds the averaging bin width ΔB = 0.2 T (which is the case for $B \leq 3$ T and $B \geq 7$ T), the oscillatory extrema $\langle dI/dB \rangle_n^{\pm}$ are directly proportional to the corresponding mean current values $\bar{I}_n^{\pm}$ defined in equation (5.54). This predicted correlation is clearly revealed in Figure 7.8, with both sets of values attaining a minimum in the transition region between the t- and s- series. The origin of this field-dependence can be understood by considering the factors

$$N_n(B) = \left(k_F^2 - k_y'(n)^2\right)^{\frac{1}{2}} \quad , \tag{7.40}$$

$$D_n(B) = \left| \frac{\hbar^2 k_y'}{m_L^*} - \frac{dE_n}{dk_y} \right|^{-1}_{k_y' = k_y'(n)} \quad , \tag{7.41}$$

and

$$W_n(B) = \frac{2\pi}{\hbar} \left| M_n(k_y) \right|^2 \tag{7.42}$$

in turn, which are shown for V = 600 mV in Figures 7.10 and 7.11. The normalised transition rate $W_n(B)$ is proportional to the product

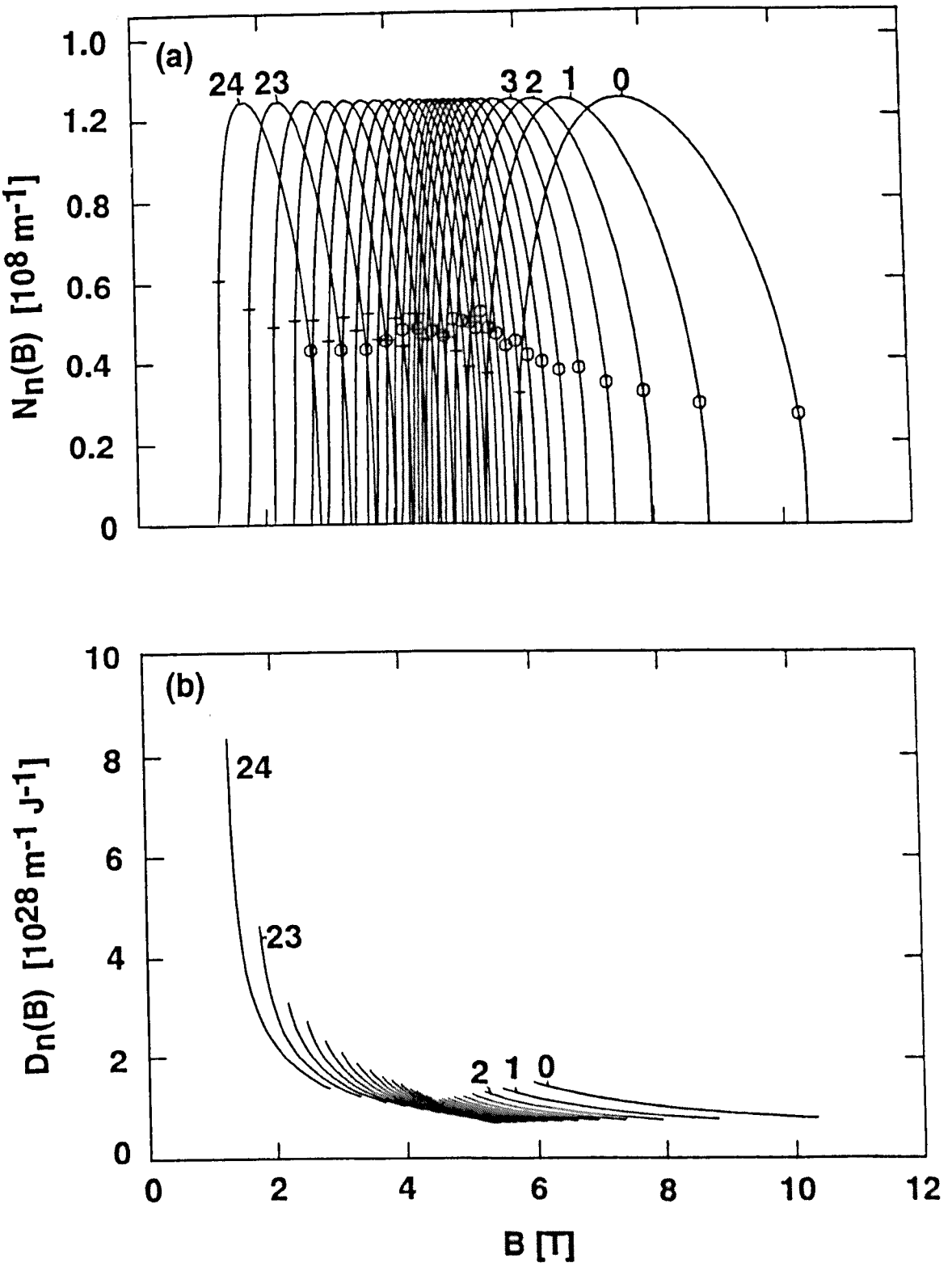

Figure 7.10 The factors (a) $N_n(B)$ and (b) $D_n(B)$ n = 0, 1, ... 24 calculated over the field ranges $B_n^+ \leq B \leq B_n^-$, for V = 600 mV and α = 2 eV^{-1}. The mean values $\bar{N}_n^+$ ($\bar{N}_n^-$) are indicated by crosses (circles).

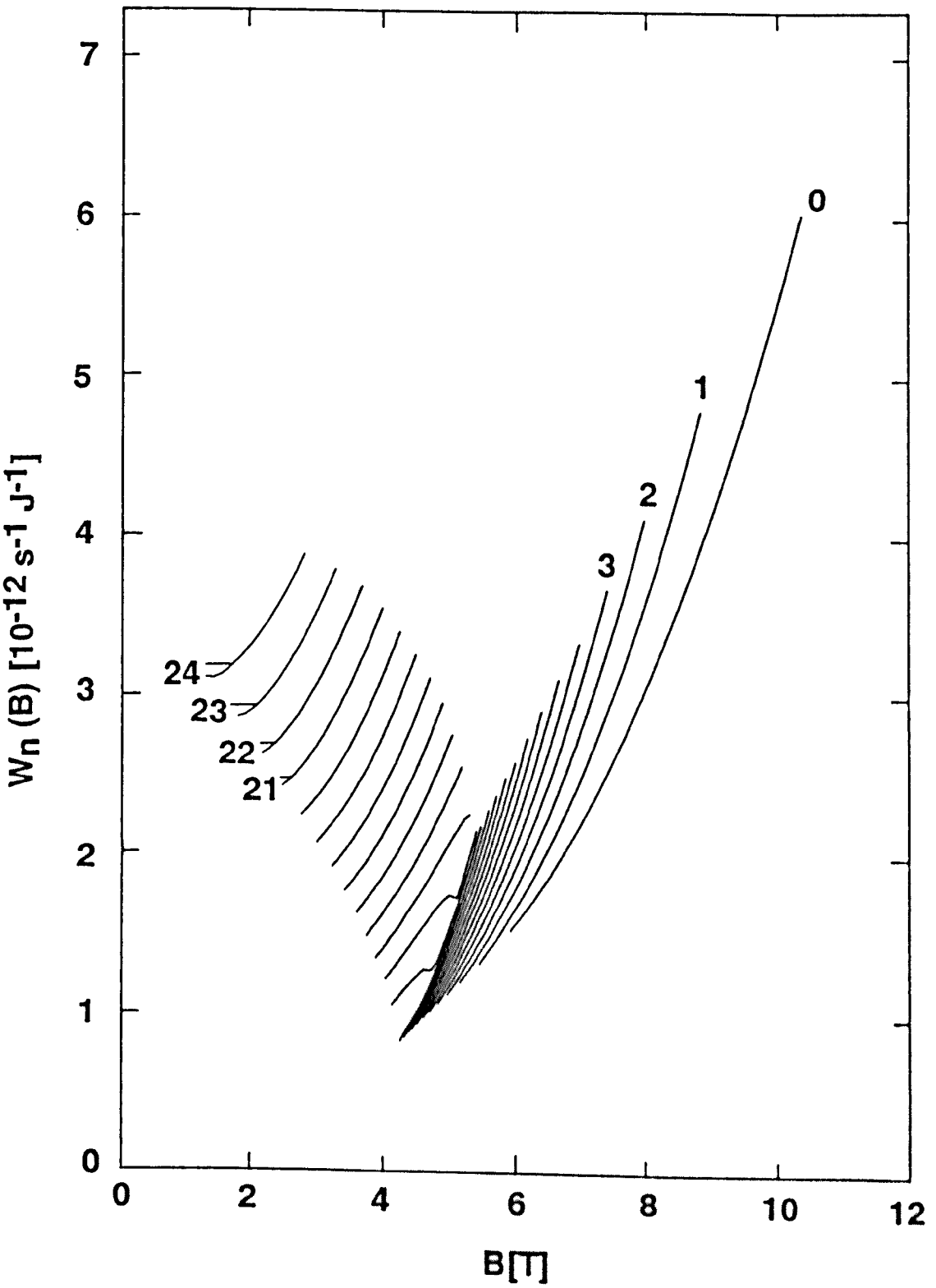

Figure 7.11 Normalised transition rates $W_n(B)$ n = 0, 1, ... 24, calculated over the field ranges $B_n^+ \leq B \leq B_n^-$ for V = 600 mV, taking α = 2 eV^{-1}.

of the emitter-barrier transmission coefficient $T_n(B)$ and the approximate collision frequency $F_n(B) = \hbar/(2m^*(0_+)Z_n)$ between an electron in the well and the emitter barrier. Both of these factors are shown for V = 600 mV in Figure 7.12.

7.12.2 The density of states factors $D_n(B)$

The field-dependence of the factors $N_n(B)$ shown in Figure 7.10a is identical to that explained in Section 5.10.2 for the single-barrier structures. By contrast, comparison of Figures 5.9b and 7.10b shows that the field-dependence of the density of states factors $D_n(B)$ is markedly different for the DBRTS. The values of $D_n(B)$ decrease rapidly with B for the traversing states, but increase with B for the cycloidal skipping states.

The values of $D_n(B_n^{\pm})$ appropriate to $\pm k_F$ transitions are inversely proportional to the absolute difference Δv_n between the mean y-component of velocity of the initial and final states. In zero field, this mean velocity component is conserved so that $D_n(B_n^{\pm}) \rightarrow \infty$. With increasing field, the traversing trajectories are further deflected by the Lorentz force so that Δv_n increases, and the values of $D_n(B_n^{\pm})$ decrease, as shown in Figure 7.10b.

Without detailed algebraic analysis, the variation of the density of states terms $D_n(B_n^{\pm})$ for $\pm k_F$ transitions into cycloidal skipping states can only be explained by a plausibility argument.

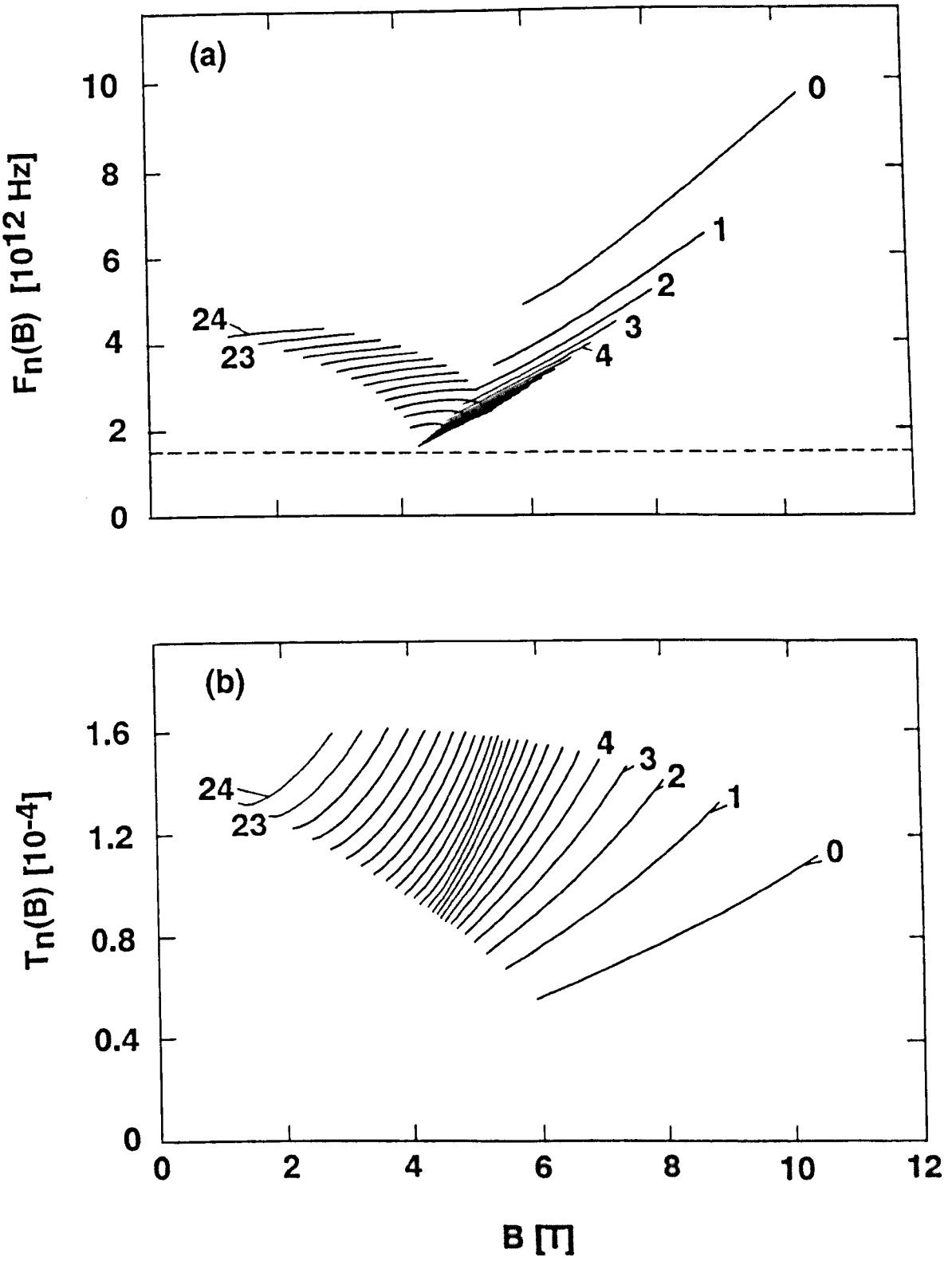

Figure 7.12 (a) Semiclassical collision frequencies $F_n(B)$ corresponding to the well states accessed in tunnelling transitions from the 2DEG and (b) emitter-barrier transmission coefficients $T_n(B)$ n = 0, 1, ... 24, calculated over the field ranges $B_n^+ \leq B \leq B_n^-$, for V = 600 mV taking $\alpha = 2\ eV^{-1}$. The broken line in (a) shows the approximate LO phonon emission rate W_{LO} in bulk GaAs divided by 2π.

Figure 7.6 shows that for B = 5 T, the gradient of the cycloidal skipping state dispersion curves (region s) exceeds $\hbar^2 k_F / m_L^*$. Consequently, from equation (7.41)

$$D_n(B_n^{\pm}) = \left(\frac{dE_n}{dk_y} \mp \frac{\hbar^2 k_F}{m_L^*}\right)^{-1} \quad . \tag{7.43}$$

The gradient of each cycloidal skipping state dispersion curve must match smoothly to that of the bulk cycloidal states in region r of the E-k_y diagram which, from equation (1.26) equals $\hbar F/B$. Since each cycloidal skipping state dispersion curve is almost linear, $dE_n/dk_y \cong \hbar F/B$ throughout region s, so that equation (7.43) predicts

$$D_n(B_n^{\pm}) \cong \left(\frac{\hbar F}{B_n^{\pm}} \mp \frac{\hbar^2 k_F}{m_L^*}\right)^{-1} \quad . \tag{7.44}$$

Consequently, the values of $D_n(B_n^{\pm})$ describing transitions into cycloidal skipping states are expected to increase with $B_n^{\pm}$ as shown in Figure 7.10b.

7.12.3 The Transmission Coefficients $T_n(B)$

Figure 7.12b shows the emitter-barrier transmission coefficients $T_n(B)$ n = 0, 1, ... 24 calculated for V = 600 mV. Over the illustrated field range $B_{24}^+ \leq B \leq B_0^-$, the $\pm k_F$ transmission coefficients $T_n(B_n^{\pm})$ decrease with increasing $B_n^{\pm}$. This is due to the increasing contribution of the magnetic potential to the effective barrier height, explained in Section 5.10.4 for the single-barrier structures.

For given n, $T_n(B)$ increases monotonically as B is raised from B_n^+ to B_n^- for the following reason. Figure 7.13 shows for the case n = 21, that as B increases from B_n^+ to B_n^-, the orbit centre moves from X_+ to X_-, thereby reducing the mean magnetic potential in the barrier region, which causes the calculated increase in $T_n(B)$. Figure 7.13 also shows that owing to the presence of the wide well, very little voltage is dropped across the emitter barrier. Consequently, the reduction in mean magnetic potential in the barrier region produces only a small percentage reduction in the total effective barrier height, resulting in slightly increased transmission.

This is in contrast to the dramatic field-dependence of the GaAs/(AlGa)As single-barrier transmission coefficients $T_n(B)$ shown in Figure 6.6b. Since about half the applied voltage is dropped across the single (AlGa)As barrier, the total effective barrier height and transmission coefficient of these structures are very sensitive to

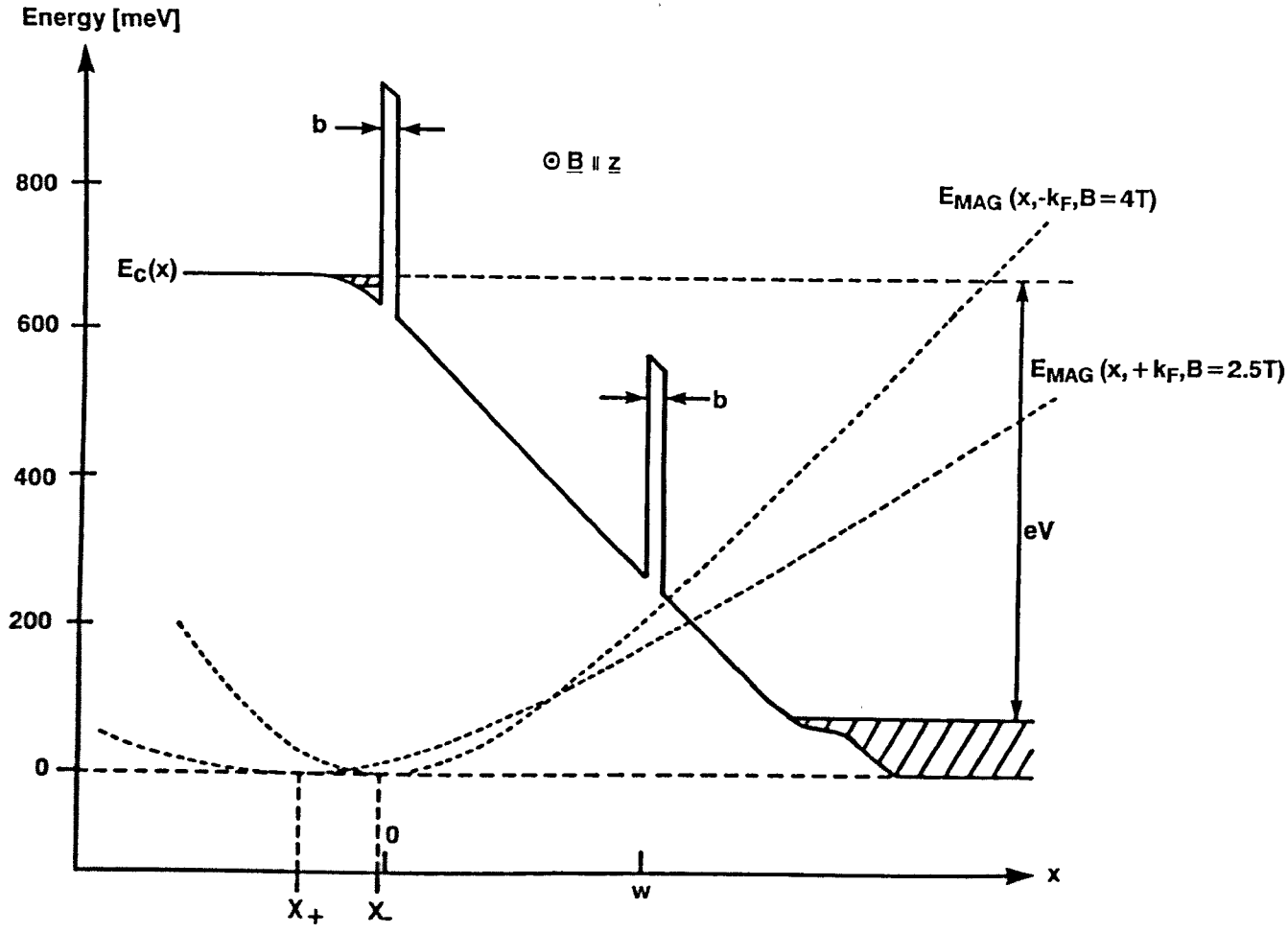

Figure 7.13 Conduction band profile $E_c(x)$ of the wide-well DBRTS together with the magnetic potential energy variation $E_{MAG}(x)$ describing the action of the Lorentz force on electrons with $k_y' = +k_F$ ($-k_F$) tunnelling into the n = 21 traversing well state when B = 2.5 T (4 T) and V = 600 mV. The conduction band nonparabolicity factor of GaAs is taken to be $a = 2\ eV^{-1}$.

changes in the mean magnetic potential in the barrier region (see Section 6.4.3).

Comparison of Figures 6.6b and 7.12b reveals that the transmission coefficient ratio $T_m(B_m^-)/T_n(B_n^+)$, for $\pm k_F$ transitions occuring at adjacent resonant fields $B_n^+ \cong B_m^-$, is much lower for the DBRTS than for the GaAs/(AlGa)As single-barrier structures. It follows from equation (5.59) that this difference is partly due to the thinner barriers of the DBRTS (56 Å compared with 230 Å), and partly because most of the applied voltage is dropped across the wide well so that the emitter barrier remains high ($\bar{E}_o \cong \Delta E_c$). This reduces the percentage contribution of the magnetic potential to the total barrier height.

7.12.4 The Semiclassical collision frequencies $F_n(B)$ and transition rates $W_n(B)$

Figure 7.12a shows that the semiclassical collision frequencies $F_n(B_n^{\pm})$ corresponding to traversing (cycloidal skipping) states accessed by 2DEG electrons with $k_y'(n) = \pm k_F$ decrease (increase) with increasing $B_n^{\pm}$. Thus, the changeover from occupied traversing states to cycloidal skipping states in the well is characterised by diminished values of $F_n(B_n^{\pm})$. Neglecting non-parabolicity, the magnetic potential energy describing the effect of the Lorentz force on the motion of $\pm k_F$ electrons in the well region is

$$E_{MAG}^{\pm}(x) = [B_n^{\pm} e(x + b + 3a_o) \pm \hbar k_F]^2/2m_L^* \quad . \qquad (7.45)$$

With increasing B_n^+, and increasing $B_n^- \geq \hbar k_F/e(b + 3a_o)$ (= 3.3 T for V = 600 mV), $E_{MAG}^{\pm}(x)$ increases throughout the well region. Classically, this corresponds to an increase in the local y-component of velocity $v_y^{\pm}(x) = (2E_{MAG}^{\pm}(x)/m_L^*)^{\frac{1}{2}}$, as the electron trajectory is further deflected by the action of the Lorentz force (see Section 1.5). Since the total energy eV + E_{FR} of $\pm k_F$ electrons and the local electrostatic potential energy $-e\phi(x)$ are unchanged by the magnetic field, so too is the total local kinetic energy. It follows that the increase in $v_y^{\pm}(x)$ with increasing field corresponds to a reduction in the longitudinal velocity component $v_x^{\pm}(x)$ throughout the well region. Since $\pm k_F$ traversing electrons still travel the same distance 2w in the x-direction between successive collisions with the emitter barrier, the traversing state collision frequencies $F_n(B_n^{\pm})$ decrease with increasing field as shown in Figure 7.12a. The lowest collision frequencies are attained in the field range corresponding to the changeover from traversing to cycloidal skipping states in the well. In this transition region, the electron trajectories are deflected by the Lorentz force to be of grazing incidence on the collector barrier, and the distance travelled bewteen successive collisions reaches a maximum ($\simeq$ 4000 Å).

Once the magnetic field reaches the threshold required for $\pm k_F$ transitions into cycloidal skipping states with soft RH turning points w_n, the distance $2w_n$ travelled in the x-direction between

successive collisions with the emitter barrier decreases with increasing field, as the electrons are magnetically bound to the emitter barrier. With increasing $B_n^{\pm}$, the shorter path lengths travelled in the x-direction more than compensate for the reduction in the local longitudinal velocity component $v_x^{\pm}(x)$, so that the $\pm k_F$ cycloidal state skipping frequencies $F_n(B_n^{\pm})$ increase as shown in Figure 7.12a.

Figure 7.13 illustrates for the case n = 21 that the collision frequency $F_n(B)$ of each traversing or skipping state increases with field because the associated shift in the orbit centre position from X_+ to X_- reduces the magnetic potential throughout most of the well region, thereby increasing the local x-component of velocity $v_x(x)$.

The magnetic potential energy variation experienced by $\pm k_F$ electrons tunnelling at adjacent resonant fields $B_{1,1}^{+} \simeq B_{2,1}^{-} = 4$ T is shown in Figure 7.14. Since $X_+ < X_-$, the magnetic potential energy, or classical y-component of velocity, of the $+k_F$ electrons exceeds that of the $-k_F$ electrons throughout the well region (corresponding to increased Lorentz deflection of the $+k_F$ electrons). Since both $\pm k_F$ electrons have the same total kinetic energy for given x, it follows that the $-k_F$ electrons have a higher longitudinal velocity component throughout the well region and consequently $F_m(B_m^{-} \simeq B_n^{+}) > F_n(B_n^{+})$ as shown in Figure 7.12a.

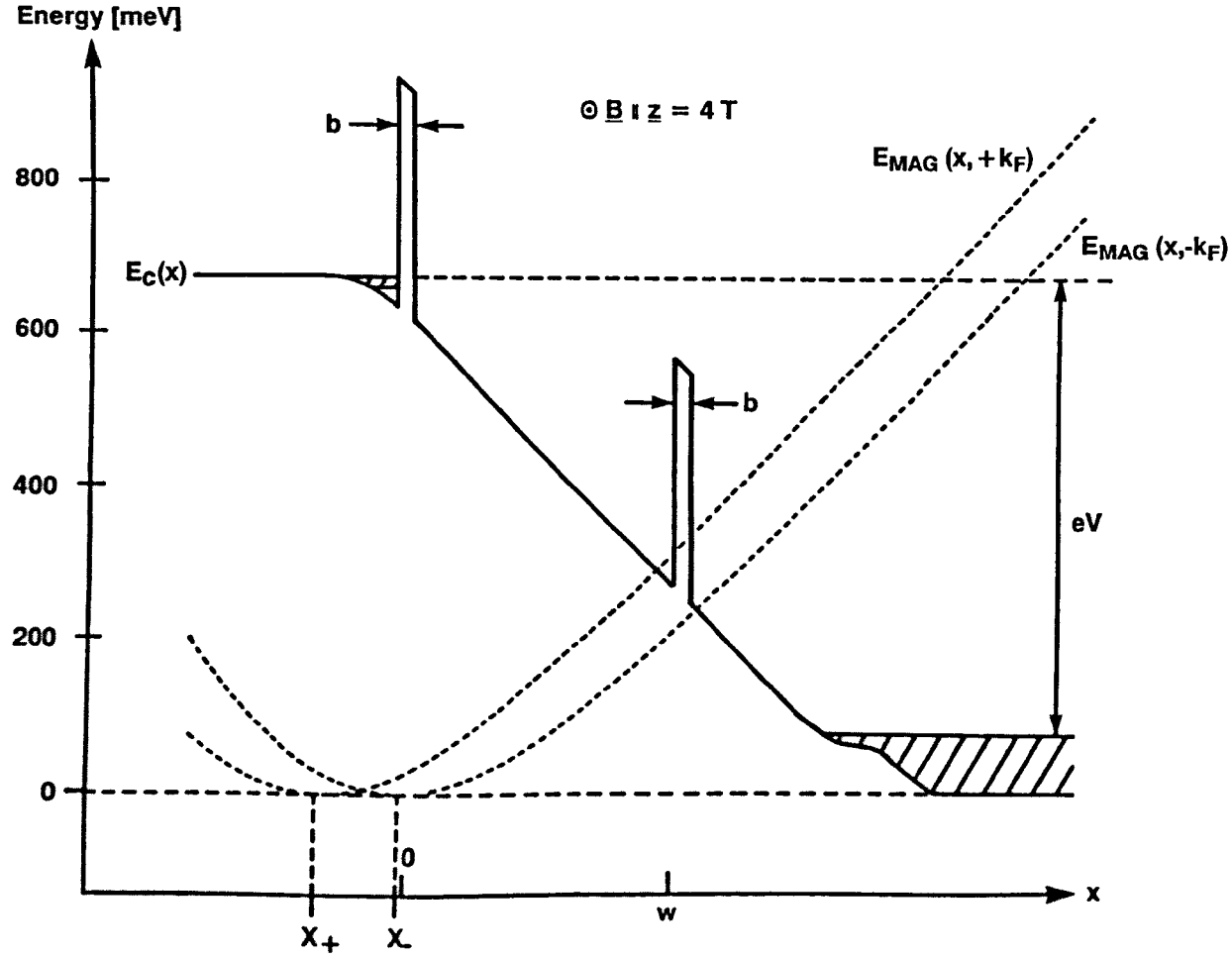

Figure 7.14 Conduction band profile $E_c(x)$ of the wide-well DBRTS together with the magnetic potential energy variation $E_{MAG}(x)$ describing the action of the Lorentz force on electrons with $k_y' = +k_F$ $(-k_F)$ tunnelling into the n = 13 (21) traversing state in the well when B = 4 T and V = 600 mV. The nonparabolicity factor of GaAs is taken to be 2 eV^{-1}.

The field-dependence of the normalised transition rates $W_n(B)$ $\propto F_n(B)\ T_n(B)$ shown in Figure 7.11 is dominated by the more rapidly-varying collision frequencies $F_n(B)$. Quantum-mechanically, the $\pm k_F$ transition rates $W_n(B_n^{\pm})$ increase following the changeover from traversing to cycloidal skipping states in the well, as increased magnetic confinement of the magneto-quantised wavefunctions, raises the amplitudes $\psi_n(0_+)$ at the RHS of the emitter barrier and thus, from equations (3.25) and (3.37), the tunnelling transition rate (Fromhold et al., 1990).

7.13 Physical Interpretation of the Field-Dependence of the Oscillatory Structure observed in $\langle dI/dB \rangle$ and $\langle d^2I/dB^2 \rangle$

7.13.1 Introduction

Figure 7.10a shows that the mean values $\bar{N}_n^{\pm}$ defined in equation (5.55) depend only weakly on n. This equation therefore predicts direct proportionality between the extremal values of $\langle dI/dB \rangle$ and the factors $D_n(B)$, $T_n(B)$ and $F_n(B)$ appropriate to $\pm k_F$ transitions into the n^{th} bound state in the well.

7.13.2 Field-dependence of the t+ series

The first (n = 24) t+ maximum revealed in the simulated derivative 7.8, is of large amplitude primarily because the density of states factor $D_{24}(B_{24}^{+})$ shown in Figure 7.10b is also large. As explained in Section 7.12.2, the values of $D_n(B)$ are generally high at low fields because the action of Lorentz force produces little change in the mean y-component of velocity of the tunnelling electrons. The low-field t+ oscillations are further enhanced by the high collision frequencies and transmission coefficients, shown in Figure 7.12, which ensure high tunnelling transition rates.

The t+ oscillatory amplitudes decrease with increasing field because increased Lorentz deflection of the traversing trajectories reduces the density of states and collision frequency factors $D_n(B_n^{+})$ and $F_n(B_n^{+})$, as shown in Figures 7.10b and 7.12a.

In addition, the increasing magnetic potential in the barrier region reduces the $+k_F$ transmission coefficients which, from equation (5.55), also contributes to the diminished t+ oscillatory amplitudes.

7.13.3 Field-dependence of the t- series

From Figure 7.8, the minimum field required for $-k_F$ transitions into traversing states in the well is $B_{24}^{-} \approx 3$ T. Figures 7.10b and 7.12 show that for $\pm k_F$ transitions into traversing states

occurring at adjacent resonant fields $B_n^+ \cong B_m^- > B_{2s}^-$, $D_m(B_m^-) \cong 0.66\, D_n(B_n^+)$, $F_m(B_m^-) \cong 1.5\, F_n(B_n^+)$ and $T_m(B_m^-) \cong 1.5\, T_n(B_n^+)$.

Owing to these disparities, which are explained in physical terms in Section 7.12, equation (5.55) predicts that for $B \geq B_{2s}^-$, the t- minima in <dI/dB> will dominate the t+ maxima. This dominance is clearly revealed in Figure 7.8; for B > 3 T, the smoothing procedure described in Section 5.11.2 removes all trace of the weakened t+ series. By contrast, this averaging procedure has little effect on the t- oscillatory structure because of the comparatively high separation $B^-_{n-1} - B_n^-$ between adjacent $-k_F$ resonant fields. This, in turn, originates from the lower energy density of states close to the $-k_F$ extremity of the 2DEG parabola which, for large n, corresponds to the higher $-k_F$ traversing frequencies $F_m(B_m^- \cong B_n^+) > F_n(B_n^+)$ shown in Figure 7.12a. Since the discrete energy levels $E_n(k_y)$ are more easily resolved close to the $-k_F$ extremity of the 2DEG parabola, the t- series is expected to dominate the oscillatory structure as, semiclassically, a higher percentage of the $-k_F$ electrons complete whole traversing orbits before scattering. Thus, in removing the closely-spaced t+ series, the averaging procedure simulates the physical effect of broadening on energy level resolution.

7.13.4 Explanation for the absence of oscillatory structure in the transition region from traversing to cycloidal skipping states

Oscillatory structure associated with tunnelling into quantised energy levels in the well is only resolved provided the level separation greatly exceeds the lifetime broadening. This condition is equivalent to the semiclassical requirement (5.58) that the frequency $F_n(B)$ of collisions between an electron in the well and the emitter barrier greatly exceeds the total scattering rate divided by 2π.

In undoped III-V compounds at 4.2 K the dominant scattering mechanism of hot electrons is LO phonon emission, which occurs at a rate $W_{LO} \sim 10^{13}\ s^{-1}$ (Levi et al., 1987, Becker et al., 1988, Hayes et al., 1988).

Figure 7.12a shows that the field range $4\ T \leq B \leq 6\ T$ corresponding to the transition from traversing to cycloidal skipping states in the well, is characterised by low collision frequencies $F_n(B)$. This has two implications for the oscillatory amplitudes. Firstly, equation (5.55) predicts that the low collision frequencies and tunnelling transition rates will give rise to weak oscillatory structure.

Secondly, the collision frequencies in the transition region are comparable with the LO phonon emission rate, indicated by the

broken line in Figure 7.12a. Thus, the already weak structure is expected to be poorly resolved due to the effects of level broadening.

The averaging routine used to calculate the derivative curves simulates level broadening in the sense that high-frequency oscillatory structure resulting from closely-spaced energy levels is removed. Thus, the t- and s- series of oscillations are separated in the measured (simulated) derivatives by a range of field, corresponding to the changeover from traversing to cycloidal skipping states in the well, where no (weak) oscillatory structure is revealed.

7.13.5 Field-dependence of the s- Series

Above 6 T, oscillatory structure due to $-k_F$ transitions into cycloidal skipping states is observed. As predicted by equation (5.55), these oscillations grow stronger as the density of states factors $D_n(B_n^-)$ and skipping frequencies $F_n(B_n^-)$ increase with field. Transitions into higher-frequency cycloidal skipping states give rise to more pronounced oscillatory structure since the transition rates $W_n(B_n^-)$, and the fraction of $-k_F$ electrons which complete whole cycloidal skipping orbits before scattering, are both higher.

7.14 Summary

When a bias voltage of several hundred millivolts is applied to a DBRTS containing a wide quantum well, the transmission coefficient of the emitter barrier is low compared with that of the collector barrier. Consequently, the tunnel current is controlled by transitions from the 2DEG into the quantum well.

Owing to the low Fermi energy of the 2DEG, transitions in the presence of a transverse magnetic field only occur into bound states in the well with hard LH turning points. These states correspond to classical traversing orbits at low fields or, at higher fields, to cycloidal skipping trajectories along the emitter barrier.

In the transverse field geometry, the requirements of total energy and transverse wavevector conservation give rise to oscillatory structure in the current-voltage and current-field characteristics of the DBRTS as intercepts with the well state dispersion curves $E_n(k_y)$ are gained or lost from the extremities of the 2DEG parabola.

Four series of oscillations can in principle be observed, associated with $\pm k_F$ transitions into traversing (cycloidal skipping) states at low (high) fields.

The extremal values $\langle dI/dB \rangle_n^{\pm}$ of the averaged derivative of the magneto-current are proportional to the factors $D_n(B_n^{\pm})T_n(B_n^{\pm})$

$F_n(B_n^{\pm})$ appropriate to $\pm k_F$ transitions into the n^{th} bound state in the well.

Since only a small fraction of the applied voltage is dropped across the emitter barrier, the total effective barrier height and barrier transmission coefficients $T_n(B)$ are only weakly field-dependent. The field-dependence of the oscillatory amplitudes in $\langle dI/dB \rangle$ and $\langle d^2I/dB^2 \rangle$ is therefore primarily determined by the density of states factors $D_n(B_n^{\pm})$ and collision frequencies $F_n(B_n^{\pm})$, which both attain minimum values in the transition region between traversing and cycloidal skipping states in the well. This minimum collision frequency coincides with the longest classical trajectory ($\simeq$ 4000 Å), as electrons in the well are deflected by the Lorentz force to be of grazing incidence on the collector barrier. As the collision frequencies fall, so too do the tunnelling transition rates, and the fraction of tunnelling electrons which complete whole orbits before scattering. Both of these effects contribute to the diminished oscillatory amplitudes characteristic of the changeover from electric to magnetic quantisation of the well states.

The presence of weak s^+ oscillatory structure in the simulated derivatives, which is not revealed in the measured d^2I/dB^2 curve, is probably due to underestimating the electronic effective mass at injection energies far above the conduction band edge in the well. Using a higher nonparabolicity parameter α prevents resolution of the closely-spaced energy levels in the transition region, thereby suppressing the s^+ series, in agreement with experiment.

The re-emergence of s- oscillatory structure at high fields confirms the assertion of Chapters 5 and 6 that the effect of the transverse magnetic field on the effective barrier height and on the degree of confinement of the final state wavefunctions (or, equivalently the semiclassical collision frequencies), must both be considered in order to interpret the oscillatory structure revealed in the magneto-current and derivatives of single-barrier structures and DBRTS containing a wide quantum well.

By contrast, for DBRTS containing a narrow quantum well (of width much less than the cyclotron radius) a transverse magnetic field has little effect on the well state wavefunctions and influences the tunnel current simply by changing the emitter barrier height and transmission coefficient (Ancilotto, 1988).

APPENDIX 1

DIVERGENCE OF dI/dB AT THE RESONANT FIELDS

The tunnel current is given by

$$I = \sum_n I_n \tag{A.1}$$

where the sum is restricted to those levels for which $|k_y'(n)| \leq k_F$. Since I_n depends on B parametrically through the dependence of the intersection point $k_y'(n)$ on B, we have $dI_n/dB = (dI_n/dk_y')(dk_y'/dB)$, and, as $k_y'(n) \to \pm k_F$,

$$\frac{dI_n}{dk_y'} \to \left[\frac{\mp 2ek_F\,|M_n|^2}{\pi\hbar(k_F^2 - k_y'^2)^{\frac{1}{2}}\Delta}\right] \quad k_y' = k_y'(n) \tag{A.2}$$

where $\Delta = |(\hbar^2 k_y'/m^*_L) - (dE_n/dk_y)|$. This expression clearly diverges at the extremal points $k_y'(n) = \pm k_F$ and, since $dk_y'(n)/dB < 0$, (see Section 5.5), it follows that

$$\frac{dI}{dB} \cong \frac{dI_n}{dB} \to \pm \infty \quad \text{as } B \to B_n^{\pm} \; .$$

APPENDIX 2

Substituting $k_0 = Be(b + 3a_0)/\hbar$, the requirement (7.27a) that the orbit centre $\bar{X}$ lies to the right of the emitter barrier for $\pm k_F$ transitions into well states with soft left-hand turning points may be written

$$G^{\pm}(B) = e(b + 3a_0)B^2 \pm (\hbar k_F)B - m_L^* F < 0 \qquad (A2.1)$$

The non-negative roots of $G^{\pm}(B)$ are

$$B_R^{\pm} = \frac{\mp(\hbar k_F) + [(\hbar k_F)^2 + 4m_L^* Fe(b + 3a_0)]^{\frac{1}{2}}}{2e(b + 3a_0)} \qquad (A2.2)$$

Since $G^{\pm}(B) \to \infty$ as $B \to \pm\infty$, (A2.1) is only satisfied for $B \leq B_R^{\mp}$ or, equivalently

$$k_0 \leq \mp \frac{k_F}{2} + \frac{[k_F^2 + 4m_L^* Fe(b + 3a_0)/\hbar^2]^{\frac{1}{2}}}{2} \qquad (A2.3)$$

For $-k_F$ electrons, (A2.3) is satisfied only if

$$k_0 - k_F \leq \frac{[k_F^2 + 4m_L^* Fe(b + 3a_0)/\hbar^2]^{\frac{1}{2}}}{2} \qquad (A2.4)$$

From equations (2.12) and (2.20), the potential energy difference across the accumulation layer is $3a_0eF = E_F + E_{bo}$, where E_F and E_{bo} are the 2DEG Fermi energy and bound state energy. Using this relation, if $k_F < k_0$, squaring both sides of inequality (A2.4) gives,

$$\frac{\hbar^2(k_0 - k_F)^2}{2m_L^*} < \frac{1}{4}\left(\frac{\hbar^2 k_F^2}{2m_L^*}\right) + \frac{Fe(b + 3a_0)}{2}$$

$$= Fe(b + 3a_0) - \left[\frac{E_F}{2} + eFb + E_{bo}\right]/2 \qquad \text{(A2.5)}$$

REFERENCES

Altarelli, M. (1988), "Envelope function approach to electronic states in heterostructures", in 'Interfaces, Quantum Wells and Superlattices', C.R. Leavens and R. Taylor, eds. Plenum, New York.

Alves, E.S., Leadbeater, M.L., Eaves, L., Henini, M. and Hughes, O.H. (1989), Solid-State Electron. 32, 1627.

Ancilotto, F. (1988), J. Phys. C 21, 4657.

Ando, T., Fowler, A.B. and Stern, F. (1982), Rev. Mod. Phys. 54, 437.

Ashcroft, N.W. and Mermin, N.D. (1976), "Solid State Physics", Butler and Tanner, London.

Azbel, M. Ya. (1983), Phys. Rev. B 28, 4106.

Bardeen, J. (1961), Phys. Rev. Lett. 6, 57.

Bastard, G. (1983), Appl. Phys. Lett. 43, 591.

Becker, P.C., Fragnito, H.L., Brito-Cruz, C.H., Shah, J., Fork, R.L., Cunningham, J.E., Henry, J.E. and Shank, C.V. (1988), Appl. Phys. Lett. 53, 2089.

Ben Amor, S., Martin, K.P., Rascol, J.J.L., Higgins, R.J., Torabi, A., Harris, H.M. and Summers, C.J. (1988), Appl. Phys. Lett. 53, 2540.

Ben Amor, S., Martin, K.P., Rascol, J.J.L., Higgins, R.J., Potter, R.C., Lakhani, A.A. and Hier, H. (1990), Proc. 4th Int. Conf. on Modulated Semiconductor Structures, eds. L.L. Chang, R. Merlin and D.C. Tsui, Surf. Sci. (to be published).

BenDaniel, D.J. and Duke, C.B. (1966), Phys. Rev. 152, 683.

Blakemore, J.S. (1982), J. Appl. Phys. 53, R123.

Brey, L., Platero, G. and Tejedor, C. (1988a), Phys. Rev. B 38, 9049.

Brey, L., Platero, G. and Tejedor, C. (1988b), Phys. Rev. B 38, 10507.

Broekaert, T.P.E., Lee, W. and Fonstad, C.G. (1988), Appl. Phys. Lett. 53, 1545.

Buttiker, M. (1988), IBM J. Res. Develop. 32, 63.

Capasso, F. (1986), J. Quant. Elect. 22, 1853.

Capri, A.Z. (1985), "Non Relativistic Quantum Mechanics", Benjamin/Cummings, Menlo Park, California.

Chan, K.S., Sheard, F.W., Toombs, G.A. and Eaves, L. (1987), unpublished.

Chan, K.S., Eaves, L., Maude, D.K., Sheard, F.W., Snell, B.R., Toombs, G.A., Alves, E.S., Portal, J.C. and Bass, S. (1988), Solid-State Electronics 31, 711.

Chang, L.L., Esaki, L. and Tsu, R. (1974), Appl. Phys. Lett. 24, 593.

Cohen-Tannoudji, C., Diu, B. and Laloe, F. (1977), "Quantum Mechanics Vol. 2", Wiley-Interscience, London.

Dicke, R.H. and Wittke, J.P. (1960), "Introduction to Quantum Mechanics", Addison-Wesley, Reading.

Dingle, R., Gossard, A.C. and Wiegmann, W. (1975), Phys. Rev. Lett. 34, 1327.

Duke, C.B. (1969), Solid State Physics Suppl. 10, Eds. Ehrenreich, H., Seitz, F. and Turnbull, D., Academic Press, London.

D'yakonov, M.I. and Raikh, M.E. (1985), Sov. Phys. JETP 61, 1125.

Eaves, L., Snell, B.R., Maude, D.K., Guimaraes, P.S.S., Taylor, D.C., Sheard, F.W., Toombs, G.A., Portal, J.C., Dmowski, L., Claxton, P., Hill, G., Pate, M.A. and Bass, S.J. (1987), Proc. 8th Int. Conf. on Physics of Semiconductors, O. Engstrom ed. World Scientific, Singapore.

Eaves, L., Alves, E.S., Foster, T.J., Henini, M., Hughes, O.H., Leadbeater, M.L., Sheard, F.W., Toombs, G.A., Chan, K.S., Celeste, A., Portal, J.C., Hill, G., and Pate, M.A. (1988), in Springer Series in Solid State Sciences 83 , 74.

England, P., Hayes, J.R., Helm, M., Harbison, J.P., Florez, L.T. and Allen, S.J. (1989a), Solid-State Electronics 32, 1219.

England, P., Hayes, J.R., Helm, M., Harbison, J.P., Florez, L.T. and Allen, S.J. (1989b), Appl. Phys. Lett. 54, 1469.

Esaki, L. (1986), J. Quant. Elect. 22, 1611.

Fang, F.F. and Howard, W.E. (1966), Phys. Rev. Lett. 16, 797.

Fowler, R.H. and Nordheim, L. (1928), Proc. Roy. Soc. (London) A119, 173.

Fromhold, T.M., Sheard, F.W. and Toombs, G.A. (1990), Proc. 4th Int. Conf. on Modulated Semiconductor Structures, eds. L.L. Chang, R. Merlin and D.C. Tsui, Surf. Sci. (to be published).

Fromhold, T.M., Sheard, F.W. and Toombs, G.A. (1990a), to be published.

Goodhue, W.D., Sollner, T.C.L.G., Le, H.Q., Brown, E.R. and Vojak, B.A. (1986), Appl. Phys. Lett. 49, 1086.

Gueret, P., Baratoff, A. and Marclay, E. (1987) Europhys. Lett. 3, 367.

Hayes, J.R., England P. and Harbison, J.P. (1988), Appl. Phys. Lett. 52, 1578.

Heiblum, M., Fischetti, M.V., Dumke, W.P., Frank, D.J., Anderson , I.M., Knoedler, C.M. and Osterburg, L. (1987), Phys. Rev. Lett. 58, 816.

Helm, M., Peeters, F.M., England, P., Hayes, J.R. and Colas, E. (1989), Phys. Rev. B 39, 3427.

Henini, M., Leadbeater, M.L., Alves, E.S., Eaves, L. and Hughes, O.H. (1989), J. Phys.: Condens. Matter 1, 3025.

Hermann, C. and Weisbuch, C. (1977), Phys. Rev. B 15, 823.

Hickmott, T.W., Solomon, P.M., Fischer, R. and Morkoc, H. (1985), J. Appl. Phys. 57, 2844.

Hickmott, T.W. (1985a), Phys. Rev. B 32, 6531.

Hickmott, T.W. (1987), Solid State Comm. 63, 371.

Hickmott, T.W. (1988), Private Communication.

Johnson, E.A., MacKinnon, A. and Goebel, C.J. (1987), J. Phys. C 20, L521.

Kane, E.O. (1956), J. Phys. Chem. Solids 1, 82.

Kane, E.O. (1957), J. Phys. Chem. Solids 1, 249.

Kane, E.O. (1982), "Energy Band Theory", in 'Handbook on Semiconductors, Vol. 1, Band Theory and Transport Properties', T.S. Moss and W. Paul, eds., North-Holland Publishing Company, Amsterdam.

Kash, J.A., Tsang, J.C. and Huan, J.M. (1985), Phys. Rev. Lett. 54, 2151.

Lassnig, R. (1985), Phys. Rev. B 31, 8076.

Lassnig, R. (1987), Solid State Comm. 61, 577.

Leadbeater, M.L., Alves, E.S., Eaves, L., Henini, M., Hughes, O.H., Celeste, A., Portal, J.C., Hill, G. and Pate, M.A. (1989), J. Phys.: Condens. Matter, 1, 4865.

Leadbeater, M.L. (1990), Ph.D. Thesis, University of Nottingham, U.K.

Levi, A.F.J., Spah, R.J. and English, J.H. (1987), Phys. Rev. B 36, 9402.

Lobentanzer, H., Ruhle, W.W., Stolz, W. and Ploog, K. (1987), Solid State Comm. 62, 53.

Luryi, S. (1985), Appl. Phys. Lett. 47, 490.

Mendez, E.E. (1988), "Physics of Resonant Tunnelling in Semiconductors", in 'Physics and Applications of Quantum Wells and Superlattices', E.E. Mendez and K. von Klitzing, eds., Plenum, New York.

Merzbacher, E. (1970), "Quantum Mechanics", 2nd Edition, John Wiley, London.

Miller, J.C.P. (1965), in 'Handbook of Mathematical Functions', M. Abramowitz and I.A. Stegun, eds., Dover, New York.

Morkoc, H., Chen, J., Reddy, U.K. and Henderson, T. (1986), Appl. Phys. Lett. 49, 70.

Olver, F.W.J. (1965), in 'Handbook of Mathematical Functions', M. Abramowitz and I.A. Stegun, eds., Dover, New York.

Oppenheimer, J.R. (1928), Phys. Rev. 13, 66.

Payne, M.C. (1986), J. Phys. C 19, 1145.

Peeters, F.M., Helm, M., England, P., Hayes, J.R., Colas, E., Harbison, J. P. and Florez, L.T. (1989), Solid-State Electronics 32, 1309.

Platero, G., Schulz, P.A., Brey, L. and Tejedor, C. (1990), Proc. 4th Int. Conf. on Modulated Semiconductor Structures, eds. L.L. Chang, R. Merlin and D.C. Tsui, Surf. Sci. (to be published).

Ricco, B. and Azbel, M. Ya. (1984), Phys. Rev. B 29, 1970.

Ridley, B.K. (1988), "Quantum Processes in Semiconductors", 2nd Edition, Oxford University Press, New York.

Sarkar, C.K., Nicholas, R.J., Portal, J.C., Razeghi, M., Chevrier, J. and Massies, J. (1985), J. Phys. C 18, 2667.

Schulz, P.A. and Tejedor, C. (1989), Phys. Rev. B 39, 11187.

Seeger, K. (1982), "Semiconductor Physics", Springer, New York.

Sheard, F.W. and Toombs, G.A. (1988), Appl. Phys. Lett. 52, 1228.

Sheard, F.W., Chan, K.S., Toombs, G.A., Eaves, L. and Portal, J.C. (1988), 14th Int. Symp. on GaAs and Related Compounds, Inst. Phys. Conf. Ser. 91, 387.

Smith, R.A. (1978), "Semiconductors", 2nd Edition, Cambridge University Press, London.

Snell, B.R., Chan, K.S., Sheard, F.W., Eaves, L., Toombs, G.A., Maude, D.K., Portal, J.C., Bass, S.J., Claxton, P.A., Hill, G. and Pate, M.A. (1987) Phys. Rev. Lett. 59, 2806.

Snell, B.R. (1987a), Ph.D. Thesis, University of Nottingham, U.K.

Stern, F. (1972), Phys. Rev. B 5, 4891.

Toombs, G.A. and Sheard, F.W. (1989), in 'Electronic Properties of Multilayers and Low-dimensional Semiconductor Structures', J.M. Chamberlain, L. Eaves and J.C. Portal, eds., Plenum, New York.

Tsui, D.C. (1975), Phys. Rev. B 12, 5739.

Vawter, R. (1968), Phys. Rev. 174, 749.

Vigneron, J.P. and Ausloos, M. (1978), Phys. Rev. B 18, 1464.

Weil, T. and Vinter, B. (1987), Appl. Phys. Lett. 50, 1281.